ISOTOPE HARVESTING OF AQUEOUS PHASE IONS FROM HEAVY-ION FRAGMENTATION FACILITIES FOR THE PRODUCTION OF A $^{47}Ca/^{47}Sc$ GENERATOR

By

Emily Paige Abel

A DISSERTATION

Submitted to
Michigan State University
in partial fulfillment of the requirements
for the degree of

Chemistry – Doctor of Philosophy

2020

ABSTRACT

ISOTOPE HARVESTING OF AQUEOUS PHASE IONS FROM HEAVY-ION FRAGMENTATION FACILITIES FOR THE PRODUCTION OF A ^{47}Ca/^{47}Sc GENERATOR

By

Emily Paige Abel

Targeted internal radiotherapy is a promising new treatment method for metastatic cancers. Several scandium isotopes, ^{43,44,47}Sc, could serve as paired diagnostic and therapeutic (or "theranostic") isotopes for these diseases. While ideal production routes for diagnostic ^{43,44}Sc have been found using small medical cyclotrons, research to find a sustainable production method for the therapeutic isotope ^{47}Sc is ongoing. At the National Superconducting Cyclotron Laboratory (NSCL) and in the future at the Facility for Rare Isotope Beams (FRIB), a supply of ^{47}Ca, the parent of ^{47}Sc, can be produced on a regular basis when a ^{48}Ca primary beam is used. While the main function of the accelerated primary beam is to produce a user-specified secondary radioactive beam for nuclear physics experiments, >90% of the primary beam goes unreacted and is collected in beam stops. When a beam blocker with a water interior is used, the ^{48}Ca primary beam produces ^{47}Ca as the most abundant fragment resulting from nuclear reactions in the beam blocker. This method of production termed "isotope harvesting" allows for the use of unreacted, accelerated beams for isotope production. In the future at FRIB, production of ^{47}Ca through isotope harvesting is predicted to reach the TBq/day level when a ^{48}Ca primary beam is in use. This supply of ^{47}Ca will facility the production of ^{47}Ca/^{47}Sc generators for research quantities of ^{47}Sc.

Isotope harvesting methods for the generation of ^{47}Sc, among other interesting products available through this production method, have been explored through several experiments at the NSCL and the Cyclotron Lab at the University of Wisconsin-Madison. An isotope harvesting system has been developed to include a flowing-water target, components to condition and monitor the water, and components to collect radionuclidic products of interest. The durability of this system to irradiation

conditions has been tested using a low intensity ^{40}Ca irradiation and a high intensity proton irradiation. Through ^{48}Ca irradiations at the NSCL, methods to collect and purify ^{47}Ca have been tested and optimized. Using these methods, samples of ^{47}Sc with high radionuclidic purity have been generated and used to radiolabel DTPA-TOC, a biologically active molecule used to target neuroendocrine tumors. This work has verified the feasibility of using isotope harvesting to generate ^{47}Sc for nuclear medicine applications.

ACKNOWLEDGEMENTS

As I was thinking of the list of people I would like to acknowledge for helping me along this path, I felt grateful for all of the support I've received from my friends and family and colleagues. I would like to start by thanking the entire isotope harvesting group. While our group has grown from four members at the start to thirteen members currently, the support and camaraderie I've found in this group have been constant. Thank you all for the time and energy you've given making the experiments in this work a success, listening to my practice talks, reading drafts of papers, and making out group activities so much fun.

I would also like to thank a few people in particular. Thank you, Hannah, for all of the hours we spent together in lab during our first few years of grad school. We accidently sprayed each other with water from the harvesting system more times than I can count, but we also learned a lot together. I would also like to give a huge thanks to Kathi for all the scandium chemistry expertise she brought to our group and all the time and ideas she contributed to the experiments presented in this work. Thank you, Kathi, for spending so much time in lab with me! I would like to give a shout out to Hannah, Kathi, and Sam for being awesome office mates. I loved our conversations about work and life in general. I also hope Colton and Wes know how grateful I am for their dedication to building an isotope harvesting system and keeping it running for experiments no matter what problems they faced. Thank you for all the long hours you both contributed and the safety hoops you jumped through for all of our experiments!

I would also like to acknowledge the faculty support I received. Thank you to my committee for their constructive comments at each of our meetings. I'm also grateful for the

support of my undergraduate advisors, Dr. Feigl and Dr. Barstis. They encouraged my interest in research and my goal of going to grad school. Thank you, Dr. Feigl, for suggesting I explore nuclear chemistry! Finally, I would like to thank my graduate advisor, Greg. I can't express how much your support and advice has meant to me. Your guidance has always been patient, kind, and encouraging, especially when I struggled to have confidence in myself. Thank you for helping me grow as a scientist through your example and advice. I don't think I could have asked for a better advisor!

I feel lucky to have such a supportive family. My parents have always supported my education and my dream to be a chemist from the age of 12. Thank you, Mom and Dad, for encouraging me when things got tough and I started to doubt that dream. I would also like to thank my sisters for being my lifelong friends and for all the love and support they've given me. I'm grateful for my loving husband, Jarom. He always had a yummy dinner and a warm hug for me when I got home from a 15-hour day in lab. I'm also thankful for my dog, Tag, who was my buddy through grad school.

For all of these things and so many more, I would like to thank everyone who has helped me reach this goal. Now, I hope to use all of the support and opportunities I've received to help others with my passion for chemistry.

TABLE OF CONTENTS

LIST OF TABLES

LIST OF FIGURES

Chapter 1: Introduction

As the second leading cause of death in the United States, cancer claimed 595,930 lives in 2015. [1] About 90% of these deaths are caused by metastatic cancer, or cancer that has spread to other parts of the body. [2] These diseases have many treatment options including surgery, chemotherapy, and radiotherapy. Large tumors (*i.e.*, >1 g) can be treated using surgery and external radiotherapy since they can be readily identified. Some micrometastatic tumors are too small to be imaged accurately, limiting treatment options for these small growths. Targeted internal radiotherapy is one possible treatment option for small metastatic and micrometastatic tumors, using the targeted delivery of radionuclides to treat subclinical growths throughout the body.

Numerous radionuclides including alpha, beta, and Auger electron emitters are being considered for use in targeted internal radiotherapy. Radionuclides emitting these forms of radiation can damage the DNA of a cell and prompt apoptosis, or cell death. This occurs when the radiation directly deposits energy in the DNA or produces chemical species, such as radicals that can secondarily interact with the DNA. When these measures are successful in inducing a double strand DNA break, they often lead to irreparable damage and apoptosis. Additionally, radionuclides that emit positrons and low energy gamma rays (*i.e.*, 100 keV-400 keV) can be used to image metastatic cancerous growths in a targeted manner with Positron Emission Tomography (PET) and Single Photon Emission Computed Tomography (SPECT) imaging,

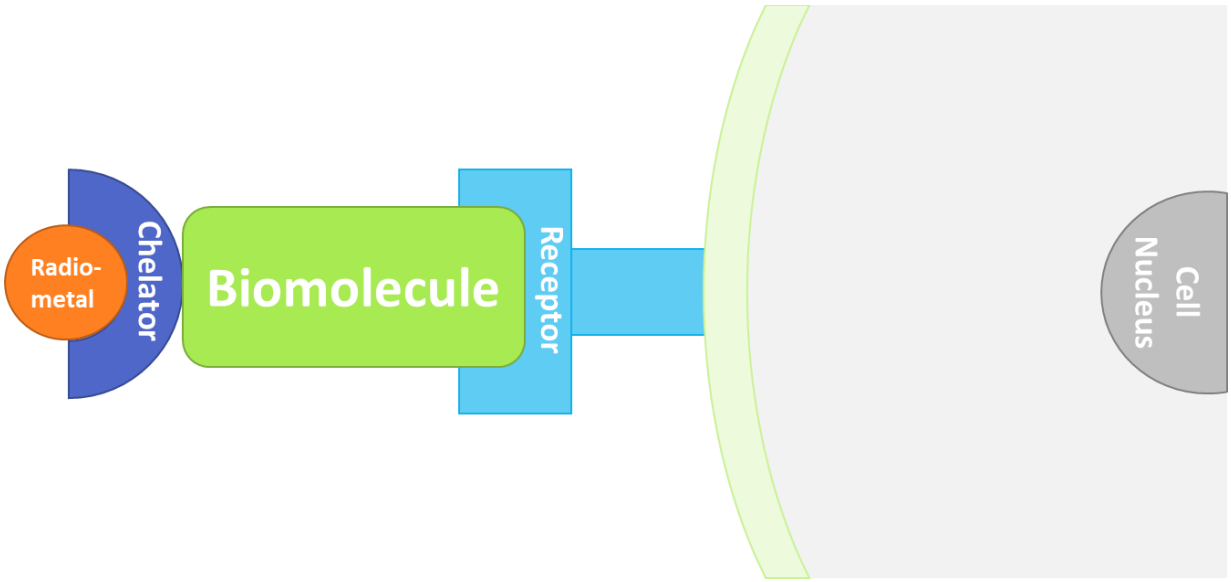

Figure 1.1: Radioconjugate Interacting with a Receptor on the Surface of a Cell.

respectively. Together, these capabilities would allow for metastatic cancer to be diagnosed and treated using targeted radionuclides.

To target cancerous growths, the radionuclides are bound to a targeting structure composed of a biologically active and a chelating component. The biological portion of the vector directs the movement of the radiopharmaceutical in the body, binding to the surface of cells upon interaction with receptors. Some radiopharmaceuticals are absorbed by targeted cells, decreasing the distance and increasing the potential for interactions between the emitted radiation and the cell DNA. Folate is one example of a small biological molecule that binds to folate receptors which are often over-expressed in a variety of cancers, including ovarian and lung cancer. [3,4] Attached to the biological entity is a chelating structure that binds to a radiometal. DOTA (1,4,7,10-tetraazacyclododecane-1,4,7,10-tetraacetic acid) is a macrocyclic chelating ligand that is known to bind to a variety of metals with its four tertiary amines and

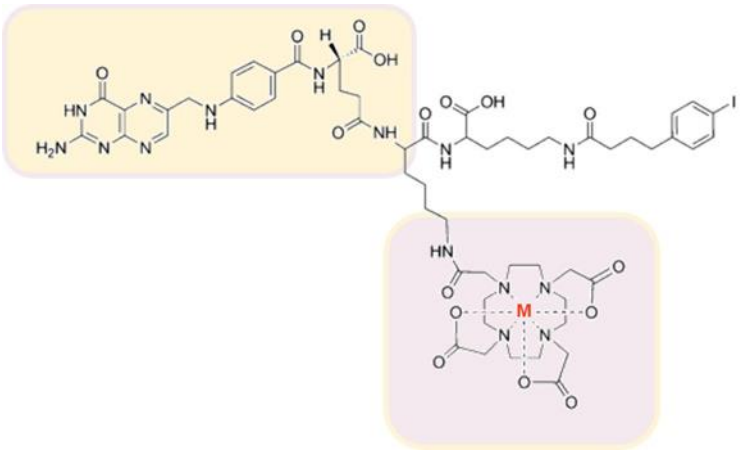

Figure 1.2: DOTA-Folate Conjugate Bound to a Radiometal [5]
The portion of the molecule highlighted on the top left is the biological folate component that binds to folate receptors; the lower portion of the molecule that is highlighted is the DOTA chelating ligand bound to a radiometal such as scandium, shown here as M. [1]

four carboxylic acid groups. This process is shown schematically in Figure 1 and an example of a DOTA-folate conjugate is given in Figure 2 (modified from [5]).

Ideally, the radionuclides used for therapy and diagnosis form a "theranostic" pair, meaning the radionuclides are isotopes of the same element. These radionuclides then have identical chemistry for radiolabeling and interacting within the body. [6] An initial low-dose imaging step can demonstrate the biodistribution and dosimetry of this chemical entity in the body. This can confidently be followed by high-dose therapy, since the therapeutic radioconjugate will behave identically to the imaging agent in the body. [7] One element that has such a theranostic pair is scandium. The β^- emitting ^{47}Sc has a 3.35 day half-life and a relatively low energy emission at an average energy of 162 keV ($E_{\beta 1avg}$ = 142.6 keV, $I_{\beta 1}$ = 68.4%;

[1] This figure was originally published in *JNM*. Cristina Müller, Maruta Bunka, Stephanie Haller, Ulli Köster, Viola Groehn, Peter Bernhardt, Nicholas van der Meulen, Andreas Türler, and Roger Schibli. Promising Prospects for ^{44}Sc-/^{47}Sc-Based Theragnostics: Application of ^{47}Sc for Radionuclide Tumor Therapy in Mice. J Nucl Med. 2014; 55; 1658-1664. © SNMMI.

$E_{\beta 2avg}$ = 203.9 keV, $I_{\beta 2}$ = 31.6%). [8] This low energy β^- particle is suited to treat small cancer metastases with a tumor diameter in the range of a few millimeters (*i.e.*, 2.0-3.8 mm). [9] This decay is also accompanied by a 159 keV gamma ray (I_γ = 68.4%) which is low enough energy to be visualized with SPECT imaging. [8] These decay properties as well as properties of ^{47}Ca, the parent of ^{47}Sc, are given in Figure 3. As a match to this therapeutic scandium isotope, both ^{43}Sc and ^{44}Sc have β^+ emissions that are suitable for PET imaging. [10–13] These isotopes have similar decay properties with low energy β^+ emissions and half-lives of approximately 4 hours. [14,15] However, ^{44}Sc has a high energy gamma ray at 1157 keV (I_γ = 99.9%), making ^{43}Sc more suitable for radiotherapy. [15]

These theranostic isotopes would be an improvement over the ^{68}Ga/^{177}Lu pair that is routinely used in the clinic for PET imaging and therapy, respectively. Since these isotopes are not of the same element, they bind to the targeting vector differently. [6] Differential binding

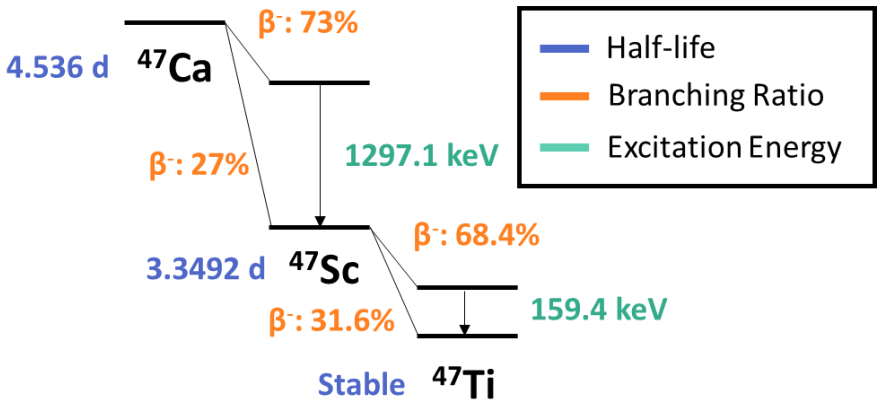

Figure 1.3: Simplified Decay Scheme for ^{47}Sc and its Parent ^{47}Ca[2] [8]

[2] Reprinted from ACS Omega, 5; E. Paige Abel, Katharina Domnanich, Hannah K. Clause, Colton Kalman, Wes Walker, Jennifer A. Shusterman, John Greene, Matthew Gott, and Gregory W. Severin; Production, Collection, and Purification of ^{47}Ca for the Generation of ^{47}Sc through Isotope Harvesting at the National Superconducting Cyclotron Laboratory, 27864-27872, Copyright (2020), with permission from the American Chemical Society under an ACS AuthorChoice License.

may affect aspects such as the pharmacokinetics of the two radiopharmaceuticals and binding with the targeted receptors. This means that the therapeutic radionuclide may have a different biodistribution than the diagnostic radionuclide, leading to lower doses for the tumorous tissue and higher doses for normal or radiosensitive tissues than was expected. In addition, the half-lives of the two radionuclides differ by more than two orders of magnitude with ^{68}Ga having a half-life of 68 minutes compared to ^{177}Lu with a half-life of 6.65 days. [16,17] After a few hours in the body, ^{68}Ga no longer provides information about the biodistribution and dosimetry of ^{177}Lu. [18] Thus, the chemical and nuclear properties of the scandium isotopes are much better matched to accomplish paired therapy and diagnosis.

In 2014, a study was performed by Müller et. al. to demonstrate the therapeutic ability of ^{47}Sc. [5] Several studies were performed including in vivo tests with a ^{47}Sc-DOTA-folate radioconjugate to take SPECT/CT images as well as to test the therapeutic effectiveness of ^{47}Sc. The radioconjugate was well localized in the cancerous tissues, allowing for excellent visualization of the tumors. The high resolution afforded by this radioconjugate would be helpful for pretherapy dosimetry. The therapeutic studies performed *in vivo* were marked by delayed tumor growth and therefore, a 54% increased survival time among the treated vs. control mice. This potential radiopharmaceutical demonstrated antitumor properties comparable to that of the ^{177}Lu- DOTA-folate radioconjugate. [5]

Even though these scandium isotopes have attracted research attention, a sustainable production route for ^{47}Sc has not yet been established. Several methods under study have encountered many of the same difficulties: prohibitively expensive target material, the formation of other scandium isotopes, or low production yields of ^{47}Sc. [10,19–26] These target

materials and scandium isotopes are shown in the relevant portion of the Chart of the Nuclides in Figure 4. The high cost of these production routes comes from the necessity of using isotopically enriched Ca and Ti target materials to increase the relative abundance of ^{46}Ca, ^{48}Ca, or ^{47}Ti in the target. The calcium targets in particular are very expensive due to their low natural abundances of ^{46}Ca and ^{48}Ca (*i.e.*, 0.004% for ^{46}Ca and 0.187% for ^{48}Ca). Additionally, $^{44m, 46, 48}$Sc are often produced as impurities even when an optimized beam energy range is used to produce ^{47}Sc. The presence of these scandium impurities could add significantly to the dose received by a patient without any added therapeutic benefit due to their gamma-ray emissions, as ^{46,48}Sc each have two high energy and intensity gamma rays (*i.e.*, ^{46}Sc: 889.3 keV at 99.98 and 1120.5 keV at 99.99% and ^{48}Sc: 983.5 keV and 1312 keV both at 100%) and ^{44m}Sc decays to its

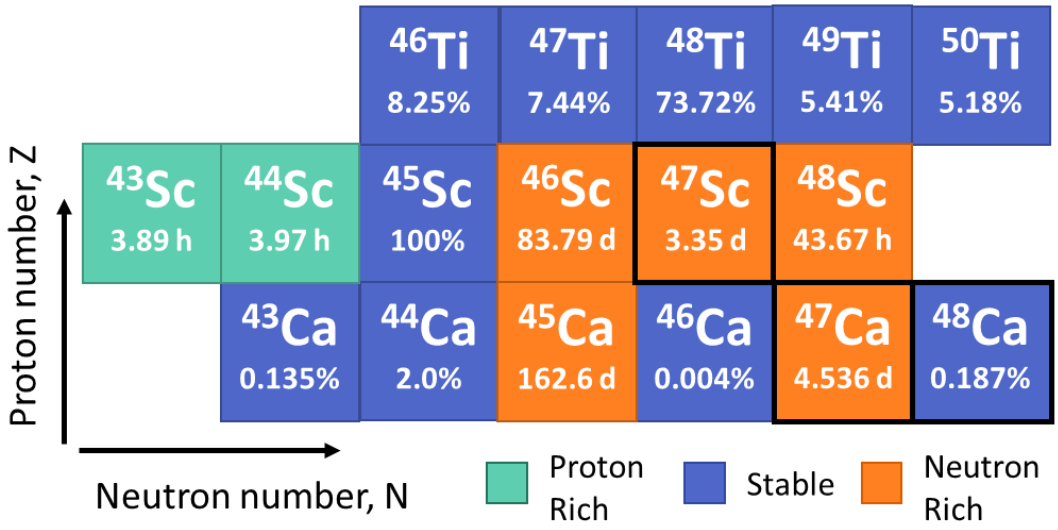

Figure 1.4: Chart of the Nuclides Region around ^{47}Sc
For the squares representing radionuclides, the half-life is given, while for the squares representing stable species, the natural abundance is given.[3]

[3] Reprinted from ACS Omega, 5; E. Paige Abel, Katharina Domnanich, Hannah K. Clause, Colton Kalman, Wes Walker, Jennifer A. Shusterman, John Greene, Matthew Gott, and Gregory W. Severin; Production, Collection, and Purification of ^{47}Ca for the Generation of ^{47}Sc through Isotope Harvesting at the National Superconducting Cyclotron Laboratory, 27864-27872, Copyright (2020), with permission from the American Chemical Society under an ACS AuthorChoice License.

daughter ^{44}Sc which has an emission of 1157 keV at an intensity of 99.9%. [15,27,28] Since all three of these isotopes are of the same element, they cannot be separated chemically to produce ^{47}Sc with a higher radionuclidic purity. Each of these radionuclides is also sufficiently long lived (*i.e.*, $t_{1/2}$ = 2.44 d, 83.79 d, and 43.67 h for ^{44m,46,48}Sc, respectively), making it is impractical to wait for them to decay to significantly improve the radionuclidic purity of the ^{47}Sc product. [15,27,28] Therefore, any method that produces a sizeable ^{44m}Sc, ^{46}Sc, or ^{48}Sc impurity is not a viable production method.

Proton and neutron irradiations as well as photonuclear reactions have been studied for the production of ^{47}Sc. [10,19–26] Several of these reactions are depicted in Figure 5 as well as described below. One production route investigated uses cyclotron irradiation of a natural calcium target or a ^{48}Ca enriched target to induce the following reaction: ^{48}Ca(p,2n)^{47}Sc. [19] Both ^{46}Sc and ^{48}Sc are produced in such irradiations by either the ^{48}Ca(p,3n)^{46}Sc or the ^{48}Ca(p,n)^{48}Sc reaction. In the energy range that most medical cyclotrons operate (< 20 MeV), the activity of ^{48}Sc produced is significant compared to that of ^{47}Sc (*i.e.*, ≥13% of the scandium activity depending on the energy range used). The quantity of ^{47}Sc produced from a natural calcium target is also quite low due to the low natural abundance of the target nucleus, ^{48}Ca. By increasing this abundance with an enriched ^{48}Ca target, the production yield for ^{47}Sc would increase. However, the production yield of ^{48}Sc as well as the production cost would also increase with such a target.

Another possible production route through proton irradiation uses a titanium target. Natural Ti targets have been employed in several studies, utilizing the following reactions to

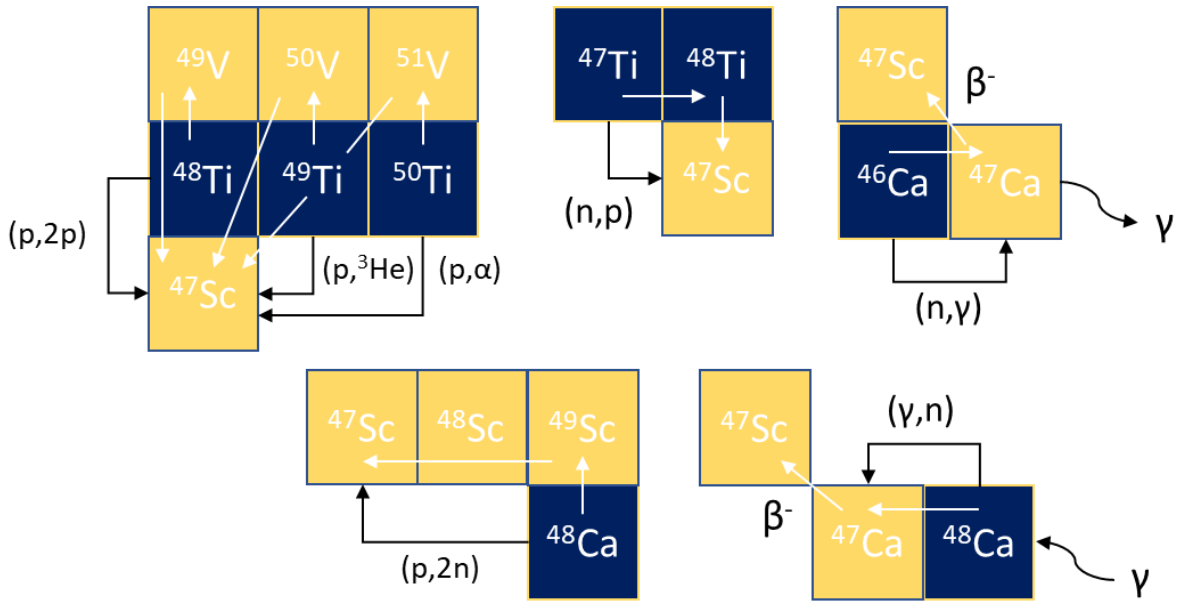

Figure 1.5: Depiction of Different Nuclear Reactions Resulting in the Production of ^{47}Sc.
Top row: ^{48}Ti(p,2p)^{47}Sc, ^{49}Ti(p,^{3}He)^{47}Sc, ^{50}Ti(p,α)^{47}Sc, ^{47}Ti(n,p)^{47}Sc, and ^{46}Ca(n,γ)^{47}Sc. Bottom row: ^{48}Ca(p,2n)^{47}Sc and ^{48}Ca(γ, n)^{47}Ca → ^{47}Sc.

produce ^{47}Sc: ^{48}Ti(p,2p), ^{49}Ti(p,^{3}He), and ^{50}Ti(p,α). [20,21] The optimal energy range for producing ^{47}Sc and minimizing ^{46,48}Sc production is 22-33 MeV, which again is higher beam energy than most medical cyclotrons can provide. [20] The ^{46,48}Sc impurity is relatively low at approximately 3% of the activity produced. However, ^{44m}Sc is a major contaminant, producing comparable activities to ^{47}Sc at all energies used with this production route. It has been suggested that using ^{50}Ti targets at proton energies of <20 MeV may allow for acceptable production yields for ^{47}Sc despite the low cross section observed in this energy range with a natural Ti target. [20] This enriched target may also reduce the coproduction of ^{44m}Sc which is primarily produced through the ^{47}Ti(p,α) and ^{48}Ti(p,nα) reactions. Work has also been done with an enriched ^{48}Ti target to reduce the ^{44m,48}Sc contaminants, but this method increases the ^{46}Sc impurities produced and has only been explored at energies >48 MeV. [21]

While the higher energy proton spallation reactions create many products, lower energy neutron reactions can be more finely controlled to favor only one nuclide. Neutron irradiations that produce ^{47}Sc involve the use of fast neutrons in the ^{47}Ti(n,p)^{47}Sc reaction or thermal neutrons in the ^{46}Ca(n,γ)^{47}Ca → ^{47}Sc reaction. [10,21] Both of these reactions require enriched target materials to reduce contaminants. The fast neutron reaction of titanium requires very high neutron fluxes on the order of 10^{14} n/(cm^2 s) to produce activities in the GBq range from a small target. [10] Few reactors can produce a neutron flux this large, limiting the practicality of this production route. The ^{46}Sc impurity from this reaction also limits its use with up to a 11.5% impurity being produced in some neutron spectra. [10] The thermal neutron reaction on an enriched ^{46}Ca target can produce GBq activities of ^{47}Sc with a several day irradiation at a thermal neutron flux of 10^{14}-10^{15} n/(cm^2 s). This production route avoids significant scandium impurities by using both an enriched target and the production of a ^{47}Ca/^{47}Sc generator. [10] The primary disadvantage of this production route is the requirement of expensive Ca target material enriched in ^{46}Ca to achieve a high yield and radionuclidic purity for ^{47}Sc.

Two photonuclear reactions have also been explored: ^{48}Ca(γ,n)^{47}Ca → ^{47}Sc and ^{48}Ti(γ,p)^{47}Sc. [22–26] In these reactions, high energy electrons are generated with an electron linear accelerator and are sent through a “radiator” material that converts some of the kinetic energy of the electrons into bremsstrahlung. The photons then pass through a target material to produce the desired radionuclide. The first photonuclear reaction listed above uses an enriched ^{48}Ca target due to the low abundance of this isotope in a natural Ca target. Even with this enriched target, however, activities of ^{47}Sc only reach the low MBq g^{-1} range using a 1 mA beam current. [22] No scandium impurities were detected using this production route as there

are no significant photonuclear reactions with a calcium target that lead to the production or generation of ^{44m,46,48}Sc.

The second photonuclear reaction mentioned above uses an enriched ^{48}Ti target. [23,24] Impurities from ^{46}Sc can be controlled by using an enriched target and by keeping the maximum photon energy below the energy threshold of the ^{48}Ti(γ,pn)^{46}Sc reaction (*i.e.*, < 22 MeV). With optimized parameters, this production route produced a ^{47}Sc yield of hundreds of MBq g^{-1}. It has been predicted but not yet experimentally verified that both of these photonuclear reactions can produce higher ^{47}Sc yields with optimized target geometries for the distribution of bremsstrahlung rays and higher beam currents. [22,24] The ^{48}Ti(γ,p)^{47}Sc production method was first studied in 1977, but has recently gained more attention as a potential sustainable production method for a ^{47}Sc supply. Recent studies by Rotsch et. al. in 2018 and Loveless et. al. in 2019 have demonstrated successful purification of ^{47}Sc produced in this way. [25,26] Additionally, the high purity ^{47}Sc sample produced in the Loveless et al study was used to radiolabel DOTA-TOC, demonstrating the feasibility of using ^{47}Sc from this production method in preclinical studies. [25]

While research into a future sustainable production method for ^{47}Sc is ongoing, an untapped supply of ^{47}Sc exists at nuclear physics accelerator facilities that provide fast, heavy ion beams, such as the National Superconducting Cyclotron Laboratory (NSCL) and in the future at the Facility for Rare Isotope Beams (FRIB). The NSCL produces high energy primary, stable beam to produce a user-specified secondary, radioactive beams through projectile fragmentation reactions. While a single isotopic secondary beam is generally used by the experimenters, the unreacted primary beam is collected in a solid metal beam blocker.

Although the amount of primary beam that passes unreacted through the target depends on the secondary beam specified by the users, often over 90% of the primary beam is unreacted. Using LISE++, a program that allows for optimization of experimental parameters for fragmentation reactions in a thin target and the separation of the resulting radioactive fragments in a zero-degree spectrometer, the amount of unreacted primary beam transmitted through the target can be estimated for a particular secondary beam. [29] For example, an experiment requiring the production of a ^{40}Mg secondary beam is predicted to have 94.8% of the primary ^{48}Ca beam left unreacted after the target.

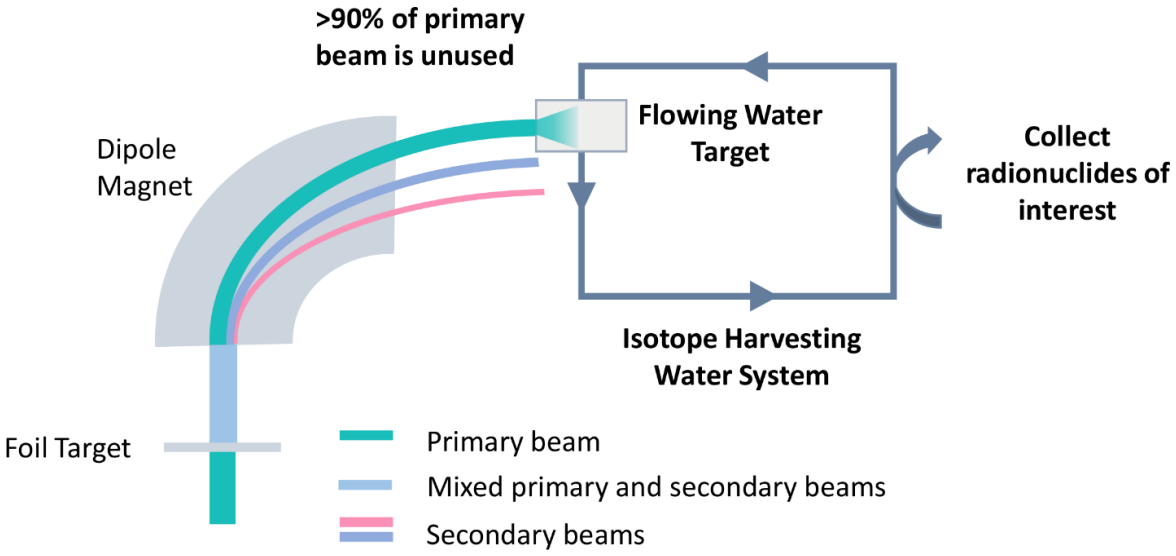

Figure 1.6: Isotope Harvesting from the NSCL
A stable, primary accelerated beam is used to produce exotic, radioactive secondary beams at the NSCL. A large portion of the initial accelerated stable beam goes unreacted at the target, is separated out of the radioactive cocktail beam at the first dipole magnet in the A1900 fragment separator and is then stopped in a beam stopper. A flowing-water target system can replace the solid metal beam blocker at the NSCL to allow for isotope harvesting.[4]

[4] Reprinted from Nuclear Instruments and Methods in Physics Research B, 478; E. Paige Abel, Katharina Domnanich, Colton Kalman, Wes Walker, Jonathan W. Engle, Todd E. Barnhart, Greg Severin; Durability test of a flowing-water target for isotope harvesting, 34-45, Copyright (2020), with permission from Elsevier.

This surplus primary beam can be collected off axis in a thick water target to induce further nuclear reactions in tandem with the primary experiment to produce longer-lived radionuclides. This emerging production method at accelerator facilities has been coined "isotope harvesting". [30] The harvesting water target can replace the solid metal beam blocker presently in the beam line after the first dipole magnet in the A1900 fragment separator at the NSCL (see Chapter 1 Figure 1.7). [31] At this point in the facility, the remaining primary beam after the fragmentation target has been separated from the radioactive beam cocktail and can be used for isotope harvesting. Figure 6 depicts the path of the primary beam as it produces exotic fragments at the fragmentation target, is separated from these exotic fragments in the first dipole magnet of the A1900 fragment separator, and is sent into a flowing-water target for isotope harvesting.

The ^{48}Ca primary beam is the second most requested primary beam at the NSCL. When the unreacted portion of this beam is implanted in a water target, ^{47}Ca is the most abundantly produced fragment. In the example of the ^{40}Mg secondary beam, the unused ^{48}Ca beam would produce 7.98(8) x 10^9 pps of ^{47}Ca (see Chapter 5 Section 5.2.3 and 5.3.1 for the measurement of this production rate). For a 120-hour experiment (the typical length of a nuclear physics experiment at the NSCL), this would result in 115(1) mCi or 4.27(4) GBq of ^{47}Ca produced in the isotope harvesting water target. Even with a 24 hour waiting period to allow for short-lived activity to decay, almost 100 mCi of ^{47}Ca would remain. In the future with FRIB, the production rate per particle should be greater than that with the ^{48}Ca beam from the NSCL due to the higher energy beam (*i.e.*, 240 MeV/nucleon at FRIB vs. 140 MeV/nucleon at the NSCL). With the anticipated FRIB ^{48}Ca primary beam intensity and the ^{47}Ca production rate measured at the

NSCL, at least 3.7 x 10^{12} pps will be produced at FRIB. This rate would result in the production of > 14 Ci or 520 GBq during a 24-hour experiment.

In addition to ^{47}Ca, other calcium and scandium isotopes including ^{45}Ca and ^{44m,46,47,48}Sc are produced in the water target. As with other production methods, these co-produced scandium isotopes cannot be chemically removed from the ^{47}Sc product and could add significant dose burden if used in therapeutic applications. Instead of harvesting ^{47}Sc directly, ^{47}Ca can be harvested and used to generate a high purity sample of ^{47}Sc. This avoids the many scandium isotopes that are co-produced in the water. While ^{45}Ca is coproduced and will not be separated from the ^{47}Ca, it decays to stable ^{45}Sc. This means that the presence of ^{45}Ca in the ^{47}Ca/^{47}Sc generator should not interfere with the radionuclidic purity of the generated ^{47}Sc. Additionally, the small number of atoms of ^{45}Ca produced and the long half-life of this radionuclide indicates that it will not affect the specific activity of the ^{47}Sc sample. This approach also allows for the processing of Ca^{2+} ions which have simple chemistry across a wide range of acidity and oxidative potentials as opposed to scandium ions which are easily hydrolyzed in neutral and basic conditions. Therefore, using a ^{47}Ca/^{47}Sc generator would allow for production of high-quality samples of ^{47}Sc.

Several experiments have been performed in the past and in the work presented here to demonstrate the feasibility of isotope harvesting and optimize techniques for collection and purification of isotope harvested radionuclides for a variety of applications. [32–37] The first proof of concept study was performed at the NSCL with an purified, fast ^{24}Na secondary beam collected in a small water volume. This experiment successfully demonstrated the ability to collect kBq quantities of an 85 MeV/nucleus ^{24}Na beam. [32] Other experiments demonstrated

successful collection and purification of a ^{67}Cu secondary beam from a mixture of other co-produced radionuclides in an aqueous medium. [34,38] In one experiment, the secondary beam contained only 2.9% ^{67}Cu among several other radionuclides. This experiment successfully recovered and purified a significant portion of the collected ^{67}Cu with a high radionuclidic purity. The purified product was then used to radiolabel a clinically significant antibody, which was used to demonstrate tumor uptake in an *in vivo* study. These experiments clearly demonstrated on a small scale the feasibility of using isotope harvesting as a production method for radionuclides with applications in nuclear medicine.

Moving forward with this isotope production method requires experiments that more closely resemble the anticipated isotope harvesting conditions at FRIB. This includes increasing the water volume, using a flowing-water target and isotope harvesting water system, and developing techniques for online collection of radionuclides from the system water. Additionally, these experiments should be carried out with higher intensity primary beams to produce radionuclides in the target compared to the low intensity radioactive secondary beams that were collected in a water target previously. The experiments presented here have allowed for the development of techniques and equipment that culminated in an 8 hour irradiation of a 50 L flowing-water isotope harvesting system with a 140 MeV/nucleon 80 pnA ^{48}Ca beam that produced a mCi level ^{47}Ca/^{47}Sc generator. A portion of the purified ^{47}Ca was also used to measure the three most intensity branching ratios for this radionuclide, reducing the uncertainty compared to values in the literature and improving the precision with which this product was quantified. These experiments allowed for the optimization of chemical techniques to produce high purity ^{47}Sc that could be used in preclinical studies. The techniques and

knowledge gained through these experiments will assist in the translation of these methods to isotope harvesting at FRIB to produce a supply of ^{47}Sc for further research.

Chapter 2: Development of Isotope Harvesting System

To capitalize on the availability of unused accelerated primary beam to produce long-lived radionuclides of interest for applications, an isotope harvesting target and water system were developed. These efforts began when collaborators built and tested a stationary 100 mL water target that was irradiated with a secondary radioactive beam. The present efforts by the Isotope Harvesting group at Michigan State University started with bridging the gap between this small, static volume used in early exploratory work and the design of the much larger flowing-water beam dump at the Facility for Rare Isotope Beams (FRIB) which is presently under construction. Several generations of isotope harvesting targets and water systems have been developed and tested through irradiations of several stable, accelerated primary beams at the National Superconducting Cyclotron Laboratory. The targets and water systems developed will be presented here.

2.1 Introduction

Previous isotope harvesting experiments at the NSCL have used a water-based target system and a secondary radioactive beam for proof-of-concept experiments for collection in and extraction from a water medium [32–35]. This target system included a 100 mL static water target enclosed in a PTFE (polytetrafluoroethylene) body with a thin Kapton front window shown schematically in Figure 2.1 [32]. Harvesting experiments with this target collected low intensity particle picoamperes (ppA) radioactive beams produced at the NSCL. Experiments with radioactive beams purified through separation in the A1900 fragment separator [31,33],

cocktail beams containing a mix of secondary radioactive fragments [32,34], and cocktail beams containing both a variety of radioactive particles and stable primary beam particles [35] were carried out. The beam particles passed through the Kapton front window and were stopped in the interior water volume demonstrating successful collection of fast, heavy ions in an aqueous medium. Separation methods performed on the collection samples also supported the feasibility of purifying the collected radioactive products of interest for use in further applications [33–35].

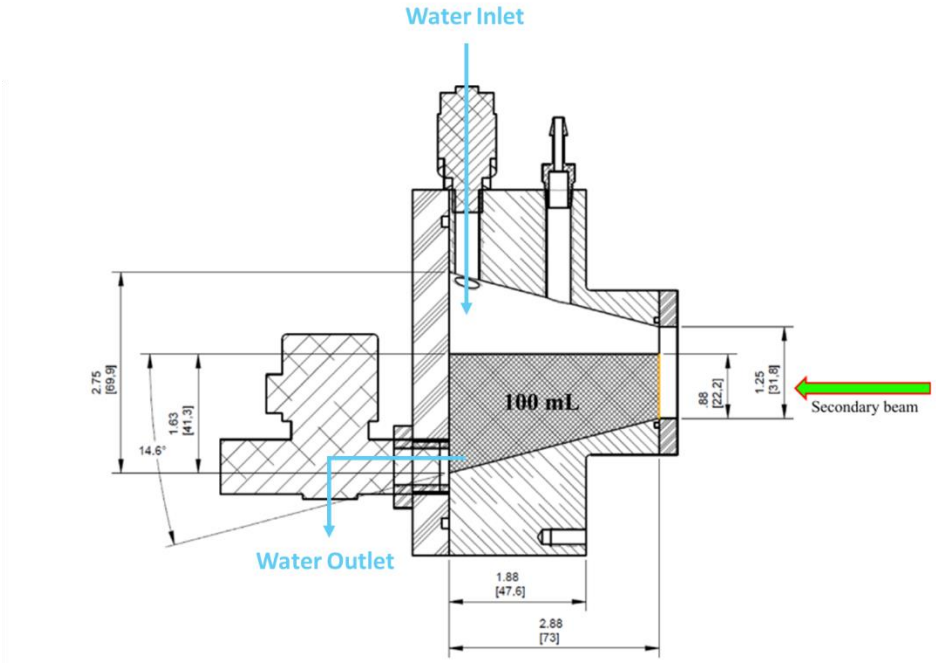

Figure 2.1: Water-Based Target for Low Intensity Collections
A vertical cross section of the water-filled target encased in PTFE and a Kapton front window is shown schematically. This target was used to collect fast radioactive secondary beams. The target was filled with water remotely through the top left port and was drained remotely with the port at the back of the target (on the left in the drawing).[5]

[5] Reprinted from Nuclear Instruments and Methods in Physics Research A, 747; Aranh Pen, Tara Mastren, Graham F. Peaslee, Kelly Petrasky, Paul A. DeYoung, David J. Morrissey, Suzanne E. Lapi; Design and construction of a water target system for harvesting radioisotopes at the National Superconducting Cyclotron Laboratory, 62-68, Copyright (2014), with permission from Elsevier.

Given that the full beam intensities at the NSCL are already on the order of particle nanoamperes (pnA) and the anticipated intensities at FRIB will be on the order of particle microamperes (pμA), the target system for isotope harvesting of the primary beam at these facilities will need to withstand with many orders of magnitude higher beam intensities than those tested with the static water-filled target system. Additionally, these heavy ion beams will be accelerated to higher energies at FRIB compared to those available at the NSCL and therefore, will deliver more power to the water. Together, these effects will result in primary beam powers of up to 400 kW with up to 325 kW deposited in the isotope harvesting beam dump at FRIB. These power levels are enormous compared to the maximum power depositions of 9×10^{-6} kW used in the previous static water target irradiations and 0.5 kW with the available beams at the NSCL.

A direct result of high beam power in the target is a large heat deposition as the beam stops and transfers kinetic energy to the target shell and water interior. One particular concern is the heat transfer from the target shell to the water interior. Insufficient heat transfer and dissipation can lead to temperatures in the target shell significantly above the boiling point of the system water, resulting in nucleate boiling at the interface between the target shell and the water. This produces vapor pockets at the interface of these materials further reducing heat transfer. If an irradiation were to continue under these circumstances, the target shell could reach extreme temperatures and potentially beyond the melting point of the material. Another effect of high-power beams is the production of corrosive radiolysis products, such as radical and oxidizing species, in the water interior of the target. Exposure of target materials to this environment could lead to degradation and mechanical weakening of the target. [39]

Both the high temperature and corrosive environment produced with a high-power deposition could result in catastrophic failure of the target. This presents a serious safety issue if a leak in the system should develop, releasing high levels of radioactivity transported in the flow of water. Additionally, failure of the beam dump would interrupt the nuclear physics program which is the primary mission of accelerator facilities like the NSCL and FRIB. To avoid target failure and interruptions to the experimental program at FRIB, the beam dump must be able to absorb the high-power primary beam in a safe manner for at least 1 year or 5500 hours of operation. Thus, the design for the isotope harvesting target at FRIB must be able to minimize and withstand damaging effects from this large power deposition a target.

The current design plan for the isotope harvesting target or beam dump at FRIB has been described in Avilov, et al [39]. The design features a rotating cylinder with a Ti64 alloy (grade 5 alloy: 6% Al, 4%V, mass balanced with Ti) shell and a flowing-water interior depicted in Figure 2.2. The target shell material of Ti64 was chosen for many reasons such as its strength and resistance to corrosion as well as its availability as a material that can be used in additive manufacturing techniques such as 3D printing. The target is a torus 70 cm in diameter and 8 cm tall along the rim that will be irradiated. To effectively dissipate the heat produced from the primary beam power deposition, the target will be rotated at 600 rpm and water will flow through the interior at a rate of 60 gallons per minutes. The target shell also includes a double wall depicted in Figure 2.2b, that directs the flow of water into the target through a narrow 2 mm space between two thin 0.5 mm Ti64 walls. This dramatically increases the flow of water over the target shell and therefore, the heat transfer between the target shell and the water.

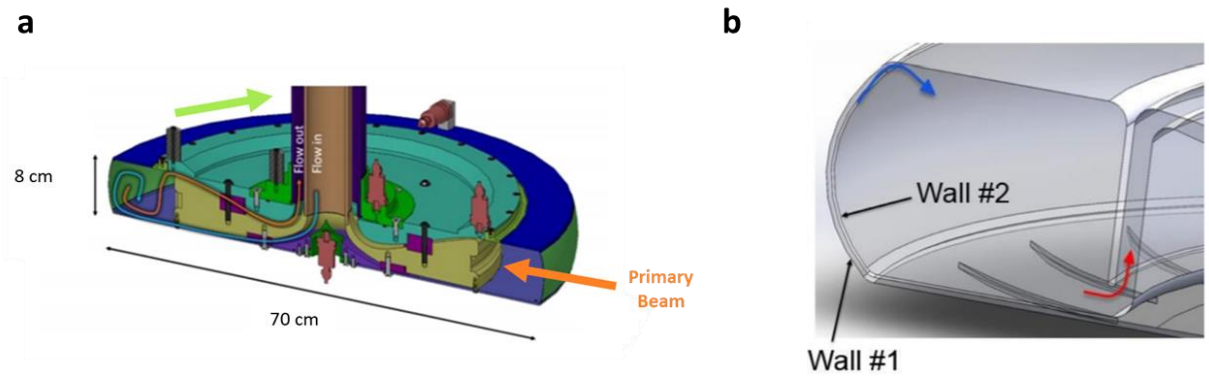

Figure 2.2: FRIB Isotope Harvesting Target Design
A cross sectional view of the isotope harvesting beam dump designed for FRIB (a) and a closer view of the double walled design of the target shell along the bottom and rim of the beam dump target (b). In both pictures, the blue arrow depicts the flow of cold water entering the beam dump and the red arrow traces the path of the higher temperature water leaving the beam dump. The picture on the left also has a green arrow that indicates the direction of the rotation of the target and an orange arrow that indicates the direction of the primary beam.[6]

All of these features facilitate the removal of heat from the target shell and prevent boiling at the interface, as described previously.

In addition to using a corrosion resistant material for the target shell, a water system is needed to monitor and reduce the effect of the corrosive products of radiolysis in the target. The present efforts focused on the long-lived molecular products of radiolysis in prototype isotope harvesting systems. Multiple sensors have been used during experiments to understand the buildup of these products as well as anticipate unsafe levels before they occur. Components were also tested to destroy or purge the system of these radiolysis products to prevent a concentrated build up. Finally, the prototype water system must contain components that

[6] Reprinted from Nuclear Instruments and Methods in Physics Research B, 376; Mikhail Avilov, Adam Aaron, Aida Amroussia, Wladimir Bergez, Carl Boehlert, Thomas Burgess, Adam Carroll, Catherine Colin, Florent Durantel, Paride Ferrante, Tiffany Fourmeau, Van Graves, Clara Grygiel, Jacob Kramer, Wolfgang Mittig, Isabelle Monnet, Harsh Patel, Frederique Pellemoine, Reginald Ronningen, Mike Schein; Thermal, mechanical and fluid flow aspects of the high power beam dump for FRIB, 24-27, Copyright (2016), with permission from Elsevier.

carryout the main purpose of isotope harvesting: the extraction of radionuclides of interest for further use in applications.

Isotope harvesting efforts at the NSCL have focused on the design and testing of targets and water systems for isotope harvesting at increasingly FRIB-like conditions. In the following chapters, several isotope harvesting experiments that have been carried out to test the durability of these systems (Chapters 3 and 5), and to demonstrate proof-of-concept for the extraction of radionuclides for further applications (Chapters 4, 6, and 7) will be described and the results analyzed. [37,40,41] The flowing-water target was used in three locations for the present experiments: (1) at the end station of a beam line at the NSCL for a low intensity experiment with ^{48}Ca (Chapter 4), (2) at the end of the beam line at the Cyclotron Laboratory at the University of Wisconsin-Madison for a high intensity proton irradiation (Chapter 5), and (3) at the beam blocker position in the A1900 fragment separator at the NSCL for two high intensity ^{48}Ca irradiations (Chapter 6, 7, and 8). The beam blocker position is indicated in a

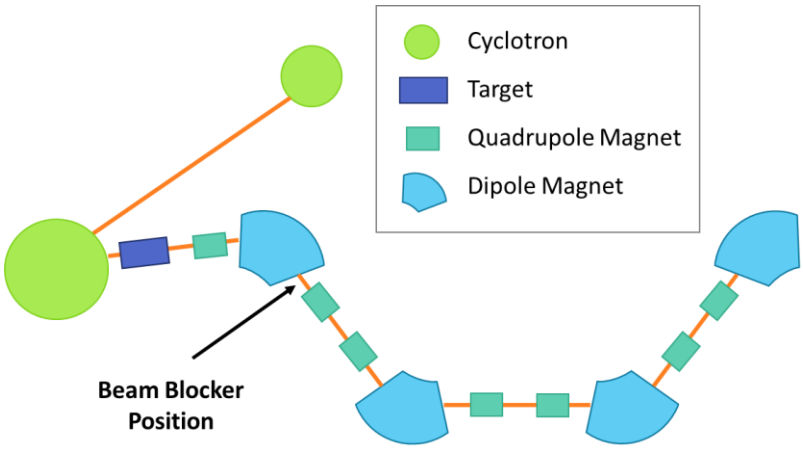

Figure 2.3: Placement of the Isotope Harvesting Target at the Beam Blocker Position
The solid metal beam blocker is positioned after the first dipole magnet in the A1900 Fragment Separator at the NSCL and was temporarily replaced with the isotope harvesting target for a few high-intensity isotope-harvesting experiments [31].

schematic of the cyclotrons and the A1900 Fragment Separator in Figure 2.3. The isotope harvesting targets and water systems used in the present experiments are introduced below.

2.2 Target Design

2.2.1 Generation 1: Low Intensity ^{40}Ca Irradiation

The first flowing water target for isotope harvesting was used to test the durability of a disk of Ti64 material and to demonstrate the production and collection of radionuclides produced from a primary beam irradiation of a water target (see Chapter 3). The target used for this experiment had a shell made mostly of high-density polyethylene. The shell of the target was designed for a flow of water to enter at an inlet in the bottom and exit through an outlet at the top. The internal chamber could hold approximately 120 mL of water at a time. The target and the placement at the end of the beam line are shown in Figure 2.4.

At the front of the target, a small Ti64 disk was used as the beam entrance window. This disk, shown in Figure 2.5, was 0.7 mm thick with a diameter of 15 mm exposed to the water. The surface of the disk was divided into two halves, with one half milled smooth and the other half left with the rough texture from the manufacturing process. The material was fabricated by Stratasys through 3D printing since this manufacturing technique which will be used to make the FRIB beam dump. [39] This technique can fabricate the complex internal design in a single process that traditional machining cannot achieve. Even though only a simple disk of the material was used in this target, this technique was used so that the material was made in an analogous way to the material to be used for the FRIB beam dump. Therefore, this target design moved closer to the anticipated FRIB beam dump design with the Ti64 front face and the flowing-water interior.

During the irradiation, a leak developed in the first-generation target between the main shell of the target and the back plate (Figure 2.4b). The target was not designed to be able to handle the periodic pressurization from the pulsing of the diaphragm pump that was used to flow water through the target. This put pressure on the backplate, deformed the O-ring that was intended to make a water-tight seal, and led to a small water leak. This target design was not used for any future irradiations due to the potential radiation safety hazard it presented.

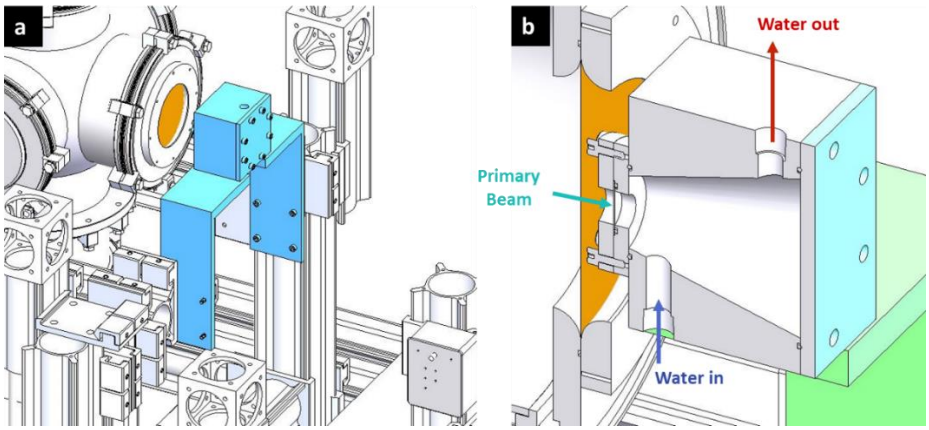

Figure 2.4: Overview and Cross-Sectional View of Target
Drawing of the placement of the flowing-water target at the end of a beam line at the NSCL (a) and a cross-sectional view of the inside of the target where beam enters through the front Ti64 disk as shown by the teal arrow (b). Water circulated through the target entering from the bottom and leaving through the top as shown by the blue and red arrows, respectively.

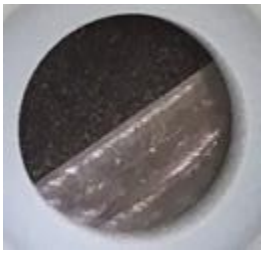

Figure 2.5: Ti64 Target Window
The Ti64 disk is shown inserted in the high-density polyethylene target body. The area shown was exposed to the irradiated water on the inside of the target during the experiment. The half towards the top has the rough texture resulting from the additive manufacturing process while the bottom half has a milled smooth texture.

2.2.2 Generation 2: ^{1}H and ^{48}Ca Irradiations

A next-generation flowing-water target was designed to resemble the FRIB beam dump more closely. This target design was used in the proton irradiation described in Chapter 5 as well as the three ^{48}Ca irradiations described in Chapters 4, 6, 7, and 8. The second generation target has a shell made of Ti64 with a hollow interior and an additional internal Ti64 wall close to the front face of the target. As with the FRIB target design, this double wall featured two 0.5 mm Ti64 walls with a 2 mm gap between them through which the cold incoming water flows. The water flow is then directed into a larger chamber behind the interior wall and out an exit channel. The target was operated with a water flow of approximately 11 L/min. The target body is 12.5 x 5.1 x 5.1 cm as shown in Figure 2.6 with an interior space that can hold approximately 86 mL of water. The dimensions of this target were chosen to match the size of the existing

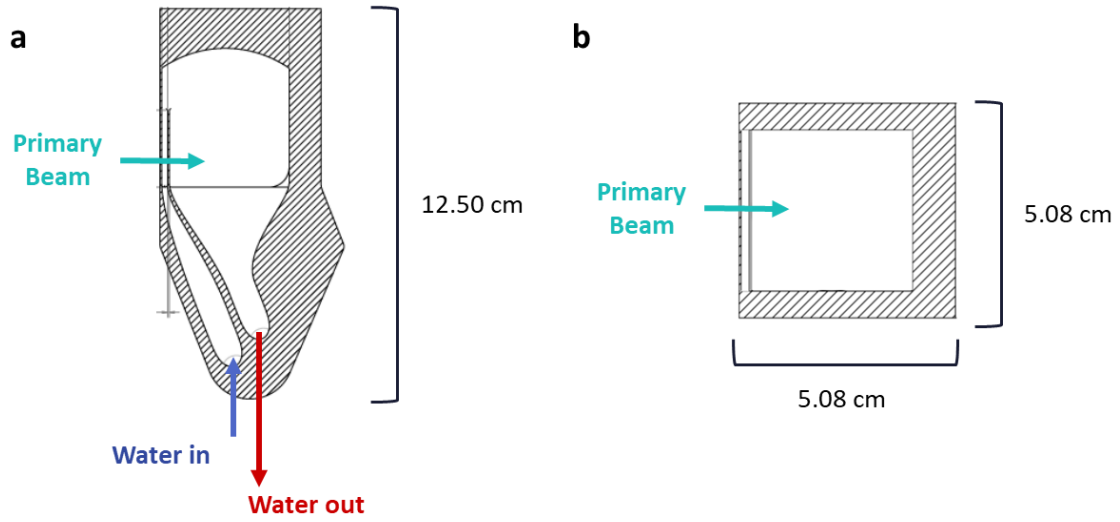

Figure 2.6: Schematic Drawing of Generation 2 Beam Blocker
A vertical (a) and horizontal (b) cross section of the inside of the target is depicted. The teal arrows show the direction of the primary beam in both pictures. The "front face" of the target is the first layer of Ti64 that the primary beam passes through while the interior wall is the second layer of Ti64 traversed by the primary beam.

beam blocker of the A1900 separator at the NSCL. This allowed the flowing-water target to replace the existing solid metal beam blocker temporarily with relatively few adjustments. The final target design was produced by 3D printing and therefore, had a rough texture as described previously.

Since the inside of the target and the uniformity of the material cannot be directly observed, CT scans were taken of several targets using a micro CT scanner (Perkin Elmer, Quantum GX μCT). Example CT images from scans of two targets are shown in Figure 2.7. The target shown in Figure 2.7a demonstrates the inconsistencies that can occur during the manufacturing process with an air bubble in the front wall and a bend in the interior wall. Air pockets in the target shell will interfere with heat transfer between the front target face and the water. Both air pockets and bends in the walls can also compromise the strength of the thin structures. In contrast, the target shown in Figure 2.7b shows uniformity in both the exterior

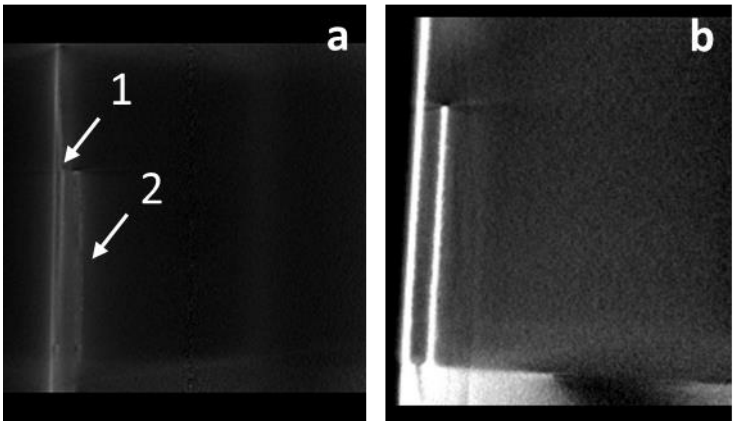

Figure 2.7: CT Scan of Beam Blocker Made through Additive Manufacturing
In the first image, an air gap in the front wall (1) and a bend in the inner wall (2) can be observed (a). The second image shows two straight and uniform walls (b).

and interior wall that is desired in the construction of these targets. Only non-defective targets such as the one shown in Figure 2.7b were used for irradiations. These scans also provided a precise measurement of the thickness of the walls. This measurement was used to calculate the energy of the beam in the water layer of the target which can aid in understanding the production of radionuclides and radiolysis products in the target.

2.3 Water System Design

2.3.1 Generation 1: Low Intensity ^{40}Ca Irradiation

2.3.1.1 Water System

The flowing water system used in the low intensity ^{40}Ca irradiation (see Chapter 3) included sensors, membrane contactors, pumps, a water reservoir, ion exchange resins, and pieces of a platinized titanium mesh arranged according to the schematic shown in Figure 2.8 and in the pictures in Figure 2.9. These components were all connected by 1/4" O.D., 3/16" I.D. high-density polyethylene tubes and polypropylene fittings through which water was pumped at a flow rate of 1 L/min using an air operated diaphragm pump (Yamada NDP-5FVT).

Three sensors were used to detect the level of radiolysis products in the water: a Honeywell Midas Gas Detector for detecting hydrogen gas (MIDAS-E-H2X), a Mettler-Toledo Thornton pHure Sensor (2003i-UPW/120), and a Mettler-Toledo Thornton High Performance Dissolved Oxygen Sensor (InPro6050 polarographic oxygen sensor). A fourth sensor, a Mettler-Toledo Thornton UniCond Conductivity Sensor (1/2" NPTM titanium 0.1 cm^{-1} sensor, part number 58 031 406), was used to detect dissolved ions in the water which could indicate the introduction of ions to the water from corrosion. An Omega Micro-Flo paddle wheel flow meter (part number FTB323D) was used to measure the flow rate of the water continuously. The

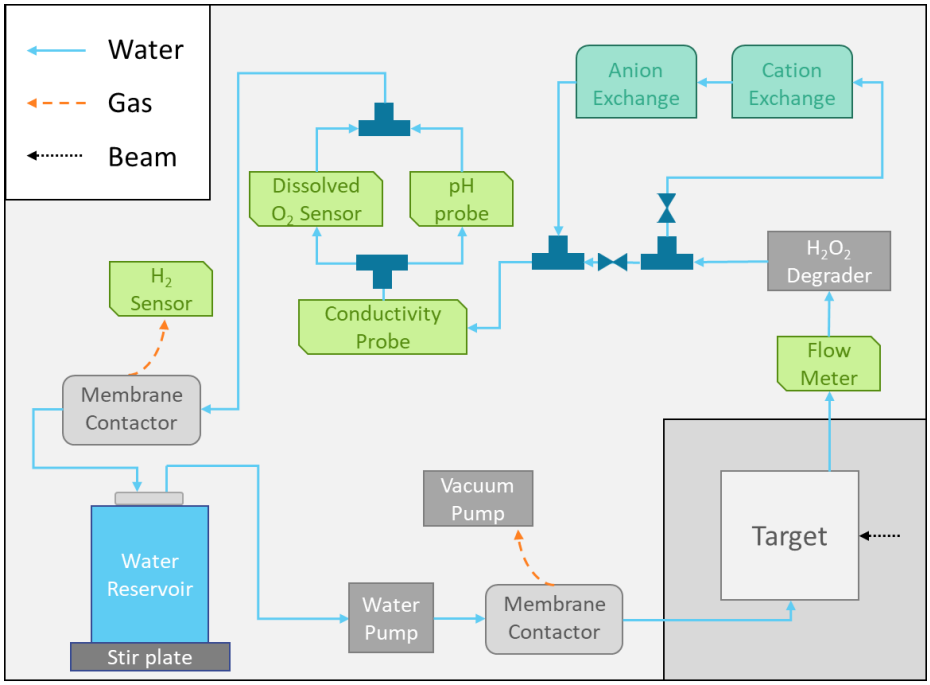

Figure 2.8: Schematic of Generation 1 Water System
The black lines around the water system and the target indicate secondary containment. The darker box around the target indicates a separate secondary containment outside of the main system. The dark blue components show important fittings including t-fittings that connect three tubing branches and valves that can direct the flow of the water.

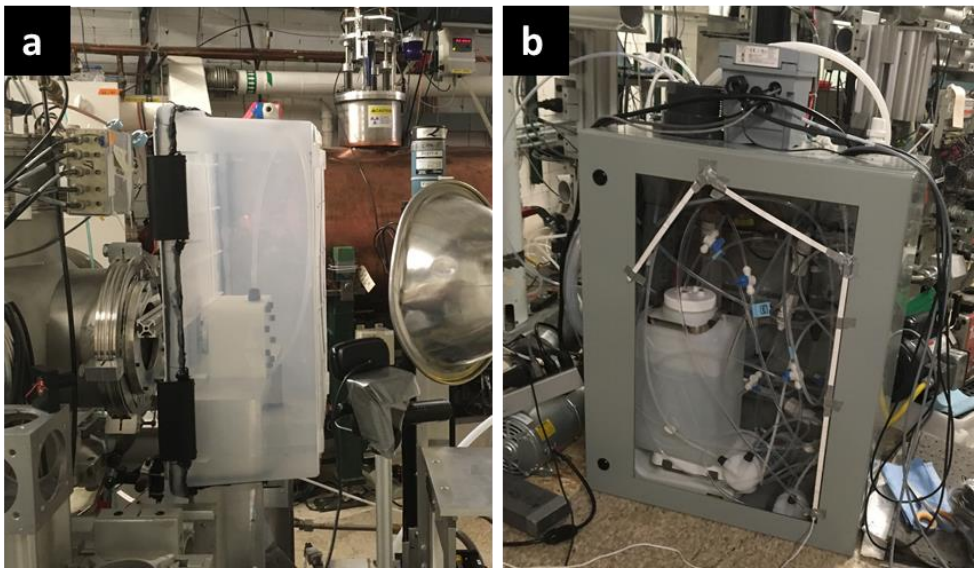

Figure 2.9: Images of Generation 1 Target and Water System at Beam End Station
The target was housed in plastic secondary containment at the beam line end station (a) and all other water system components were enclosed in water-tight secondary containment adjacent to the beam line (b).

outputs of the conductivity, pH, and dissolved oxygen sensors as well as the flow meter were connected to a Mettler-Toledo M800 multi-parameter transmitter, which recorded readings from each probe every 5 seconds.

Two 3M Liqui-Cel membrane contactors (2.5 x 8 EXF, Membrane X40) were used to manipulate the dissolved gas content of the water. One of the membrane contactors (MC) was connected to a Marathon electric vacuum pump (M100GX, 1/6 HP) on the lumen side of the MC and was placed before the target to degas the water just before it entered the target volume. This reduced the number of possible air bubbles in the target to maximize heat transfer between the Ti64 disk and the water. The second MC was connected to the hydrogen gas sensor on the lumen side and, allowed H_2 to escape the water and be measured by the MIDAS gas sensor. Due to the operating requirements of the H_2 sensor, laboratory air flowing at 500 mL/min was used as flush gas to deliver H_2 to the sensor. This led to a re-equilibration of the water with atmospheric oxygen and carbon dioxide at the second MC, which in turn effected the readings of the dissolved oxygen sensor and the pH probe.

The system water was also exposed to small pieces of platinized titanium mesh that were held in place with glass wool and a set of polypropylene fittings. This component, referred to as the degrader, was included as a catalyst to break down H_2O_2 produced through radiolysis. This process was expected to proceed through the following reaction: [42]

$$H_2O_2 \rightarrow H_2O + \frac{1}{2}O_2.$$

This reaction was utilized to break down the main long-lived corrosive radiolysis product, H_2O_2, to water and molecular oxygen.

Cation and anion exchange resin beds (AG 50W-X8 and AG 1X8, respectively; 20-50 mesh size; BioRad) depicted in Figure 2.10 were made using 3/4" O.D., 5/8" I.D. polyethylene tubing and were connected to the rest of the system via polypropylene compression fittings and reducing unions on both sides of the tubing. About 10-15 mL of resin was used in each column and was held in place by glass wool plugs at the top and bottom of the resin beds. The larger tubing and low mesh size of the resin allowed a flow rate of 1 L/min through the columns with minimal back pressure. An additional set of resin beds constructed in the same way were used prior to the experiment to purify the water to a minimum conductivity of 250 nS/cm. These resin beds were connected to the system by closing the valve to the ion exchange resin bed loop in the system and connecting the tubing from either side of this loop to the resin beds used to purify the water.

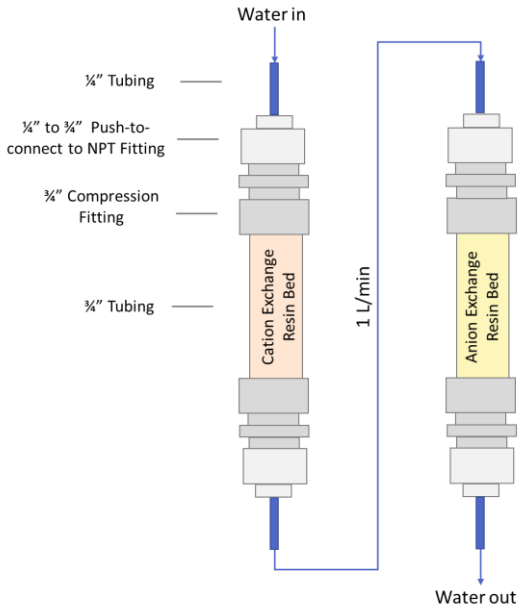

Figure 2.10: Column Configuration for Aqueous Ion Collection
The flow of water is indicated by the blue arrows from the top left of the figure, through both resin beds and ending at the bottom right of the figure.

The system was organized in this order for optimal sensor readings and conditions at each component. The first membrane contactor that served to degas the water was placed before the target and after re-equilibration with atmospheric air at the second membrane contactor and at the head space of the reservoir. The degrader was placed after the target so that the water coming from the target, with the highest concentration of H_2O_2, was put in contact with the degrader material before going through the rest of the system. The membrane contactors, in particular, are sensitive to degradation from H_2O_2 exposure. Two sensors in the system had competing flow rate requirements. The flow meter produced reliable readings at flow rates of about 1 L/min or higher. However, the pH probe had a pressure limit that required lower flow rates, significantly below 1 L/min in this system, to produce reliable readings. This conflict was solved by setting the flow rate at 1 L/min and placing the dissolved O_2 and the pH probe in parallel. This allowed for accurate flow meter readings while cutting the flow rate to the pH probe down to about 500 mL/min. Finally, the ion exchange resins were placed on a loop that could be bypassed using two valves to accomplish the two phases of the experiment: 1) the water bypassed the resin beds during the irradiation to allow the accumulation of any ions resulting from corrosion and subsequent detection by the conductivity probe and 2) after the irradiation, the valves were used to direct the flow of water over the resin beds to collect radionuclidic and stable ions from the water.

2.3.1.2 Conclusions about the Generation 1 Water System

The membrane contactors contain a material, called a potting material, which maintains a water-tight seal between the lumen and the shell side and is sensitive to decomposition by H_2O_2. After the irradiation, water droplets were discovered in the tubing that connected the

lumen side of the first membrane contactor to the vacuum pump, indicating that the level of H_2O_2 that built up in the system was sufficient to degrade the potting compound. It was concluded that other means of degassing the water should be used given the level of H_2O_2 produced in the system and that the capacity for catalytic degradation of H_2O_2 should be increased.

An elemental analysis of the ions in the water system showed a large amount of potassium ions in the system. These ions mainly originated from the pH probe which uses a flow of counter ion from its electrolyte solution to measure the pH of the water. This source of ions interfered with measurements of corrosion with the conductivity probe. Exposure of the system water to the air for the H_2 measurement at the second membrane contactor and through the vented headspace at the reservoir led to equilibration of the degassed system water with atmospheric O_2 and CO_2. This interfered with both the measurement of dissolved O_2 and the pH level. These competing measurements demonstrated that more compatible sensors should be used and that when compatible sensors are unavailable, the most important measurements should be prioritized. These lessons were implemented to improve the design of the subsequent generations of water systems.

2.3.2 Generation 2 and 3: ^{1}H and Low Intensity ^{48}Ca Irradiation

Two experiments with a low intensity ^{48}Ca beam (Chapter 4) and a high intensity proton irradiation (Chapter 5) were performed with identical targets and very similar next-generation water systems. [36,40] Due to their similarities, these systems will be described collectively with the minor differences indicated. A schematic diagram of the isotope harvesting system used in low intensity ^{48}Ca irradiation is shown in Figure 2.11 while that for the high intensity

proton irradiation is shown in Figure 2.12. The system used for these experiments resembled the first-generation harvesting water system with adjustments for lessons learned from the first experiment. One important difference was the larger size of the system with 36 L of water flowing through many more feet of tubing. The water flow was supported by a centrifugal pump (Grundfos CRNE 3-6) running in constant pressure mode, as opposed to the pulse mode diaphragm pump used previously. The water was directed through multiple specialized loops, branching out from the 40 L water reservoir (McMaster Carr, portable stainless-steel dispensing tank). This allowed for more flexibility in the flow rates directed to each section of the system. Flow to the target was adjusted by changing the pressure on the pump while each of the smaller loops had precision flow valves (Ham-let, 316 stainless steel) that could adjust their flow rates.

The target loop had the largest water flow at 10 L/min, directing water through nylon-reinforced polypropylene tubing to a second-generation isotope harvesting target. The lines to the target contained non-spill coupling valves that could be disconnected and reconnected to a series of large mixed bed resins (McMaster-Carr, Filter media PVC water deionizer). The water was cycled rapidly through these resin beds to remove dissolved ions from the system water. This step was performed so that the final radionuclidic product would contain the lowest possible level of stable ionic contaminants.

Another section of the system, the hydrogen peroxide decomposition box, conditioned the water throughout each irradiation. The decomposition box received water at a rate of 300 mL/min through ¼" polypropylene tubing. This loop was the most significant difference between the water systems used in the two experiments. During the low intensity ^{48}Ca

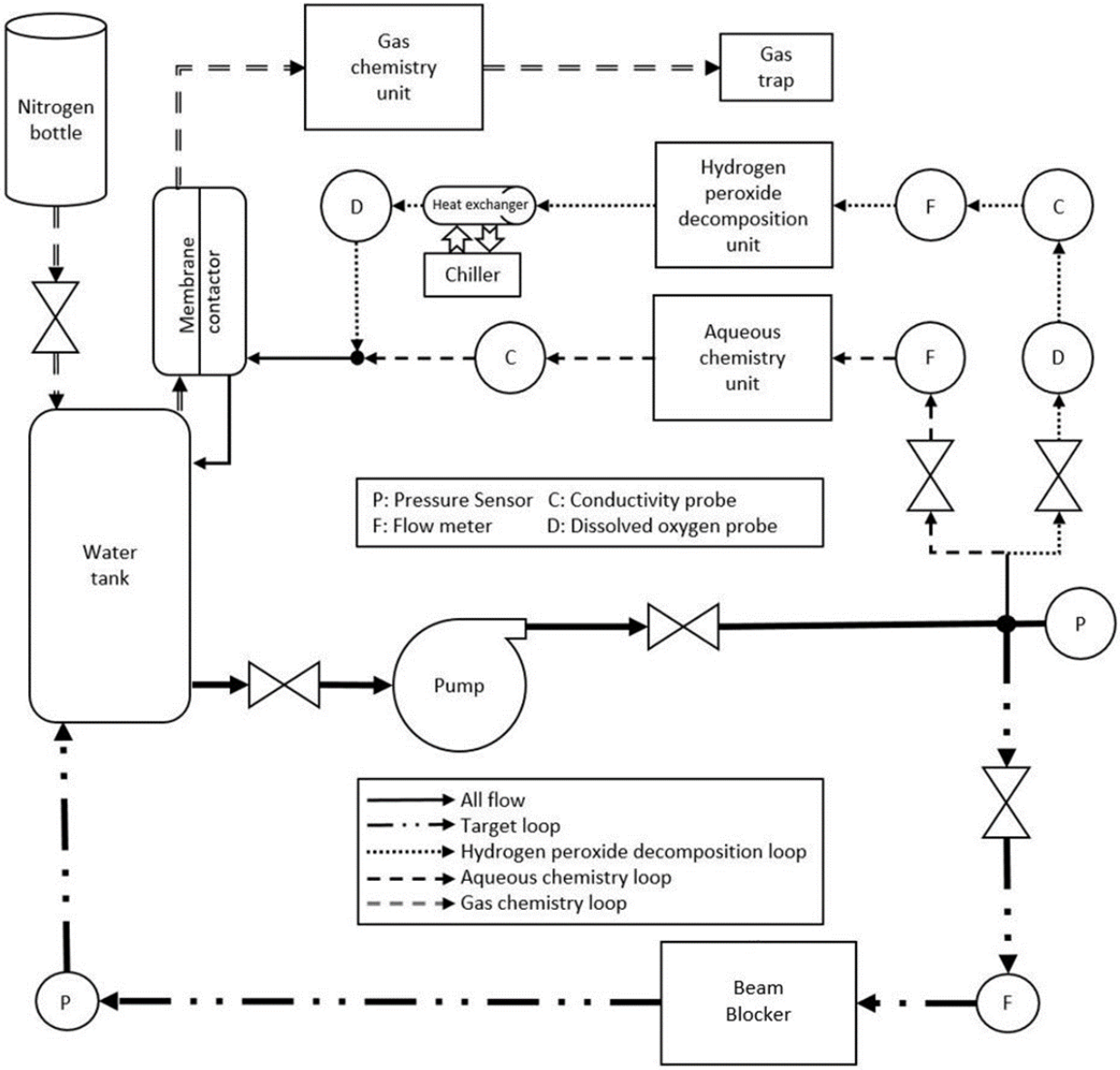

Figure 2.11: Diagram of Isotope Harvesting System for Low Intensity ^{48}Ca Irradiation [36]
Each loop in the system is designated by different dashed lines as shown in the figure legend. The circles at intersecting lines indicate a T-connection, the double triangles facing each other represent manual valves in the line, and the large circles represent sensors with the letters specified in the legend.

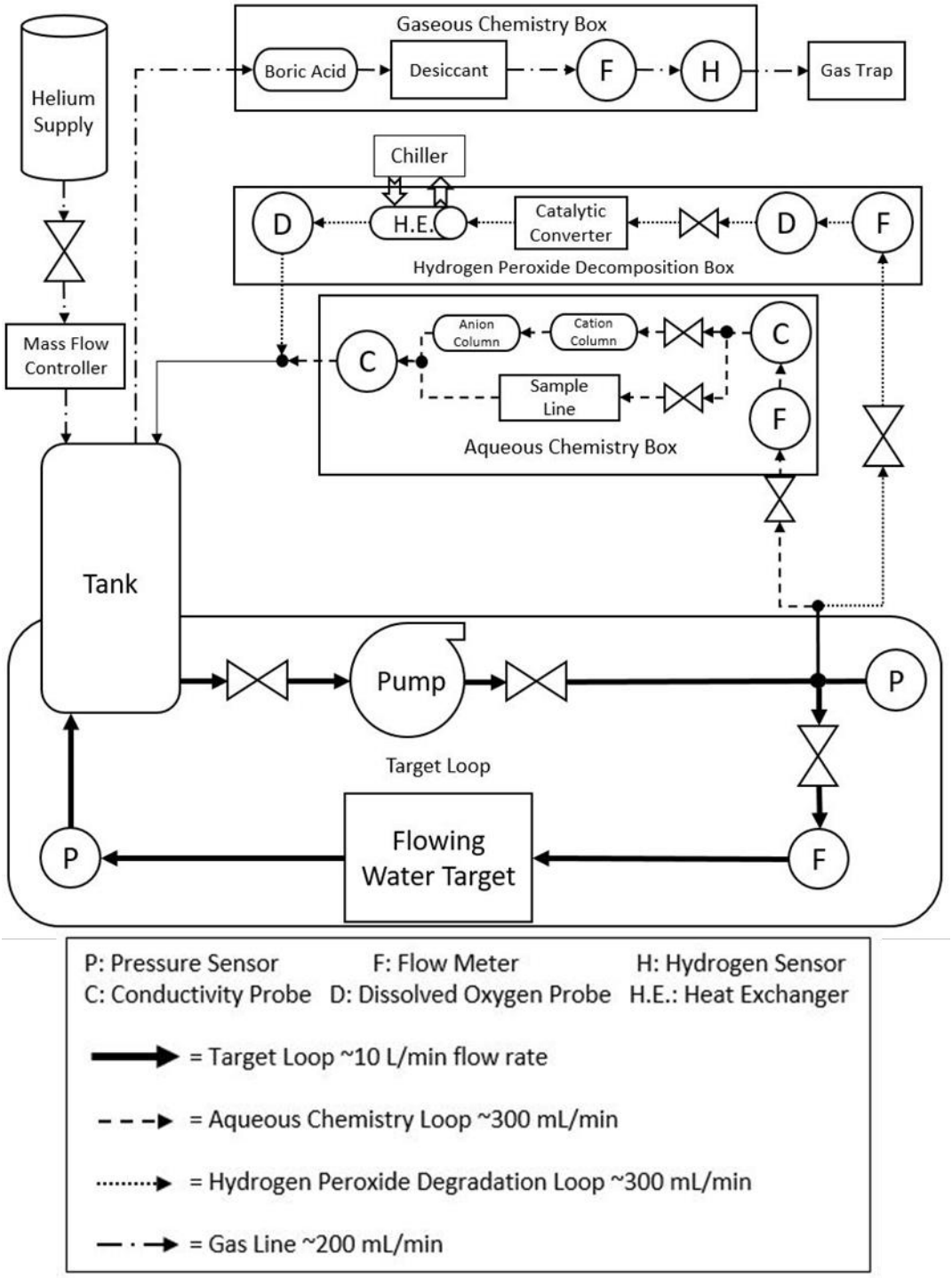

Figure 2.12: Diagram of Isotope Harvesting System for the Proton Irradiation [40]
The solid outlines designate the different main subsystems: target loop, aqueous chemistry box, hydrogen peroxide decomposition box, and gas chemistry box. The solid circles at the intersection of more than two lines indicate a T-connection, the double triangles with points facing each other indicate manual valves, and the large circles represent sensors with the letters specified in the legend.

experiment, the water was pushed through eight particulate filters (Swagelok, SS-6F-60, 316 stainless steel, 60 μm pore size) each filled with 4-7 g stainless steel metal gauze (Alfa Aesar, 316 stainless steel, 100 or 200 mesh) in series. These filters were wrapped with heating tape strips (HTS/Amptek, length 120 cm), surrounded with insulation wool (Knauf Insulation, high-temperature fiberglass), and enclosed in a metal box. This construction maximized the catalytic decomposition capacity for H_2O_2 by providing a large stainless-steel surface area and elevating the temperature of the water to about 45°C. Unfortunately, this experiment demonstrated that the stainless-steel surfaces gradually lost the catalytic decomposition ability, most likely due to the growth of a passivation layer. This H_2O_2 decomposition unit was replaced with a catalytic converter (Yonaka 2.5" ID Ultra High Flow Metal Core Race Universal Cat Catalytic Converter) for the high intensity proton irradiation. This proprietary unit contained noble metals (*i.e.*, Pd and Pt), immobilized on a metallic honeycomb support, which can catalytically decompose hydrogen peroxide. [42] In both experiments, this loop also contained a heat exchanger (Brent Industries Titanium Pool Heat Exchanger SP-55Kti-S) with a counter-current of chilled water (Thermo Scientific, Thermoflex 1400 W) to maintain the system water temperature at ~25°C. This component was vital to remove heat deposited in the system water by the high intensity beam and with the heating elements used in the decomposition box from the low intensity ^{48}Ca irradiation.

Finally, there were separate aqueous and gaseous chemistry sections in the system to collect the radioactive products from the irradiation. Both loops were connected to the system through ¼" polypropylene tubing. The aqueous chemistry loop passed water over cation and anion exchange resins at 300 mL/min to remove any ionic species, stable or radioactive, from

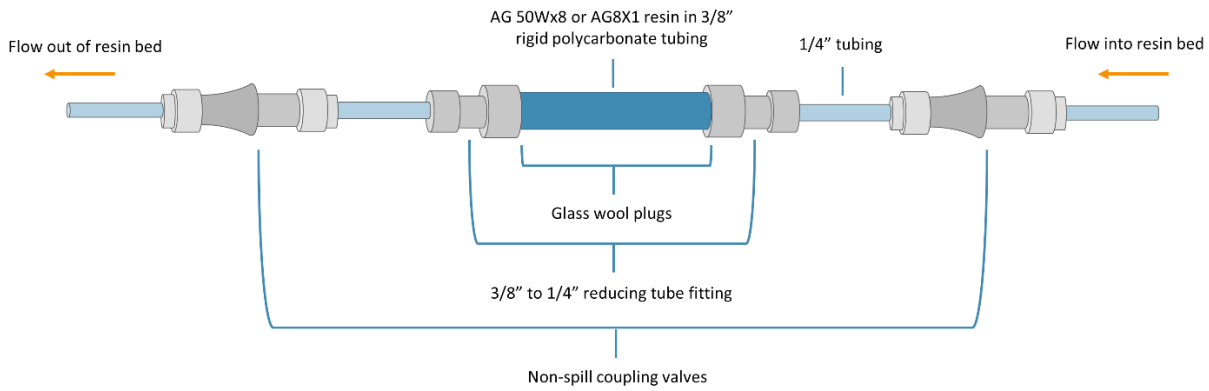

Figure 2.13: Drawing of Ion Exchange Resin Bed

the water. The construction of the ion exchange resin beds is shown in Figure 2.13. The non-spill coupling valves (Cole-Parmer, CPC non-spill quick-disconnect and coupling body) on each side of the resin beds enabled easy and safe removal of the resin beds during an irradiation. This loop also includes a sample line with a manually operated valve to allow for easy withdrawal of water samples from the system.

The gaseous chemistry section of the system uses an acid and a base trap as well as a desiccant to remove species such as $[^{13}N]NH_3$, $[^{11}C]CO_2$, and water, respectively. Additional traps could be used to trap gas through cryogenics (*e.g.*, stainless-steel traps cooled with liquid N_2) or with porous material (*e.g.*, molecular sieves or activated charcoal). The gas dissolved in the water was carried by a purge gas that passed from the bottom of the reservoir water to the headspace at a rate of 200 mL/min. Gas released from the water or already in the headspace of the reservoir flowed to the gaseous chemistry elements in the stream of purge gas. In the ^{48}Ca irradiation, a purge gas of nitrogen with 0.1% hydrogen was used and directed through the lumen side of the membrane contactor placed directly after the hydrogen decomposition box. In the proton irradiation, helium was used as the purge gas and the membrane contactor was

removed from the system due to the sensitivity of the potting material to H_2O_2 as previously discussed. With no membrane contactors in the system, all gas removal was performed with the purge gas through the reservoir.

Throughout the system, the flow rate on each loop was monitored by a flow meter (Target Loop: McMaster Car, Flowmeter for chemicals, ¾" NPT female, 2 to 20 gpm; Hydrogen Peroxide Decomposition Box: Brooks Instrument, 1250–55; Aqueous Chemistry Box: Omega FTB323D Micro-Flo; Gaseous Chemistry Box: Brooks Instrument Sho-Rate Model 1250A). In addition, the conductivity sensors (Mettler Toledo, UniCond Conductivity Sensor) before and after the ion exchange resins provided a measurement of the overall conductivity in the system water and the effectiveness of the resins in removing the ionic species. Similarly, the dissolved oxygen sensors (Mettler Toledo, polarographic dissolved oxygen sensor) before and after the hydrogen decomposition box provided information on the bulk dissolved oxygen in the system as well as the breakdown of hydrogen peroxide (described above), a reaction which produces molecular oxygen. A hydrogen sensor (H2Scan, HY-OPTIMA 710B) on the gas chemistry line monitored the production and evolution of molecular hydrogen. The temperature of the bulk water was also monitored using temperature sensors incorporated into the conductivity probes. A significant difference between the first and later generations of the water system was the lack of a pH probe and that the system was closed to atmospheric air. These changes allowed for the effective measurement of dissolved O_2 and ions due to radiolysis and corrosion, respectively. These sensors were monitored and controlled with a Programmable Logic Controller unit or PLC (Automation Direct Productivity 2000) through the Productivity Suite (v3.3.0.17, Automation Direct).

Several safety measures were put into place for chemical and radiological safety while operating the system. All components and tubing through which water or gas flowed were enclosed in secondary containment. The outlines around different sections of the system shown in Figures 2.11 and 2.12 indicate how the system was grouped into secondary containment units. The containment was achieved through a variety of boxes and carts

Figure 2.14: Images of the Isotope Harvesting System for the High Intensity Proton Irradiation
Pictures showing the target at the end of the cyclotron line (a), the water system in secondary containment sitting behind a shielding wall (b), the inside of the aqueous chemistry box (c), and the inside of the hydrogen peroxide decomposition box (d).

enclosed with sheets of acrylic, and the tubing between each secondary containment unit was run through semi-rigid PVC tubing, shown in the pictures in Figure 2.14. Additionally, the end of the gaseous chemistry line was equipped with air-tight gas collection bags to capture the stream of purge gas and any remaining radionuclidic or radiolytic gases not previously captured in the gas traps. Any remaining safety hazards (*i.e.*, radioactive gases and radiolytically produced hydrogen gas) were collected rather than being vented into the experimental vault. The PLC unit which monitored and controlled the sensors in the system was also in communication with the NSCL's logic system during the ^{48}Ca irradiation to facilitate a safety interlock on the cyclotron RF (*i.e.*, the frequency used to accelerate the beam) based on the water system readings. This system was designed to interrupt the irradiation of the isotope harvesting target if a large enough difference between a preset threshold and the measured pressure or water flow was detected, among other interlocks. With this interlock, system failures would become readily apparent and the irradiation of the system would be automatically stopped.

2.3.3 Generation 4: High Intensity ^{48}Ca Irradiations

The final version of the water system used in this work was used in the two highest intensity ^{48}Ca irradiations discussed in Chapter 6, 7, and 8 and is shown schematically and with pictures in Figure 2.15 and 2.16. This water system was similar in design to that used in the high intensity proton irradiation with a few exceptions. The main difference in these systems was the separation of the different sections of the system. The isotope harvesting target was placed in the beam line at the beam blocker position after the first dipole magnet in the A1900 fragment separator (Figure 2.3), the aqueous and gaseous chemistry box were placed on the

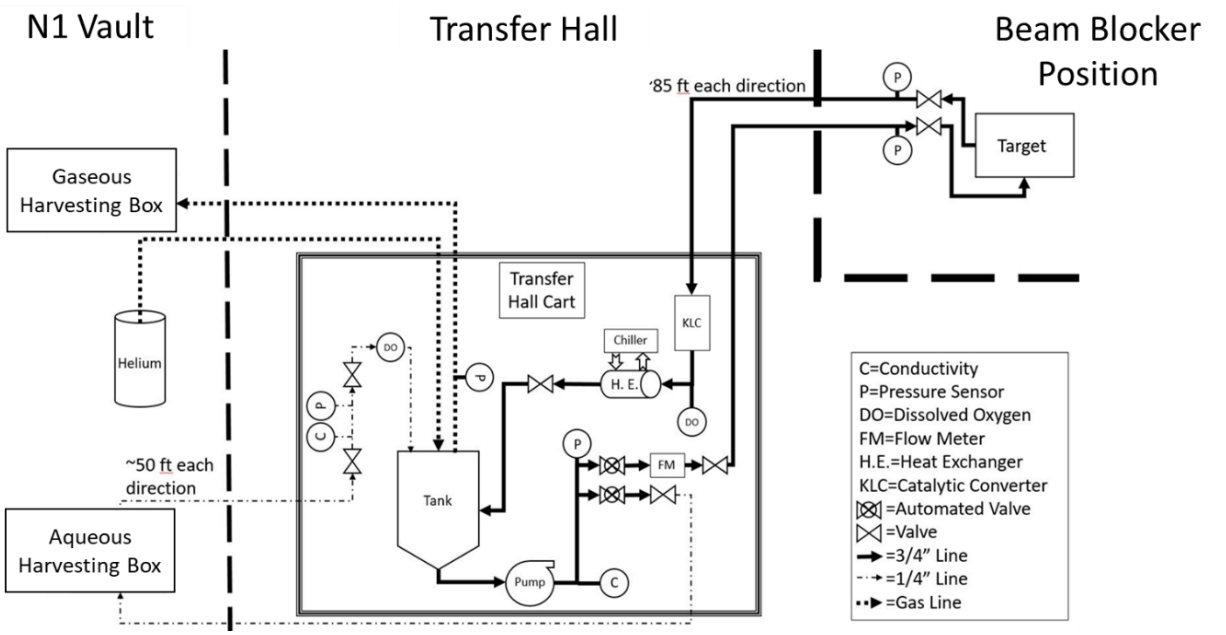

Figure 2.15: Schematic Diagram of Isotope Harvesting System for High Intensity ^{48}Ca Irradiation
The three different locations that housed components of the system are delineated with dashed lines and indicated by the labels at the top of the drawing. The thick line around the components in the "Transfer Hall" represents secondary containment around all these components.

south wall of the N1 vault, and all other components (*e.g.*, water reservoir, water pump, catalytic converter, PLC, etc.) were placed at the east side of the transfer hall where the A1900 fragment separator is housed. The main section of the system in the transfer hall was about 85 and 50 feet away from the target and the chemistry boxes, respectively. Placement of the target at the beam blocker position instead of an experimental end station allowed for a full power 80 pnA ^{48}Ca beam irradiation. While most of the components were held in the transfer hall, aqueous and gaseous chemistry boxes were placed in the N1 vault for easy access to collection components during the irradiation. Due to the distance between the components, longer lengths of tubing between the components and therefore a large water volume (approximately 50 L) were used in the system.

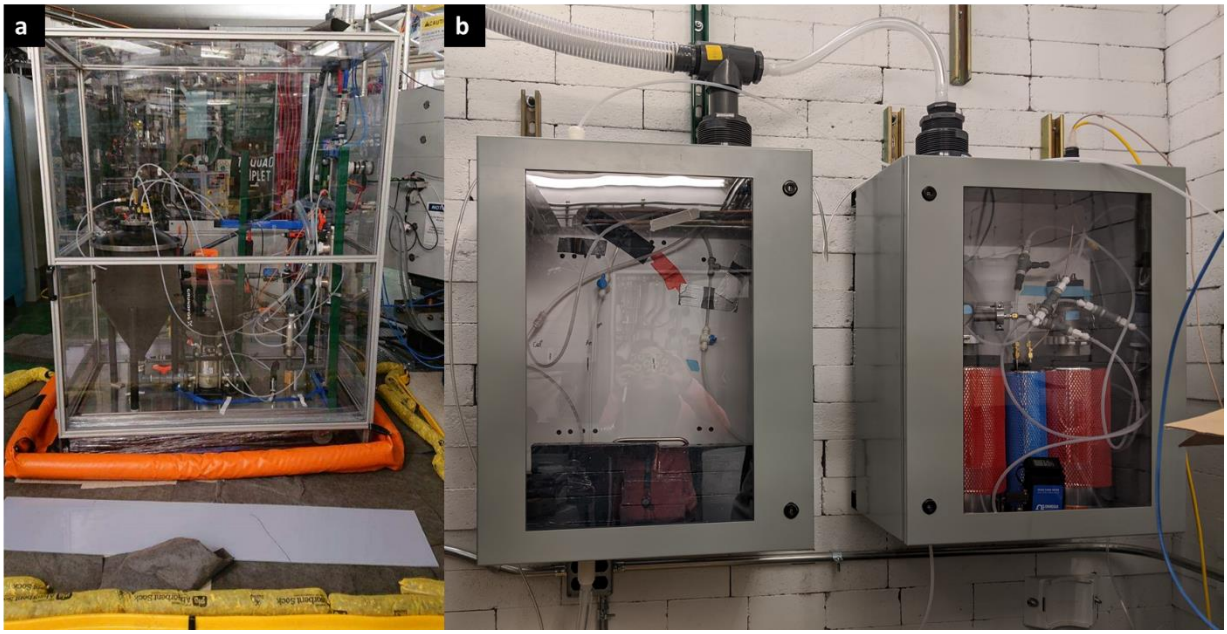

Figure 2.16: Images of the Isotope Harvesting System for High Intensity ^{48}Ca Irradiations
The main secondary containment unit in the transfer hall (a) and the aqueous and gaseous chemistry boxes in the N1 vault (b).

Other changes to the system included placing the catalytic converter (labeled “KLC” in Figure 2.14) on the target loop with a much larger flow rate of 10 L/min through this unit as compared to the previously used 300 mL/min. This reduced the residence time of the water in the converter while increasing the number of passes of the water through the system in a given time period, potentially increasing the decomposition capacity of the unit. Another change in the main loop of the system was the use of a new Teflon-coated brewing kettle as the water reservoir. The mixed bed resins used to purify the system water were also placed in a permanent, more easily accessible position after the aqueous chemistry box compared to the temporary insertion in the target loop used previously. While this was more convenient placement, this configuration reduced the flow rate through the mixed bed resins, requiring more time to fully purify the system water. Another change in the aqueous chemistry box was

the addition of lead shielding. A wall of lead bricks was built on the bottom of the secondary containment in front of the cation exchange resin bed where the activity accumulated. A cylinder of shielding material was also constructed with a hole through the middle in which the resin bed could be inserted. This provided shielding while users worked in and near the aqueous chemistry box and for the transportation and offline handling of the resin bed. A schematic drawing and pictures of the aqueous chemistry box interior are given in Figure 2.17. Finally, additional interlocks between the isotope harvesting system and the NSCL beam control were integrated to protect equipment such as monitoring the beam line humidity in the case of a leak in the water-flowing target.

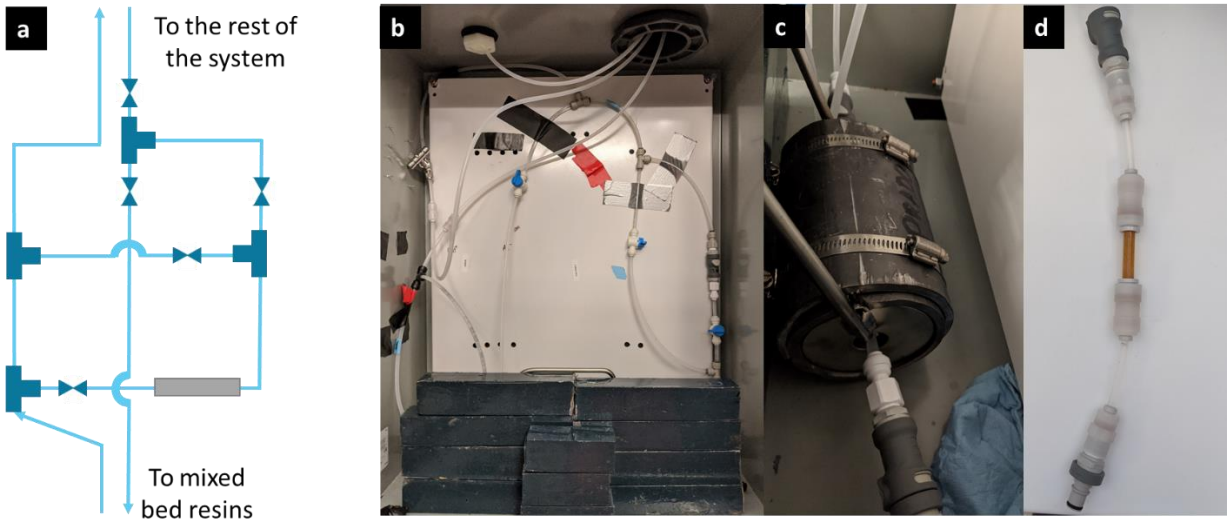

Figure 2.17: Aqueous Harvesting Loop for High Intensity ^{48}Ca Irradiation
A schematic (a) and photograph (b) of the isotope harvesting box, lead shielding around a cation exchange resin bed (c), and a cation exchange resin bed (d). In the schematic on the left, the column is indicated by the grey rectangle, valves are depicted as blue double triangles facing each other, T-connectors are shown as blue "T" shapes, and the ¼" tubing connecting all components is drawn as light blue lines.

2.4 Conclusion

Efforts in the isotope harvesting group have led to the development of a reliable and flexible water system for the production and recovery of radionuclides produced by the interaction of high-energy heavy-ion beams with flowing-water target. Several experiments have been performed to provide information on the detailed water chemistry during an irradiation and to design an isotope harvesting system for safe and convenient use for research purposes. Chapter 3 presents the results of an experiment with a low intensity ^{40}Ca irradiation that used the first-generation flowing water target and isotope harvesting system to test the durability of Ti64 as the target material. This test was followed by a higher intensity proton irradiation discussed in Chapter 4 that tested the durability of the second-generation isotope harvesting target and the third-generation water system at NSCL-scale beam power depositions that more closely resembled the conditions anticipated at FRIB.

The target and system durability demonstrated at these beam power levels allowed for full power irradiations of the second-generation water target (*i.e.*, 0.5 kW power with 80 pnA 140 MeV/nucleon ^{48}Ca beam) at the NSCL (Chapters 6 and 7). The first ^{48}Ca irradiation of a prototype flowing-water target used the second-generation flowing water target and started with a low intensity ^{48}Ca irradiation (*i.e.*, < 1 pnA) discussed in Chapter 4 and lead to higher intensity ^{48}Ca irradiations (*i.e.*, 1-80 pnA) presented in Chapters 6 and 7. The second-generation water system was used in an experimental vault for the first ^{48}Ca irradiation, while the fourth-generation water system was used with the isotope harvesting target in the A1900 beam blocker position for the final higher irradiations. This series of experiments provided valuable

information for the development of a system and techniques that will facilitate isotope harvesting at the higher beam powers available at FRIB.

Chapter 3: Low Intensity ^{40}Ca Beam Ti64 Durability Test[7]

A flowing-water target was irradiated with a 140 MeV/u, 8 nA $^{40}Ca^{20+}$ beam to test the feasibility of isotope harvesting at the upcoming Facility for Rare Isotope Beams. Among other radionuclides, 2.6(2)E-6 ^{48}Cr and 5.6(5)E-6 ^{28}Mg nuclei were formed through fusion evaporation and fragmentation reactions, respectively, for every impingent ^{40}Ca and were collected on an ion exchange resin bed. Radiolysis-induced molecular hydrogen evolved from the target at an initial rate of 0.91(9) H_2 molecules per 100 eV of beam energy deposited. No radiation-accelerated corrosion of the target material was observed through radioactive and stable element tracing and surface analysis.

3.1 Introduction

Previous isotope harvesting experiments at the NSCL have involved the implantation of secondary radioactive beams into a static volume of water [32–34]. These experiments demonstrated success in recovering the radioactive products from an aqueous medium and subsequent chemical purification and use in applications such as nuclear medicine. With these encouraging results, subsequent isotope harvesting experiments were designed to simulate more closely the harvesting conditions expected at FRIB in the future. A new water system was developed (see Chapter 2 Section 2.2.1 and 2.3.1) to include a flowing-water target with a

[7] The material presented in this chapter draws heavily from the published paper E. Paige Abel, Hannah Clause, and Greg Severin, Radiolysis and radionuclide production in a flowing-water target during a fast $^{40}Ca^{20+}$ irradiation, *Appl. Radiat. Isotopes.* **2020**, *158*, 109049.

beam window of Ti64 alloy, the material that will be used in the FRIB isotope harvesting beam dump. [39] Attached to this target was a system that monitored and conditioned the water as well as collected radioactive products from the flowing water. Additionally, realistic isotope harvesting conditions at the NSCL or in the future, at FRIB, will involve a much higher intensity beam of primary (*i.e.*, stable) particles. With a higher intensity beam, the implanted beam particles interact to a greater extent with the water through both nuclear and chemical reactions. The extent and effect of these reactions should be studied through a series of isotope harvesting experiments with increasing beam intensity.

The nuclear reactions that occur in the isotope harvesting target allow for production of radionuclides from accelerated primary beams (*e.g.*, the production of ^{47}Ca from a ^{48}Ca primary beam). The important nuclear interactions in this context are fragmentation (FR) reactions at high energies, and fusion-evaporation (FE) reactions at low energies. FR reactions result from high energy interactions, where beam particles collide with target nuclei and break apart, forming fragments of the original nucleus. As the energetic beam loses energy in the target, FE reactions begin to occur, primarily at the end of the particle tracks. It is important to know the extent to which these reactions occur to be able to predict the activity of a particular radionuclide of interest and the overall level of activity produced for experimental and safety planning, respectively. These reaction rates can be measured directly through experiments or predicted through simulation codes like PACE4, LisFus, and LISE++. [29,43,44] Additionally, it is important to test if the radionuclides produced in a water medium react chemically as expected for planning methods or collection, purification, and use in applications.

In addition to these nuclear reactions, chemical reactions also occur as a result of implanting a fast, heavy ion beam into a water target. As the beam particles pass through the target, the water molecules are ionized and undergo dissociation reactions in a process called radiolysis. This produces a variety of ionic, radical, and molecular species such as H^+, OH^-, $^{\cdot}OH$, $^{\cdot}H$, H_2, O_2, and H_2O_2. While some of these products quickly recombine especially when produced by high linear energy transfer (LET) particles, the molecular species in particular can be long-lived. [45–48] Conventionally, the production rate of these molecular species have been quantified as the G-value, which is defined as the number of molecules formed per 100 eV of energy deposited. In the present isotope harvesting systems, the measured value gives an understanding of the survival rate of the longer-lived species since they are measured after recombination of radiolysis products occurs in the target volume. This rate is of interest since many of the radiolysis products such as the radical products and H_2O_2 form a corrosive environment in the water and gases such as O_2 and H_2 can lead to a relatively high pressure and potentially explosive condition. Measurements of the long-lived radiolysis in the isotope harvesting system with increasingly high intensity irradiations can demonstrate the extent to which these products buildup, recombine, or decompose as experiments come closer to FRIB conditions.

To test the nuclear and chemical reactions in a water target, an experiment was carried out at the NSCL with a stable primary beam impinged on the first-generation flowing-water target. The production rate of several radionuclidic products were measured and compared to predicted rates with PACE4, Lisfus, and LISE++. The activity collected on ion exchange resin beds were measured to gain an understanding of the collection efficiency with this method and the

chemical behavior of radionuclidic products formed in the water target. Additionally, H_2 gas was removed from the system and measured as an indication of the extent of radiolysis in the target. The potential corrosive effects of radiolysis were monitored by looking for corrosion of the water side of the Ti64 beam window in the target through an analysis of the stable elements and radionuclides collected on the ion exchange columns. Altogether, this experiment provided a small-scale test of isotope harvesting at the NSCL and FRIB.

3.2 Materials and Methods

3.2.1 Isotope Harvesting System Irradiation

A $^{40}Ca^{+20}$ beam was accelerated to an energy of 140 MeV/nucleon by the Coupled Cyclotron Facility at the NSCL. The beam was initially delivered to the target at the end of an experimental beam line at an intensity of 0.11(1) particle nanoamperes (pnA) or 2.1(3) electrical nanoamperes (enA) for approximately 17 minutes. After this initial test, the intensity was increased to 0.42(4) pnA or 8.4(9) enA for about 3.5 hours. These beam current readings were obtained by using frequent unsuppressed current readings from the target and intermittent current readings from an upstream calibrated Faraday cup. The unsuppressed measurements (*i.e.*, proportional but not equivalent to the true value) were scaled using the calibrated beam current measurements.

The current measurements from the unsuppressed target, calibrated Faraday cup, and scaled target readings are shown in Figure 3.1. The scaling of the unsuppressed target current readings was performed using three averages for each of the two beam current intensities: the average Faraday cup measurements, the average target measurements above a certain threshold, and the average of all the target measurements. These thresholds were set at 2 enA

for the lower intensity beam setting and 5 enA for the higher intensity beam setting to represent both the main band of measurements as well as the lower fluctuations in the measurements that can be observed in Figure 3.1. Since the Faraday cup measurements were intermittent, they did not reflect the fluctuations in the target current readings. To make the Faraday cup measurements more representative of these lower fluctuations these readings were scaled by the ratio of the average of all target measurements divided by the average of the target measurements above the thresholds. These ratios were found to be 0.89 and 0.97 for the lower and higher intensity beam settings, demonstrating that the lower fluctuations in the beam current were small relative to the beam current measurements throughout the irradiation. These ratios were used to find a scaled average of the calibrated beam current values for both beam intensity settings. Additionally, the ratio between the scaled average Faraday cup readings and the average target readings (1.71 and 1.17 for the lower and higher

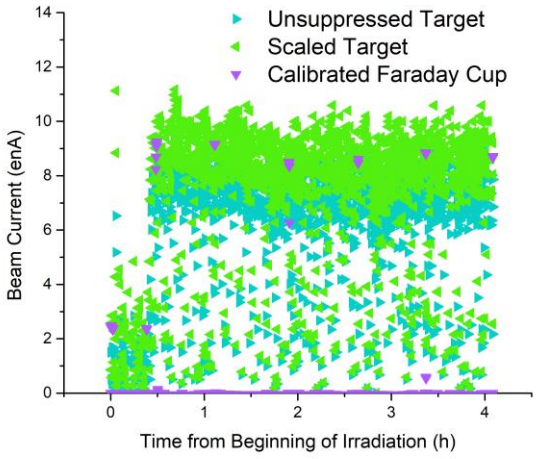

Figure 3.1: Scaled Beam Current During Experiment
The beam current recorded every 5 seconds by the unsuppressed target (teal) and intermittently recorded by an upstream calibrated faraday cup (purple) are plotted. The Faraday cup readings were used to calibrate the unsuppressed target readings, resulting in the scaled beam current readings in the plot (green).

beam intensities, respectively) were used to scale the frequent target readings as plotted in Figure 3.1. With ratios greater than 1 for both beam intensity settings, the scaled target readings are higher than the unsuppressed target current measurements.

The target used for this experiment was made of a flowing-water filled polyethylene body with a disk of grade 5 titanium alloy (Ti64, 6% aluminum and 4% vanadium by mass, balance titanium) beam window (Figure 2.1, Section 2.2). This outer shell of polyethylene and Ti64 was needed to contain the flowing-water target medium. The beam passed through several layers of material that were used to separate the water from the beam line vacuum and contain the water, depicted in Figure 3.2, before passing through the Ti64 disk and finally entering the water volume inside the target. The energy of the beam as it traveled through these layers was estimated by using stopping powers obtained from SRIM and is shown in Figure 3.2. [49] The surface of the disk facing the water was divided into two halves, with one

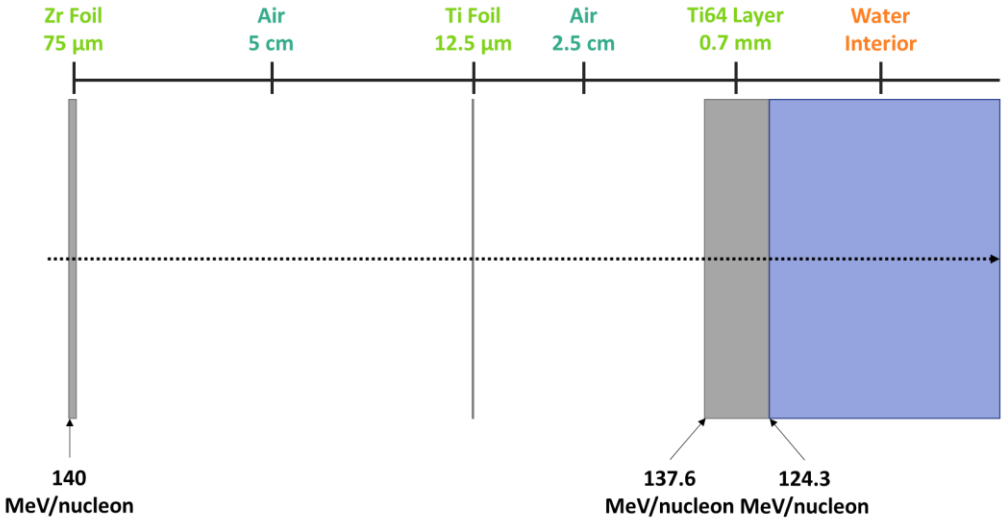

Figure 3.2: Depiction of Layers Traversed by $^{40}Ca^{20+}$ Beam
The 140 MeV/nucleon ^{40}Ca beam (black dotted line) passed through two layers of air, a Zr foil, and a Ti foil before passing through the Ti64 target disk and into the interior water layer of the target. The energy of the beam particles before entering the target set up, before the target front face, and before entering the water in the target is given in the figure.

half milled smooth and the other half left as received after additive manufacturing through 3D printing. During the experiment, the beam was directed to enter the target through the half of the Ti64 disk that was not milled.

A flowing-water system containing components such as sensors, membrane contactors, ion exchange resin beds, a water reservoir, and a water pump was attached to this target (see Figure 2.8 and Section 2.3.1.1). Approximately 6 L of ultra-pure water was circulated through the system. Prior to irradiation, the water flow was directed through a set of cation and anion exchange resin beds (AG 50W-X8 and AG 1X8, respectively) to reduce the conductivity of the water to about 250 nS/cm. The baseline conductivity increased to approximately 800 nS/cm after removal of the columns, presumably due to re-equilibration with atmospheric CO_2 across the post-target membrane contactor. The pH of the water was also consistent with atmospheric CO_2 equilibration, ranging from 5.1 to 5.8 throughout the experiment. After irradiation, the water flow was redirected sequentially through a cation exchange (AG 50W-X8, 20-50 mesh) and an anion exchange resin bed (AG 1X8, 20-50 mesh) at a flow rate of 1 L/min to remove ions from the water.

3.2.2 Radionuclide Quantification and Comparison to Production Estimates

Following the ion exchange process, components of the water system were removed and analyzed using a Canberra BEGe Gamma-ray Detector (BE2020). An energy and efficiency calibration were performed using a ^{152}Eu point source at 50 cm from the face of the detector. Gamma spectra in this work were primarily taken at 50 cm from the detector. In cases where counting rates required a different distance, the detector efficiency was corrected mathematically rather than using a recalibration.

The physical components analyzed with gamma spectroscopy included the water in the reservoir; the target cell; the hydrogen peroxide degrader; and the cation and anion exchange columns. The spectra allowed for identification, quantification, and localization of radionuclides on these components. The shorter-lived species were quantified using spectra obtained within a few hours after the irradiation. To reduce background from the shorter-lived nuclides, the longer-lived species were quantified from spectra obtained approximately 2 days after the irradiation. The characteristic gamma-ray energies and the branching ratios used to identify and quantify the radionuclides are given in Table A1 Appendix A [14,15,28,50–56].

Contributions to the 511 keV gamma-ray peak from radionuclides such as ^{34m}Cl, ^{43}Sc, ^{44}Sc, ^{48}V, ^{48}Cr, and ^{52}Mn were calculated based on the activities found on each component using the characteristic gamma rays listed in Table A1. Since the remaining counts demonstrate a decay half-life close to that of ^{18}F (*i.e.*, a measured half-life of 116.9 min from four data points vs. the accepted half-life for ^{18}F of 109.77 min), they were used to make an estate of the amount of ^{18}F produced.

Due to interferences such as a high Compton background and their relatively short half-lives (^{43}Sc $t_{1/2}$ = 3.891 h, ^{44g}Sc $t_{1/2}$ = 3.97 h), the activity of ^{43}Sc and ^{44g}Sc in some system components could not be measured. In particular, ^{43}Sc was not observed in the water, ^{44g}Sc was not observed on the cation exchange resin bed, and neither scandium isotope was observed on the hydrogen peroxide degrader. The values were estimated using the observed scandium isotope activities with the assumption that the distribution of all scandium isotopes on the system components is the same due to their identical chemistry. The longer-lived ^{44m}Sc ($t_{1/2}$ = 58.61 h) was quantified two days after the irradiation with low-background spectra. The

distribution of ^{44m}Sc on the anion exchange resin bed, the cation exchange resin bed, the hydrogen peroxide degrader, and in the system water was then used to find corresponding activities of ^{43}Sc and ^{44g}Sc in these locations. In practice, the known activities for ^{43}Sc and ^{44g}Sc on these components were scaled by the proportion of ^{44m}Sc on each system component to find estimates for the unknown activities of ^{43}Sc and ^{44g}Sc. The calculated values for these scandium isotopes are labeled in Table 3.1.

For comparison to the observed activity, cross-sections obtained from PACE4 and LisFus through the program LISE++ and stopping powers obtained from SRIM were used to estimate the expected FE reaction production rates for ^{43}Sc, ^{44,44m}Sc, ^{48}V, ^{48}Cr, and ^{52}Mn. These radionuclides were assumed to be produced solely through FE reactions between ^{40}Ca and ^{16}O. The cross sections from either PACE4 or LisFus were used in Equation 3.1 to find a production rate, *P*, in terms of particles produced per incoming particle for each of the radionuclides observed:

$$P = \int_{E_i}^{E_f} \frac{\sigma(E)}{S_p(E)} \frac{\rho N_A}{M} \, dE \tag{3.1}$$

where $\sigma(E)$ represents the cross section of a fusion-evaporation product at a given energy E, $S_p(E)$ is the stopping power of the beam in the target material at a given energy, ρ and M are the density and molar mass of the target material, and N_A is Avogadro's number. The integral was approximated as a sum over energy steps from E_i to E_f, the initial and final energy of an interacting particle in the target, respectively. The production rate in Equation 3.1 is the number of nuclei produced per incoming $^{40}Ca^{20+}$ and was converted to particles produced per second by multiplying by the incoming beam intensity. The cross sections from PACE4 and LisFus are given as a function of beam energy in Tables B1-10 in Appendix B.

FR production rates were calculated with LISE++ using a primary beam of $^{40}Ca^{20+}$ at an energy of 137.59 MeV/nucleon (*i.e.*, the resulting energy after passing through the first four layers of materials shown in Figure 3.2) and an intensity of either 0.11 pnA or 0.42 pnA. Layers representing the target face, the water volume, and a detector material were specified in this order in the program to find a production rate in the unit particles produced per second during the experiment. The production values found for all methods previously described were used with the typical activation equation to find the final predicted activities.

3.2.3 Radiolysis Measurement

The production of H_2 gas was measured as an indicator of radiolysis in the water target during the irradiation. While the H^+ and O_2 levels in the water were measured with a pH meter and a dissolved oxygen sensor, these levels were influence by the equilibration of the water with atmospheric air. In particular, the pH was decreased by the equilibration with atmospheric CO_2 in the air and the dissolved O_2 level was increased by the equilibration with atmospheric O_2. Therefore, the measured levels of these radiolysis products were not a direct indicator of radiolysis with the isotope harvesting system used in this experiment.

Previous experiments have reported G-values for ion beams at different average linear energy transfer (LET) values [47,57–59]. The average LET values were found using Equation 3.2:

$$\left(\frac{1}{E_0}\right)\int_0^{E_0}\left(\frac{dE}{dx}\right)dE \tag{3.2}$$

where E_0 is the initial energy and $\frac{dE}{dx}$ is the stopping power of the ion beam. [59] In practice, this equation can be approximated as a sum from the initial energy to the end of the beam track. A logarithmic trend has been found between the average LET values vs. the measured G-values

for different ion beams. Examples of such relationships are shown in Figure 3.3 for ^{60}Co gamma rays, a 1 MeV ^{1}H beam, a 5 MeV ^{4}He beam, and fission fragments [47,57–59]. The average LET calculated value for the ^{40}Ca beam as it passed through the water layer of the target was used with this relationship to predict a G-value of 1.57 H_2 molecules/100 eV of deposited beam energy.

Throughout the experiment, the H_2 gas production was measured with a Midas gas detector at the second membrane contactor in the system. This detector used a sweep gas of air moving at 500 mL/min through the detector and measured H_2 in this diluted stream in ppm. The measured concentration of H_2 gas was converted to the number of H_2 gas molecules produced per second during the irradiation, by estimating the dilution factor from the sweep gas using the ideal gas law. To find an experimental G-value for H_2, this production rate was

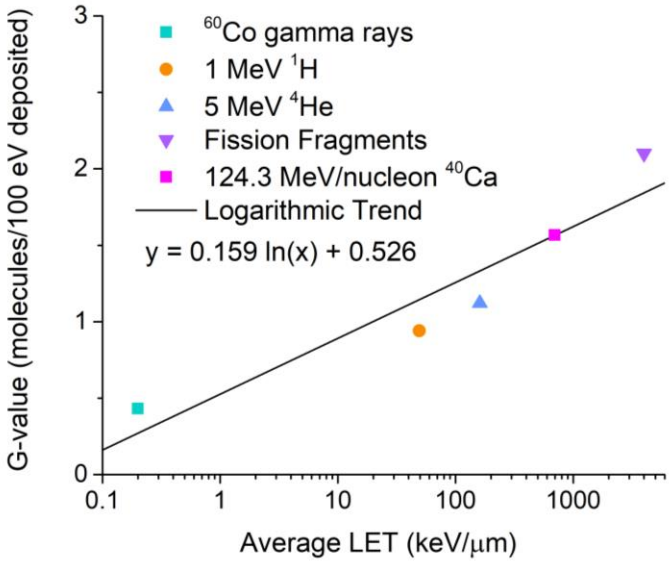

Figure 3.3: Average LET vs. Experimental G-Values
The logarithmic trend between the average LET value and experimentally determined G-values for various ionizing radiation sources from the literature [47,57–59]. This trend was used to predict a G-value for the 124.3 MeV/nucleon ^{40}Ca beam (698 keV/μm average LET) in the water during this irradiation.

combined with the measured beam current and the energy of the beam as it entered the water as estimated with SRIM.

The irradiation was separated into a different segment each time the calibrated Faraday cup was inserted to measure the beam current. At these points, the beam no longer reached the target and no H_2 gas was produced through radiolysis. As expected, the level of H_2 gas measured at these short intervals rapidly dropped to zero. The G-value corresponding to the average beam current and H_2 gas production rate during each irradiation period are presented and discussed in Section 3.3.3.

3.2.4 Corrosion Assessment

3.2.4.1 Ion Exchange Resin Processing

After measuring the gamma spectra of the columns to quantify and locate the radionuclides that were produced and collected on the ion exchange resins, both the cation and anion columns were processed to remove any stable ions collected from the water. First, the water in the tubing above the resins was drained and saved. The cation column was then treated with solution of increasing acid molarity in the following order: about 11 mL of 0.6 M HNO_3, 12 mL of 2 M HNO_3, 12 mL 3 M HNO_3, 12 mL 4 M HCl, and 12 mL 8 M HCl. After each addition, an equivalent volume of solvent was pulled through the column and removed in small fractions. Gamma spectra of each group of eluents were taken after removing 12 mL between each addition to ensure ions were being removed. In a similar way, the anion column was treated with the following solutions: 12 mL water, 12 mL 2 M HCl, 12 mL 4 M HCl, and 12 mL 8 M HCl. Between each addition, an equivalent amount of liquid was removed from the columns in small fractions and analyzed with gamma spectroscopy as for the cation resin samples. This

acid elution gradient was performed on the ion exchange resins to remove as many ionic species as possible from the columns [60,61].

All fractions from the cation and separately the anion resin were later combined and analyzed by inductively coupled plasma-optical emission spectroscopy (ICP-OES) with an Agilent TCP700 spectrometer. This analysis was performed to quantify any stable elements that accumulated in the system water during the irradiation. First, a semi-quantitative ICP-OES method was used to identify the elements present as well as a rough order of magnitude estimate for the concentration of elements present in the cation and anion resin eluates. The following elements were found to be present at a concentration of approximately 0.1 ppm or higher: B, Na, Mg, Al, Si, P, S, K, Ca, Fe, Ni, Zn. Further quantification of these elements was performed by preparing standards containing these elements in 2% nitric acid (v/v). The samples from the cation and anion resin were each diluted to a total acid concentration of about 0.7 M HCl and were run with the prepared standards and a blank of 0.7 M HCl on ICP-OES. The measured concentrations are presented and discussed in Section 3.3.4.1. The wavelengths used for quantification of each element are given in Table C1 in Appendix C.

3.2.4.2 Surface Assessment

Images of the Ti64 target window were taken with a Perkin Elmer IVIS Lumina LT In Vivo Imaging System (CLS136331) to visualize the location of the beam strike. First, a picture was taken of the disk with the camera in the IVIS imaging system. With the disk in the same place and orientation, a thin piece of scintillating plastic was placed over the disk and a second picture was taken to localize the area of the disk that was activated by the beam strike. These

images were then overlaid to verify the location of and attribute any visual differences to the beam strike. The resulting image is presented and discussed in Section 3.3.4.2

3.2.4.3 Corrosion Rate Estimation

An analysis of the corrosion rate of the target window was also performed to understand the effects of radiolysis and the energy deposition of the beam on the target window. This analysis used ^{47}Sc produced in the Ti64 beam window as a radiotracer to find an upper limit for the corrosion rate of the window material. The methods for estimating fusion evaporation cross sections described previously indicated that the cross section for ^{47}Sc production in the water was very low. Through gamma spectroscopy, ^{47}Sc was found as a product in the target window. Therefore, any ^{47}Sc found in the water or accumulated on other system components would indicate target degradation. After the irradiation, no detectable amount of ^{47}Sc was measured in the water or on any of the other system components. Based on this measurement, the limit of detection of ^{47}Sc with HPGe measurements of these components was used as the upper limit for the degradation of the target material.

The limit of detection was approximated as the uncertainty in the sum of background counts where the 159 keV peak from ^{47}Sc would have been detected in each gamma spectrum considered. Specifically, the sum of counts from 158.8 to 160.3 keV was found for each spectrum and the error in this region was taken as the square root of the sum of counts. This uncertainty was then set equal to the number of counts that could have resulted from ^{47}Sc in the system water but were not observed due to statistical counting errors. Spectra in which ^{44m}Sc was detected were used in this analysis: the anion exchange resin bed, the cation exchange resin bed, the hydrogen peroxide degrader, and the water in the reservoir. It was

assumed that ^{47}Sc would have accumulated on these components as well since all scandium isotopes behave the same chemically. As three of these components (*i.e.*, the cation exchange column, the anion exchange column, and the hydrogen peroxide degraded) contained glass wool, it appears that they filtered out neutral but aqueous forms of scandium such as $HScO_2$ and the rest remained in the water [62].

It was also assumed that the proportions of ^{44m}Sc found in each area of the system was equivalent to the distribution of ^{47}Sc. Using the count limit and the proportions of ^{44m}Sc found on each component, values were calculated for the activity of ^{47}Sc that could have also accumulated on each of the other three components (*e.g.*, the count limit found for the anion resin was used to find the ^{47}Sc activity that could have accumulated on the cation resin, the hydrogen peroxide degrader, and the water reservoir). The total amount of ^{47}Sc that could have been in the system water without being detected was the sum of activity found in this way for all four parts of the system where Sc isotopes were detected. The lowest activity sum was found using the count limit for the anion resin (appears as "L" in Equation 3.4 below).

This total activity of ^{47}Sc was used to model the target degradation as a time dependent process. The ^{47}Sc activity was built up in the target using small time steps and by assuming a production rate that was proportional to the beam intensity:

$$A_i = P\frac{I_i \Delta t_i}{\sum_{i=1}^{n} I_i \Delta t_i} + A_{i-1} e^{-\lambda \Delta t_{i-1}} \tag{3.3}$$

where P was a constant production rate that produced a final estimated activity in the window equal to that measured value. This production rate was multiplied by a factor involving the integrated beam intensity in each time step where Δt_i is the difference between t_{i+1} and t_i. The sum of activity in the window at each time step was found by adding the decay corrected

activity from the previous step where Δt_{i-1} is the difference between t_i and t_{i-1}. It was also assumed that ^{47}Sc would enter the water from the target as a constant percent of the ^{47}Sc present in the window per unit time:

$$F = \frac{L}{\sum_{i=1}^{n} A_i \, \Delta t} \tag{3.4}$$

where F is the fraction that degraded per unit time, L is the total activity limit determined as described previously, and the denominator is the sum of activity across all the time steps. In this way, a percent degradation per hour and over the course of the experiment was found. It is important to note that this method limits the degradation rate of only the beam strike area on the target window since this is the only part of the window in which ^{47}Sc was produced. Therefore, a limit on the degraded mass at the beam spot was calculated using the relative area of the beam spot to the whole disk and the mass of the whole disk.

3.3 Results and Discussion

3.3.1 Isotope Harvesting System Irradiation

During the irradiation of the harvesting system, the temperature was measured by the dissolved oxygen sensor, the conductivity probe, and the pH meter. Since the temperatures recorded by these three sensors were found to be comparable, only the temperature data from the dissolved oxygen sensor will be discussed here. The temperature of the bulk water, as measured by the dissolved oxygen sensor over the course of the experiment, is shown in Figure 3.4. A temperature change of 0.93 °C was observed over the course of the irradiation, resulting from the deposition of approximately 28 kJ in the water and 3 kJ in the target window [49]. Based on the energy and current of the beam as well as the volume of water running through the system, a maximum temperature increase of 1.10-1.21 °C was anticipated. The upper and

lower limits of this range were found with the assumption that all of the heat or none of the heat deposited in the target face, respectively, was removed by the flowing water. Since the estimated temperature increase of the water due to beam energy deposited directly in the water was approximately 18% higher than the measured temperature increase, passive cooling of the system water most likely occurred to a small extent to produce this difference.

The temperature of the target window during this irradiation was not a concern since only about 9.5% of the total energy of the beam is deposited in the Ti64 beam window, the beam current was low throughout this short irradiation, and cooling occurred as the 24.3-25.3 °C water flowed by the target window at 1 L/min. Assuming this cooling by the water occurred according to Fourier's Law, the temperature of the water and the Ti64 window were estimated by evaluating the energy deposition and the heat transfer between these materials for short time steps throughout the irradiation time. This procedure resulted in an estimated temperature of 25.5 °C for the water and 25.7 °C in the Ti64 window (*i.e.,* +1.2 °C and +1.4 °C temperature change, respectively). Based on these estimates, it is likely that the water provided sufficient cooling of the Ti64 beam window and that passive cooling of the water occurred in this experiment.

The conductivity of the water was measured throughout the experiment to provide a qualitative measurement of the level of dissolved ions in the water. These conductivity measurements taken before and during the irradiation are shown in Figure 3.4. Initially, a saturation behavior is observed as the water came into equilibrium with the carbon dioxide in the air. This provided a baseline of about 800 nS/cm for the conductivity of the water before

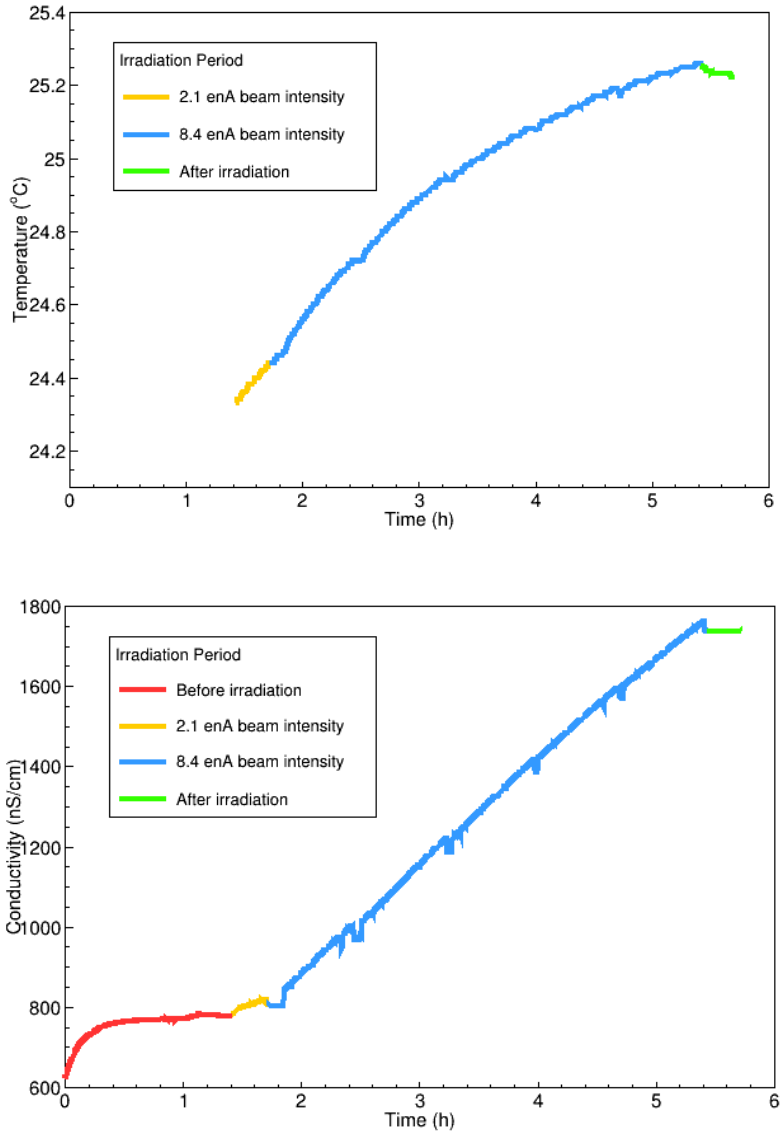

Figure 3.4: Measurements of the Temperature and Conductivity of the Water during the Irradiation The temperature and conductivity of the bulk water are shown as a function of the time elapsed since the water was purified using ion exchange resins. Each irradiation period is indicated by a different color: before irradiation (red), 2.1 enA irradiation (gold), 8.4 enA irradiation (blue), and after irradiation (green).

the irradiation. During both irradiation periods, the conductivity increased linearly. However, the magnitude of the slope increased with the higher intensity beam current, indicating a higher production of ionic species in the water as the intensity increased. Additionally, the

sudden decreases shown in Figure 3.4 correspond to times when the Faraday cup was inserted to measure the beam current. Less stable ionic species such as radicals with short lifetimes were no longer produced through radiolysis at the target, corresponding to a decreased conductivity. After this initial decrease when the Faraday cup was inserted, the presence of relatively stable ionic species in the water was shown by a constant conductivity reading. At the end of the irradiation, ion exchange columns removed both stable and radioactive ions from the water, lowering the conductivity to about 100 nS/cm. This low conductivity value demonstrates the effective, nearly complete removal of ions from the irradiated water.

At some point during the approximately 4-hour irradiation, a small leak developed at the flowing-water target. This led to less than 100 mL of water leaking from a gap between the target body and the back plate of the target. This volume, at less than 2% of the total water used, falls within the precision with which the total water volume was known. Therefore, the effects of this leak on quantifications of the stable and radioactive ions in the system was deemed negligible.

Based on an inspection of the target following the irradiation, two important observations were made: (1) The O-ring which provided a seal between the target body and the back plate of the target was out of place and had been noticeably stretched. This indicated that pressure inside the target put stress on the seal at the back plate. (2) The screws that held the back plate on the target body developed significant oxidation. This most likely occurred as the beam entered humid air before reaching the target. In these conditions, a high energy particle beam can create a corrosive atmosphere of ozone and nitric acid in the air. This environment potentially compromised one or more of the screws securing the back plate of the target. It is

also possible that the temperature of the bulk water as recorded by the sensors in the system did not provide an accurate understanding of the local temperature in the target volume. Additionally, an increased pressure in the target could have led to flexibility in the polyethylene target shell material, making the seal at the back of the target less secure. Any one of these possibilities could have led to the minor leak that was observed at the target. This target set up was not used further, as a target shell made completely of the Ti64 alloy was used for the next several experiments.

3.3.2 Radionuclide Quantification and Comparison to Production Estimates

The gamma-ray spectra shown in Figure 3.5 demonstrate the activity collected on the cation resin, the anion resin, the hydrogen peroxide degrader, and the reservoir water. Table 3.1 provides the quantification by gamma-ray spectroscopy of each radionuclide on these components. Additionally, the production rate of these radionuclides in atoms produced per incident ^{40}Ca ion was calculated based on the measured total activities and the beam current during the irradiation and are given in Table 3.1.

The location of the radionuclides collected in the system matches the expected chemical speciation [62]. For instance, sodium, magnesium, and manganese were collected on the cation exchange resin and chlorine, vanadium, and chromium were found on the anion exchange resin. For the most part, fluorine was also collected on the anion exchange resin. The remaining activities from beryllium and scandium isotopes were found on a few system components; this was expected as they are known to form neutral species in an aqueous solution that is slightly acidic and oxidizing. The efficiency of the system for ion extraction was demonstrated by the very low level of activity found in the water after it was circulated over

the ion exchange resins. Most radionuclides were not observed in the water above the background in the measurement. Even ^{18}F, the main radionuclide found in the reservoir water, was collected with an efficiency of 94(1) %.

Table 3.1: Quantification of and Production Rate Estimate for Radionuclides Produced in Water Target
The quantification of each radionuclides was decay corrected to the end of bombardment (EOB) and was determined with HPGe spectroscopy. The activities denoted with an asterisk (*) are calculated activities based on the distribution of ^{44m}Sc on the system components.

Radionuclide	Activity Measured (kBq)					Production Rate (atoms produced per incident ^{40}Ca atom)
	Cation Resin	Anion Resin	Degrader	Water	Total	
^{7}Be	13.9(4)	3.3(2)	-	-	17.2(4)	$3.2(3) \times 10^{-3}$
^{18}F	39(9)	$1.194(5) \times 10^{3}$	-	80(4)	$1.31(1) \times 10^{3}$	$6.6(7) \times 10^{-4}$
^{24}Na	125(7)	-	-	6(1)	130(7)	$3.0(3) \times 10^{-4}$
^{28}Mg	1.7(1)	-	-	-	1.7(1)	$5.6(7) \times 10^{-6}$
^{34m}Cl	-	$4.5(9) \times 10^{3}$	-	-	$4.5(9) \times 10^{3}$	$1.7(4) \times 10^{-3}$
^{43}Sc	11(1)	23.5(9)	10.0(6)*	11(1)*	56(2)	$4.3(5) \times 10^{-5}$
^{44g}Sc	4(1)*	6(3)	3(1)*	2.4(7)	16(3)	$1.2(3) \times 10^{-5}$
^{44m}Sc	1.15(3)	1.59(4)	0.81(1)	0.83(9)	4.4(1)	$3.8(4) \times 10^{-5}$
^{48}V	-	0.54(3)	-	-	0.54(3)	$3.0(4) \times 10^{-5}$
^{48}Cr	-	0.79(6)	-	-	0.79(6)	$2.7(4) \times 10^{-6}$
^{52}Mn	0.68(4)	-	-	-	0.68(4)	$1.3(6) \times 10^{-6}$

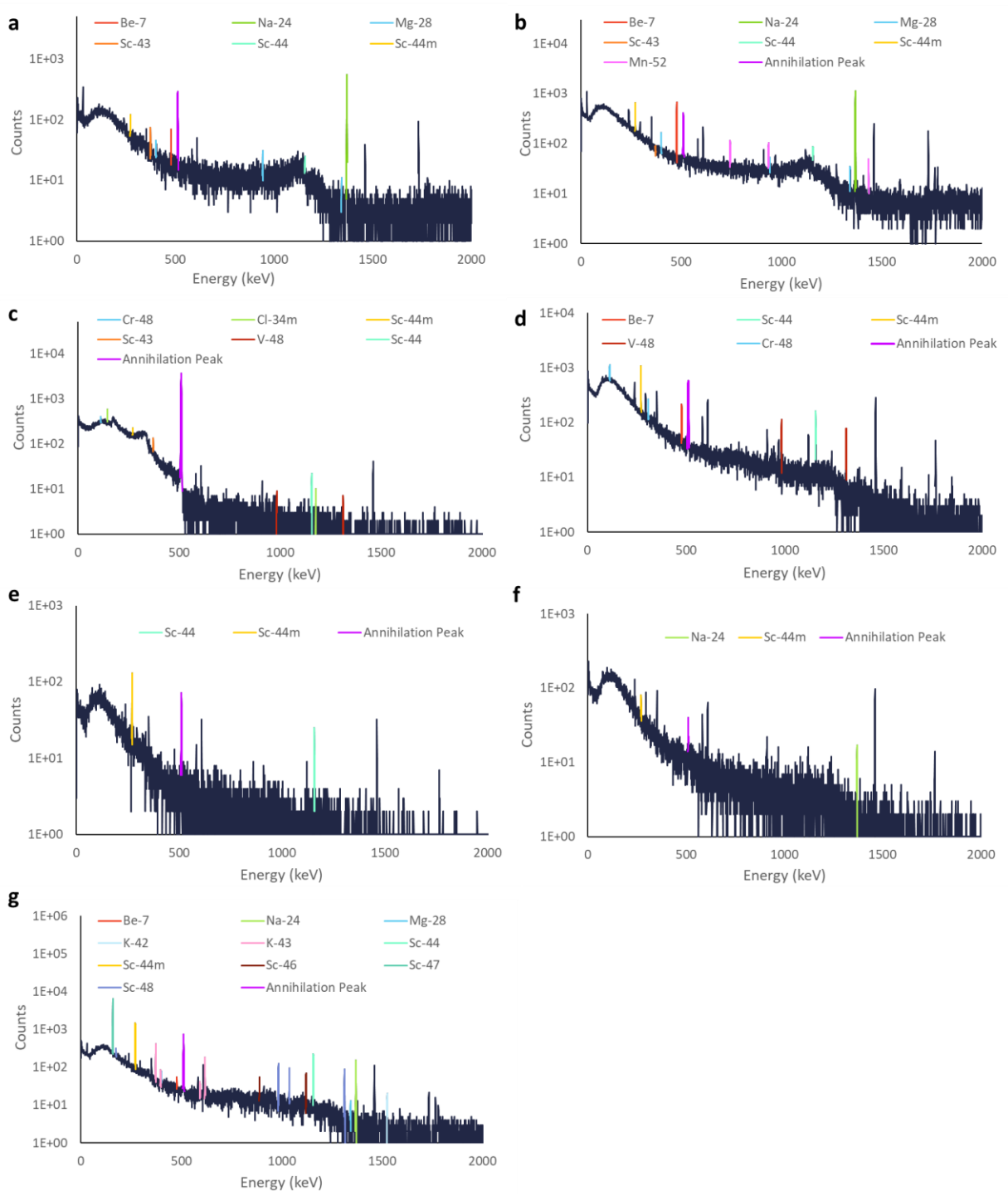

Figure 3.5: Example Gamma-Ray Spectra of System Components
Gamma-ray spectra with their live counting time given in parenthesis: (**a**) cation resin on the day of the irradiation (520 s), (**b**) the cation resin two days after the irradiation (2959 s), (**c**) the anion resin on the day of the irradiation (517 s), (**d**) the anion exchange resin two days after the irradiation (3957 s), (**e**) the hydrogen peroxide degrader two days after the irradiation (429 s), (**f**) the reservoir water on the day of the irradiation (1275 s), (**g**) and the target window two days after the irradiation (1397 s). All unlabeled peaks in the spectra are at energies corresponding to known background gamma rays.

Production estimates for the FR and FE reaction products were performed using LISE++, LisFus, and PACE4. The estimates as well as the measured activities are shown in Table 3.2 for the FR reactions and Table 3.3 for the FE reactions. These values were calculated for the average beam current values over the two different intensity sections of the irradiation: 0.11 pnA for 17 minutes followed immediately by 0.42 pnA for 3.5 hours. Since the production distribution between the metastable and the ground state of radionuclides such as ^{44}Sc and ^{34}Cl are not given by codes, the following distributions were used for these radionuclides. The projected isomeric ratios from both PACE4 and LisFus were found to be closer to the observed ratio when the production proportion was 3:1 ^{44m}Sc:^{44g}Sc. Attributing 100% of the production rate for ^{34}Cl calculated with LISE++ to producing ^{34m}Cl achieves an activity of 3.2 X 10^3 kBq which is within two sigma of 4.5(9) X 10^3 kBq the observed activity for ^{34m}Cl. Activities corresponding to these distributions for ^{44}Sc and ^{34}Cl are given in Table 3.3.

Table 3.2: Activity Measured and Predicted for Radionuclides Produced through Fragmentation Reactions.
The asterisk (*) denotes that the ratio of produced ^{34g}Cl to ^{34m}Cl is not known so 100% of the production rate found with LISE++ was attributed to making ^{34m}Cl as this assumed production distribution provides a predicted activity closest to the measured activity.

Radionuclide	Activity (kBq)	
	Measured	Predicted with LISE++
^{7}Be	17.2(4)	1.4
^{18}F	1.32(1) X 10^3	1.6 X 10^3
^{24}Na	130(7)	246
^{28}Mg	1.7(1)	14.3
^{34m}Cl	4.5(9) X 10^3	3.2 X 10^{3*}

Table 3.3: Activity Measured and Predicted for Radionuclides Produced through Fusion Evaporation Reactions.
The asterisks (*) denote that information about the percent of ^{44}Sc produced in the metastable vs. the ground state is unknown. Instead, percentages were found that most closely matched the produced ^{44m}Sc to ^{44g}Sc ratio. The predicted activities shown in the table for both PACE4 and LisFus were found, assuming 25% of the ^{44}Sc produced is ^{44g}Sc and 75% is ^{44m}Sc.

Radionuclide	Activity (kBq)		
	Measured	Predicted with PACE4	Predicted with LisFus
^{43}Sc	56(2)	62.5	148
^{44g}Sc	16(3)	22*	14*
^{44m}Sc	4.4(1)	6.03*	3.77*
^{48}V	0.54(3)	1.30	0.39
^{48}Cr	0.79(6)	5.18	19.0
^{52}Mn	0.68(4)	2.00	0.68

The methods used here for estimating production in the water-filled target vary in the accuracy of their predictions. While the estimates for ^{18}F, ^{24}Na, and ^{34m}Cl are inaccurate by only a factor of four or less, the predictions for ^{7}Be and ^{28}Mg differ by about an order of magnitude from observation. For the fusion evaporation estimates, the values are mostly within a factor of 4 of the measured values. The exception is ^{48}Cr with values differing by a factor of 7 for PACE4 and 24 for LisFus. For the level of activity produced in this short, low-intensity test, the differences in predicted and measured values did not present a safety hazard or an experimental hurdle. However, as the irradiation length and intensity increase, it will become more important to correctly estimate production rates. This will allow adequate radiological controls, and guide harvesting efforts to products that will be present in significant enough quantities for use in off-line experiments.

3.3.3 Radiolysis Measurement

To observe the behavior of the hydrogen measurements within each irradiation period, the measured hydrogen concentration was overlaid on the beam current in Figure 3.6. As in Figure 3.1, the scaled beam current readings from the unsuppressed target are shown as the large number of points in green while the calibrated beam current readings from the Faraday cup are shown as the smaller number of points in purple. The hydrogen gas measurements are given on the secondary y-axis and are represented in pink.

The graph shows that shortly after a Faraday cup measurement was taken, during which the irradiation of the water was interrupted, the hydrogen concentration drops significantly. This occurs as the hydrogen production through radiolysis is interrupted during these disruptions in the irradiation of the water. Additionally, the decrease in H_2 concentration is not instantaneous after the Faraday cup insertion as it took a short amount of time for the accumulated hydrogen gas to escape the system as the hydrogen-rich water passed by the second membrane contactor in the system.

A qualitative trend in the hydrogen concentration is shown in Figure 3.6 for the higher intensity irradiation setting. During the first period at this intensity setting, the highest hydrogen concentration occurred at the beginning of the irradiation period. Within this period, however, the measured hydrogen concentration decreases. The second higher-intensity irradiation period starts at a lower concentration than the first and then exhibits a similar trend of decreasing concentration measurements through the irradiation period. The hydrogen concentration appears to reach a lower limit during the last three higher-intensity irradiation periods.

An average effective G-value was found for each of the six irradiation periods (Table 3.4). With this value, the hydrogen production during the irradiation periods can be quantitatively compared, as the effective G-value factors in the average beam current and the average dilution factor for the hydrogen concentration measurement for each irradiation period. The effective G-value for the radiolytic production of hydrogen gas demonstrates the decrease in hydrogen production that is visually apparent in Figure 3.6. However, with the normalization of the beam current in the effective G-value measurement, it is shown that the highest relative hydrogen production occurred in the first irradiation period at the lower-intensity beam setting. The largest difference between the effective G-value of two beam intensities occurred between the first two irradiation periods with smaller differences thereafter.

While the trend demonstrated in Figure 3.3 could be improved with more data points and a more comprehensive fitting function, it demonstrates a clear relationship between experimentally measured G-values for H_2 and the average LET of a particle. Using this trend, a G-value for the production of hydrogen gas was predicted at almost double the maximum rate observed experimentally in this irradiation. One practical reason for the low observed value could be due to the permeability of most plastic materials to H_2 gas. The isotope harvesting system used here produced H_2 gas at the target, sent the hydrogen-rich water through a section of polyethylene tubing, and measured the H_2 gas that escaped from the water through a membrane contactor. This set up potentially allowed for some escape of the produced H_2 gas. A possible explanation for the decrease in H_2 concentration measured as the irradiation progressed is the occurrence of recombination events between radiolysis products. While many

radiolysis products recombine rapidly within the particle track, some molecular species such as H_2, O_2, and H_2O_2 remain for are longer-lived in the water. Buildup of these products, particularly H_2O_2 in the water could have affected recombination within the particle tracks, resulting in a suppressed experimental value for hydrogen production resulting in the measurement of an "effective" G-value. [40]

Most likely, the effective G-values presented here are suppressed values compared to the true production rate. However, these measurements provide an understanding of the overall level of H_2 that results from production and recombination reactions in an isotope harvesting irradiation. The suppression observed here may also indicate that lower levels of radiolysis products than predicted will be observed in future irradiations and that radiolysis product levels will be more manageable than anticipated. More measurements of a wider range

Table 3.4: Average Hydrogen Gas Production and Experimental G-value for Six Irradiation Periods
A 5% uncertainty was used for the measured H_2 concentration based on the manufacturer's reported variance in repeatability for a measurement of less than ±5%.

Irradiation period	Average Beam Current (enA)	Measured H_2 Concentration (ppm)	Experimental G-value (H_2 molecules/100 eV)
1	2.0	130(7)	0.86(4)
2	8.69	459(23)	0.70(4)
3	8.69	438(22)	0.67(3)
4	8.3	391(20)	0.62(3)
5	8.43	392(20)	0.62(3)
6	8.52	392(20)	0.61(3)

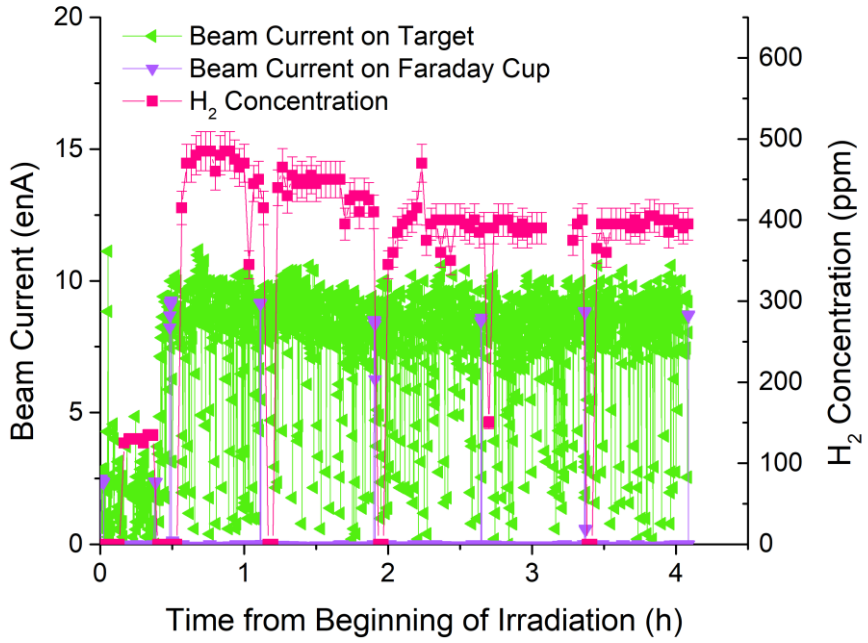

Figure 3.6: Hydrogen Gas Production and Beam Current
The hydrogen gas measured in ppm and the beam current in enA are shown as a function of irradiation time. Although the beam current remains relatively steady for about four hours of the irradiation, the measured hydrogen gas production decreases throughout this time period.

of radiolysis products have been performed (not as a part of the present work) to better understand the dynamics of radiolysis products in the isotope harvesting system, particularly as irradiations use increased beam intensities to more closely match those expected at FRIB.

3.3.4 Corrosion Assessment

3.3.4.1 Ion Exchange Resin Processing

The vast majority of the ions in the system water were collected on the cation and anion exchange resins used following the irradiation. This is demonstrated by the very low conductivity and the small activity of ^{18}F in the bulk water after it was passed over these resins. Therefore, the concentrated samples collected from the resins should provide a quantitative

understanding of the ions present in the system water at the end of the irradiation. In the ion exchange column eluate, the following elements were identified and quantified: B, Na, Mg, Al, Si, P, S, K, Ca, Fe, Ni, Zn. Table 2.5 provides information about the amount of each element that was found on either the cation or the anion exchange resin.

Table 3.5: Quantification of Stable Elements Eluted from Ion Exchange Resins after Irradiation, Collection, and Elution

The values in this table are measured using ICP-OES. The upper limits provided for vanadium are estimates of the limit of detection from this measurement.

Element	Mass Eluted (mg)		
	Cation Resin	Anion Resin	Total Recovered from Columns
B	-	0.50(2)	0.50(2)
Na	1.45(4)	0.22(2)	1.67(5)
Mg	0.17(2)	0.39(2)	0.57(3)
Al	0.07(3)	0.66(3)	0.72(4)
Si	0.10(9)	3.28(7)	3.4(1)
P	0.13(2)	-	0.13(2)
S	0.034(3)	0.229(3)	0.264(4)
K	67(2)	-	67(2)
Ca	0.52(5)	0.29(3)	0.81(6)
V	< 0.006	<0.009	<0.014
Fe	0.022(1)	0.029(1)	0.051(1)
Ni	-	0.035(2)	0.035(2)
Zn	0.064(6)	0.021(1)	0.085(6)

When removing ions in the water with the resins, the water circulated over first the cation exchange resin and then the anion exchange resin. The cation exchange resin had a H^+ counter ion while the anion exchange resin had an OH^- counter ion. This arrangement was used so that overall, the two counter ions would recombine to form water molecules instead of adding additional ions to the system (*e.g.*, Na^+ and Cl^-) and increasing the conductivity of the system water. However, the chemical state of the anion resin with an OH^- counter ion may have had the unexpected effect of precipitating a fraction of the Ca^{2+} and the Mg^{2+} in the water as it passed over the resin. While the presence of Na+ on the anion exchange resin is also unexpected, this may have resulted from residual traces of the NaOH rinse used prior to the experiment to convert the anion resin to the OH^- form.

The potassium level found on the cation resin most likely resulted from the pH probe in the system. This probe uses a KCl electrolyte solution and the pH measurement depends on this solution passing through a semipermeable membrane into the test solution. This means that the electrolyte was passing through the probe into the system water for several hours as the beam was tuned, during the irradiation, and while the ion exchange resins removed the accumulated ions from the water after the irradiation.

Finally, the level of aluminum found on the anion exchange column was a concern at first, as no aluminum containing parts were expected to be in contact with the water except the Ti64 beam window disk that contained 6% Al by mass. The source of the aluminum is now thought to be the screws that held the backplate of the target in place. Although these were black oxide steel screws, dissolved aluminum was detected in both dilute HCl and H_2O_2 that had been in contact with new screws. These screws were not intended to be exposed to the water

but when a small leak resulted from over-pressurizing the system, the backplate loosened. This allowed the screws to be exposed to irradiated water, leading to a small amount of aluminum in the system water.

The hypothesis that the aluminum did not originate in the target window is supported by the observation that no vanadium was found in the eluate from either column. Since ^{48}V, a product from the irradiation, was found on the anion exchange resin and nowhere else in the system, it is to be expected that stable vanadium would have been mainly collected on the anion exchange column as well. Therefore, vanadium would have been detected at least in part in the samples eluted from the anion exchange resin. A limit of detection estimate is included in Table 3.5 demonstrating that the possible level of undetected vanadium in the eluate was very low, not exceeding about 0.015 mg total. An estimate of the amount of vanadium expected in the eluate if the aluminum resulted from target degradation can be made based on two assumptions: 1) vanadium and aluminum had the same removal efficiency from the columns and 2) the amount of vanadium corroded from the window is related to the amount of aluminum corroded by the mass proportions of each element in the window material (6% aluminum and 4% vanadium in Ti64). Based on these reasonable assumptions, 0.48 mg of vanadium should have been detected in the column eluate. This is a significant amount of vanadium, well above the limit of detection using ICP-OES. Therefore, it is very unlikely that this amount of aluminum resulted from target degradation.

Except for the potassium level, the amount of each stable ion removed from the system is fairly low. However, this analysis of the stable ion contaminants in the system provides information on the identity and relative level of competitive ions for future separations,

radiolabeling experiments, and other chemical processes or measurements with harvested radionuclides.

3.3.4.2 Surface Assessment

The two images of the irradiated Ti64 disk described above are shown in Figure 3.7. The most notable result is that the beam activation spot on the disk image in Figure 3.7b appears at the same spot on the disk where a visual difference can be observed in the photograph shown in Figure 3.7a. This visual difference between the irradiated and non-irradiated areas of the Ti64 disk could also be observed on the disk with the human eye. Since this difference is so readily apparent, this indicates significant changes to the water-facing side of the disk at the beam strike. This change likely resulted from the ionizing beam of $^{40}Ca^{20+}$ passing through the Ti64 material and from radiolysis products in the water medium in contact with the disk at the beam strike. These conditions could induce changes in the internal structure of the alloy (*e.g.*, atom displacements) and changes to the passivation layer of the alloy in contact with the water

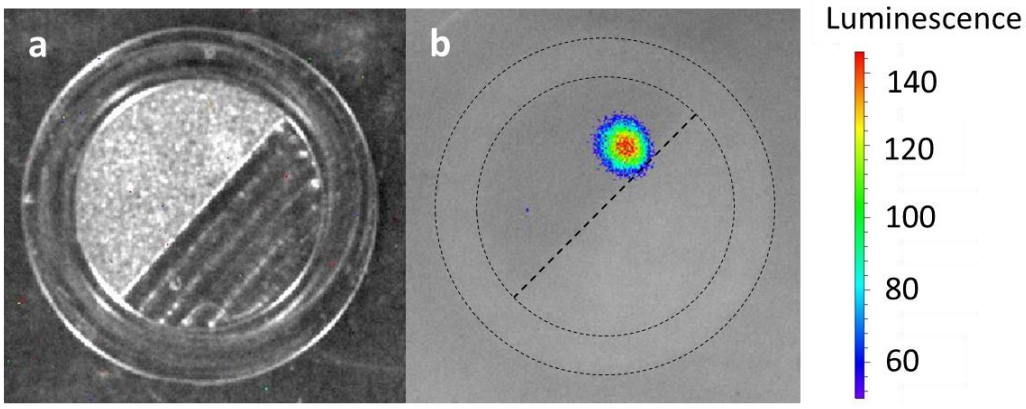

Figure 3.7: Optical Image of Irradiated Ti64 Disk
The optical image from the Ti64 without (a) and with (b) a scintillating plastic sheet over the Ti64 disk. Both images were taken with the disk in the same placement in the instrument, allowing for the verification of the beam strike location in the left picture of the disk. The luminescence scale to the far right is an uncalibrated scale that indicates relative intensity of activity in the beam spot.

interior of the target, respectively. While these effects may lead to corrosion of the Ti64 target material, it is also possible that they could stimulate a hardening effect of the material that will make it more corrosion resistant. Further studies are necessary to resolve these questions since the extent of material erosion observed in this experiment was small.

3.3.4.3 Corrosion Rate Estimation

Using gamma spectroscopy, a ^{47}Sc activity of 16.4(12) kBq was measured in the Ti64 beam window. No equivalent activity of ^{47}Sc was found on the components. A limit of detection estimate was used to set an upper limit on the activity of ^{47}Sc that could have entered the water from the window. The gamma spectrum of the hydrogen peroxide degrader and the relative proportions of ^{44m}Sc found on various system components provided an upper limit of 60(10) Bq of ^{47}Sc could have degraded into the water (*i.e.*, less than 0.4% of the ^{47}Sc measured in the Ti64 beam window).

The amount of ^{47}Sc in the window and the water was assumed to build up in the water over time. The production in the window followed the beam intensity, while the degradation from the window was assumed to be a constant percent of the activity in the window. The percent degradation of the beam spot was found to be ≤ 0.21(3) % per hour or ≤ 0.7(1) % over the course of the 3.5 h experiment. The difference between the 0.4% upper limit of ^{47}Sc degradation determined with gamma spectroscopy and the 0.7% upper limit on the beam spot degradation can be explained by the time dependent production of ^{47}Sc in the beam window. Although the degradation of the window was assumed to be constant, the ^{47}Sc accumulated in the window throughout the irradiation. Only if the final measured ^{47}Sc activity in the Ti beam window was present from the beginning of the irradiation would these two upper limits match.

The percent degradation can also be converted to the amount of mass degraded from the beam spot. Using the mass of the beam spot only, the amount of mass degraded could have been ≤ 0.18(4) mg, which was ≤ 0.02% of the total target disk mass. It should be emphasized that this value is an upper limit of the degradation of the Ti disk at the beam spot, meaning the actual degraded mass was equal to or smaller than the limit presented here.

3.4 General Discussion

This isotope harvesting experiment demonstrated the ability to use a flowing water-filled target to produce and harvest radionuclides from a high-energy heavy-ion primary beam. Several radionuclides were identified and quantified as reaction products from either fragmentation or fusion evaporation reactions. The collection efficiency of the ion exchange resins in the system was quite high as only scandium isotopes and a small amount of ^{18}F was observed through gamma spectroscopy in the reservoir water following collection on ion exchange resins. The conductivity of the water also dropped to 100 nS/cm after using the resins, indicating the removal of most stable ions as well. This test of the initial prototype system showed the feasibility of producing and using radionuclides generated through isotope harvesting.

During this experiment, the isotope harvesting system was tested under the effects of an irradiation. A minor leak developed, showing that the target system used in this experiment is not suitable for handling this level of irradiation effects such as an increased temperature and pressure. This experiment was intended to test the durability of the target window material, Ti64, under bombardment by beam particles and the harsh radiolysis effects in the interior water. Therefore, a new target system was designed in which the entire target shell will be

made of Ti64. This target was designed to handle high pressure, elevated temperatures, and high flow rates, making it unlikely that leaks would develop at the target in future experiments. Additionally, this experiment used a low beam intensity over a short irradiation period, resulting in only a minor increase in temperature. As future irradiations increase in intensity, changes were made to the system including active cooling with a water chiller, larger water volumes, and higher flow rates. Furthermore, for the 400 kW beam power anticipated at FRIB, the beam will irradiate a circulating target, which will spread the deposited energy over a large area on the target face [39] but a rotating target is beyond the scope of the present work. Each of these adjustments will allow for more efficient cooling of the target face than with the methods used in this experiment (*e.g.,* cooling the target window with 6 L of water flowing at 1 L/min and passive cooling of the water in the reservoir).

The production and effects of radiolysis products were also explored during this irradiation. The hydrogen gas produced through radiolysis was measured at the two different beam intensities and was compared to theoretical production estimates. The amount of hydrogen gas measured was lower than the predicted level, indicating that radiolysis products in this system may recombine to a larger extent than previously thought or might be lost through diffusion through plastics. Additionally, the value continued to decrease slowly as the irradiation progressed, suggesting that the build-up of radiolysis products in the water led to a lower amount of H_2 being produced or escaping from the target system. Although this experiment did not provide a G-value measurement for *pure* water radiolysis, the observed hydrogen production was indicative of what can be expected in future isotope harvesting experiments at NSCL and FRIB. Relative measurements of radiolytic products in future

experiments can provide a benchmark that will indicate changes in water chemistry. This will be important as upgrades are made to the target and water purification system and higher beam intensities are used.

The effects of radiolysis on the system components, especially the target window, were explored using an analysis of the stable and radioactive ions in the system water as a result of corrosion. Since the levels of stable ions detected in the system were relatively low, there was no indication of wide-spread system degradation. Although aluminum was detected in the system, no corresponding vanadium was observed with ICP-OES. This strongly suggests the aluminum did not originate in the target disk but from a different component in the system. Additionally, ^{47}Sc was not found in the system water or on any components in the system even through it was produced in the target disk. Together, these observations strongly indicate that no target disk degradation was observed in this preliminary experiment.

3.5 Conclusion

The results of this experiment demonstrated that isotope harvesting with a stable ion beam and a flowing-water target is a viable way to produce radionuclides for research purposes, give a measurement for the production of H_2 as a radiolysis product, and provide evidence that Ti64 may be able to withstand the effects of an irradiation and the resulting radiolysis products. The comparison of predicted to measured activities of the radionuclides produced in this irradiation demonstrated the importance of measuring the production rates for accurate estimates and experimental planning. As the measurement of H_2 gas production in this experiment was far lower than predicted using literature G-values, further experimental measurements of the radiolysis species produced in the isotope harvesting system are also

necessary to understand the extent of the effect of radiolysis in isotope harvesting experiments. The results of this experiment and improvements to the isotope harvesting target and water system (see Chapter 2 Section 2.2.2 and Section 2.3.2) facilitated the next stage of isotope harvesting experiments with low intensity ^{48}Ca and ^{78}Kr beams at the NSCL.

Chapter 4: Low Intensity ^{48}Ca Irradiation for the Production, Collection, and Purification of ^{47}Ca[8]

An experiment was performed at the National Superconducting Cyclotron Laboratory using a 140 MeV/nucleon ^{48}Ca beam and a flowing-water target to produce ^{47}Ca for the first time with this production route. A production rate of 0.020 ± 0.004 ^{47}Ca nuclei per incoming beam particle was measured. An isotope harvesting system attached to the target was used to collect radioactive cationic products, including ^{47}Ca, from the water on a cation exchange resin. The ^{47}Ca collected was purified using three separation methods optimized for this work: 1) DGA extraction chromatography resin with HNO_3 and HCl, 2) AG MP-50 cation exchange resin with an increasing concentration gradient of HCl, and 3) AG MP-50 cation exchange resin with a methanolic HCl gradient. These methods resulted in ≥99 ± 2% separation yield of ^{47}Ca with 100% radionuclidic purity within the limits of detection for HPGe spectroscopy. ICP-OES was used to identify low levels of stable ions in the water used in the isotope harvesting system during the irradiation and in the final purified solution of ^{47}Ca. For the first time, this experiment demonstrated the feasibility of the production, collection, and purification of ^{47}Ca through isotope harvesting for the generation of ^{47}Sc for nuclear medicine applications.

[8] The material presented in this chapter draws heavily from the published paper E. Paige Abel, Katharina Domnanich, Hannah Clause, Colton Kalman, Wes Walker, and Greg Severin, Production, Collection, and Purification of ^{47}Ca through Isotope Harvesting at the NSCL. *ACS Omega*, **2020**, *5*, 27864.

4.1 Introduction

After testing the first-generation isotope harvesting flowing-water target and system (described in Chapter 3), the equipment was upgraded to a target shell made completely of Ti64 and a larger water system (see Chapter 2 Section 2.2.2 and 2.3.2). This new system was used for isotope harvesting with a high-energy ^{48}Ca beam to produce ^{47}Ca for the first time with this production route. In a wide range of oxidation potentials and pH values, calcium is expected to be in the Ca^{2+} form in water. This simple chemistry should allow for the ^{47}Ca produced in this harvesting experiment to be easily removed from the water and processed in the laboratory with high yields. The ease of working with calcium is a major advantage to harvesting ^{47}Ca for use in a ^{47}Ca/^{47}Sc radionuclide generator. Other elements that are easily hydrolyzed in near neutral pH conditions, such as ^{48}V and ^{88}Zr, have also been produced through isotope harvesting. [63] These radionuclides, with more complicated chemistries, have proven less easily collected and chemically modified offline.

As in the previous experiment with a high-energy ^{40}Ca beam, all cationic radionuclides were collected by flowing the system water over a cation exchange resin bed and the observed radionuclides were quantified. With these measurements, the production rate for ^{47}Ca was measured and used to extrapolate potential production rates at the higher beam intensities available at the NSCL and anticipated at FRIB. Three ^{47}Ca purification methods were optimized to produce a high purity ^{47}Ca/^{47}Sc generator. An analysis of the stable contaminants in the water and collected on cation exchange resin beds was also performed to understand what stable ions may interfere with the use of generated ^{47}Sc from isotope harvested ^{47}Ca for future radiolabeling experiments. Particular attention was paid to the radionuclidic purity of the final

^{47}Ca samples and practical considerations for using any of the three purification methods for routine use in future isotope harvesting experiments. This work clearly demonstrated the significant production of ^{47}Ca in the isotope harvesting target, the relatively easy collection of ^{47}Ca from a large volume of flowing water, and the purification of ^{47}Ca from radionuclidic and stable ionic impurities. These results show promising potential for the use of isotope harvested ^{47}Ca for the generation of high purity ^{47}Sc for preclinical applications.

4.2 Materials and Methods

4.2.1 Materials

4.2.1.1 Reagents

Before the irradiation, the water in the isotope harvesting system was purified using mixed bed resins (McMaster-Carr, Filter media PVC water deionizer), resulting in a conductivity level of 250 nS/cm. Chemical processing of the products was performed with the following reagents: hydrochloric acid (VWR Chemicals, ACS grade, 36.5-38%), nitric acid (VWR Chemicals, ACS grade, 68-70%), methanol (Macron Fine Chemicals, anhydrous, ACS grade), and MilliQ water (Thermo Scientific MicroPure Ultrapure Water System, 18.2 MΩ cm).

4.2.1.2 Extraction Chromatography and Ion Exchange Resins

DGA exchange chromatography resin (N,N,N',N'-tetra-n-octyldiglycolamide, normal resin, particle size 50-100 µm, TrisKem International) was dry loaded into a column and sequentially pre-rinsed with 20 mL of 5 M HCl, 5 M HNO_3, and MilliQ water before use in the separations. Two cation exchange resins (AG50W-X8, mesh size 20-50, BioRad and AG MP-50, 100-200 mesh size, BioRad) and an anion exchange resin (AG8X1, mesh size 20-50, BioRad) were prepared in large quantities by rinsing with the following solutions: 50 mL of 2 M HCL, 50

mL of 4 M HCL, 50 mL of 6 M HCL, and 100 mL MilliQ water. The rinsing steps described here were performed twice to remove ionic impurities, especially metallic impurities, from the resins before loading the resins into the columns.

4.2.1.3 Column Construction

The columns used for collection and separation were made of rigid polycarbonate tubing (3/8” OD, 1/4" ID, McMaster Carr, PN:9176T1) and push-to-connect fittings with a PBT (polybutylene terephthalate) body and stainless steel tube gripping clamps on both ends of the column (Pneumatic NITRA Union Reducer, 3/8” to 1/4"). Two pieces of glass wool were used on each end of the column to stabilize the resin. These columns were inserted in the water system by connecting them to the 1/4” polypropylene tubing in the aqueous harvesting loop of the isotope harvesting system (Figure 4.1).

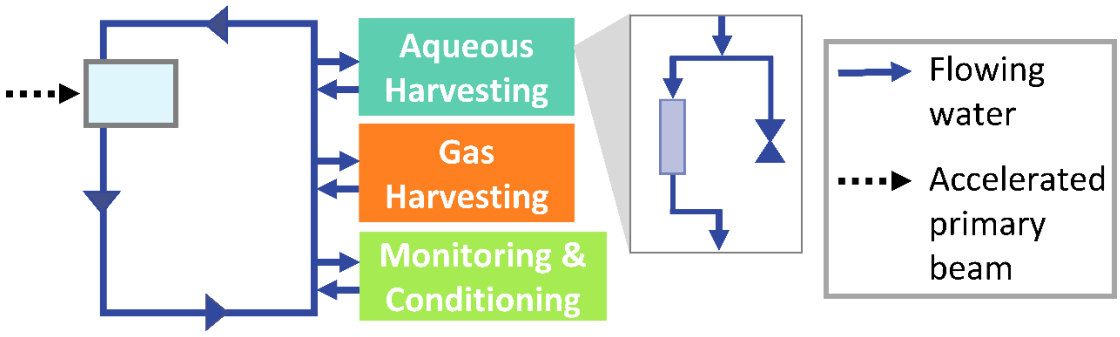

Figure 4.1: Harvesting System Overview
The harvesting system contains a main loop in which 37 ± 4 L of water were circulated from a reservoir at 10 L/min through a titanium alloy (Ti64) target shell (grey box with light blue interior). Subsystems off the main loop collected radioactive and stable ions from the water with ion exchange resins, collected radioactive gases, and monitored and conditioned the water. The inset shows the flow of water through an ion exchange resin and a valve-capped line for water sampling in the aqueous harvesting loop.

4.2.1.4 Instruments

Identification of stable ions was performed with an Agilent Inductively Coupled Plasma-Optical Emission Spectrometer (TCP700.) Identification and quantification of radionuclides were performed with an HPGe Canberra BEGe Gamma-ray Detector (BE2020). Energy and efficiency calibrations of this detector were previously performed with a ^{152}Eu point source 50 cm from the detector face. Analysis of spectra was performed with Genie 2000 software (Mirion Technologies).

Even though non-standard sample geometries were used for gamma spectrometry, no correction factors or additional errors were considered in quantifying radionuclides. Measurements were performed that demonstrated about a 10% difference in the quantification of these nuclides between a point source geometry and a water sample at 25 or 50 cm from the detector face and less than 10% for that between a point source geometry and ions adsorbed on a resin bed also at 25 or 50 cm from the detector face. Absolute quantification based on the water samples was only performed to determine the total activity and production rate for ^{47}Ca, where the 19-20% error in the branching ratios far outweighs the uncertainty from the geometry [8]. When quantification was performed for radionuclides on the cation exchange resin beds, separation columns, or small volumes in falcon tubes at 25 cm from the detector face, no additional uncertainty for the geometry was used as it is a small correction. These measurements taken for the separation methods were also used to calculate the percent activity eluted, so the absolute quantification was not necessary.

4.2.2 ^{48}Ca Irradiation

A 140 MeV/nucleon $^{48}Ca^{20+}$ beam was used to irradiate a flowing-water target over 8.5 hours. Beam current measurements were automatically recorded every second on average from the unsuppressed target (*i.e.*, the recorded values were proportional but not equivalent to the true beam current.) Intermittently, an intercepting Faraday cup was inserted into the beam to get an absolute measurement of the current. The measurements with the Faraday cup were used to calibrate the concurrent unsuppressed readings from the target. Figure 4.2 shows a linear relationship between the unsuppressed target current readings and the calibrated readings from the Faraday cup. This relationship was used to scale the beam current readings on the target measured on average every second throughout the experiment. After a short tuning period at an intensity of 0.26 pnA, the beam intensity was increased and maintained at an average of 0.92 pnA for approximately 5.1 hours.

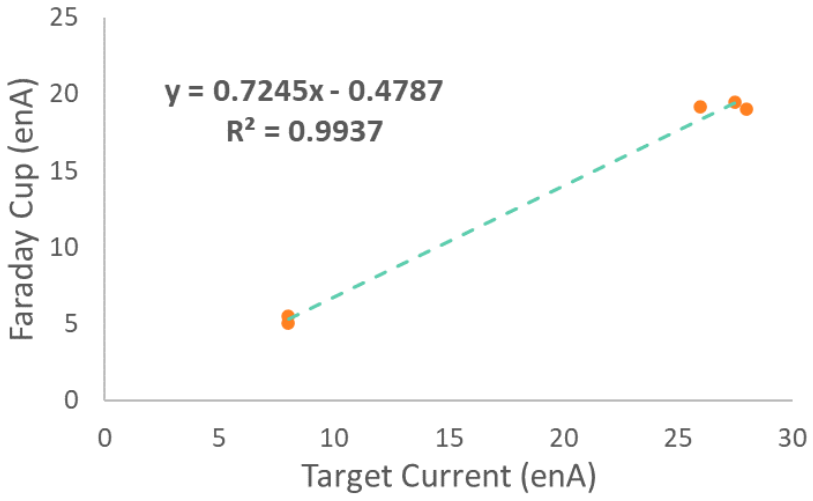

Figure 4.2: Calibration of Target Current Readings
The current recorded on a calibrated faraday cup and the unsuppressed target are given in electrical nanoamps (enA).

The irradiation was paused occasionally for samples of the system water to be withdrawn from the system and ion exchange resin beds to be removed and inserted. According to the timeline in Figure 4.3, three 1-liter water samples were taken during the irradiation, and a fourth sample was taken after the end of the irradiation (named Water Samples 1-4 for reference, respectively). After Water Sample 3 was withdrawn, a cation exchange resin bed (AG 50W-X8, mesh size 20-50, H^+ form, 1.5 g, 8.9 cm x 0.6 cm ID) was inserted in the system with a water flow of approximately 180 mL/min over the resin bed. This cation exchange resin bed was then replaced with fresh resin beds after two more irradiation periods (Resin 1, 2, and 3, respectively). Resin 3 was left in the system for two hours after the irradiation ended with the flow rate increased to 500 mL/min for the second hour to increase the collection rate. Two more cation resin beds (Resin 4 and 5, respectively) were put in the system in parallel as well as an anion exchange resin bed in series the day after the irradiation.

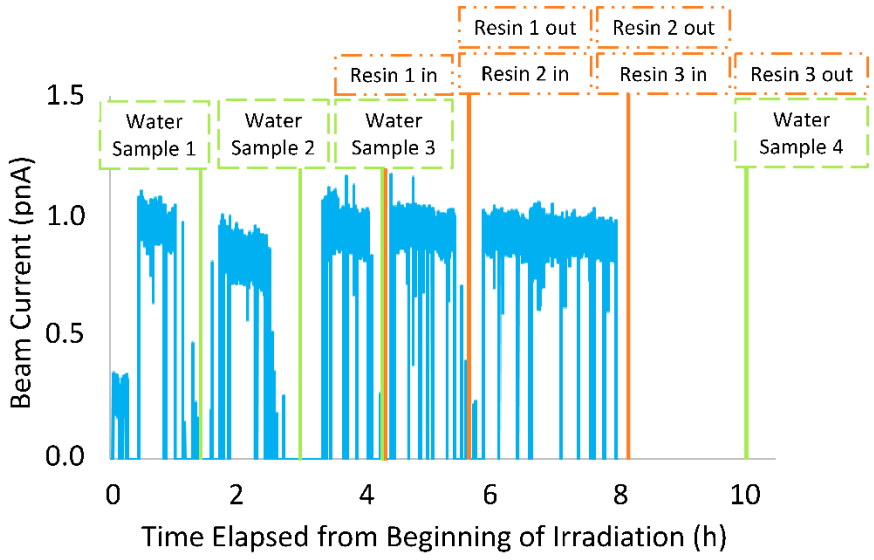

Figure 4.3: Timeline of Irradiation
The beam current (blue), water sample collection (green), and resin bed changes (orange) are shown as a function of time. The beam current shown are the calibrated values of the current on the target.

A final 1 L water sample was taken at the end of the collection effort (Water Sample 5). Altogether, activity was collected in five 1-liter water samples and five cation exchange resin beds that were used for further measurements and experiments.

4.2.3 Production of ^{47}Ca

The activity of ^{47}Ca found in the water samples and on the cation exchange resin beds was measured with the HPGe detector. Analysis of these spectra was performed with Genie software to detect and integrate peaks, implement baseline corrections, and calculate efficiencies at each peak energy. This allowed for the detection and quantification of radionuclides based on their characteristic gamma ray energy emissions. Photopeaks from three characteristic gamma rays were used to quantify the activity of ^{47}Ca: 489.2 keV at 5.9 ± 1.2%, 807.9 keV at 5.9 ± 1.2%, and 1297.1 keV at 67 ± 13%. [51]

The total produced activity of ^{47}Ca was estimated as the sum of activity found in each water sample, on each of the collection ion exchange resin beds, and in the water after collection with the resin beds. The activity remaining in the system water was approximated by measuring the activity in a water sample taken when the last column was removed from the system and scaling up this activity to account for the total remaining water volume of 33 $\pm$ 4 L. This large uncertainty in the water volume mainly resulted from difficulties in draining the water from all components and tubing in the system. Due to this 11% uncertainty in the total water volume of the system and 19-20% uncertainties in the branching ratios, the estimated activity has a large associated uncertainty. For future measurements of this production rate, other indirect methods of measurement will be used to determine the system water volume more accurately and these branching ratios will be remeasured to reduce the associated errors.

The total produced ^{47}Ca activity and the recorded beam intensity throughout the irradiation were used to find the production rate, P, of ^{47}Ca in the flowing-water target in terms of particles produced per incoming beam particle with Equation 4.1:

$$N_P = \sum_{i=1}^{n}[P \times I(t_i) \times \left(1 - e^{-\lambda \Delta t_i}\right) \times e^{-\lambda t_d}] \quad (4.1)$$

where N_P is the number of produced nuclei, $I(t_i)$ is the beam current during the *i*th irradiation interval from t_i to t_{i+1}, λ is the decay constant of the produced radionuclide, and t_d is the time between the *i*th irradiation interval and the end of the irradiation. This segmented production equation accounts for fluctuations in beam intensity during the irradiation.

The production rate of ^{47}Ca in a water target has also been predicted using two simulation codes that predict the production rate of radionuclides in nuclear reactions: PHITS (Particle and Heavy Ion Transport code System) and LISE++. [29,64] For both estimates, a model of the target was used in the program to account for a 500 µm layer of Ti alloy followed by a water layer. Additionally, both fragmentation reactions (at higher particle energies) and fusion evaporation reactions (at lower particle energies) with ^{16}O and ^{1}H were included in the production rate estimates. Finally, the measured production rate for ^{47}Ca in this experiment was used to predict the production at higher beam intensities available at the NSCL and FRIB. Since the ^{48}Ca primary beam expected to be available at FRIB will be accelerated to a higher energy than the currently available ^{48}Ca beam at the NSCL, LISE++ was used to find the relationship between the production of ^{47}Ca at 140 and 189 MeV/nucleon. This comparison was used to qualify the accuracy of this extrapolated activity prediction for FRIB. The settings used

in LISE++ to find a predicted production rate for ^{47}Ca and to compare the production of ^{47}Ca at NSCL and FRIB energies are given in Appendix B.

4.2.4 Collection and Sample Processing

In addition to ^{47}Ca, the following radionuclides were collected on the resins and identified with gamma spectroscopy: ^{24}Na, ^{27,28}Mg, ^{42,43,44,45}K, and ^{44m,47,48}Sc. These activities were quantified using characteristic gamma-rays observable above the background and with the branching ratios reported in the Evaluated Nuclear Structure Data File for each radionuclide (see Appendix A). [14,15,27,28,50,51,53,65–67] The collection efficiency for ^{47}Ca was calculated by comparing the total activity collected on the cation exchange resin beds to the total activity, including that estimated to be remaining in the system water as described previously.

The ^{47}Ca activity collected on five cation exchange resin beds was removed with 50-70 mL of 3 M HNO_3 per resin bed with a flow rate of 1.8-2.0 mL/min. This eluate from each resin bed contained a mixture of cationic radionuclides and was separated into several fractions for

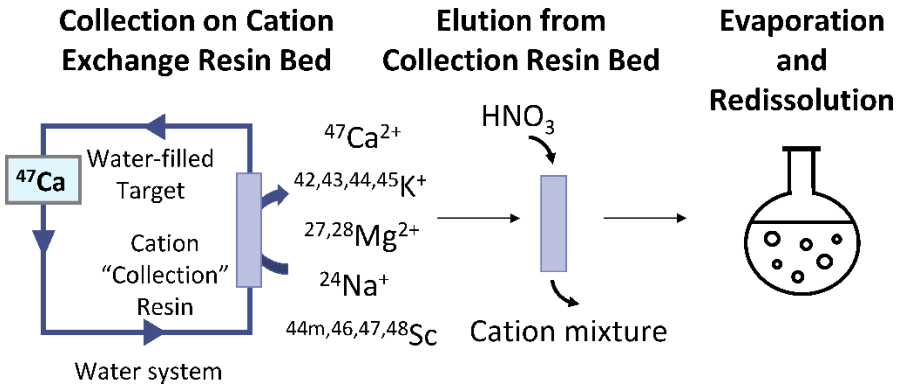

Figure 4.4: Collection, Elution, and Preparation of Cationic Radionuclides
Sample processing was performed in this manner except for samples used with separation method 1, which were used directly after elution from the collection resin.

use in three separation methods. Method 1 used the eluate directly as the load solution. Fractions used for methods 2 and 3 were evaporated to dryness on a rotary evaporator and reconstituted in 0.1 M HCl and 0.5 M HCl/90% methanol, respectively. See Figure 4.4 for a schematic overview of the sample processing.

4.2.5 Purification of ^{47}Ca

The following three methods were developed and optimized in this work to separate Ca from Na, Mg, K, Sc, and Fe. These elements were present as ^{24}Na, ^{27,28}Mg, ^{42,43,44,45}K, ^{44m,47,48}Sc, and stable Fe (*i.e.*, natural) during the experiment. After each separation, the columns were rinsed with water for storage.

4.2.5.1 Separation Method 1: DGA resin with HCl and HNO_3

A column of 1.07 g of DGA resin (dry packed, 7.2 cm x 0.6 cm ID) was preconditioned with 20 mL of 3 M HNO_3 and a 10-20 mL sample of the collection column eluate in 3 M HNO_3 was loaded at a flow rate of 1.8 mL/min. These conditions were chosen to elute many of the co-produced radionuclides such as ^{24}Na, ^{28}Mg, and ^{43,44}K as well as stable Fe while retaining ^{47}Ca on the resin. The flow rate was decreased to 1.3 mL/min and an additional 10-15 mL of 3 M HNO_3 was used to rinse the column and ensure that all Na, Mg, and K isotopes were entirely removed. Elution of ^{47}Ca was carried out with approximately 20 mL of 3 M HCl to selectively remove ^{47}Ca and leave any Sc isotopes adsorbed on the resin.

4.2.5.2 Separation Method 2: AG MP-50 with HCl

A column of 1.5 g AG MP-50 resin (slurry packed, 7.5 cm x 0.6 cm ID) was pre-conditioned with 0.1 M HCl. Evaporated fractions from the collection columns were re-

dissolved in 20 mL of 0.1 M HCl. This concentration was used since Ca has a large distribution coefficient with AG MP-50 at this condition, allowing for the creation of a narrow ^{47}Ca band during the loading step. This solution was loaded on the column and was followed by rinse steps of 10 mL of 0.1 M and 23-25 mL of 2 M HCl. Rinsing with these HCl concentrations allowed for the elution of co-produced radionuclides such as ^{7}Be, ^{24}Na, ^{28}Mg, and ^{43,44}K and any stable Fe. Then, 10 mL of 5 M HCl was used to elute ^{47}Ca while retaining the Sc isotopes on the column. This separation was carried out with a flow rate of 0.8 mL/min throughout.

4.2.5.3 Separation Method 3: AG MP-50 with Methanolic HCl

1.0 g of AG MP-50 resin (slurry packed, 5 cm x 0.6 cm ID) was pre-conditioned with 0.5 M HCl in 90% methanol. Evaporated fractions from the collection columns were reconstituted in 20 mL of 0.5 M HCl in 90% methanol and the solution was loaded on the column. Rinse solutions of 0.5 M HCl/90% methanol (20 mL, 1 mL/min), 2 M HCl/60% methanol (50 mL, 0.75 mL/min), and 2 M HCl/30% methanol (35 mL, 0.75 mL/min) were used in succession. The load and rinse solution of 0.5 M HCl/90% methanol was chosen due to the high distribution coefficient of Ca and the low distribution coefficient of Fe under these conditions. Therefore, any stable Fe present could be eluted in this step while forming a narrow ^{47}Ca band on the column during loading. The two intermediate rinse steps were used to elute coproduced radionuclides such as ^{7}Be, ^{24}Na, ^{28}Mg, and ^{43,44}K. Specifically, the 2 M HCl/30% methanol rinse step was added during optimization of this separation to allow for complete separation of the K isotopes from ^{47}Ca. Elution of ^{47}Ca from the column was performed with 15 mL of 4 M HCl at a flow rate of 1.25 mL/min. The high distribution coefficient of Sc for all rinse media used in this separation ensured that any Sc isotopes remain on the column.

4.2.5.4 Separation Yield and Radionuclidic Purity

For each separation performed, the separation yield was calculated as the activity of ^{47}Ca in the purified fractions divided by the total activity loaded on the column for the separation. The radionuclidic purity was found as the activity of ^{47}Ca in the purified fractions divided by the total activity in these fractions. Both the separation yield and radionuclidic purity of the purified ^{47}Ca were found using the rate at which characteristic gamma rays for each radionuclide were observed by the gamma detector to avoid using the reported branching ratios and their large associated errors for ^{47}Ca. This was made possible as all spectra were taken at 25 cm from the detector face and the yield and purity were calculated in terms of ratios, avoiding the need for absolute activities. Therefore, the only error considered in the gamma-ray rates was the statistical counting errors.

Since the yield and radionuclidic purity of the ^{47}Ca for each of the separation methods was quite high (*i.e.*, 100% yield and radiopurity), the limit of detection (LOD) for radionuclides that would affect these values was also found. For the yield, the LOD for ^{47}Ca was the sum of the LOD for gamma spectra of (1) the fraction taken just before ^{47}Ca was observed in the eluate, (2) any fractions taken after ^{47}Ca was no longer observed in the eluate, and (3) the column after all fractions were taken for a separation. These were the samples that were most likely to contain ^{47}Ca that was at or below the LOD. The largest influence on the radionuclidic purity was any activity below the LOD for ^{43}K, since this was the radionuclide of the highest activity that eluted close to ^{47}Ca. Tailing elution of this radionuclide could have occurred into the ^{47}Ca elution peak, affecting the radionuclidic purity. Therefore, the LOD of ^{43}K was found in each fraction that was part of the total yield of ^{47}Ca.

In determining the LOD, only the highest intensity gamma-ray energy was considered for each radionuclide (*i.e.*, 1297 keV for ^{47}Ca and 372 for ^{43}K). The LOD was taken as the uncertainty in the counts over a range of 3.5 keV for ^{43}K and 5 keV for ^{47}Ca centered at their most intense characteristic gamma-ray energy. The total LOD for each of these values was the sum of the limit in each spectrum considered. The limit was then converted to a percentage in terms of the total ^{47}Ca activity (*i.e.*, the sum of eluted ^{47}Ca activity in each separation). This LOD was smaller than the error associated with the separation yield and the radionuclidic purity in all cases.

Any activity of ^{45}Ca that was present in the purified ^{47}Ca fractions was not measurable due to the absence of reasonably intense gamma-rays from this radionuclide (*i.e.*, the only gamma ray has an energy of 12.47 keV at an intensity of 3E-6%). While this calcium isotope, if present, would follow ^{47}Ca through all separation methods, it would also follow ^{47}Ca through the previously published pseudo generator. [10] Additionally, ^{45}Ca decays slowly ($t_{1/2}$ = 162.61 d) to stable ^{45}Sc, which would not affect the radionuclidic purity and only minorly affect the specific activity of the final radiolabeling solution. Since ^{45}Ca should not interfere with the generation of highly radiopure ^{47}Sc in future work, the radionuclidic purity reported for ^{47}Ca does not consider any ^{45}Ca present in the purified product.

4.2.6 Stable Elemental Analysis

Water Samples 1-4 and the final purified ^{47}Ca solution containing fractions from each separation were analyzed using a semi-quantitative ICP-OES method to identify and semi-quantify ions above the LOD of the instrument. [68] Samples of 200 mL from water sample 1-4 were evaporated on a rotary evaporator and reconstituted in 10 mL of 1.4% HNO_3 each. The

round bottom flasks used for the evaporation were first rinsed with 1.4% HNO_3 and then with MilliQ water twice. Additionally, all the purified ^{47}Ca samples from the three separation methods were combined and a sample was diluted by half for analysis, resulting in a solution of about 1.5 M HCl.

The semi-quantitative method used preset calibration information for 69 elements with a one-point calibration at 5 ppm from the following calibration check standards: Rare Earths, Precious Metals, Tellurium, Alkaline Earth Non-Transition Elements, and Fluoride Soluble Group. Among these elements were those that would indicate corrosion of the target or metal components in the system (*e.g.*, Ti, V, Al, Fe, Ni, Cr) and elements that have been previously identified as common contaminants in the isotope harvesting system [37] (*e.g.*, Na, Mg, Ca, Si, Zn). The samples were run with a blank check solution of 1.4% HNO_3 for the concentrated water samples and 1.5 M HCl for the combined, purified ^{47}Ca fractions. These blank samples served to help set the baseline for stable ions from the acid content of the samples and for the blank readings from the semi-quantitative method. Elements with readings from the sample above the "blank" value were considered to be present and were used as a semi-quantitative estimate of the amount present.

4.3 Results and Discussion

4.3.1 Production of ^{47}Ca

The total activity of ^{47}Ca measured (decay corrected to the end of the irradiation) was 3.7 ± 0.7 MBq (100 ± 20 μCi). The errors considered in this measurement include the counting statistics, errors in reported gamma-ray branching ratios, and an uncertainty in the total water volume of the system. By far, the dominant factor is the error in the reported branching ratios

Table 4.1: ^{47}Ca Activity Measured in Each Water Sample and Cation Exchange Resin Bed

Sample	Activity (kBq)	Sample	Activity (kBq)
Water sample 1	7(1)	Cation Resin 1	3.0(6) X 10^2
Water sample 2	16(3)	Cation Resin 2	9(2) X 10^2
Water sample 3	25(5)	Cation Resin 3	1.2(2) X 10^3
Water sample 4	34(7)	Cation Resin 4	2.3(5) X 10^2
Water sample 5	42(8)	Cation Resin 5	3.1(6) X 10^2
Remaining water	7(1) X 10^2	Anion Resin	5(2)

of 19-20% error for the three main gamma rays. Table 4.1 gives the decay corrected activity for ^{47}Ca in each of the samples measured.

A production rate of 0.020 ± 0.004(4) ^{47}Ca nuclei produced per incoming ^{48}Ca nuclei was measured. The reported error for this rate is solely from the uncertainty in the quantification of the total activity of ^{47}Ca produced. The production rate can also be thought of as a 2.0 ± 0.4 % conversion rate of beam particles to the desired nucleus, which is relatively high for a charged particle irradiation. In comparison, this rate is 10 to 20 times higher than that for ^{18}F through the routine production route of ^{18}O(p,n)^{18}F. [69]

The predicted production rates using both PHITS and LISE++ are given in Table 4.2. These predictions are significantly lower than the production rate measured in this work. This difference demonstrates the importance of measuring the actual production rate of radionuclides in the isotope harvesting system as predictions have been found to be inaccurate as seen previously with a ^{40}Ca beam experiment with a water target at the NSCL. [70]

Table 4.2: Predicted and Measured Production Rates of ^{47}Ca in Isotope Harvesting Water Target with a 140 MeV/nucleon ^{48}Ca Beam
The production rate is given as the percent of beam particles converted to ^{47}Ca.

Source of Production Rate	Beam Energy at Isotope Harvesting Target (MeV/nucleon)	Production Rate (%)
Experimentally measured	140	2.0 ± 0.4
Predicted with PHITS	140	1.19
Predicted with LISE++	140	1.03
Predicted with LISE++	189	1.72

The measured production rate should be the same for higher intensity irradiations anticipated at the NSCL and FRIB. This allows for estimates for the activity anticipated at these higher intensities and for more detailed safety and experimental planning for future isotope harvesting of ^{47}Ca. Approximately 4.8 GBq (130 mCi) would be expected at the end of a 120-hour (*i.e.*, 5-day) irradiation with a 140 MeV/nucleon 80 pnA ^{48}Ca beam, assuming 90% of the primary beam is directed to the isotope harvesting beam blocker. Since ^{47}Ca would be produced as a byproduct of the NSCL experimental program, this estimate uses the average length of a typical nuclear physics experiment at the NSCL and the standard settings for the ^{48}Ca beam available at this facility. Without any dedicated beamtime or additional use of enriched ^{48}Ca, a significant supply of ^{47}Ca could be produced for research purposes during normal NSCL operations.

The measured production rate can be extended to the ^{48}Ca beam at FRIB as an underestimation of the potential production of ^{47}Ca. At FRIB, the ^{48}Ca beam that reaches the isotope harvesting beam dump will have an estimated energy of 189 MeV/nucleon. With a

higher energy beam, a larger fraction of the beam particles undergo fragmentation reactions, resulting in a higher production rate of ^{47}Ca. For example, the predicted rates from LISE++ for the two different beam energies are given in Table 3.2. [29] While it has been noted that the absolute production rates predicted by LISE++ differs from the experimentally measured rates, this program provides reliable relative trends. Using the production rate measured in this experiment, a 1-day irradiation of the isotope harvesting beam dump at FRIB full beam power (189 MeV/nucleon 30 pμA ^{48}Ca beam, 86% primary beam transmission to beam dump) would produce >520 GBq (14 Ci) of ^{47}Ca. As with the ^{47}Ca produced at the NSCL, the ^{47}Ca production at FRIB will occur simultaneously with the nuclear physics program as the unused primary beam from these experiments is stopped in an aqueous beam dump. [39]

4.3.2 Collection and Sample Processing

The efficiency with which ^{47}Ca was collected from the system on Resins 1-3 with approximately 5.5 hours of water flow on the day of the irradiation was found to be 65 ± 1%. Two additional resin beds were used subsequently to increase the collected fraction, resulting in 82 ± 3% of the ^{47}Ca collected on five resin beds. The uncertainties considered for these efficiencies result from counting statistics and an uncertainty in the volume of water in the system. Offline experiments have demonstrated that increasing the flow through the ion exchange resins can increase the overall collection efficiency. While there is a lower collection efficiency “per pass” of water, the high flow rate increases the frequency of water passing over the column. [36] For future experiments in which the half-life of the radionuclide of interest is short, the flow rate through ion exchange resins can be increased to expedite the collection process.

In addition to ^{47}Ca, other cationic radionuclides were collected on the cation exchange resin beds. The activities on these resins decay corrected to when they were removed from the system are given in Table 4.3. Short lived radionuclides were not observed on Resin 3 because it was removed hours after the irradiation ended. Therefore, the activities on Resins 1 and 2 give a view of the radionuclides and their activities that would be encountered soon after an irradiation and the activities on Resin 3 represent the activities that would be present after a 21-hour cool down period.

Using 3 M HNO_3, an average of 96 ± 1% (n=4) of the ^{47}Ca collected on the cation exchange resins was removed with 50-70 mL. The highest removal rate was observed when 70 mL were used to remove 99.8 ± 0.7% of the ^{47}Ca from Resin 1 and the lowest was observed when 55 mL were used to remove 89 ± 2% from Resin 4. The sodium, magnesium, and potassium isotopes were entirely eluted from the collection resins, while the scandium isotopes were eluted to a lesser extent (Table 4.3). The first 50-55 mL of 3 M HNO_3 used to remove ^{47}Ca from each column were used in the separations. When more than this volume was used in the elution from the collection resins, the last few milliliters contained a low activity of ^{47}Ca due to tailing elution behavior.

For the fractions evaporated to dryness for separation methods 2 and 3, the activity was reconstituted in the proper matrix for each load solution with a high yield: >99% for separation method 2 and >98% for separation method 3. Since no ^{47}Ca was detected on the flasks after the transfer, these yields are lower limits found using the LOD in the gamma spectra at the ^{47}Ca characteristic energies.

Table 4.3: Quantification of Radionuclides Collected on Cation Exchange Resins 1-3
The activities collected with and eluted from resin beds 1-3 are reported with the uncertainty in parenthesis afterwards. The activities eluted from resin beds 1-3 were achieved in 70, 62, and 55 mL, respectively. Additionally, the activity eluted for each radionuclide is given as a percentage of the activity removed from each column based on measurements of each column before and after elution.

Nuclide	Half-life	Activity Collected (kBq)			Activity Eluted (%)		
		Resin 1	Resin 2	Resin 3	Resin 1	Resin 2	Resin 3
^{7}Be	53.22 d	-	12(2)	21(2)	-	100(22)	100.0(2)
^{24}Na	14.997 h	92(4)	250(10)	290(10)	100(1)	100.0(7)	100.0(1)
^{27}Mg	9.458 m	26(2)	-	-	-	-	-
^{28}Mg	20.915 h	13(1)	37(3)	46(3)	100(3)	100(2)	100.0(1)
^{42}K	12.355 h	280(8)	740(50)	990(70)	100(2)	100(1)	100.0(1)
^{43}K	22.3 h	236(5)	639(8)	930(10)	100.0(3)	99.8(2)	100.0(1)
^{44}K	22.13 m	650(100)	1.0(2) X 10^{3}	-	-	-	-
^{45}K	17.18 m	470(30)	560(40)	-	-	-	-
^{47}Ca	4.536 d	300(60)	880(170)	1.2(2) X 10^{3}	99.8(7)	93.9(4)	92.42(1)
^{44m}Sc	58.61 h	5.7(5)	15.5(6)	16.5(9)	75(4)	57(3)	64.97(8)
^{47}Sc	3.3492 d	53(3)	159(9)	310(20)	79(2)	67(3)	62.9(1)
^{48}Sc	43.67 h	30.3(6)	85(2)	85(2)	77(1)	60(1)	64.98(4)
^{46}Sc	83.79 d	1.8(3)	3.9(4)	3.6(4)	100(20)	60(14)	100.0(1)

4.3.3 Purification of ^{47}Ca

4.3.3.1 Separation Methods

Each separation method was performed three times to confirm the elution profiles of all radionuclides involved and the separation yield and radionuclidic purity for ^{47}Ca. A representative elution profile for the replicate with the most finely collected fractions for each method is given in Figure 4.5 with details of the fraction volumes and compositions given in Tables 4.4 to 4.6 for Separation Methods 1 to 3, respectively. The error bars in Figure 4.5 result only from statistical uncertainties in the detection method.

Depending on the time each separation was performed, a slightly different mix of radionuclides was identified due to their half-lives and production rates. For example, separation methods 2 and 3 required optimization, so ^{42}K was not observed in the final elution profiles for either of these methods. As would be expected, ^{42}K followed the elution pattern of ^{43}K in all separations performed in this work, including the separations performed to optimize these two methods. Therefore, it can be confidently assumed that the elution profile for ^{42}K is the same as that of ^{43}K in the final protocols for methods 2 and 3. Conversely, ^{46}Sc was not observed for any of the three replicates performed for separation method 1 due to the level of activity of other radionuclides at the time of separation and the relatively long half-life of ^{46}Sc. However, this scandium isotope should behave identically to ^{44m}Sc, ^{47}Sc, and ^{48}Sc and each of these isotopes were found exclusively on the DGA resin after the elution of ^{47}Ca.

Two radionuclides appear during purification as daughters of isotopes produced during the irradiation: ^{28}Al as the daughter of ^{28}Mg, and ^{44}Sc as the daughter of ^{44m}Sc. The half-life of ^{28}Al ($t_{1/2}$ = 2.245 min) is so short that it has an apparent elution with ^{28}Mg in all separations. Like all the scandium isotopes observed, ^{44}Sc remained on the column through each of these separations. Therefore, neither of these daughters affected the radionuclidic purity of the final ^{47}Ca sample.

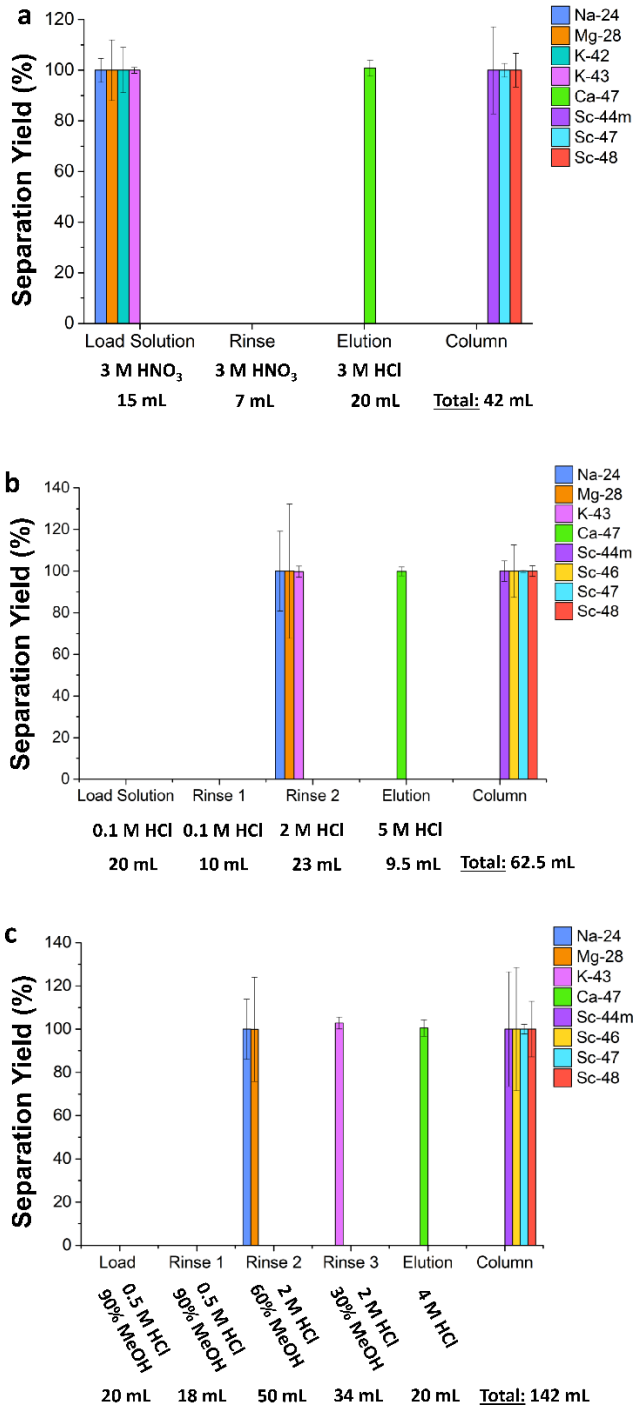

Figure 4.5: Elution Profiles for Separation Methods 1, 2, and 3
The separation profiles for methods 1 to 3 (1: DGA with HNO_3/HCl, 2: AG MP-50 resin with an HCl gradient, and 3: AG MP-50 resin with HCl/methanol gradient) are shown in a to c, respectively. The liquid phase as well as its composition and volume are indicated along the x-axis for each separation method. The "column" label to the right side of each figure are the species that remained on the column through the separation. The error bars are from counting statistics for one replicate of each method and not from deviations across replicates, with large errors resulting from low activities in the samples.

Table 4.4: Example Replicate with Separation Method 1: DGA with 3 M HNO_3/3M HCl
The recovery percentage is given for each elution fraction. Two rows at the bottom of the table give the percentage that remained on the column after the last fraction was collected ("Column") and the total percent that was eluted from the column ("Total"). Any cell in the table that is blank indicates a value of zero.

Liquid Phase	Fraction Number	Fraction Volume (mL)	Volume Sum (mL)	Recovery Percent (%)							
				^{24}Na	^{28}Mg	^{42}K	^{43}K	^{47}Ca	^{44m}Sc	^{47}Sc	^{48}Sc
3 M HNO_3	1	15	15	100(5)	100(12)	100(9)	100(2)				
	2	7	22								
3 M HCl	3	10	32					3.4(5)			
	4	10	42					97(3)			
			Column						100(17)	100(3)	100(7)
			Total	100(5)	100(12)	100(9)	100(2)	101(3)			

Table 4.5: Example Replicate with Separation Method 2: AG MP-50 with HCl Gradient
The recovery percentage is given for each elution fraction. Two rows at the bottom of the table give the percentage that remained on the column after the last fraction was collected ("Column") and the total percent that was eluted from the column ("Total"). Any cell in the table that is blank indicates a value of zero.

Liquid Phase	Fraction Number	Fraction Volume (mL)	Volume Sum (mL)	Recovery Percent (%)							
				^{24}Na	^{28}Mg	^{43}K	^{47}Ca	^{44m}Sc	^{46}Sc	^{47}Sc	^{48}Sc
0.1 M HCl	1	20	20								
	2	10	30								
2 M HCl	3	5	35	100(19)	100(32)						
	4	4.5	39.5								
	5	4.5	44			34(2)					
	6	2	46			40(2)					
	7	2	48			19(1)					
	8	3	51			6.3(7)					
	9	2	53								
5 M HCl	10	2.1	55.1				15.8(7)				
	11	5	01.1				82(2)				
	12	2.4	62.5				1.7(3)				
			Column					100(5)	100(13)	100(1)	100(3)
			Total	100(19)	100(32)	100(3)	100(2)				

Table 4.6: Example Replicate with Separation Method 3: AG MP-50 with HCl/Methanol Gradient
The recovery percentage is given for each elution fraction. Two rows at the bottom of the table give the percentage that remained on the column after the last fraction was collected ("Column") and the total percent that was eluted from the column ("Total"). Any cell in the table that is blank indicates a value of zero.

Liquid Phase	Fraction Number	Fraction Volume (mL)	Volume Sum (mL)	Recovery Percent (%)							
				^{24}Na	^{28}Mg	^{43}K	^{47}Ca	^{44m}Sc	^{46}Sc	^{47}Sc	^{48}Sc
0.5 M HCl/90% MeOH	1	13	13								
	2	6	19								
	3	10	29								
	4	8	37								
2 M HCl/60% MeOH	5	14	51	6(3)	53(19)						
	6	16	67	57(10)	47(15)						
	7	13	80	37(9)							
	8	6	86								
2 M HCl/30% MeOH	9	7.5	93.5			7.5(5)					
	10	4.5	98			19(1)					
	11	3	101			23(1)					
	12	3	104			25(1)					
	13	4	108			17(1)					
	14	4.5	112.5			10(1)					
	15	4	116.5			1.6(5)					
	16	3.5	120								
4 M HCl	17	13	133				99(4)				
	18	7	140				1.6(4)				
			Column					100(27)	100(28)	100(2)	100(13)
			Total	100(14)	100(24)	103(3)	100(4)				

4.3.3.2 Separation Yield and Radionuclidic Purity

The average separation yields and radionuclidic purities for the three replicates for ^{47}Ca processed with these separation methods were quite high as shown in Table 4.7. The only separation that demonstrated less than 100% separation yield was one of the replicates for separation method 3 and even then, it had a 99 ± 2% average separation yield with high radionuclidic purity. The LOD with HPGe measurements for ^{47}Ca and ^{43}K for the separation yield and radionuclidic purity, respectively, were found to be within the statistical errors of the final values. Therefore, within the limits of detection, these methods resulted in 99-100% separation yield with 100% radionuclidic purity of the ^{47}Ca recovered. This high purity indicates that any of the three methods would facilitate the generation of ^{47}Sc with high radionuclidic purity for radiolabeling applications. Figure 4.6 demonstrates through gamma-ray spectra the radionuclidic purity of the final ^{47}Ca sample from a replicate separation for Separation Method 1 compared to the radionuclidic mixture in an irradiated water sample from this experiment.

Table 4.7: Separation Yield and Radionuclidic Purity of ^{47}Ca for Three Separation Methods
Separation method 1 used DGA resin with HNO_3/HCl, 2 used AG MP-50 resin with an HCl gradient, and 3 used AG MP-50 resin with HCl/methanol gradient.

Separation Method	Average Separation Yield (%)	LOD for ^{47}Ca (%)	Radionuclidic Purity (%)	LOD for ^{43}K (%)
1	100 ± 1	0.9	100 ± 4	0.5
2	100 ± 2	0.5	100 ± 4	1
3	99 ± 2	0.8	100 ± 5	0.9

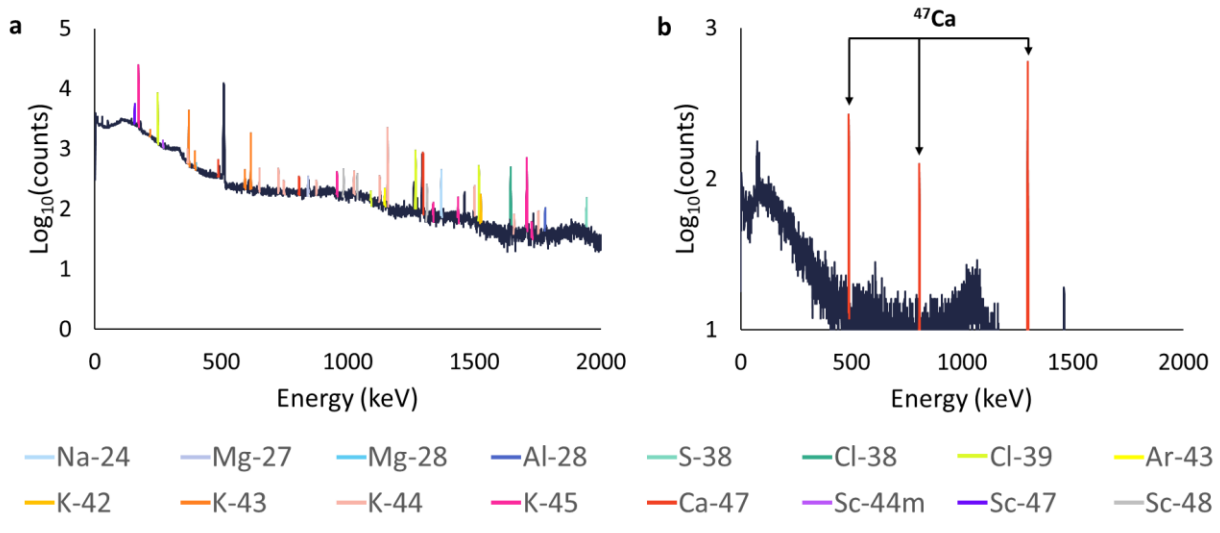

Figure 4.6: ^{47}Ca Purification Gamma Spectra
Gamma spectra for an irradiated water sample (a) and a purified sample of ^{47}Ca after a replicate separation with Separation Method 1 (b) that demonstrate the effectiveness of the purification process including collection with a cation exchange resin, a waiting period to allow for decay of short-lived cationic radionuclides, and the column based chromatographic separation.

4.3.4 Comparison of Separation Methods

Each of the three separation methods used in this work resulted in 10-20 mL of a 3-5 M HCl solution containing essentially 100% of the ^{47}Ca loaded on the column at 100% radionuclidic purity. This is a relatively small volume at an appropriate acid concentration for use as the loading solution in a previously published pseudo generator procedure to be used in future experiments. [10] These results indicate that any of the three methods could be used for further work with harvested ^{47}Ca. Once a method is selected, elution of ^{47}Ca from the collection resin bed and sample processing can be tailored to the selected method to avoid an evaporation step in future experiments. For example, the collection resin bed could be processed with HCl instead of HNO_3. The resulting solution could then be diluted to the correct loading solution concentration for separation methods 2 and 3, avoiding the use of an evaporation step.

The advantages and disadvantages of these methods are found in practical considerations for routine use: volume required, suitability of the final solution, and durability of the resin. In terms of the volume required, it is likely that a small reduction in the early rinse stages and loading solutions could be implemented with further optimization. Even with these optimizations, separation method 3 requires the highest volume to achieve purification of ^{47}Ca. Though each of the separation methods result in ^{47}Ca in 3-5 M HCl, separation method 3 uses significant levels of methanol in all other rinse steps. This could potentially lead to small amounts of methanol in the final radiolabeling solution, which is not acceptable under current guidelines for radiopharmaceuticals. The TODGA extraction molecule used in DGA resin has been shown to be less durable than cation exchange resins like AG MP-50 to the high radiation levels expected in isotope harvesting at FRIB. [71,72] Additionally, the surface tension interactions that immobilize TODGA on DGA resin are less strong than the covalent bonding in AG MP-50, leading to an increased risk of leaching extractant molecule from the resin after repeated use. [73] Both durability issues could result in organic material from the DGA resin contaminating the final product and requiring an additional purification step. Finally, DGA resin is used in the ^{47}Ca/^{47}Sc generator that will be used in future experiments. By using one of the AG MP-50 resin methods, orthogonal resins can be used to potentially maximize the purification ability of the final procedure.

After these practical considerations, the most suitable separation method for future harvesting efforts with ^{47}Ca is separation method 2. Adjustments can be made to this procedure based on future experimental results, including generator performance and radiolabeling efficiency. This separation method will be used in combination with the published ^{47}Ca/^{47}Sc

generator [10] in future experiments at the NSCL to determine the feasibility of generating ^{47}Sc from harvested ^{47}Ca for radiolabeling biological molecules.

4.3.5 Stable Elemental Analysis

The stable elemental analysis was performed on water samples 1-4 and the combined, purified solution of ^{47}Ca from these separations. There is a concern that high levels of elements, such as iron, in the final purified solution may inhibit future radiolabeling experiments. The present analysis identified only low levels of a few stable elements. In the total water volume of 35 L when water sample 3 was removed from the system, < 750 μg of Ca, Mg, Na, Si, B, Zn and < 100 μg of Fe, Ni, Cu were detected. The approximately 130 mL purified ^{47}Ca solution had concentrated levels of stable calcium (200-400 μg) as expected, lower levels of Mg, Na, Si, Fe, and Zn (<40 μg), and a very low level of Sc (<2 μg).

The elements detected with the semi-quantitative ICP-OES method at a concentration of 0.05 ppm or higher in any of the samples are shown in Table 4.8. The concentrations listed for the combined, purified ^{47}Ca sample are corrected for the dilution made before analysis and are dissolved in approximately 150 mL of 3-5 M HCl. The elements detected in the concentrated water sample are only reported for water sample 3 since this sample was the last withdrawn before cation exchange resins were put in the system. The values for the water sample are given at the concentrated level (column 6 in Table 4.8 “Concentrated Water Sample #3”) and are also scaled up to account for the total water volume in the system (35 ± 4 L) at the time that water sample 3 was withdrawn (column 7 in Table 4.8 “Estimated Mass in Total System Water Based on Sample 3”).

Table 4.8: Stable Element Semi-Quantification
All values reported in this table are given to only one significant figure with unknown accuracy due to the semi-quantitative nature of the measurement. The measured concentrations for elements in the blank for each sample type was approximately zero (-0.03 to 0.03 ppm) except for those listed in the table and cesium, which read about -14 ppm for blanks and samples, indicating that the preset calibration was misaligned. A dash signifies that an elemental concentration was < 0.05 ppm for that sample. The "Total System Water" referred to in the rightmost column is the 35 L remaining in the system after water sample 3 was removed.

Element	Wavelength (nm)	Concentration (ppm)				Estimated Mass in Total System Water Based on Sample 3 (µg)
		Blank- 1.5 M HCl	Combined Purified ^{47}Ca samples	Blank- 1.4% HNO_3	Concentrated Water Sample #3	
Ca	396.847	-	2	-	0.1	200
Ca	422.673	-	3	-	0.2	400
Mg	279.553	-	0.2	-	0.08	200
Na	589.592	0.1	0.2	0.09	0.4	700
Si	251.611	0.7	0.2	-	0.09	400
B	249.772	0.06	-	-	0.3	200
Fe	238.204	-	0.1	-	0.05	80
Zn	213.857	-	0.3	-	0.3	100
Cu	327.395	-	-	-	0.05	80

Only small amounts of stable ions were found in the water samples, indicating that the system did not contribute significant amounts of stable ions under these irradiation conditions. This was a concern as a beam of energetic particles creates corrosive radiolysis products such as H^+, OH^-, $HO^\cdot$, $H^\cdot$, $HO_2^\cdot$, and H_2O_2 as it deposits energy and stops in water. [36] While most of these radiolysis products recombine rapidly, H_2O_2 is long-lived and can cause oxidative damage to metal components exposed to the system water. In this water system, only a few stainless-steel components are in contact with the water and could become a source of Fe, Cr, and Ni. This stable element analysis demonstrates that under the irradiation conditions in this

experiment, the mass of stable ions that accumulated in the water was low, and therefore, the corrosive effects of radiolysis in the water system were minimal.

The measured stable ion masses in the water system and in the purified ^{47}Ca product demonstrate that the stable ion content was reduced through the purification steps (Figure 4.7). The remaining stable ions in the purified sample is not surprising as reagent grade chemicals as opposed to high purity chemicals were used in each step of the purification process. It is anticipated that these levels of stable ions can be reduced in future experiments when higher purity chemicals are used. The only high level of ions observed in the purified fraction was stable calcium which should follow ^{47}Ca through the pseudo generator and not affect a purified ^{47}Sc solution. Additionally, the total estimated masses of the elements detected in the water sample are low enough that, if collected on a single resin in future experiments, they should not

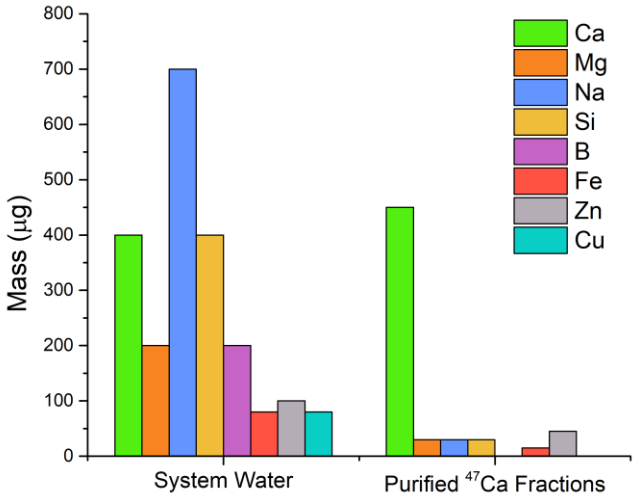

Figure 4.7: Stable Ions in System Water Compared to Purified ^{47}Ca Fractions
The far lower levels of all but calcium ions in the purified ^{47}Ca fractions compared to the ions in the water system indicate a reduction in stable ions due to the purification process. Calcium ion levels remain high in the final solution since the stable calcium ions behave as ^{47}Ca does through each process.

interfere with any chemistry steps following collection. These results indicate that stable elements in the water system and in the final purified ^{47}Ca solution will not impede radiolabeling with ^{47}Sc generated through isotope harvesting.

4.4 Conclusion

In this work, ^{47}Ca was produced with a ^{48}Ca beam on a flowing-water target for the first time. A relatively high 2.0 ± 0.4% beam conversion to ^{47}Ca was measured and used to predict GBq to TBq ^{47}Ca activities through isotope harvesting at the NSCL and FRIB. The ^{47}Ca produced in this experiment was effectively collected on cation exchange resin beds in the isotope harvesting water system, eluted from the collection resin beds, and purified with three different separation methods that were optimized in this work. These methods resulted in ≥99% separation yield for ^{47}Ca with 100% radionuclidic purity. Together, the low levels of stable contaminants and the high radionuclidic purity in the purified ^{47}Ca sample indicate that radiolabeling with ^{47}Sc generated through isotope harvesting at the NSCL holds promising potential. Overall, the results from this experiment demonstrate for the first time the feasibility of producing, collecting, and purifying ^{47}Ca for a ^{47}Ca/^{47}Sc generator through isotope harvesting.

Chapter 5: Higher Intensity ^{1}H Beam Target Durability Test[9]

*A high intensity proton irradiation was performed with the flowing-water isotope harvesting target at the University of Wisconsin-Madison Cyclotron Laboratory to measure the rate of degradation of the Ti64 target shell under high-intensity irradiation conditions. Radionuclides formed in the target shell were measured in the system water as a radiotracer for target degradation. Using a simple, beam intensity dependent model, a corrosion rate of 1.5E-6 μm/(μA*s) was found to match the measured radiotracer activities at various points in the irradiation. This rate was used to extrapolate the lifetime of future isotope harvesting targets at the NSCL and FRIB, using the areal power density of different ion beams to scale the corrosion rate.*

5.1 Introduction

To safely harvest isotopes at the beam intensities available at the NSCL and in the future at FRIB, the second-generation flowing-water isotope harvesting target (see Chapter 2 Section 2.2.2) was tested under the intense irradiation conditions anticipated. In particular, the durability of the Ti64 alloy (6% aluminum, 4% vanadium, mass balanced by titanium) target shell must be assessed before the harvesting system is used for routine operation. During

[9] This chapter draws heavily on the published paper E. Paige Abel, Katharina Domnanich, Colton Kalman, Wes Walker, Jonathan W. Engle, Todd E. Barnhart, Greg Severin; Durability test of a flowing-water target for isotope harvesting, *Nuclear Inst. And Methods in Physics Research B*, **2020**, *478*, 34-45.

irradiation, three main conditions might lead to degradation of the Ti64 target face: 1) displacements of the atoms caused by the energetic beam as it passes through the Ti64 layer, 2) corrosion by radiolysis products in the target water produced as the accelerated beam deposits energy in the water, and 3) erosion by the rapid flow of water over the interior surface of the Ti64 layer.

The first two of these conditions may become more problematic as the beam intensity increases. Previous isotope harvesting experiments, summarized in Table 5.1, have been performed at the NSCL using a target shell in part or entirely made of Ti64 using $^{40}Ca^{20+}$, $^{48}Ca^{20+}$, $^{78}Kr^{35+}$, and $^{78}Kr^{36+}$ beams with power depositions from 0.42 to 22.2 W (see Chapter 3 and 4 for a discussion of the $^{40}Ca^{20+}$ and $^{48}Ca^{20+}$ beam experiments, respectively) [36,37]. An increasingly intense fast, heavy ion beam was used in these experiments with no observed degradation, but even still, the target will be expected to receive much higher beam intensities when installed at the beam blocker position at the NSCL and in the future, at FRIB. For comparison, the present proton irradiation which is intended to replicate the higher power depositions expected at the NSCL and FRIB is summarized in the bottom row of Table 5.1.

There are published techniques for investigating irradiation accelerated corrosion at a metal-water interface [74,75]. For example, Wang and Was studied the interface between a zirconium alloy and super-heated water by irradiation with protons by using focused ion beam milling to create a cross-sectional view of the sample and techniques in transmission electron microscopy to characterize the sample [75]. After irradiation, surface alterations and corrosion rates were determined electrochemically. For the case of the NSCL beam-blocker, and eventually the beam dump at FRIB, the design of the target includes a fully enclosed interior

surface, making the use of similar post-irradiation analysis impossible without destruction of the target.

To approach the high-power density scenario expected at NSCL and FRIB, and to assess material degradation non-invasively, the harvesting beam blocker was temporarily installed at the University of Wisconsin-Madison Cyclotron Laboratory. There, a GE PETtrace cyclotron was used to implant a 16 MeV proton beam at currents up to 34 μA into the Ti64 flowing-water target and isotope harvesting system. The purpose of the irradiation was to measure the degradation rate of the target material in a comparable power density setting to that expected at the heavy ion facilities by observing corrosion products in the water. The UW proton beam deposited 540 W of total beam power into the target shell and the interior water at the maximum beam intensity in this experiment. This power deposition is comparable to that for beams potentially implanted in the beam blocker at the NSCL (*e.g.* 540 W of power would be deposited in the beam blocker by a typical 80 pnA, 140 MeV/nucleon ^{48}Ca beam and 517 W of power would be deposited by a typical 45 pnA, 140 MeV/nucleon ^{82}Se beam). The results of the present experiment as well as the implications for future isotope harvesting at FRIB are discussed here.

Table 5.1: Summary of Experiments Performed with Ti64 Target Material and Isotope Harvesting Water System

Experiment Index	Particle Beam	Energy (MeV/nucleon)	Average Intensity (pnA)	Average Power Deposition (W)	Duration (h)
1	$^{40}Ca^{20+}$	140	0.42	2.4	3.5
2	$^{48}Ca^{20+}$	140	0.92	6.2	5.1
3	$^{78}Kr^{35+}$	150	1.6	18.7	5.8
4	$^{78}Kr^{36+}$	150	1.9	22.2	7.6
5	$^{1}H^{+}$	16	2.1×10^{4}	337	3.3

5.2 Experimental Methods

5.2.1 Experiment Design

At the University of Wisconsin-Madison Cyclotron Laboratory, a 16 MeV proton beam was impinged on the flowing-water target (or "beam blocker") with a beam intensity of 5.6 to 34 µA over the course of approximately 3.3 hours of irradiation time. The irradiation was broken into four irradiation periods (referred to as periods 1, 2, 3, and 4) as shown in Figure 5.1 and the beam intensity was increased with each successive period.

With the implantation of an energetic proton beam into the target, both reactions with the interior water and the front layer of the Ti64 target shell were expected as depicted in Figure 5.2. In the water, $^{16}O(p,\alpha)^{13}N$ and $^{18}O(p,n)^{18}F$ reactions were expected to be the most

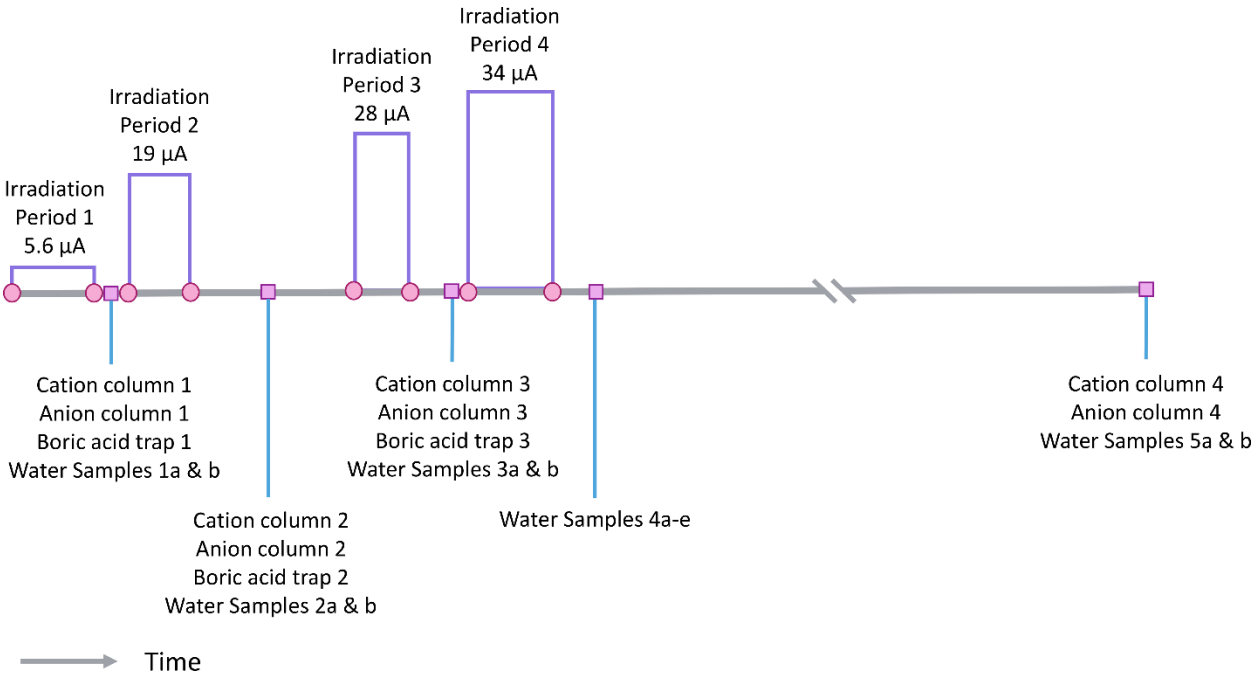

Figure 5.1: Timeline for Proton Irradiation
The timeline shows the average beam intensities of each irradiation period and when water samples, ion exchange resins, and boric acid traps were removed from the system. The total elapsed time from the start of the irradiation to collection of the final columns and water samples was approximately 24 h.

significant reactions. The target shell material, which was made mainly of natural Ti and smaller amounts of Al and V, was expected to undergo ^{48}Ti(p,n)^{48}V and ^{51}V(p,n)^{51}Cr reactions which produce a sufficient activity of long-lived products for detection. For the purposes of testing the durability of the target material, both ^{48}V ($t_{1/2}$ = 16.0 d) and ^{51}Cr ($t_{1/2}$ = 27.7 d) [28,76] produced in the front Ti64 layer served as radiotracers for target degradation. Any activity from these radionuclides found in the water would indicate the removal of material from the front layer of the target shell, as this is the only location they were produced. Each of these radionuclides was observed and the methods used for detecting and quantifying these radionuclides will be described in the Radiation Measurements section below.

Beam intensity values were manually recorded throughout the experiment (measured with a Keithly 414A ammeter connected to the target). The design of the target system did not allow for suppression of the current measurement, meaning that the recorded values were

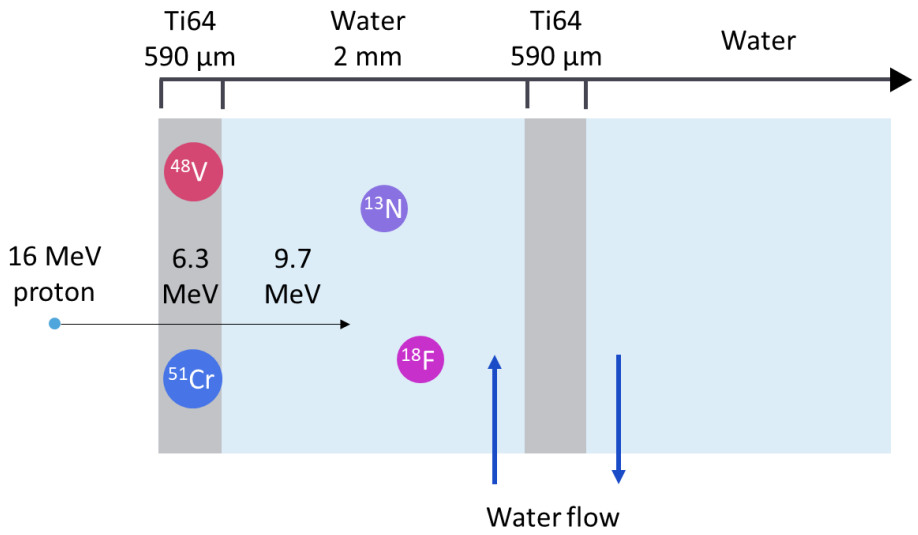

Figure 5.2: Schematic Cross Section of the Isotope Harvesting Target
The layers of the isotope harvesting flowing-water target are shown with the left side of the picture corresponding to the front of the target. The energetics of the proton beam are given for the first Ti64 layer or the "target face" and the first water layer. Additionally, ^{48}V and ^{51}Cr are shown as products in the target face and ^{13}N and ^{18}F as products in the first water layer.

expected to be proportional to, but not equivalent to, the true beam current. A scaling factor of 0.67(3) between the true current and the recorded beam current (*i.e.*, μA true/μA recorded) was determined by benchmarking the total production of ^{48}V and ^{51}Cr against the expected production computed using data from the IAEA monitor reaction cross-section database [69,77]. The measured activities of ^{13}N and ^{18}F that were produced in the water were found to be consistent with the scaling factor, but due to a large systematic uncertainty that arose from an uncertainty in the total water volume, and the lack of uncertainties in the IAEA evaluation, those values were not used to calculate the scaling factor [69].

By experimental design, the 3.4 to 34 μA range of beam current was chosen to simulate the beam power deposited in the target shell and water by the highest power beams available at the NSCL, such as the 140 MeV/nucleon ^{82}Se beam at 45 pnA. Based on SRIM calculations [49],this beam would deposit approximately 67 W in the first layer of Ti64 in the target shell and 450 W in the interior volume of water. A 16 MeV proton beam between 9 and 55 μA can simulate this power deposition. The irradiation started with an average beam current of 5.6 μA for the first irradiation period and the current was increased gradually up to 34 μA for the last irradiation period, achieving approximately two-thirds the intended high intensity beam. The implications of these power deposition comparisons will be discussed later with regards to quantifying the degradation of the target.

The slow increase in beam current allowed for multiple measurements in the system, such as the activity of radionuclidic products and the conductivity of the water, to be correlated with the beam intensity. To make measurements of the radioactivity in the water, samples of the system water were taken, and the ion exchange columns and the boric acid trap were

exchanged for fresh components between each run segment. Figure 5.1 shows the timeline of when water samples, ion exchange columns, and boric acid traps were removed from the system during the experiment.

5.2.2 Quantification of Radionuclides

5.2.2.1 Radiation Measurements for the Quantification of Radionuclides

The activities of ^{13}N and ^{18}F in the water samples, ion exchange columns, and boric acid traps removed from the system were measured with Capintec CRC-15R ionization chambers calibrated for quantification of their 511 keV gamma rays. The sample positions were not changed as activity measurements were recorded over time, allowing for a decay curve analysis for the quantification of ^{13}N and ^{18}F. No activity was observed on the boric acid trap throughout the experiment.

Equation 5.1 was used for the determination of the activity of ^{13}N and ^{18}F on the anion exchange columns and the water samples:

$$A_T = A_1 e^{-\lambda_1 t} + A_2 e^{\lambda_2 t} + b \quad (5.1)$$

where A_1 and A_2 were fitted variables for the initial activity of ^{13}N and ^{18}F, respectively; λ_1 and λ_2 are the decay constants of ^{13}N and ^{18}F, respectively; b represented the background which was restricted to be greater than or equal to zero; and t is the time at which a total activity value, A_T, was recorded. The data for water sample 1 was fitted with the background factor set to zero. The activity found in each water sample was scaled by a factor comparing the volume of the water sample to the total system volume (*i.e.*, approximately 50 mL samples were

measured and the activity was scaled to account for about 36 L in the water system.) to produce an approximate activity in the total water volume.

Only ^{13}N was found on the cation column. This was verified by fitting the ionization chamber values for the cation columns with Equation 5.2:

$$A_T = Ae^{-\lambda t} + b \tag{5.2}$$

where A was a fitted variable for the initial activity of ^{13}N, λ is the decay constant of ^{13}N, b represented the background which was restricted to be greater than or equal to zero, and t is the time at which a total activity value, A_T, was recorded. The activity found on the ion exchange columns and in the total volume of water were used to find a total activity of ^{13}N or ^{18}F in the system at the end of each irradiation period.

Longer-lived radionuclides such as ^{48}V and ^{51}Cr were quantified by gamma spectrometry using two energy, efficiency, and peak shape calibrated Al-windowed Ortec HPGe detectors (measured resolution 1.8 keV FWHM at 1333 keV). The activities measured in each water sample were scaled to account for the total system water volume as described previously. Spectra were taken starting the day after the irradiation to reduce the background from the shorter-lived co-produced radionuclides. In particular, ^{48}V was quantified with its characteristic gamma rays at 983.525 keV (99.98(4)%) and 1312.106 keV (98.2(3)%) [28] and ^{51}Cr was quantified with its 320.08 keV (9.910(10)%) gamma ray [76]. Two HPGe detectors were used for quantification at the Cyclotron Lab. Since detector 1 was more well characterized than detector 2, spectra from detector 1 were preferentially used in the quantification. When

spectra from detector 2 were the only data available for a sample, an additional 10% error was added in quadrature with the counting error.

To improve the quantification, spectra were taken of the water samples over long time periods within a month of the irradiation. These spectra were taken in the Department of Chemistry at Michigan State University, using a Canberra BEGe Gamma-ray Detector (BE2020). The anion exchange columns were also measured for long counting times about a month and a half after the irradiation at the Cyclotron Lab in Madison to better quantify ^{51}Cr. The target shell was analyzed using gamma spectrometry three and a half months after the irradiation due to the high level of long-lived activity produced in the front Ti64 layer of the target.

Analysis of the spectra taken at the Cyclotron Lab were performed by hand and involved finding the peak sum and subtracting an average baseline from the sum. The efficiencies used were calculated from existing characterizations of the detectors. The spectra taken at Michigan State University were analyzed using Genie 2000 software (Mirion Technologies), which performed peak summing, baseline corrections, and efficiency calculations also based on existing calibrations.

Table 5.2: Estimated Production Rates for Radionuclides Produced in Water and Target Shell

Radionuclide	Estimated Production Rate (product nuclei/incoming beam particle)
^{13}N	4.05E-5
^{18}F	1.66E-6
^{48}V	9.86E-4
^{51}Cr	5.64E-5

5.2.2.2 Estimated Production of Radionuclides

Estimated production rates of ^{13}N, ^{18}F, ^{48}V, and ^{51}Cr were calculated using the recommended cross sections from the IAEA evaluations for the following reactions, respectively: $^{16}O(p,\alpha)^{13}N$, $^{18}O(p,n)^{18}F$, $^{nat}Ti(p,x)^{48}V$, and $^{51}V(p,n)^{51}Cr$. These cross sections were used in Equation 5.3:

$$P = \frac{N_A \rho}{M} \int_{E_i}^{E_f} \frac{\sigma(E)}{S_P(E)} dE \tag{5.3}$$

where σ(E) is the cross section of the reaction at energy, E; S_p(E) is the stopping power of the projectile at energy, E; ρ is the density of the target nuclei; M is the molar mass of the target nucleus; and N_A is Avagadro's number. The protons energy was estimated using SRIM and ranged from 16 to 9.7 MeV in the target shell material and from 9.7 to 0 MeV in the water layer. The production rates in Table 5.2 were found using these parameters and were used with the recorded beam current in Equation 5.4 to find estimated activities produced, A:

$$A = P \times I(t) \times (1 - e^{-\lambda t}) \tag{5.4}$$

where lambda is the decay constant of the radionuclide and t is the time over which the beam current was I(t).

5.2.3 Estimating Activity of ^{48}V and ^{51}Cr in the System Water from Nuclear Recoil

A study on recoil range distributions by Alexander and Sisson demonstrated that the total momentum of a projectile is transferred to the compound nucleus formed in a nuclear reaction [78]. Due to this full momentum transfer and subsequent symmetric particle emission, Equation 5.5 describes the average recoil energy of the resulting product:

$$E_R = \frac{E_b A_R A_b}{(A_b + A_T)^2} \quad (5.5)$$

where E and A represent the energy and mass, respectively, and the subscripts R, b, and T represent the recoil, the projectile, and the target nuclei, respectively. This process and the assumptions involved are depicted schematically in Figure 5.3. Using stopping power values from SRIM to estimate E_b in Ti64, the recoil energies of ^{49}V and ^{52}Cr (*i.e.*, the compound nuclei for the reactions ^{48}Ti(p,n)^{48}V and ^{51}V(p,n)^{51}Cr, respectively) were estimated with Equation 5.5 in the target shell at 1 µm intervals. The recoil energies are predicted to be approximately 199 keV for ^{49}V and 187 keV for ^{52}Cr in the last 1 µm of the target shell where recoil escape was able to occur (*i.e.*, the remaining layer of Ti64 was small enough that these recoil energies moved some of the compound nuclei into the water layer).

The percent of ^{49}V and ^{52}Cr recoils that would travel through the remaining target shell material and into the water layer was evaluated in steps of every 0.001 µm in the last 0.2 µm of

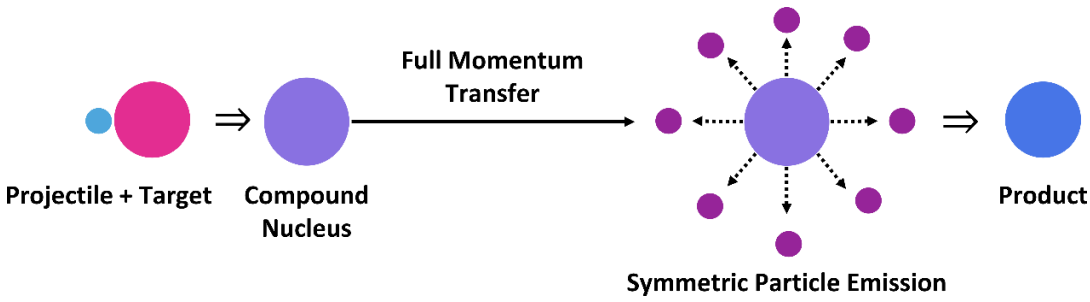

Figure 5.3: Depiction of Recoil and Production of Radionuclides.
The reaction between a projectile and a target nucleus forms a compound nucleus moving in the same direction as the projectile with an energy described by Equation 5.5. The compound nucleus emits a particle in any direction, forming the product of the nuclear reaction. This symmetric distribution statistically results in no net shift in recoil range distribution.

the shell based on the following information: the average range and range distribution of the recoiling compound nucleus in Ti64 at the estimated recoil energies and a standard normal distribution table. A Gaussian distribution was fitted to the range distribution of these recoiling compound nuclei. The resulting mean (μ) and standard deviation (σ) were used to standardize the distance (x) a recoiled particle in each 0.001 µm layer would travel to exit the target shell:

$$x_s = \frac{x-\mu}{\sigma} \tag{5.6}$$

Then, the probability of a recoiled particle traveling through the remaining standardized distance (x_s) was found using a standard normal distribution table. This probability of "escape" is depicted in Figure 5.4. The final product nucleus is produced when the compound nucleus symmetrically (*i.e.*, isotropically) emits a particle as shown in the right half of Figure 5.3. Due to

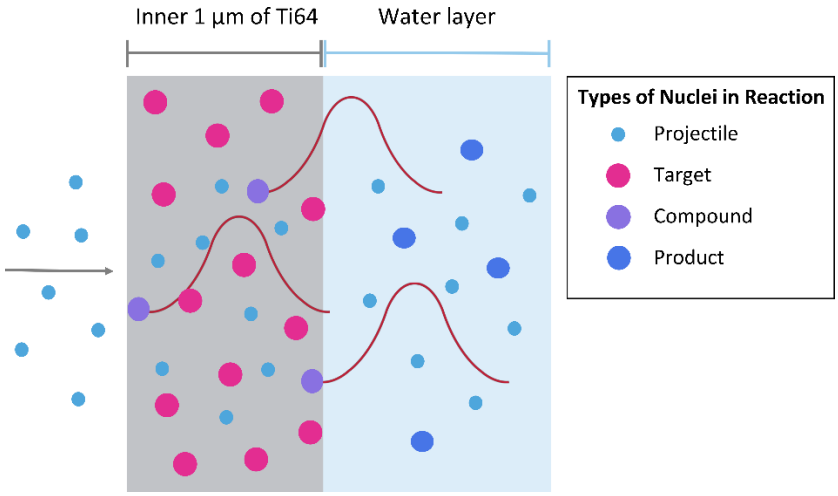

Figure 5.4: Depiction of Recoil Fraction Estimation
Projectiles are shown traveling to the right through the last 1 um of Ti64 and into the water layer. When the projectiles react with the target nuclei, compound nuclei are formed and continue to travel to the right. The red gaussian curves depict the recoil range of the compound nuclei. The fraction of red curve overlapping with the water layer is proportional to the fraction of product nuclei that recoil into the water layer.

this symmetric emission, the position of the recoiled compound nucleus estimated as described previously represents the average position of the product nucleus.

IAEA evaluated cross section values for $^{nat}Ti(p,x)^{48}V$ and $^{51}V(p,n)^{51}Cr$ were used to find production rates at 0.001 um intervals in the last 0.2 um of the target shell. The probability of recoiling compound nucleus "escaping" the Ti64 target layer that was found for each of these intervals was used to scale the corresponding production rate. A total "escape rate" of the recoiling compound nuclei was found for each reaction by adding the rates at each layer. Using the beam current values described in the Materials and Methods: Experimental Design Section 5.2.1, the activity of ^{48}V and ^{51}Cr in the system from recoiling particles traveling out of the target shell was estimated and subsequently subtracted from the total activity measured in the water for each irradiation period.

5.2.4 Degradation of the Target

A model was developed to describe the degradation of the first Ti64 layer of the target based on the measurements of the ^{48}V and ^{51}Cr produced in this layer and found in the water system. The amount of ^{48}V or ^{51}Cr which had escaped from the first Ti64 target layer into the water at each time point was the sum of activity on the ion exchange resins and the scaled activity in the water samples. These activities were corrected for the estimated activity in the water resulting from nuclear recoil following the $^{48}Ti(p,n)^{48}V$ and $^{51}V(p,n)^{51}Cr$ reactions in the target shell. Therefore, the final activities used in this model represent the activity that resulted from degradation of the target material. This calculation was carried out with 1- to 2-minute time steps and the scaled beam intensities described in the Experimental Design section.

The measured activity of ^{48}V and ^{51}Cr in the target and the beam current during the irradiation were used to calculate a production rate for these radionuclides in the first Ti64 target layer. This production rate was used to find activities for ^{48}V and ^{51}Cr in the Ti64 target layer at each time step in these calculations using Equation 5.7:

$$P_T(t_i) = I(t_i) * r * (1 - e^{-\lambda(t_{i+1} - t_i)}) \quad (5.7)$$

where $P_T(t_i)$ is the production of ^{48}V in the Ti64 target layer over the time step starting at time t_i, $I(t_i)$ is the beam intensity at t_i (pps), r is the constant production rate of ^{48}V or ^{51}Cr (particles produced per each incoming proton), λ is the decay constant of ^{48}V or ^{51}Cr, and t_{i+1} is the beginning of the next time step. The total activity in the first Ti64 target layer at each time step, $A_T(t_i)$, was found by adding the activity produced at t_i (Equation 5.7) to a decay corrected value for the accumulated activity in this target layer at t_{i-1}, the previous time step, as shown in Equation 5.8:

$$A_T(t_i) = P_T(t_i) + A_T(t_{i-1}) * e^{-\lambda(t_i - t_{i-1})} \quad (5.8).$$

The value produced with Equation 5.8 for the last time step in the irradiation is equal to the amount of ^{48}V or ^{51}Cr produced by the end of the irradiation.

The amount of ^{48}V or ^{51}Cr that degraded from the first Ti64 target layer at each step, t_i, was assumed to be a function of the activity of each radionuclide in the target face at that time step. Equation 5.9 describes the way the target is thought to degrade over time:

$$D_T(t_i) = \frac{A_T(t_i) * I(t_i) * \Delta t_{i,i+1}}{T} * C \quad (5.9)$$

where $D_T(t_i)$ is the activity of ^{48}V or ^{51}Cr that was removed from the Ti64 target layer over the time step starting at time t_i, $I(t_i)$ is the beam intensity at time t_i, and T is the thickness of the first Ti64 layer. This model uses one variable, C, which is the corrosion rate of the first Ti64 layer in units of degraded target thickness per integrated beam current (μm/(μA*s)). The results of this model are presented in Section 5.3.2.1.

The area of the proton beam strike and the power deposited per integrated beam current are two factors that were used to scale the corrosion rate resulting from Equation 5.9 to the dimensions of volume per energy deposited (cm^3/J). These units allow the corrosion rate to be rescaled to other irradiation conditions (*i.e.*, different beam strike areas and power depositions with a range of beams types and intensities) expected at the NSCL and FRIB. The scaled corrosion rate from this experiment as well as extrapolations for other beam conditions are discussed in Section 5.3.2.2.

The accumulated activity of ^{48}V or ^{51}Cr in the system, A_s, was found in a similar way to the total activity in the front Ti64 target layer. Equation 5.10 shows how the accumulation occurred at each time step:

$$A_s(t_i) = D_T(t_i) + A_s(t_{i-1}) * e^{-\lambda(t_i - t_{i-1})} \quad (5.10).$$

The Microsoft Excel solver plug-in was used to a find value for C in Equation 5.9 that minimizes the X^2 difference between the measured activity of ^{48}V and ^{51}Cr in the system at the end of each irradiation period and the value produced by Equation 5.10 at these times. The results of this model are presented in Section 5.3.2.1.

5.3 Results and Discussion

5.3.1 Quantification of Radionuclides Produced in Water Target

The total activity of ^{13}N and ^{18}F measured in the water system and predicted activities based on the scaled beam current after each irradiation period are given in Table 5.3. The predicted activities are lower than the measured activity in each case. However, the predicted activities for ^{13}N are within the error of the measured activity. The larger discrepancy in the ^{18}F data most likely results from two factors: the much lower ^{18}F activity compared to the ^{13}N activity in each sample and the large number of resonances in the cross section for the $^{18}O(p,n)^{18}F$. The low ^{18}F activity was a small component in the fit used for the decay curve analysis, so the uncertainty in the fitted activity was likely underestimated. Additionally, the IAEA recommended cross sections were used to find a predicted activity [69]. These recommended values do not sufficiently represent all observed resonances, making it possible that the predicted activity is an underestimation. Finally, uncertainty information for the IAEA

Table 5.3: ^{13}N and ^{18}F Activities Produced in the Flowing-Water Target
The values given in the last column are ratios of the measured to predicted activities after each irradiation period.

Radionuclide	Irradiation Period	Total Activity Produced after Each Irradiation Period(mCi)		
		Measured	Predicted	Ratio
^{13}N	1	60(10)	50	1.29
	2	150(30)	130	1.14
	3	200(30)	180	1.09
	4	250(40)	220	1.11
^{18}F	1	1.0(2)	0.5	1.91
	2	2.0(3)	1.5	1.33
	3	2.8(3)	2.0	1.42
	4	5.8(8)	4.2	1.36

recommended values were not available for either ^{13}N or ^{18}F, so it is unclear how precise the predicted values are.

Regardless of these relatively small discrepancies, the level of these radionuclides produced in the water provide information about the conditions in the interior water layer. Due to the high LET of the protons, the temperature of the Ti64 front target layer has been predicted to be much higher than the boiling temperature of the water in the system. This condition introduces the possibility of partial or total vaporization of the 2 mm layer of water between the front Ti64 shell and the internal Ti64 baffle depicted in Figure 5.5. A significant decrease in the expected production of ^{13}N and ^{18}F could indicate that the water had vaporized to an extent that the beam passed through the water layer and was implanted in the second

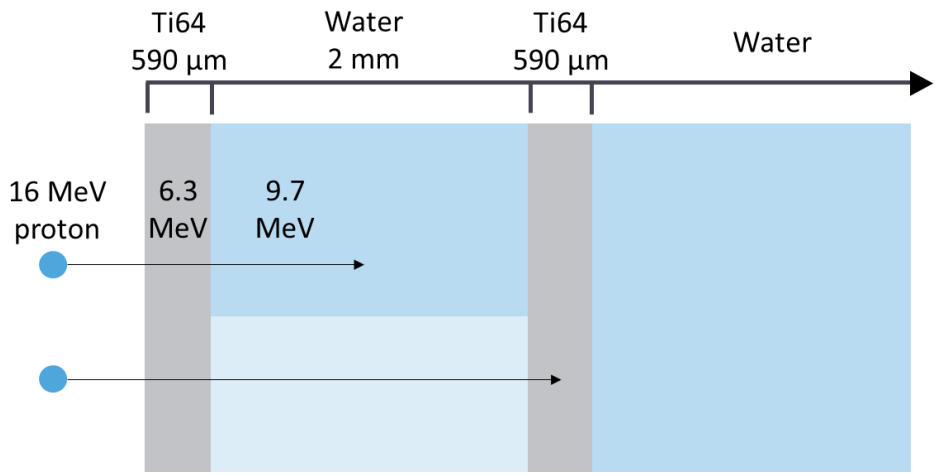

Figure 5.5: Proton Beam Implanted in Isotope Harvesting Target
The layers of the isotope harvesting target are shown with the front Ti64 target layer on the left followed by a water layer (darker blue), an interior layer of Ti64, and a second large water layer. The 16 MeV protons are expected to deposit approximately 6.3 MeV of energy in the front Ti64 layer and the remainder in the first water layer with an estimated range of 1.1 mm. However, if the average density of the water layer were to decrease due to local boiling (shown in the lighter blue), the range of the proton through the water could exceed 2 mm and some of the energy of the protons could be implanted in the second Ti64 layer.

layer of Ti64. However, a comparison between the measured and predicted activities for these radionuclides produced in the water interior of the target does not show a decrease in production, indicating that the proton beam was most likely implanted entirely in the water layer. This means that the corrosion of the front Ti64 target layer was assisted by realistic levels of radiolysis products from the proton beam.

5.3.2 Degradation of the Target

5.3.2.1 Estimating the Corrosion Rate

The model created to describe the degradation of the front Ti64 target layer used the fitted constant corrosion rate introduced above. Additionally, the amount of ^{48}V that was removed from this target layer at each time step was assumed to be proportional to the beam intensity and inversely proportional to the area of the beam spot. These relationships are

Table 5.4: ^{48}V and ^{51}Cr Activity in the Water
The total measured, recoiled, recoil corrected, and modeled activities (left to right) are given for the end of each run segment. For ^{48}V, the fitted data from Equation 5.10 matched the measured data relatively well with X^2 (3, n=4) = 1.71.

Radionuclide	Irradiation period	Total Activity (μCi)			
		Measured in System	Estimated from Recoil into Water	Estimated from Target Shell Degradation (Recoil Corrected)	Predicted in System by Degradation Model
^{48}V	1	0.33(6)	0.35	-0.01(6)	0.04
	2	1.7(2)	1.1	0.6(2)	0.4
	3	4.0(4)	2.4	1.6(5)	2.0
	4	11.7(3)	4.49	7.2(7)	7.0
^{51}Cr	1	0.028(2)	0.014	0.013(2)	
	2	0.082(8)	0.046	0.036(5)	
	3	0.157(9)	0.097	0.060(6)	
	4	0.54(4)	0.18	0.35(4)	0.35

intuitive, fit the experimental data well, and allow for the resulting corrosion rate constant to be scaled by the areal beam power of other particle beams for estimates of future degradation.

The measured activities of ^{48}V and ^{51}Cr in the water system were corrected for estimated contributions from nuclear recoils from the front Ti64 target shell layer. About 39% of the ^{48}V and 34% of the ^{51}Cr measured in the water system were attributed to recoiled products that "escaped" from the target shell with average estimated ranges of 0.113 and 0.110 μm, respectively. The recoil-corrected values in Table 5.4 were used in the target shell corrosion model. The optimized results from Equation 5.10 for the recoil-corrected ^{48}V activities are shown in Figure 5.6. The modeled values all fall within the error for each measured value and the overall fit has a X^2 (3, n=4) of 1.71. The resulting corrosion rate constant as defined in Equation 5.9 is 1.5E-6 μm/(μA s).

The measured activities of ^{51}Cr in the system were much lower than those of ^{48}V due to a lower target nucleus density in the Ti64 target shell. Additionally, the highest intensity gamma ray for ^{51}Cr is a 320 keV gamma ray with a branching ratio of only 9.90% [76]. Together these factors resulted in ^{51}Cr present below the detection limits in the 200-300 mL water samples withdrawn for HPGe spectrometry. Spectra were collected a few weeks after the irradiation for live times on the order of days. This measurement was supported by estimating the limit of detection of these spectra at 320 keV as the uncertainty in the background counting rate in this energy region. Then, the amount of ^{51}Cr in the total water volume was estimated by assuming the ratio of activity in the water and on the anion exchange column followed that of ^{48}V. For all of the water samples, this amount of ^{51}Cr predicted in the water fell below or at the limit of detection.

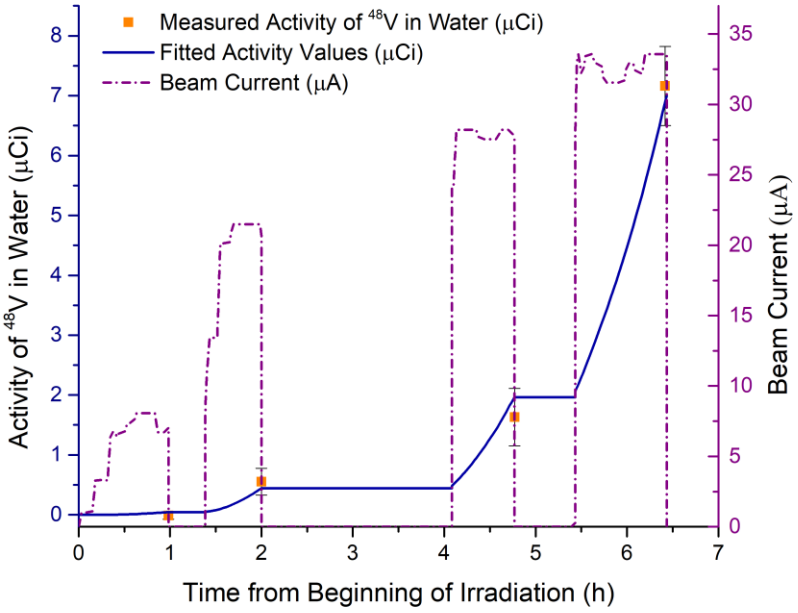

Figure 5.6: Activity of ^{48}V in the System
The fit results of Equation 5.10 are plotted every 1 to 2 minutes throughout the irradiation in the solid navy-blue line. These results match the measured data points, plotted in orange, within the estimated errors.

Due to this uncertainty in the total ^{51}Cr in the water system throughout the irradiation, only the total activity on the four anion exchange columns corresponding to the total activity removed from the front Ti64 target layer at the end of the irradiation was used in the degradation model. This assumption that the total ^{51}Cr activity was represented in the activity measured on the four anion exchange columns is supported by the very low relative activity of ^{48}V in the water at the end of the collection period. The system water was passed over the fourth ion exchange resins overnight to remove as much ^{48}V and ^{51}Cr from the water as possible. This resulted in 98(3)% of the total ^{48}V being collected on the four sets of ion exchange resins. Assuming that ^{51}Cr behaves similarly to ^{48}V in the system, the sum of activity on these four columns was recoil-corrected and used in the degradation model as the total amount

degraded from the Ti64 front target layer. The model reproduced this value for ^{51}Cr with a corrosion rate of 2.3E-6 µm/(µA s). This value is within a factor of two of that found with ^{48}V, verifying the reproducibility of the estimated corrosion rate.

5.3.2.2 Extrapolating Corrosion Rate to Predict Target Lifetimes

When extrapolating the corrosion constant measured in this proton irradiation to that for other beams, there are a few important factors to consider. It is particularly important to take into consideration the area of the target shell that will be irradiated when making estimates for isotope harvesting at FRIB. Figure 5.7 shows the beam power that has been used in previous experiments, a full power ^{48}Ca beam at the NSCL, and beam powers that are expected at FRIB during the ramp up phase and full power operation. This figure also shows how this comparison between the experiments changes when we consider the total *areal*

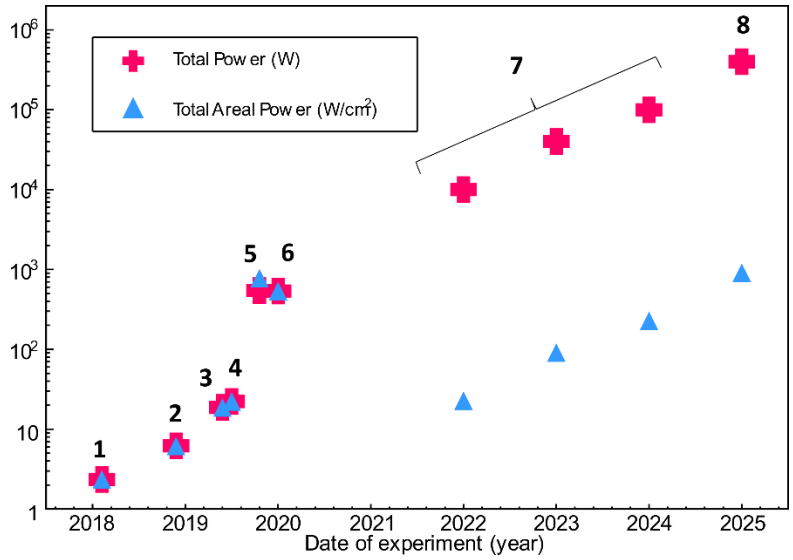

Figure 5.7: Total Power and Areal Power for Various Beams
Points labelled 1 to 4 in this figure correspond to the experiments listed in Table 5.1. Point 5 shows the proton irradiation described here and point 6 is given for the experiments with a ^{48}Ca beam (140 MeV/nucleon, 80 pnA) described in Chapter 6 and 7. The ramp up of FRIB is represented by the points collectively labeled 7 and point 8 shows FRIB at full beam power. The total power of these beams is shown as pink crosses and the total areal power of these beams is given in blue triangles.

power (W/cm^2) instead of simply the total power (W). Although FRIB will have orders of magnitude higher beam powers (through both higher energy and intensity beams), this power is spread over a much larger area on the proposed target for isotope harvesting [39]. This means, in terms of total areal power deposited in a target, the present proton irradiation is comparable in magnitude to future full power FRIB irradiations.

Additionally, both the amount of power deposited in the front Ti64 target layer, leading to high temperatures and atom displacements in the target shell, and the amount of power deposited in the water in contact with the inner surface of the Ti64 target layer, producing high temperatures and a corrosive radiolysis environment in the water, are instrumental in the degradation of the front target shell layer. Since it is unclear how to scale the degradation rate based on these factors, three estimates were made based on the following beam power scenarios for degradation with future irradiations: 1) using the beam power deposited in the front layer of the target shell, 2) using the beam power deposited in the front layer of the target shell and the 2 mm water layer, and 3) using the beam power deposited in the last 0.1 mm of the front layer of the target shell and in the first 0.1 mm layer of water in contact with the inner

Table 5.5: Scaled Corrosion Rates for Different Beam Power Considerations
The corrosion rate is given for the three different beam power scenarios given in the text in which different regions of power deposition in the target are considered.

Beam Power Scenario		Scaled Corrosion Rate (cm^3/J)
Number	**Description of Power Deposition**	
1	In the first layer of Ti64	1.7E-11
2	In the first layer of Ti64 and 2 mm water layer	6.5E-12
3	At the interface between the first layer of Ti64 and the 2 mm water layer	6.6E-11

surface of the front target shell layer. These three estimates provided different power depositions per integrated beam current. The results are given in Table 5.5 and 5.6 for these three scenarios. The time estimates in Table 5.6 are given as the irradiation time until 50 µm or approximately 10% of the front Ti64 target shell layer is degraded with various beams at the NSCL and FRIB. The ^{48}Ca and ^{82}Se beams were selected because they have the highest total power deposition and the highest power deposition in the front layer of the target shell of the beams available at the NSCL, respectively.

The NSCL beam blocker design used for the estimated target lifetimes (shown in Figure 5.2 and 5.5 and described in detail in Chapter 2 Section 2.2.2) involves a double-walled design with two 500 µm layers of Ti64 and a 2 mm water gap between the walls. For FRIB, the 40-kW ramp up beam intensity and the 400-kW full beam power level are considered for ^{48}Ca, ^{82}Se, and ^{238}U. The first stage of beam intensity at FRIB will use a first-generation beam dump with a single-walled target: 1 mm layer of Ti64 in contact with a large volume of flowing water. The higher beam power stage will use a second-generation beam dump with a double-walled target design, as in the NSCL isotope harvesting target system. This second-generation beam dump will differ from the one used at the NSCL in that it is much larger and is a circular rotating target instead of a rectangular stationary target to maximize the beam strike area at FRIB.

It is clear from these estimates that the proton irradiation demonstrated accelerated degradation compared to the irradiation conditions expected at the NSCL and FRIB to observe degradation over this short experiment. For perspective on the length of calendar time these predictions correspond to, it has been estimated that the NSCL produces beam for about 4000 hours each year. For the ^{48}Ca and ^{82}Se beams at the NSCL, about 1500-2900 hours are

Table 5.6: Estimated Target Durability for the Highest Power Primary Beams at the NSCL and Equivalent Beams at FRIB

The target lifetime estimates for the NSCL were made with the NSCL double-walled beam blocker described in the text. For each beam at FRIB, the first row with a lower beam intensity assumes the first-generation single-walled beam dump design will be used and the second row with a higher beam intensity assumes the second-generation double-walled beam dump design will be used. For each of these nine irradiation conditions, target lifetime estimates were made using the three beam power scenarios described in the text.

Facility	Nucleus	Energy (MeV/ nucleon)	Intensity (pps)	Total Power in Window		Total Power in Window and 2 mm Water		Power at Interface of Window and Water	
				Areal Power Deposition (W/cm^2)	Time until 10% Degraded (hours)	Areal Power Deposition (W/cm^2)	Time until 10% Degraded (hours)	Areal Power Deposition (W/cm^2)	Time until 10% Degraded (hours)
UW-M	^{1}H	16	2.12E+14	306	275	777	275	76	275
NSCL	^{48}Ca	140	4.99E+11	122	2445	261	2890	28	2689
	^{82}Se	140	2.81E+11	196	1521	430	1758	45	1662
FRIB	^{48}Ca	189	1.87E+13	4	19605	7	31840	1	38560
			1.87E+14	20	4215	46	4650	5	3953
	^{82}Se	186	1.16E+13	8	10602	12	17193	1	20777
			1.16E+14	36	2332	84	2534	10	2169
	^{238}U	154	4.91E+12	27	3148	49	4337	4	5426
			4.91E+13	119	707	301	709	33	634

estimated for a 10% degradation in the thickness of the front Ti64 target layer, which corresponds to approximately 4.5 to 8.7 months of operation.

5.3.2.3 Validity and Limitations of Extrapolation

The present experiment used a proton beam to form long-lived radiotracers selectively in the Ti64 target shell. Fast, heavy ion beams available at the NSCL are predicted to produce the same long-lived radionuclides in the shell and water through fragmentation of the beam, making them more difficult to interpret than the irradiation presented here. Additionally, proton beams are widely available at the areal power level needed to replicate those anticipated at the NSCL and FRIB.

While this experimental design allowed for the measurement of target degradation and extrapolation to other irradiation conditions, there are some important factors that affect the validity of this method. Most notably, the interaction of a proton beam with the target system differs greatly from that of fast, heavy ion beams. The main fundamental difference comes from the linear energy transfer (LET) of these different beams. The LET values of a 16 MeV proton, 140 MeV/nucleon ^{48}Ca, and 140 MeV/nucleon ^{82}Se beam as they stop in the target were converted to linear power deposition values by using beam intensities of 34 μA for the proton beam and the NSCL beam list intensities for ^{48}Ca and ^{82}Se. The resulting values as a function of the distance through the isotope harvesting target are plotted in Figure 5.8. Though all these beam conditions have similar total power depositions, the 16 MeV proton has a much higher power deposition in the front Ti64 target shell layer and in the adjacent 2 mm water layer than the 140 MeV/nucleon ^{48}Ca and ^{82}Se beams due to the significantly shorter range of the proton beam.

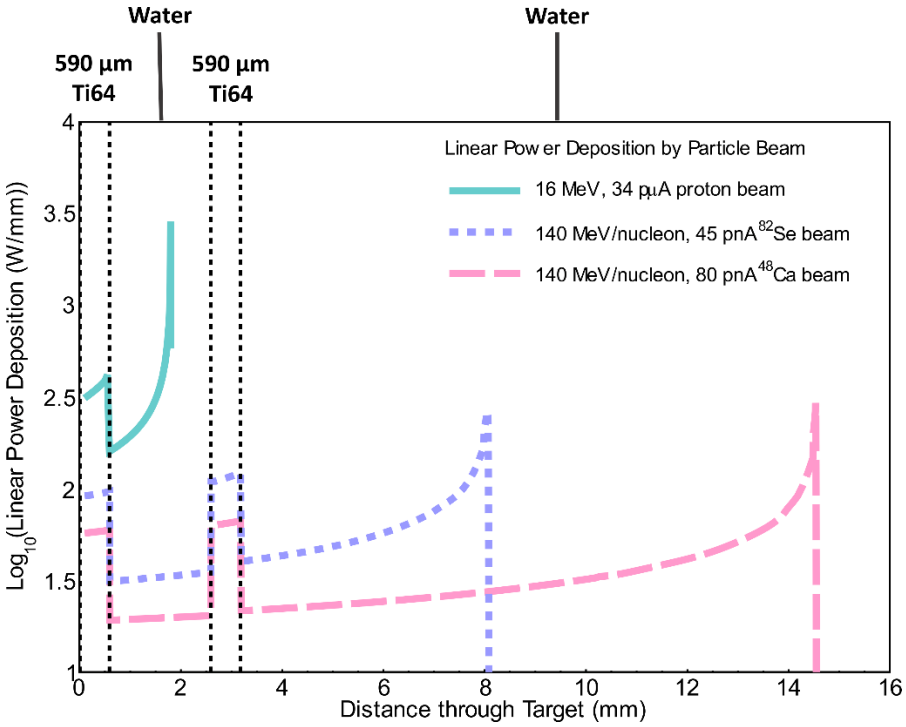

Figure 5.8: Linear Power Deposition of Various Beams through the Target
The linear power deposition (W/mm) is plotted for a 16 MeV, 34 pµA proton beam; a 140 MeV/nucleon, 45 pnA ^{82}Se beam; and a 140 MeV/nucleon, 80 pnA ^{48}Ca beam through the target. The target materials are shown in order: 590 µm of Ti64, 2 mm flowing water, 590 µm Ti64, and a large flowing water volume.

One practical result of this different linear power deposition profile for the proton beam is that the front Ti64 target layer most likely reached a very high temperature of several hundred °C range during this irradiation. While the bulk water was conditioned with a chiller and maintained at below 30 degrees C, the water flowing by the front layer of the target shell was subject to a large increase in temperature as a result of heat transfer from the high temperature target shell and the power deposition of approximately 9.7 MeV per proton in this small volume of water. It is possible that partial vaporization of the water occurred leading to a lower capacity to cool the front layer of the target shell. The high temperature resulted from trying to reach high areal power levels with a short-range proton beam and is not expected to

occur with much longer range fast, heavy ion beams. It is known that high temperatures accelerate degradation rates of materials due to changes in the microstructure of material. Therefore, the corrosion rate measured in this experiment is suspected to be higher than the rate which would be present at lower temperature conditions used for future isotope harvesting experiments. This means the target lifetimes predicted from the measured degradation rate in this experiment are most likely lower than the actual lifetimes.

Another clear limitation of this experiment is the large difference in time between the experimental irradiation period and the predicted lifetime of the target. Extrapolating to much longer time scales introduces significant uncertainties to these predictions. One noteworthy uncertainty is that the short time scale of the irradiation presented here was not able to uncover any long-term changes under irradiation conditions (*e.g.*, hardening of the target shell material) that could influence the rate of degradation. The degradation is assumed to be constant through hundreds to tens of thousands of hours of irradiation when the degradation rate may change with developing conditions in the target over time.

The results of this experiment have provided confidence in the integrity of the isotope harvesting system, including the durability of the target. This has enabled full power ^{48}Ca irradiations of the isotope harvesting target at the NSCL (see Chapter 6 and 7). Additionally, the lifetimes predicted in Table 5.6 support the integrity of the target during the first few years of increasing the beam intensity at FRIB. During these initial years, the state of the isotope harvesting target to be used at FRIB will be monitored (*e.g.*, measuring the thickness of the target face before and after long periods of irradiating). These measurements will benchmark the real corrosion rate with fast, heavy ion beams at FRIB.

5.4 Conclusion

A proton irradiation of the current isotope harvesting system was performed to test the durability of the target under the large power depositions expected in the isotope harvesting targets at the NSCL and FRIB. Degradation of the first Ti64 target layer was observed and extrapolated to relevant beams that will be used at the NSCL and FRIB. These estimates show that a 10% reduction in the front Ti64 target layer thickness occurs on the time scale of several months of operation at the NSCL. Estimates for the ramp-up period at FRIB with the first-generation FRIB beam dump indicate that thousands to tens of thousands of hours of irradiation can be performed before a 10% reduction in thickness should occur due a much larger surface area that will be irradiated. Shorter time estimates of hundreds to thousands of hours are predicted for the degradation at the full power operations of FRIB with a second-generation beam dump. It is strongly suspected that the corrosion rate measured here is higher than that at the NSCL and FRIB, resulting in underestimates of the lifetime of the NSCL isotope harvesting target and all generations of the FRIB beam dump under the anticipated irradiation conditions. Measurements will be made of the target degradation as FRIB increases the beam power used in the first few years of operation. Overall, these results indicate that the degradation of the target should be manageable obstacles for isotope harvesting at the NSCL and in the future at FRIB.

Chapter 6: ^{48}Ca Beam Experiment 2: Proof of Concept for ^{47}Ca/^{47}Sc Generator and ^{47}Sc Radiolabeling with Isotope Harvested ^{47}Ca

A stepwise increasingly higher intensity ^{48}Ca irradiation of the flowing-water isotope harvesting target was performed at the NSCL with the target in the beam blocker position in the A1900 fragment separator. The ^{47}Ca produced in the first three lowest intensity irradiation segments was used to find a production rate of 0.0167(4) ^{47}Ca nuclei per incident beam particle. The production rates of other cationic radionuclides were also measured to understand the level of activity that would accumulate on the cation exchange resin beds. Through the remainder of the irradiation, the beam intensity was increased up to a maximum intensity of 80 pnA. A majority of the ^{47}Ca produced in this irradiation was effectively collected on two cation exchange resin beds in the aqueous chemistry loop of the water system. The first resin bed with the majority of the ^{47}Ca activity was processed and the eluted activity was used in several steps: purification of ^{47}Ca, generation of ^{47}Sc in the purified ^{47}Ca solution, purification of ^{47}Sc from the generator solution, and radiolabeling DTPA-TOC with the purified ^{47}Sc. The generator procedure for the purification of ^{47}Sc produced a high purity ^{47}Sc sample in terms of both radionuclidic and stable ion purity, allowing for radiolabeling of DTPA-TOC with essentially 100% radiolabeling yield. Each of these steps demonstrated the proof-of-concept that harvested ^{47}Ca can be used to generate ^{47}Sc of sufficient quality for nuclear medicine research.

6.1 Introduction

Following the high intensity proton irradiation that demonstrated the durability of the second-generation isotope harvesting target (see Chapter 2 Section 2.2.2), the target and water system were used in a higher intensity ^{48}Ca beam irradiation at the NSCL. The target was installed at the A1900 beam blocker position (Figure 2.3 in Chapter 2 Section 2.1) and was connected to the water system in the final configuration (Chapter 2 Section 2.3.3). This experiment was designed to demonstrate both isotope harvesting of ^{47}Ca at the full ^{48}Ca beam intensity available at the NSCL and to further the purification process investigated in the first ^{48}Ca irradiation (see Chapter 4). The approximately 1.8 mCi of ^{47}Ca produced in this irradiation allowed for optimization of the generator purification procedure and the radiolabeling of DTPA-TOC (*i.e.*, diethylenetriamine pentaacetate-(Tyr^3)-octreotide) with ^{47}Sc. DTPA-TOC, which is shown in Figure 6.1, consists of an open chain chelator (DTPA) and a biologically active peptide

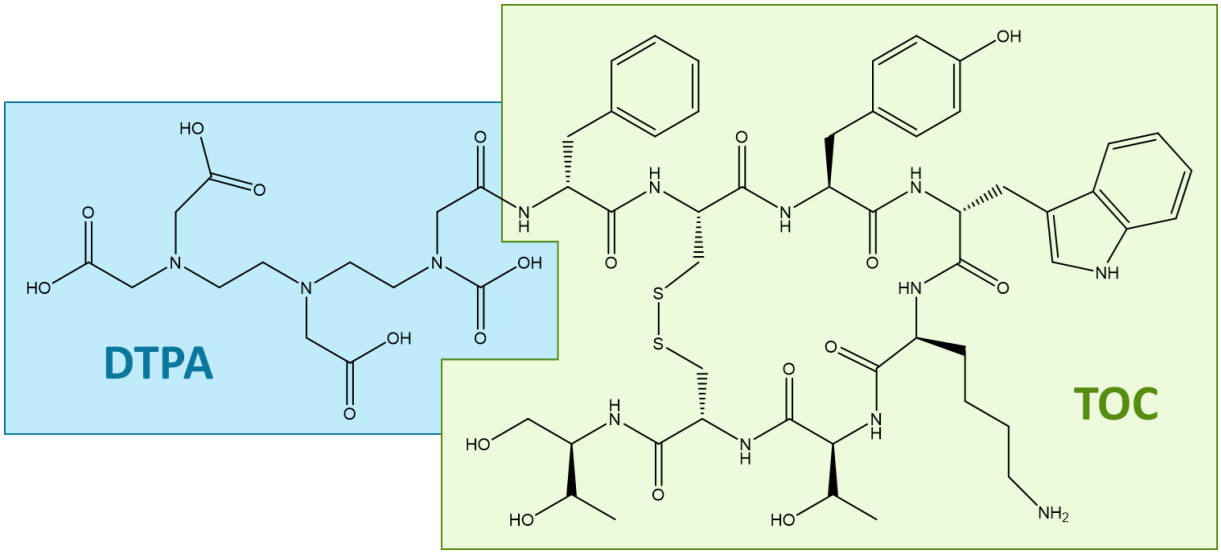

Figure 6.1: Chemical Structure of DTPA-TOC
The open chain ligand DTPA is highlighted in blue while the peptide TOC is highlighted in green.

that has been shown to interact with somatostatin receptors on the surface of neuroendocrine tumors (TOC). [79] The methods presented here produced high quality [^{47}Sc]Sc-DTPA-TOC, supporting the feasibility of using isotope harvested ^{47}Sc for preclinical targeted internal radiotherapy research.

6.2 Materials and Methods

6.2.1 Materials

6.2.1.1 Chemicals and Resins

Prior to the irradiation, the water in the isotope harvesting system was purified with a mixed bed resin (McMaster-Carr, Filter media PVC water deionizer) to lower the conductivity of the water to about 250 nS/cm. Three resins types were used in this work for collection and purification of radionuclides: AG 50Wx8 cation exchange resin (BioRad, mesh size 20-50), AG MP-50 cation exchange resin (BioRad, 100-200 mesh size), DGA extraction chromatography resin (TrisKem International, N,N,N',N'-tetra-n-octyldiglycolamide, normal resin, particle size 50-100 μm). Both cation exchange resins were pretreated separately in large quantities with the following rinse order: 50 mL of 2 M HCL, 50 mL of 4 M HCL, 50 mL of 6 M HCL, and 100 mL MilliQ water. This procedure was repeated for a total of 2 complete rinse cycles, removed ionic impurities, especially metal ions, from the resin, and ensured that the resin was in the H^+ form. For all elutions, dilutions, and column separations, metal free hydrochloric acid (Merck, Suprapur, 30%) and nitric acid (Merck, Suprapur, 65%) as well as MilliQ purified water (Thermo Scientific MicroPure Ultrapure Water System, 18.2 MΩ cm) were used. All centrifuge tubes used in this work were rinsed with MilliQ purified water and only plastic and glass were used for processing radioactive samples to avoid contact with metal contaminants.

The radiolabeling solution was pH adjusted with metal free sodium acetate (Alfa Aesar, anhydrous power, 99.997%) prepared in MilliQ purified water. 1 mg of DTPA-TOC was dissolved in ultrapure water to make a 10 mM solution. A portion of this stock solution was diluted to 1mM using ultrapure water for use in the radiolabeling experiments. Silica gel thin layer chromatography plates (Merck, TLC Silica gel 60 F_{254}) were used with sodium citrate dissolved in MilliQ purified water and pH adjusted with sodium hydroxide (Macron, ACS reagent grade) for the TLC mobile phase.

The ICP standards were prepared from 8 *Trace*Cert mixed solutions for ICP from Millipore Sigma that included 67 elements altogether: 100 ppm Alkali metal mix in 2% nitric acid (Li, Na, K, Rb, and Cs), 100 ppm Alkali earth metal mix in 2% nitric acid (Be, Mg, Ca, Sr, Ba), 100 ppm Transition metal mix 1 in 2% nitric acid (V, Cr, Mn, Fe, Co, Ni, Cu, Zn, Ag, and Cd), 100 ppm Transition metal mix 2 in 2% nitric acid and 1% hydrofluoric acid (Ti, Zr, Hf, Nb, Ta, Mo, W, and Re), 100 ppm Transition metal mix 3 in 10% hydrochloric acid (Ru, Rh, Pb, Os, Ir, Pt, and Au), 100 ppm Post-transition metal mix in 2% nitric acid (Al, Ga, In, Tl, Pb, and Bi), 100 ppm Metalloid and non-metal mix in 2% nitric acid and ≤0.5% hydrofluoric acid (B, Si, P, S, Ge, As, Se, Sn, Sb, and Te), and 50 ppm Rare earth metal mix in 2% nitric acid (Sc, Y, La, Ce, Pr, Nd, Sm, Eu, Gd, Tb, Dy, Ho, Er, Tm, Yb, and Lu). These standards were diluted with the appropriate concentration of Suprapur HNO_3 and HCl required for the standards to match the solution matrices of the samples analyzed. When running the calibration and sample analyses, Suprapur 3% HNO_3 and 3% HCl were used for the HNO_3 and HCl sample matrices, respectively. Additionally, the falcon tubes used were rinsed at least twice with ultrapure water to remove any background stable ions before samples were added.

6.2.1.2 Instruments

Identification and quantification of radionuclides were performed with an HPGe Canberra BEGe Gamma-ray Detector (BE2020). The HPGe detector was calibrated for energy and efficiency with a ^{152}Eu point source at 25 and 50 cm from the detector face. Genie 2000 software (Mirion Technologies) was used to analyze gamma spectra. An AccuSpin Micro 17 microcentrifuge (Thermo Fisher Scientific) was used at 7000 g/min for ease in working with the concentrated ^{47}Sc radiolabeling sample. An Amersham Typhoon™ Biomolecular Imager (GE Healthcare, Chicago, USA) and phosphor imaging films (BAS-IP SR 2040, GE Healthcare) were used to visualize radioactivity on TLC plates. These images were analysed with ImageQuant TL software (version 8.2.0.0, GE Healthcare) to perform background subtractions and quantify the relative intensities observed in the image. Stable elemental analysis was performed with an Agilent 5900 SVDV ICP-OES equipped with an Advanced Valve System and a 0.5 mL sample loop.

6.2.2 ^{48}Ca Irradiation

The second-generation isotope harvesting target at the A1900 beam blocker position was irradiated with a 140 MeV/nucleon ^{48}Ca beam (see Figures 2.5 and 2.7). During the experiment, the beam intensity was increased from 1 to 80 pnA over 5.1 hours for a total integrated beam intensity of 80 pnA h. The irradiation was separated into four irradiation periods of increasing beam intensity. After each of the first three periods, a water sample was withdrawn through the sample line in the aqueous chemistry box. Following removal of the third water sample, a cation exchange resin bed was inserted in the system in the aqueous chemistry box and remained in the system for 16 hours. This collection period included the

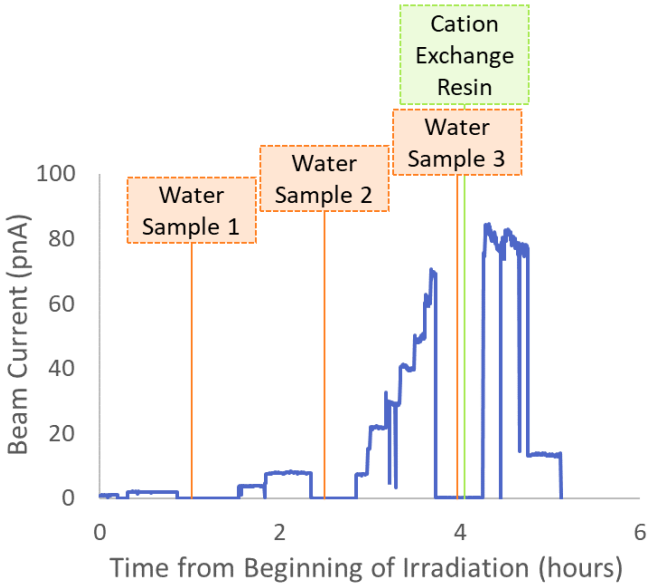

Figure 6.2: Beam Structure and Sample Collection
The measured beam current is shown as a function of time (blue line). A cation exchange resin bed was inserted before the fourth irradiation period and removed 16 hours later with a water sample withdrawn concurrently. A second cation exchange resin bed was inserted at that time and was removed 24 hours later with another water sample.

fourth irradiation period as well as several hours after the end of the irradiation. The first resin bed was removed for use in offline experiments and a second cation exchange resin bed was used to continue collection of ^{47}Ca for the next 24 hours. Based on HPGe measurements of the first resin bed and a water sample removed at the time this resin bed was removed, a total of 1.79(6) mCi of ^{47}Ca were produced during this irradiation. The beam current structure and the time points at which sampling was performed during the experiment are shown in Figure 6.2.

6.2.3 Production of ^{47}Ca

Production rate measurements were carried out by removing 250 mL water samples from the thoroughly mixed isotope harvesting water after the first three irradiation periods. Gamma-ray spectrometry used to identify and quantify radionuclides in the sample. The

activities measured in the 250 mL water samples were scaled up to estimate the total activity of each radionuclide in the total water volume of the system. After completion of the experiment, an accurate value for the total water volume was found by spiking a known volume and concentration of $CaCl_2$ solution into the flowing-water system, allowing the water to thoroughly mix (as determined by constant conductivity readings of the system water), and withdrawing a sample of known volume. The concentration of calcium in the water sample was determined with ICP-OES, and the dilution of the calcium concentration was used to calculate the total water volume in the system when each of the three water samples were withdrawn.

An additional correction was made to the gamma-ray spectroscopic measurements to account for the non-standard geometry of the samples. This correction factor was found by making gamma-ray measurements of a small volume (*i.e.*, 250 µL) which resembled a point source and contained each of the radionuclides listed in Table 6.3 (see Section 6.3.1). The 250 µL sample was then quantitatively transferred to 250 mL of water to replicate the same geometry as the 250 mL water samples withdrawn during the experiment. The measurements from these two sample geometries were compared to find a geometry correction factor for the 250 mL water samples. Approximately 5 to 20% fewer counts (depending on the gamma-ray energy and the distance from the detector) were observed from the 250 mL water sample compared to the smaller 250 µL volume most likely due to more extensive attenuation of gamma-rays in the larger water volume. Both the measurement of the water volume in the system and the geometry correction factors are discussed in more detail in Appendix D.

Based on the geometry-corrected total activity measurement of each radionuclide in the water system and the beam current during each corresponding irradiation period, a production

rate, P, in terms of particles produced per incoming beam particle was found with Equation 6.1 for each radionuclide in each irradiation period:

$$N_P = \sum_{i=1}^{n}[P \times I(t_i) \times \left(1 - e^{-\lambda \Delta t_i}\right) \times e^{-\lambda t_d}] \quad (6.1)$$

where N_P is the number of produced nuclei remaining at the end of the irradiation, $I(t_i)$ is the beam current during the *i*th irradiation interval from t_i to t_{i+1}, λ is the decay constant of the produced radionuclide, and t_d is the time between the *i*th irradiation interval and the end of the irradiation. This segmented production equation was used to account for fluctuations in beam intensity during each irradiation period.

6.2.4 Collection of ^{47}Ca from Isotope Harvesting System

After the radioactive products were formed in the interior of the flowing water target, the water transported these products from the target to the rest of the isotope harvesting system. This system contained components that measured the conductivity of the water to understand the level of dissolved ions in the water and that removed ions from the flowing water to use these products in further studies. In this experiment, cation exchange resins were used to remove $^{47}Ca^{2+}$ from the water. Essentially all the cationic radioactive products as well as stable cations in the water were collected on the cation exchange resin beds.

When designing the resin beds, two important functions were considered: 1) effective collection of ions from the flowing water and 2) removal of ions from collection resin bed for use as the loading solution in further purification. To satisfy both requirements, 1.5 g of resin was used for the collection resin bed. This quantity has a large capacity to capture the radionuclidic products even in the presence of significant stable ion contamination while being

small enough that a multiple resin bed volume rinse for elution purposes remains practical. The ideal solution resulting from elution has the smallest volume with the lowest acidity possible. This allows for a dilution step instead of a time consuming and less practical evaporation step to prepare the load solution for the HCl gradient purification process.

The cation exchange resin AG 50Wx8 in the form of large diameter resin beads (mesh size 20-50) was used in all the collections described in this work. The large bead size allowed for a rapid flow of water through the resin bed without a large pressure drop across the resin bed. Each resin bed used 1.5 g of cation exchange resin in a rigid polycarbonate tubing (3/8" OD, 1/4" ID, 3.5" length) with a piece of glass wool and a PVDF (polyvinylidene fluoride) plastic tube fitting on each end of the tube. The glass wool immobilized the resin against the flow of water and the fitting on each provided a water-tight seal between the tube housing the resin and the 1/4" tubing in the isotope harvesting water system. Non-spill coupling valves (1/4" NPT valved coupling body, NS4D10004 and NS4D24004) were also used on each side of the resin bed in the system to allow for rapid, spill-free removal of the resin beds from the system (depicted in Figure 2.13).

The collection started about 4 hours into the irradiation after the withdrawal of water samples for the production rate measurements. The first cation exchange resin collected cations for 16 hours including 4 hours during the irradiation and 12 hours following the irradiation. A second cation exchange resin bed was then used for the next 24 hours to increase the total collected activity. The average flow rate of the water over the resin beds was maintained around 400 mL/min for this experiment (430 mL/min for the first resin bed, 380 mL/min for the second). The percent of the ^{47}Ca collected was used as a metric to understand

the collection efficiency with these resin beds. When a resin bed was removed from the system during either experiment, a water sample was withdrawn from the system. Gamma-ray spectroscopy was used to measure the activity of each radionuclide on the column and in the water samples. The activity measured in the water sample was then scaled up to account for the entire volume of the water system. The percent collected was found using the activity collected on the cation exchange resin beds compared to the remaining activity in the water as determined with the water sample.

Once collected, the ^{47}Ca was eluted from the collection resin beds with 1 or 2 M HCl. These relatively low concentrations of HCl were used to find the ideal solution, as discussed previously, to produce a final ^{47}Ca solution with as small a volume and as low an acidity level as possible. The first resin bed was rinsed with 71 mL of 1 M HCl in fractions of 5-10 mL followed by 18 mL of 2 M HCl in 5 mL fractions. The second resin bed from this experiment was rinsed with 40 mL of 2 M HCl in fractions of 5 mL. Each fraction and each of these resin beds before and after elution were measured with gamma-ray spectroscopy to determine the percent elution for each radionuclide.

6.2.5 Purification of ^{47}Ca

The load solution for the purification of ^{47}Ca was prepared from the first 47 mL of 1 M HCl used in the elution of the first collection cation exchange resin bed. This solution was diluted to 95 mL using ultrapure water to produce a solution of 0.5 M HCl and was divided into four equal fractions. Three of these fractions were used to perform the purification process in replicate, while the fourth was left unpurified. Each fraction contained 0.28(1) mCi of ^{47}Ca at the time they were prepared.

The three replicate purifications were performed using the same column containing 2 g of AG MP-50 resin in a 3/8" OD, 1/4" ID rigid polycarbonate tubing with a small piece of glass wool and a PVDF (polyvinylidene fluoride) plastic 3/8" to 1/4" union reducing tube fitting on each end of the tube. The cation exchange resin was preconditioned with approximately 25 mL of 0.5 M HCl before each separation. A pump speed of 1.5 mL/min was used throughout the separation. The approximately 24 mL load solution at 0.5 M HCl was added to the column followed by a 28 mL 2 M HCl rinse step. This load and rinse step were designed to remove ^{7}Be, ^{24}Na, ^{28}Mg, ^{42,43}K as well as any stable Fe from the column. Elution of ^{47}Ca was carried out in approximately 20 mL of 4 M HCl. Throughout the separation, all scandium isotopes loaded remained on the column due to their high distribution coefficient on this resin at these conditions. After the elution step, the column was rinsed with about 50 mL of water prior to storage. The steps of this separation as well as the general behavior of the radionuclides are illustrated in Figure 6.3.

An additional purification step was used for one of the purified ^{47}Ca solutions following the AG MP-50/HCl method. This step involved passing the 4 M HCl solution over a 1.5 g DGA resin and using an additional 20 mL of 4 M HCl to ensure a quantitative removal of ^{47}Ca from the resin. Then, 3 M HNO_3 was used to elute any stable Fe that was removed from the purified ^{47}Ca solution as it passed through the column. These 3 M HNO_3 samples were analyzed for their stable ion content as described in Section 6.2.8.

These separations were evaluated using the separation yield and the radionuclidic purity of ^{47}Ca. The separation yields measured the percentage of ^{47}Ca that was recovered in the 4 M

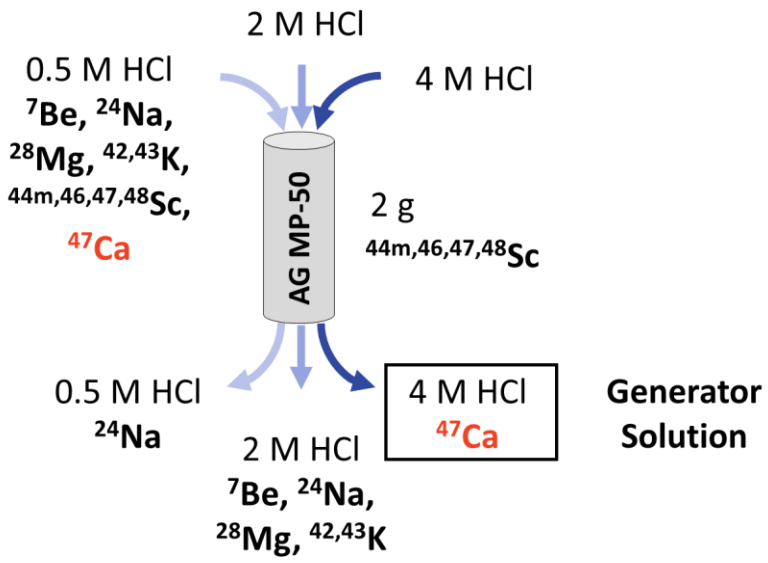

Figure 6.3: Separation Scheme for the Purification of ^{47}Ca
The color gradient of the arrows indicates the increasing molarity of acid used in the gradient elution. The placement of the radionuclides in the figure show where each species was at the beginning (load solution) or at the end of the separation (rinse solutions or on the column).

HCl used in the final elution step. This value was found for each separation as the ratio of the ^{47}Ca activity in the purified 4 M HCl elution compared to the original ^{47}Ca activity in the load solution, where the activity in the purified fraction was decay corrected to the time that the load solution was measured. The radionuclidic purity of the ^{47}Ca in the 4 M HCl solution was taken to be the percentage of ^{47}Ca activity in the final purified solution compared to the total activity of all radionuclides in the solution. The activity of ^{47}Sc was not included in the total activity in the solution as this activity inevitably grows in after the purification of ^{47}Ca. Additionally, the activity of ^{45}Ca was included in the total activity in the solution since it follows the chemical behavior of ^{47}Ca in each step and decays to stable ^{45}Sc, and therefore, does not affect the radionuclidic purity of the final ^{47}Sc solution.

6.2.6 Generation of ^{47}Sc

The purified solution of ^{47}Ca in 4 M HCl was used as the generator solution for ^{47}Sc. After 2 to 4 days of decay time, 68 to 93% of the theoretical maximum ^{47}Sc activity will be generated. Therefore, the generator solution was used approximately 3 days post-purification (*i.e.*, the AG MP-50/HCl separation or for successive generations of ^{47}Sc, the pseudo generator separation). This approach provided a good balance between generating a sufficient ^{47}Sc activity for radiolabeling while not wasting time or ^{47}Ca by waiting until the maximum activity that would occur after approximately 5.6 days of decay. The theoretical activity of a ^{47}Ca/^{47}Sc generator is shown in Figure 6.4 for an initial ^{47}Ca activity of 0.28 mCi.

A slightly modified version of the pseudo generator separation procedure outlined by Domnanich et al (2017) was used in this work to purify ^{47}Sc. [10] This procedure involves two

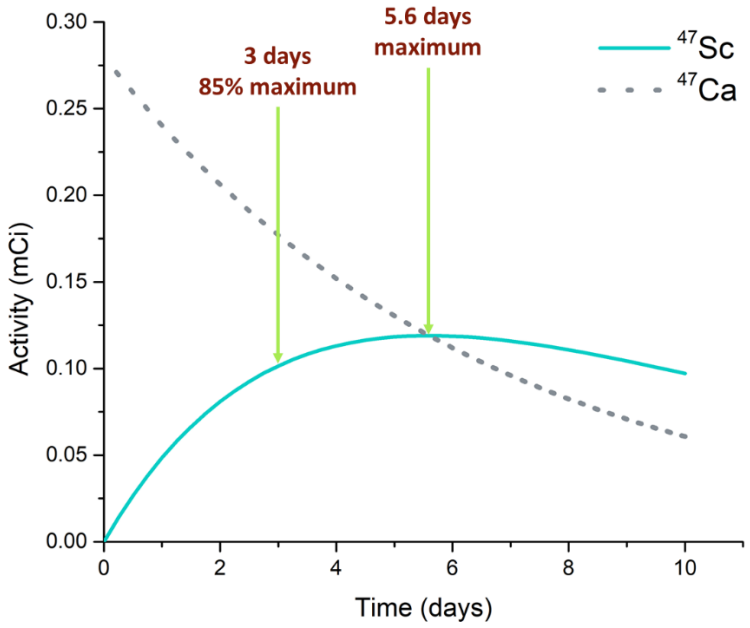

Figure 6.4: ^{47}Ca/^{47}Sc Generator Activity
The calculated ^{47}Sc activity generated with 0.28 mCi of purified ^{47}Ca is shown as a function of time. The two arrows indicate the ^{47}Sc activity at 3 and 5.6 days of decay time.

main steps using two DGA extraction chromatography columns to first purify the ^{47}Sc and then concentrate the ^{47}Sc activity in a small volume (Figure 6.5). Both columns were preconditioned with about 10 mL of 4 M HCl. In the first step, the 4 M HCl generator solution was loaded onto a 50-70 mg DGA resin column ("DGA 1") at a flow rate of 1.2 mL/min. At this concentration of HCl, Ca^{2+} passes through the column easily while Sc^{3+} is extracted from solution and retained on the column. A small 4 mL rinse of 4 M HCl was then used to rinse the load solution vessel and the column to ensure all the ^{47}Ca activity passed through the column. Then, 7 mL of 0.1 M HCl was used to remove ^{47}Sc from the column.

The second step in the pseudo generator process involved first re-acidifying the ^{47}Sc solution from the first DGA column to 3 M HCl through the addition of about 3 mL of 9.46 M HCl. This loading solution acidity ensured the retention of ^{47}Sc on the second DGA resin column ("DGA 2"). This solution was passed over the column at a flow rate of 0.3 mL/min, allowing any

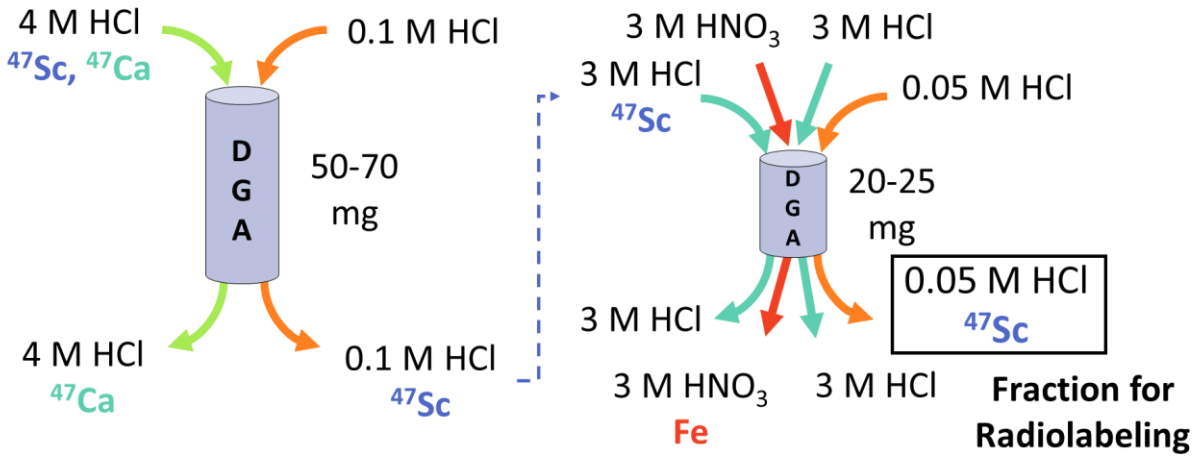

Figure 6.5: Modified Pseudo Generator Procedure
The procedure proceeds from left to right starting with loading the generator solution on the first DGA column and ending with eluting ^{47}Sc from the second DGA column.

residual ^{47}Ca to pass through and the ^{47}Sc to be retained in a tight band on the 20-25 mg of DGA resin. Both the low flow rate and the small mass of resin were selected to reduce the dispersion of the ^{47}Sc and assist in the concentration step. A rinse step of 7 mL 3 M HNO_3 was added to the original pseudo generator procedure to remove any residual Fe that was not removed during the purification of ^{47}Ca. This step was added due to low radiolabeling efficiencies observed after multiple uses of the original pseudo generator procedure. After this rinse step, a 7 mL 4 M HCl rinse step was used to retain ^{47}Sc on the column while switching the acid matrix on the column. With a flow rate of 0.5 mL/min, ^{47}Sc was eluted for the column in 0.05 M HCl and collected in the following fractions: 1) 1-2 drops, 2) 700 µL, 3) 500 µL, 4) 500 µL, 5) 2 mL. These fractions were designed to catch the largest portion of the activity in the second 700 µL fraction for use in radiolabeling.

As with the purification of ^{47}Ca, this separation procedure was characterized by finding the separation yield and radiopurity of the final purified ^{47}Sc sample. These values were found by using an HPGe detector to find the activity in each fraction and on both DGA 1 and 2 before and after each loading step. The separation yield from DGA 1 was found by comparing the activity on the column after loading and after elution. The yield for DGA 2 was found by comparing the activity in the load solution with that in the second ^{47}Sc fraction. A total separation yield was found as the product of these two yields from DGA 1 and 2.

Due to the long half-live of ^{46}Sc, it is both important and more difficult to measure the activity of ^{46}Sc in the final purified samples. Therefore, a long measurement of each radiolabeling solution was taken between 24 and 35 days after this purification was performed. For samples where ^{46}Sc was not detected, the limit of detection for this radionuclide was found

by taking the square root of the sum of counts over 7.5 keV centered around 889 keV, which corresponds to a characteristic gamma ray energy for this radionuclide. The activity found with this method is given as the upper limit of the activity of ^{46}Sc in the sample and is used to find a lower limit for the radionuclidic purity for ^{47}Sc in the radiolabeling solutions. These values are given for each radiolabeling solution in Table 6.4 in Section 6.3.4.

6.2.7 Radiolabeling DTPA-TOC with ^{47}Sc

The second ^{47}Sc fraction from the second DGA column in the pseudo generator procedure contained the majority of the ^{47}Sc activity in a volume of approximately 700 µL. Approximately 50 to 100 µL was removed from this solution ("free Sc" control) and the remainder was used as the radiolabeling solution each time the pseudo generator procedure was carried out. Activity measurements were taken of the final solution (approximately 650 µL) with the HPGe detector to determine the radionuclidic purity of the ^{47}Sc and the specific activity of the final radiolabeled complex.

The first step in preparing the radiolabeling solution was to pH adjust the solution to a level at which both the Sc^{3+} and the DTPA-TOC peptide would be in a suitable chemical form. Since scandium tends to hydrolyze at pH levels approaching neutral conditions, an acidic pH ensures that scandium is dissolved in solution as Sc^{3+}. However, peptides like TOC can degrade under strongly acidic conditions through cleavage of the peptide bond between the amino acids by acid hydrolysis. A mildly acidic solution around pH 3 to 3.5 can be used to maintain scandium solubility and prevent significant degradation of the peptide. With a portion of the solution set aside, pH adjustment tests were carried out for each generator. With the second DGA column of the generator using 3 M HCl immediately before elution of ^{47}Sc in 0.05 M HCl, there is a

potential for residual acid in the column to change the acidity of this elution step. Additionally, there is potential variability in the extent of this change depending on the condition of the column when this elution step starts and how much volume is collected in the first ^{47}Sc fraction. For these reasons, these pH adjustment tests are performed for each replicate of the generator procedure.

These adjustment tests involved combining different volume ratios of the radiolabeling solution and the 0.5 M sodium acetate buffer that was used to adjust the pH. These solutions were vortexed and spun down in the microcentrifuge before testing the pH with pH strip paper. The ratio that produced a pH of 3 to 3.5 was used to pH adjust the radiolabeling solution. In almost all cases, the ratio of the radiolabeling solution to the buffer used to achieve this pH was 4:1. The pH of this solution was also checked with pH strip paper before the addition of the peptide. The volume of 1 mM DTPA-TOC required to achieve 1.5 MBq/nmol was added to each radiolabeling solution. The final solution was shaken by hand and spun down for 10 seconds with a microcentrifuge. The exact formulations used for each radiolabeling solution are given in Table 6.1. The radiolabeling solutions were heated gently at about 80-85°C for 10 minutes to encourage chelation between the $^{47}Sc^{3+}$ and DTPA-TOC in solution. Once the solution had cooled, it was again shaken by hand and spun down with a microcentrifuge.

For radiolabeling solution 1, the concentrated ^{47}Sc fraction was split in two, resulting in two solutions described in two rows in the table. For radiolabeling solution 2 to 4, the sodium acetate buffer and the first, smaller addition of DTPA-TOC listed in the table were added as a first radiolabeling attempt. The second row in the table represents an addition of more DTPA-

Table 6.1: Radiolabeling Conditions

Radiolabeling Solution	Generator Number	Activity Used (MBq)	Buffer Added (µL)	Total Peptide Content (nmol)	Specific Activity (MBq/nmol)
1	1	0.640(5)	62.5	0.5	1.28(1)
		0.636(5)	62.5	2	0.318(2)
2	2	1.74(1)	150	1.2	1.34(1)
		1.65(1)	-	1.7	0.895(7)
3	3	1.33(1)	150	1.2	1.02(1)
		1.09(1)	-	2.4	0.418(4)
4	5	3.60(3)	120	1.2	3.00(2)
		3.29(3)	-	3.2	1.03(8)
5	6	1.36(1)	95	1.2	1.14(1)

TOC followed by another 10-minute heating step in a second attempt at raising the radiolabeling yield. The total amount of DTPA-TOC added to the radiolabeling solution at this point is given in the second row for solutions 2 to 4. No additional buffer was added in this second attempt as indicated by the dash in the second row for these solutions.

Thin Layer Chromatography (TLC) was used as a quality control test to determine the radiolabeling efficiency, defined as the percent of ^{47}Sc radiolabeled compared to the total activity in the radiolabeling solution. The method used silica gel TLC plates on an aluminum backing as the stationary phase and a solution of 0.1 M sodium citrate in 0.2 M HCl to achieve a pH of 4.7 for the mobile phase. With these conditions, any free [^{47}Sc]Sc would migrate up the TLC plate with an R_f value of 0.5 and any [^{47}Sc]Sc-DTPA-TOC complex would remain at the origin where originally spotted (Figure 6.6). Dilutions of both the free [^{47}Sc]Sc control solution (*i.e.*, the 50-100 µL set aside from the second fraction collected from DGA 2) and the radiolabeling

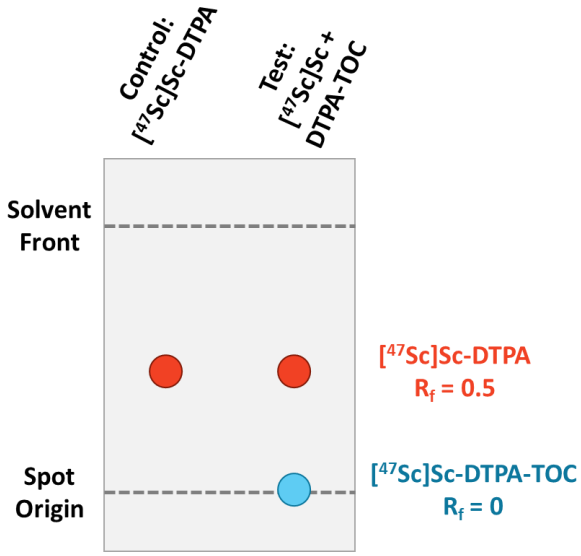

Figure 6.6: TLC Quality Control Test
Schematic description of two TLC lanes used for each test: the control with [^{47}Sc]Sc-DTPA (left) and the radiolabeling solution with [^{47}Sc]Sc-DTPA-TOC and/or [^{47}Sc]Sc-DTPA (right).

solution were prepared for use in the TLC quality control tests. Both solutions were diluted in a ratio of 9:1 (water to [^{47}Sc]Sc solutions) with ultrapure water and a final concentration of 30 µM DTPA. These dilutions were prepared for two reasons: to reduce the activity spotted on the TLC plates in 1 µL of each solution to avoid overexposure of the phosphor imaging films used to quantify the radiolabeling efficiency and to add DTPA to both solutions to chelate free [^{47}Sc]Sc. The DTPA chelated form of [^{47}Sc]Sc made the control spot of "free" [^{47}Sc]Sc more centralized and uniform and therefore, easier to quantify with the phosphor imager without changing the R_f value of the spot.

After performing the TLC test, the plates were dried and placed in plastic bag to contain the dispersible radioactivity. The plates were then laid on a phosphor imaging film in a dark environment for about 3 minutes. The TLC plates were removed, and the film was read by the

phosphor imager. ImageQuant TL software was used to define regions of interest at both R_f = 0.5 and 0 for both the control and the test lane. A background correction was made for each of these regions of interest and the percent activity in the two regions of interest was found for each lane.

6.2.8 Stable Elemental Analysis

Stable elemental analysis was performed with a broad spectrum ICP-OES method. As used previously for the first ^{48}Ca irradiation (see Chapter 4 Sections 4.2.6 and 4.3.5), a semi-quantification method was used to identify and quantify any stable ions present in the samples analyzed. This method was chosen for the wide range of elements and concentrations that can be simultaneously identified and quantified in a small sample volume. In the present experiment, the IntelliQuant broad spectrum analysis was used on a different instrument and with a more careful calibration than previously used. While this method is typically used for identification and semi-quantification of stable ions, the instrument can be carefully calibrated before use each time to produce reliable quantification of stable ions. The careful calibration of the instrument and uncertainty quantification for the measurements is a significant difference between the use of a semi-quantitative ICP-OES method used previously in the first ^{48}Ca irradiation and the present investigation.

The accurate quantification was supported by linear readings of standards from 5 ppb to 5 ppm for most elements and with a few quality control check standards used before and after all samples were analyzed. The relative deviation of the standards compared to the line of best fit and the deviation of the quality control check standards from their true concentrations were added in quadrature to find an uncertainty for the quantification of each element. This resulted

in about 4-15% uncertainty in the quantification of all elements identified in the samples. The calibration was performed for different sample matrices since the presence of high acid concentrations can change concentration readings due to changes in the physical characteristics of the solution. Since most samples fell into one of four sample matrix categories, calibrations were performed for standards in a 3 M HNO_3, 1 M HCl, 2 M HCl, and 4 M HCl matrix. For each matrix, standards were used from 5 ppb to 5 ppm with a pure acid sample as a "blank". These samples included 67 elements altogether including ions of interest such as Ca, Fe, and Sc. The identical instrument settings were used for both the calibration and the sample analysis and are given in Appendix C.

6.3 Results and Discussion

6.3.1 Production of Radionuclides with ^{48}Ca Beam

Production rates from the 140 MeV/nucleon ^{48}Ca beam irradiation of a flowing-water target were measured for all radionuclides with an activity above the limit of detection with HPGe gamma-ray measurements at 10 to 20 min after the irradiation period and are given in Table 6.2 production rates are given in nuclei produced per incoming ^{48}Ca beam particle. These values are also converted to a percent to represent the percent conversion of the primary beam to each radionuclide by atom. Additionally, these measured production rates were used to extrapolate the activity that would be produced in the isotope harvesting system if it were to be used to collect left-over beam for a typical ^{48}Ca primary beam experiment at the NSCL. The activities are those immediately after the irradiation period and after a 24-hour waiting period in which the radionuclides decay before experimenters access the activity. A correction was

Table 6.2: Production Rates of Radionuclides in Flowing-Water Target with 140 MeV/nucleon ^{48}Ca Beam

Production rates reported as radionuclide produced per incoming ^{48}Ca beam particle and as percent conversion of the beam to each radionuclide. Extrapolated activities based on the measured production rates are given for isotope harvesting for a typical ^{48}Ca primary beam experiment at the NSCL (*i.e.*, 4.5E11 pps at 140 MeV/nucleon for 120 h) and after a 24-hour cool down period following this irradiation. When a dash is given, it indicates that the activity level has dropped below 10 Bq.

Nuclide	Production Rate	Percent Conversion	Activity (GBq)	
			After Irradiation	After 24-hour cool down
Na-24	8.2(1)E-4	0.082(1)	0.367(7)	0.121(2)
Mg-27	3.07(2)E-4	0.0307(2)	0.138(1)	-
Mg-28	1.9(1)E-4	0.019(1)	0.081(5)	0.037(2)
S-38	1.28(7)E-4	0.0128(7)	0.057(3)	1.6(1)E-4
Cl-34m	3.9(1)E-5	0.0039(1)	0.0175(6)	-
Cl-38	1.16(4)E-3	0.116(4)	0.57(5)	-
Cl-39	6.5(5)E-4	0.065(5)	0.29(2)	-
K-42	3.34(7)E-3	0.334(7)	1.50(3)	0.391(8)
K-43	4.1(1)E-3	0.41(1)	1.81(6)	0.86(3)
K-44	2.6(5)E-3	0.26(5)	1.2(2)	-
K-45	1.6(2)E-3	0.16(2)	0.71(9)	-
Ca-47	1.67(4)E-2	1.67(4)	4.02(9)	3.45(8)
Sc-44m	4.69(8)E-4	0.0469(8)	0.160(3)	0.120(2)
Sc-46	5.2(6)E-3	0.52(6)	0.09(1)	0.09(1)
Sc-47	4.62(5)E-3	0.462(5)	2.8(4)	3.0(6)
Sc-48	2.17(3)E-3	0.217(3)	0.83(1)	0.567(8)

applied to the measured production rates for ^{47}Sc and ^{38}Cl to account for contributions from their co-produced parents. The reported production rates for ^{47}Sc and ^{38}Cl in Table 6.2 reflect the rate of direct production for these radionuclides. However, the activities extrapolated in Table 6.2 account for both direct production and decay contributions from their parent radionuclides.

In a previous isotope harvesting experiment with a ^{48}Ca primary beam described in Chapter 4, the production rate for ^{47}Ca was found to be 0.020(4) with a large systematic error. [41] The measured rate of 0.0167(4) in this experiment agrees well with the previous value with a much smaller uncertainty. The production rates were measured with two different methods, giving credibility to the accuracy of the result. The production rate for ^{47}Ca is the highest measured in this irradiation and is high for charged particle reactions in general. Given this production rate, a typical experiment at the NSCL using a ^{48}Ca primary beam could produce 4.02(9) GBq of ^{47}Ca for the generation of ^{47}Sc. The ^{48}Ca primary beam anticipated for isotope harvesting at FRIB is higher in energy and more than 400 times more intense than the available beam at the NSCL. This should result in a higher production rate and a higher number of possible nuclear interactions, respectively.

6.3.2 Collection of ^{47}Ca from Isotope Harvesting System

Collection of ^{47}Ca from the 50 L isotope harvesting water system was achieved with a cation exchange resin with high efficacy. During the present experiment, 92(5)% of the 77(3) MBq of ^{47}Ca produced was collected on a single 1.5 g cation exchange resin bed with a water flow of 430 mL/min over the resin bed for 16 hours. The remaining ^{47}Ca in the water was removed with a second cation exchange resin bed of the same size over 24 hours at a similar flow rate of 380 mL/min. Overall, 101(5)% of the ^{47}Ca was removed from the water with the^{47}Ca activity remaining in a 500 mL sample of water below the limit of detection with an HPGe gamma-ray detector after the second cation exchange resin was removed.

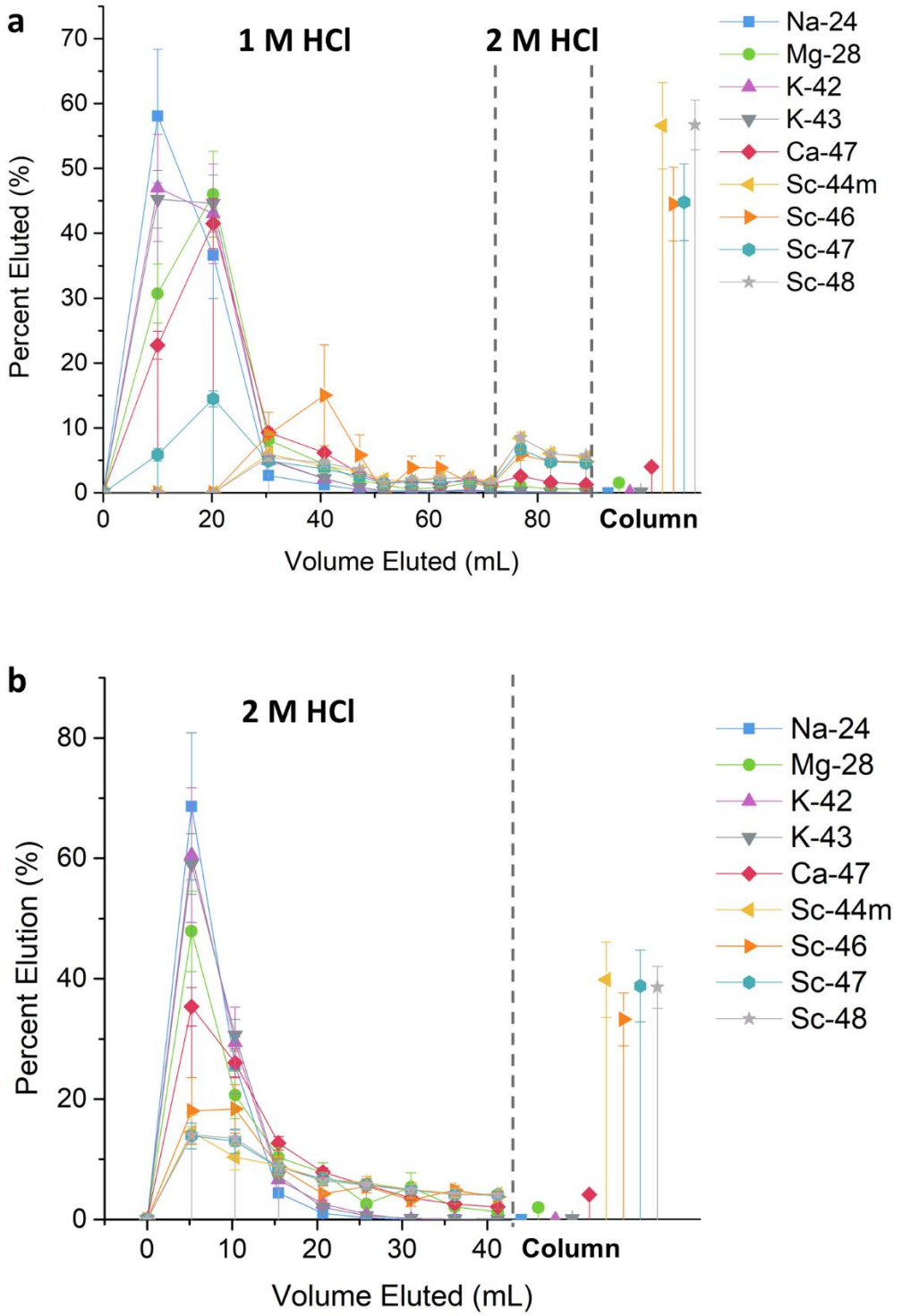

Figure 6.7: Collection Resin Bed Elution Profiles
Elution profile for the first (a) and second (b) cation exchange resin beds used for collection of ^{47}Ca.

The ^{47}Ca was effectively removed from the cation exchange resin beds for further processing using 1 or 2 M HCl. The elution profiles for all radionuclides on the cation exchange resin bed are given for these two elutions in Figure 6.7. For both elutions, Ca, Na, K, and Mg isotopes elute in a sharp peak at the beginning of the elution, with their peaks reaching a maximum value earlier and occurring in a smaller volume for the 2 M HCl elution as expected. 47 mL of 1 M HCl eluted 83(5)% of the ^{47}Ca on the first cation exchange resin bed used in the collection step. For the second collection cation exchange resin bed, 21 mL of 2 M HCl was used to elute 82(4)% of the ^{47}Ca adsorbed to the resin. This earlier peaking in the elution curve results in a similar elution percentage in less than half the volume for the 2 M HCl. This would result in a smaller dilution factor to reach the same acidity level for the purification load solution using the 2 M HCl elution compared to the 1 M HCl elution.

All Sc isotopes elute to a much lower extent throughout the elution and 40 to 60% of the activities of these isotopes remain on the column after the elution. The Sc isotope elution curve with the most reliable trend for the 1 M HCl elution is ^{47}Sc as it is present on the column with the highest activity. The other Sc isotopes are present at a lower activity than other radionuclides in the elution fractions at the time that the measurements were made, making reliable measurements of the activities of the Sc isotopes difficult in the presence of the relatively large background created by other radionuclides. Since the elution of the second column was performed a few days after that of the first, the activity of ^{44m,46,48}Sc in each fraction and on the resin bed are more accurately measured with a significant decay of other shorter-lived radionuclides present on the resin bed. This can be clearly observed as the elution profiles of all Sc isotopes from the second cation exchange resin bed are almost

indistinguishable with in the error bars on the points. These profiles also are similar in character to that observed for ^{47}Sc from the first resin bed.

6.3.3 Purification of ^{47}Ca

The AG MP-50/HCl method was successfully repeated three times with the eluate from the first collection resin bed used. HPGe gamma-ray measurements of each fraction for one of these replicates were used to produce the elution curve in Figure 6.8. These separations demonstrated the reproducibility and efficacy of this purification method with an average separation yield of 97.5(3)% at a radionuclidic purity of 99.8(4)% immediately following the separation. During the time that ^{47}Sc was generated after this purification step, the main impurities in the ^{47}Ca samples (i.e., ^{42,43}K) had decayed significantly, resulting in a radionuclidic purity of 100.0(4)% at the time that the generated ^{47}Sc was separated from its parent.

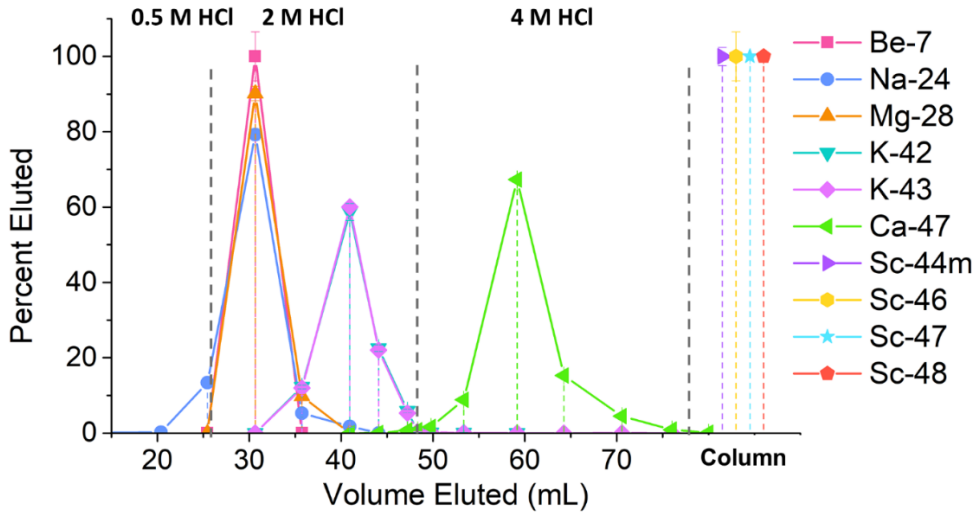

Figure 6.8: Elution Profile for Purification of ^{47}Ca

6.3.4 Generation of ^{47}Sc

The separation yields from DGA 1, DGA 2, and the complete pseudo generator procedure for each replicate of the generator procedure are given in Table 6.3. The separation yield from DGA 1 is high at >97% of the ^{47}Sc in the 7 mL elution step except for that for generator 4 (discussed below). The yield is lower for DGA 2 due to the limited volume required for radiolabeling to maximize the interactions between ^{47}Sc and DTPA-TOC. This separation yield was found only for the activity eluted in the 700 µL ^{47}Sc fraction from DGA 2, which is shown as the highlighted portion of the elution profile in Figure 6.9. The total separation yield was ≥75% for all cases except for generator 4, meaning that ≥75% of the ^{47}Sc in the generator solution was purified in the final 700 µL sample. This process also significantly concentrated the ^{47}Sc activity from the generator solution which contained about 20 mL for generator 1 to 3, 50 mL for generator 4, 150 mL for generator 5, and 160 mL for generator 6.

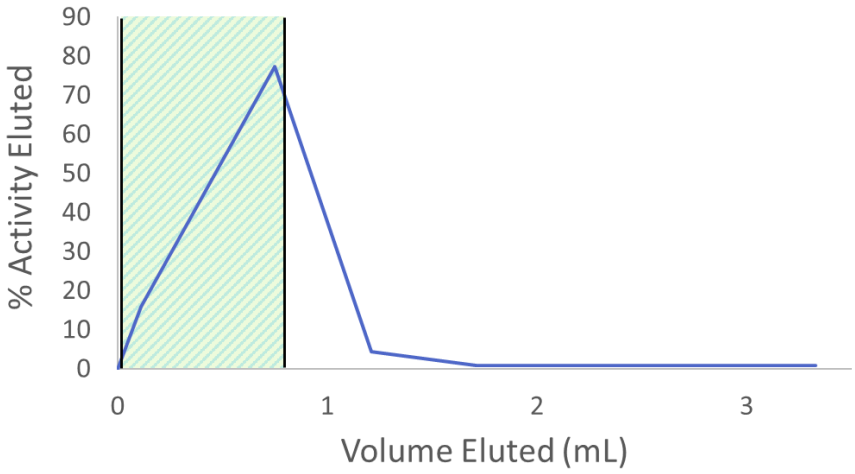

Figure 6.9: Elution Profile of ^{47}Sc from DGA 2
The approximate region of activity collected in about 700 µL is shown in the shaded portion of the graph.

Table 6.3: Generator 1 to 6 Results
The activities of ^{47}Ca and ^{47}Sc in the generator were measured before the start of the pseudo generator process. All activities used to calculate the separation yields were decay corrected to the end of the generator procedure.

Generator #	Activity of ^{47}Ca (MBq)	Activity of ^{47}Sc (MBq)	Separation Yield from DGA 1 (%)	Separation Yield from DGA 2 (%)	Total Separation Yield (%)
1	4.12(1)	2.10(2)	99(1)	95.3(1)	94.5(2)
2	3.40(2)	2.38(2)	97.7(7)	84.5(2)	82.5(3)
3	3.32(1)	2.31(2)	98(1)	76.0(9)	75(1)
4	3.18(1)	3.34(3)	94(1)	38.6(4)	35.4(6)
5	4.98(8)	4.95(4)	99(1)	79.3(9)	78(1)
6	2.03(4)	1.66(1)	98(1)	91(1)	89(1)

The radionuclidic purity of the final 700 µL ^{47}Sc fraction was determined to be quite high for all generators except for generator 4 with no activity other than ^{47}Sc being detected in the gamma-ray spectra taken right after the generator procedure and about one month later. The limit of detection for ^{46}Sc in the spectra from one month after the generator procedure was found for all generators except generator 4 and used to find a lower limit on the radiopurity of the ^{47}Sc radiolabeling solutions. This limit for the activity of ^{46}Sc and the radionuclidic purity of ^{47}Sc are both given in Table 6.4 for each radiolabeling solution.

Generator 4 purified the fourth fraction from collection resin bed 1 that was not purified using the AG MP-50/HCl method. This fraction contained about 25 mL of 0.5 M HCl and the mixture of radionuclides that eluted from the collection cation exchange resin bed: ^{7}Be, ^{24}Na, ^{28}Mg, ^{43}K, ^{47}Ca, $^{44m, 46,47,48}$Sc. This fraction was purified using the pseudo generator solution to demonstrate that all non-scandium radionuclides left in the sample have the same elution behavior as ^{47}Ca. Even with these radionuclides present, they do not interfere with the

purification of ^{47}Sc through the pseudo generator as shown in Figure 6.10. The generated ^{47}Sc isolated in this example was accompanied by the all the sufficiently long-lived scandium isotopes produced in the fragmentation reactions in the isotope harvesting target. As these scandium isotopes were produced in a water medium and circulated in the system in a near neutral pH, they were most likely hydrolyzed to a oxide form with low solubility (*e.g.* $HScO_2$ or Sc_2O_3) and filtered out of the water on the glass wool in the cation exchange resin bed. Therefore, the scandium species present in this separation scheme were not all Sc^{3+} in solution. This led to unpredicted elution behavior and the poor yields shown in Table 6.3.

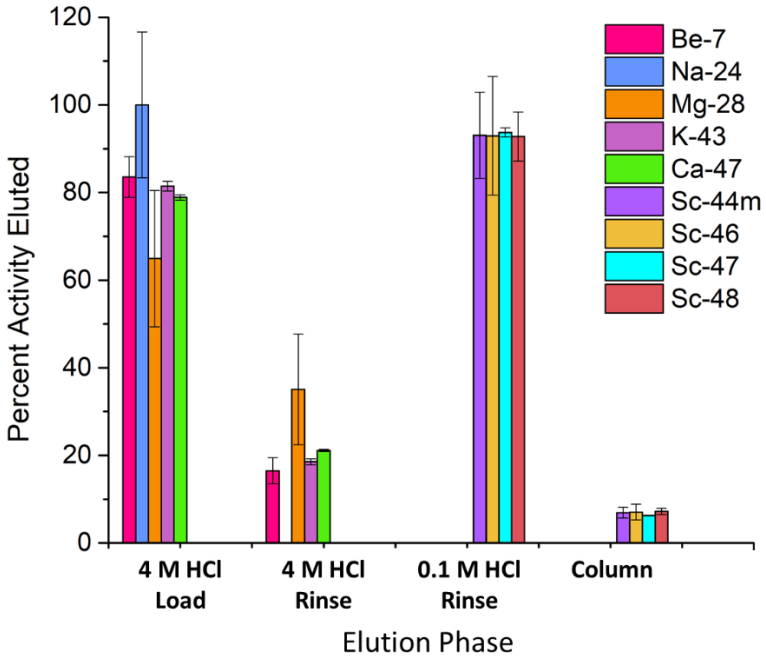

Figure 6.10: Elution from DGA 1 in Generator 4
The x-axis gives the phase of the separation while the y-axis gives the percent of each radionuclide that had eluted. The graph demonstrates that ^{7}Be, ^{24}Na, ^{28}Mg, ^{43}K, and ^{47}Ca elute with almost identical profiles, leaving only the scandium isotopes in the final eluted solution for concentration with DGA 2.

Using the elution behavior shown with generator 4, an alternative purification procedure can be proposed. To remove the scandium isotopes initially, DGA 1 from the pseudo generator procedure could be used as a purification step after elution of the radionuclides from the collection column. As demonstrated by the elution profile in Figure 6.10, this step would leave isotopes of Be, Na, Mg, K, and Ca in the generator solution while removing all scandium isotopes. This semi-purified generator solution would be sufficiently prepared to produce a sample of generated ^{47}Sc with high radionuclidic purity after a wait period of 3 to 5 days and using the pseudo generator procedure. A further discussion of the merits and flaws of this separation procedure is given in Chapter 9.

6.3.5 Radiolabeling DTPA-TOC with ^{47}Sc

The details for each radiolabeling solution checked with the TLC quality control are listed in Table 6.4. Modest specific activities of 0.3-3 MBq of ^{47}Sc/nmol of DTPA-TOC were attempted since the level of ^{47}Sc activity available was low. The TLC quality control results for

Table 6.4: Radiolabeling Results

Solution	Generator Number	Activity of ^{47}Sc (MBq)	Activity of ^{46}Sc (Bq)	Radio-nuclidic Purity (%)	Specific Activity (MBq/nmol)	Percent ^{47}Sc Radiolabeled	Percent ^{47}Sc Free
1	1	0.640(5)	<104	>99.9826	1.28(1)	11	89
1	1	0.636(5)			0.318(2)	88	12
2	2	1.74(1)	<102	>99.9936	1.34(1)	26	74
2	2	1.65(1)			0.895(7)	38	62
3	3	1.33(1)	<92	>99.9912	1.02(1)	43	57
3	3	1.09(1)			0.418(4)	35	65
4	5	3.60(3)	<127	>99.9990	3.00(2)	0	100
4	5	3.29(3)			1.03(8)	0	100
5	6	1.36(1)	<102	>99.9931	1.14(1)	100	0

radiolabeling solutions 1-3 (from generators 1-3, respectively) demonstrate that a low level of radiolabeling occurred. Specifically, the 10 to 40% of ^{47}Sc that successfully radiolabeled is not high enough to be considered successful and indicates that there is a metal contaminant interfering with the chelation between ^{47}Sc and DTPA-TOC. Radiolabeling solution 4 resulted from combining the generator solutions produced from generator 1-4 and running the generator procedure a fifth time (generator 5). No matter the level of DTPA-TOC used, no radiolabeling was observed with this solution. Again, this result indicates that there was a metallic contaminant in the radiolabeling solution that limited the success of the radiolabeling. Since the generator solution resulting from generator 4 was not purified with the AG MP-50/HCl purification step, it is possible the a higher amount of a metallic ion remained in the generator solution even after processing it with the pseudo generator procedure. The addition of this generator solution most likely introduced enough of this contaminant to drop the radiolabeling success rate from the low level observed with radiolabeling solutions 1-3 to 0% with the combined solutions.

The only notable change that occurred between generator 5 and 6 (producing radiolabeling solutions 4 and 5, respectively) was the addition of the 3 M HNO_3 rinse step in the generator procedure. With this change, the radiolabeling yield increased dramatically to essentially 100%. Since the 3 M HNO_3 rinse step was designed to remove metallic impurities such as Fe, this strongly indicates that a small amount of ionic impurity in the generator solution was concentrated in the radiolabeling solution and interfered with previous radiolabeling attempts. An example phosphor image from the TLC quality control tests for radiolabeling solutions 3, 5, and 6 are shown in Figure 6.11. In the first image, the single spot in

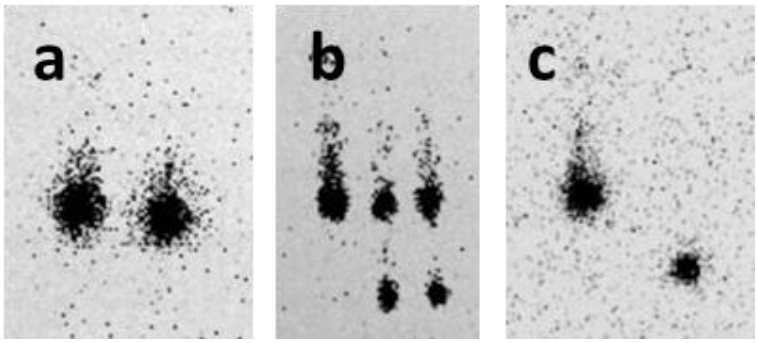

Figure 6.11: Phosphor Images for Thin Layer Chromatography Quality Control Tests
Phosphor image for TLC from (a) radiolabeling solution 4 with no radiolabeling (*i.e.*, 0% yield), (b) radiolabeling solution 3 with partial radiolabeling for both specific activities used (*i.e.*, 43% yield for 1 MBq/nmol in the middle lane and 35% yield for 0.4 MBq/nmol in the right most lane), (c) and radiolabeling solution 5 with complete radiolabeling (*i.e.*, 100% yield). In all three images, the leftmost spot is the control spot of [^{47}Sc]Sc-DTPA at an R_f value of about 0.5.

the radiolabeling solution test lane (right) at the same R_f value as the control [^{47}Sc]Sc-DTPA solution (left) indicates no radiolabeling occurred in radiolabeling solution 4. The spots at the origin and at about R_f = 0.5 for radiolabeling solution 3 at both specific activities used (middle and right lane) demonstrates the partial radiolabeling, while the single spot at the origin for radiolabeling solution 6 shows complete radiolabeling.

6.3.6 Stable Elemental Analysis

The results of the stable elemental analysis on the eluted fractions from the cation exchange resin beds are given in Tables 6.5 and 6.6. The stable ions in these fractions demonstrate that mg quantities of Al and Mn, hundreds of μg of Ca and Ni, and lower levels of Co, Cr, Cu, Fe, Mg, and Zn were present in the water system and collected on the cation exchange resins during the course of this irradiation. Additionally, Si was identified in these samples. Due to non-linear responses from Si at this concentration range, a quantification of this element was not made. It is likely that this ion content resulted from stainless steel (*e.g.*,

Fe, Cr, Mn, Ni, Si) and aluminum alloy (*e.g.*, common aluminum which is 3003 aluminum alloy contains Al, Mn, Fe, Si, Cu, Zn in decreasing mass percent) components in the system that were in contact with the water.

The samples tested from the purification of ^{47}Ca and ^{47}Sc are given in Table 6.7. After the collected radionuclides were eluted from the first cation exchange resin bed, the solution was diluted and separated into four equal volume fractions as explained in Section 6.2.5. The stable content of these fractions is shown in Table 6.7 grouped as "^{47}Ca Purification". Fractions 1 to 3 which were purified through the AG MP50/HCl method have very low stable ion masses except for Ca^{2+}. Fraction 4 which was not purified after elution from the cation exchange resin bed contains significant levels of several elements, especially Al, Mn, and Ni. This comparison demonstrates the ability of the AG MP-50/HCl purification method to remove stable impurities from the final purified ^{47}Ca product. It is also clear that the DGA resin step used from the first fraction from the cation exchange resin bed is not needed since the AG MP-50/HCl method provides sufficient purification and there is not significant difference between the ICP-OES results for Fraction 1 before and after the DGA resin step.

Since the generator solutions resulting from all four fractions of purified ^{47}Ca (*i.e.*, Generator solution 1-4) were combined after each fraction was processed with the generator procedure once, the total stable content of Fractions 1-4 are essentially equal to that measured in Generator solution 7. Characterization of this generator solution demonstrates that the presence of significant levels of Al, Co, Cu, Mg, Mn, and Ni did not interfere with radiolabeling since they pass through DGA 1 into the new generator solution with Ca. Notably, the Cr, Fe, and Zn content in the unpurified Fraction 4 are absent from Generator solution 7. Since no

significant stable ion content was observed in the 3 M HNO_3 rinse step added to Generator 6 (shown as Generator 6 DGA 2 Fr 2 in Table 6.6), it is most likely that the Cr, Fe, and Zn content were removed from the generator solution when generator #4 or 5 were performed. These stable ions eluting with the ^{47}Sc fraction in Generator 5 would explain why the radiolabeling solution from Generator 5 resulted in a radiolabeling yield of 0%. With these ions removed from the generator solution, the radiolabeling solution produced with Generator 6 would have contained lower levels of competing ions, resulting in a 100% radiolabeling yield. Potentially, if the 3 M HNO_3 rinse is used from the first generator purification, interfering ions such as Cr, Fe, and Zn could be removed from the generated ^{47}Sc.

Table 6.5: ICP-OES Analysis of Eluate from Cation Exchange Resin Bed 1

Fractions 6-13 from the elution of the first cation exchange resin bed were analyzed with ICP-OES. These were the fractions that were not used for the next purification step.

Collection	Fraction	Mass (µg)									
		Al	**Ca**	**Co**	**Cr**	**Cu**	**Fe**	**Mg**	**Mn**	**Ni**	**Zn**
Cation Exchange Resin Bed 1	Fr 6 1 M HCl	170(20)	22(2)	1.6(2)	0.60(5)	10(1)	2.4(2)	1.5(1)	260(20)	100(10)	2.3(2)
	Fr 7 1 M HCl	180(20)	24(2)		0.68(6)	7.4(8)	2.2(2)	1.7(1)	270(20)	100(10)	2.1(2)
	Fr 8 1 M HCl	160(20)	20(2)		0.52(5)	5.9(6)	2.0(2)	1.2(1)	200(10)	76(9)	1.7(1)
	Fr 9 1 M HCl	230(30)	30(2)	2.4(2)	0.99(9)	13(1)	4.4(3)	3.3(2)	390(30)	150(20)	3.7(3)
	Fr 10 1 M HCl	130(20)	19(2)	1.2(1)	0.51(4)	6.1(6)	2.3(2)	1.9(1)	200(10)	73(9)	1.9(2)
	Fr 11 2 M HCl	370(20)	34(3)	0.81(3)	1.6(2)	9.0(6)	4.6(4)	2.8(2)	250(20)	96(7)	2.5(2)
	Fr 12 2 M HCl	250(20)	23(2)		1.1(1)	5.5(4)	3.1(3)	1.8(1)	150(10)	63(5)	1.5(1)
	Fr 13 2 M HCl	230(10)	17(2)		0.92(9)	3.7(3)	2.5(2)	1.4(1)	120(10)	43(3)	0.98(9)
	Total:	**$1.7(1) \times 10^3$**	**200(10)**	**6.0(6)**	**7.0(4)**	**60(4)**	**23(1)**	**15.7(7)**	**$1.83(9) \times 10^3$**	**700(60)**	**17(1)**

Table 6.6: ICP-OES Analysis of Eluate from Cation Exchange Resin Bed 2

The second cation exchange resin bed was eluted in eight 5 mL fractions of 2 M HCl.

Collection	Fraction	Mass (μg)									
		Al	**Ca**	**Co**	**Cr**	**Cu**	**Fe**	**Mg**	**Mn**	**Ni**	**Zn**
Cation Exchange Resin Bed 2	Fr 1	2.6×10^3	150(10)	70(8)	9.2(9)	180(10)	27(2)	38	$2.3(2) \times 10^3$	$2.4(2) \times 10^3$	45(4)
	Fr 2	2.0×10^3	110(10)		6.5(7)	103(7)	18(2)	22(2)	$1.4(1) \times 10^3$	$1.4(1) \times 10^3$	27(2)
	Fr 3	910	56(5)	18(2)	3.5(4)	40(3)	8.4(7)	9.5(9)	610(50)	570(40)	9.8(9)
	Fr 4	640	38(4)	11(1)	2.3(2)	20(1)	5.5(5)	5.8(5)	380(30)	340(30)	5.1(5)
	Fr 5	520	25(2)	6.9(8)	1.7(2)	11.6(8)	4.3(4)	3.8(3)	270(20)	220(60)	3.1(3)
	Fr 6	380	18(2)	4.3(5)	1.3(1)	6.6(5)	2.9(2)	2.6(2)	180(10)	140(10)	1.8(2)
	Fr 7	280	12(1)	2.8(3)	1.0(1)	3.9(3)	2.4(2)	1.5(1)	116(9)	88(6)	1.2(1)
	Fr 8	280	9.9(9)	2.5(3)	1.2(1)	3.3(2)	2.6(2)	1.5(1)	106(8)	80(6)	1.2(1)
	Total:	**$7.6(2) \times 10^3$**	**200(10)**	**6.0(6)**	**7.0(4)**	**60(4)**	**23(1)**	**15.7(7)**	**$1.83(9) \times 10^3$**	**700(60)**	**17(1)**

Table 6.7: ICP-OES Analysis of Samples from the Purification of ^{47}Ca and ^{47}Sc

The first 25 mL of 1 M HCl used to elute ^{47}Ca from the first cation exchange resin bed were diluted to 100 mL of 0.5 M HCl. This solution was divided into four fractions described in the table as Fr 1-4. The results from fraction 1 are given as both "before" and "after" meaning before and after the fraction was passed through a 1.5 g DGA resin, respectively. Fractions 2 and 3 are labeled as "purified" since they were purified with the AG MP-50/HCl method and fraction 4 as "not purified" since it was not processed after the dilution step. The total mass for each element across Fr 1 after, Fr 2 purified, Fr 3 purified, and Fr 4 not purified is given at the bottom row of the table.

Sample		**Mass (μg)**									
		Al	**Ca**	**Co**	**Cr**	**Cu**	**Fe**	**Mg**	**Mn**	**Ni**	**Zn**
Generator 6 DGA 2											
Generator 7		1.0(1) x 10^3	790(50)	24(2)		150(10)		31(2)	3.0(2) X 10^3	1.28(8) X 10^3	
^{47}Ca Purification	Fr 1 before		220(10)					2.0(1)	4.5(3)		
	Fr 1 after		210(10)					3.7(2)	4.3(3)		
	Fr 2 purified		210(10)		0.26(2)			0.74(4)	4.8(3)		
	Fr 3 purified		200(10)					0.44(2)	3.3(2)		
	Fr 4 not purified	1.0(1) x 10^3	210(10)	28(2)	5.6(4)	170(10)	20(2)	25(2)	3.0(2) x 10^3	1.36(8) x 10^3	46(3)
	Total	**1.0(1) x 10^3**	**830(30)**	**28(2)**	**5.8(4)**	**170(10)**	**20(2)**	**29(2)**	**3.0(2) x 10^3**	**1.36(8) x 10^3**	**46(3)**

6.4 Conclusion

An irradiation of the isotope harvesting system with a 140 MeV/nucleon 80 pnA ^{48}Ca beam was performed, producing approximately 1.8 mCi of ^{47}Ca. The ^{47}Ca activity was effectively collected from the 50 L water system and purified through an AG MP-50/HCl gradient separation method. Stable elemental analysis demonstrated that significant levels of several elements such as Al, Mn, Ca, and Ni were present in the water and collected on the cation exchange resin bed. A majority of the stable ions were removed from the purified ^{47}Ca through the AG MP-50/HCl method. The purified ^{47}Ca was used as a generator solution for the generation of ^{47}Sc. Repeated use of the generator procedure likely resulted in the removal of low levels of Cr, Fe, and Zn which may have interfered with radiolabeling. The pseudo generator procedure presented previously was used with this isotope harvested sample of ^{47}Ca/^{47}Sc to produce concentrated samples of ^{47}Sc with radionuclidic purities of >99.99%. These samples were used to troubleshoot the generator and radiolabeling procedures to radiolabel DTPA-TOC with a radiochemical yield of 100%.

The experiment described here allowed for testing and optimizing each step in the process of isotope harvesting from producing ^{47}Ca in the isotope harvesting system to using purified ^{47}Sc generated from ^{47}Ca for radiolabeling experiments. The high quality [^{47}Sc]Sc-DTPA-TOC produced with the harvested sample of ^{47}Ca demonstrated the feasibility of using radionuclides produced through isotope harvesting for nuclear medicine research. The procedures demonstrated with a low-level activity sample of ^{47}Ca in this experiment can be applied to experiments with higher integrated beam currents, producing a higher activity sample of ^{47}Ca.

Chapter 7: ^{48}Ca Beam Experiment 3: High Activity ^{47}Ca/^{47}Sc Generator and ^{47}Sc Radiolabeling with Isotope Harvested ^{47}Ca

A full power ^{48}Ca beam experiment was performed at the NSCL with the isotope harvesting target in the beam blocker position. This experiment produced approximately 10 mCi of ^{47}Ca that was effectively collected from the 50 L water system. This radionuclide was purified with an AGMP-50/HCl gradient purification method to produce a ^{47}Ca/^{47}Sc generator with high radionuclidic purity. The generated ^{47}Sc was purified in three successive replicates and was used to radiolabel DTPA-TOC with a preclinically useful specific activity of 6 MBq/nmol.

7.1 Introduction

Following the optimization of procedures for the purification of generated ^{47}Sc and radiolabeling DTPA-TOC with ^{47}Sc described in Chapter 6, another higher integrated beam power ^{48}Ca irradiation was performed at the NSCL. The irradiation produced approximately 10 mCi of ^{47}Ca which was used to produce a ^{47}Ca/^{47}Sc generator. The purification of ^{47}Sc from the generator for use in radiolabeling experiments was performed three times in succession to demonstrate the reproducibility of producing [^{47}Sc]Sc-DTPA-TOC. This experiment was designed to produce a high quality [^{47}Sc]Sc-DTPA-TOC product at a high enough activity to use in preclinical targeted internal radiotherapy studies. Additionally, this study demonstrated the feasibility of using isotope harvesting as a production technique for radionuclides with medical applications.

7.2 Materials and Methods

7.2.1 Materials

The materials and instruments used in this experiment are described in Chapter 6 Section 6.2.1.

7.2.2 ^{48}Ca Irradiation

The present experiment started with a 2-hour irradiation segment at 60 pnA beam as a warm-up period to monitor operations of the system under irradiation and then ran at 80 pnA for 7.7 hours. Thus, the experiment extended over 11.7 hours with a total integrated beam intensity of 703 pnA-h. There were no intentional interruptions of the irradiation of the target. The gaps in the beam current shown in Figure 7.1 were necessary for beam tuning before increasing the beam intensity to 80 pnA and due to issues with the accelerated beam upstream of the target.

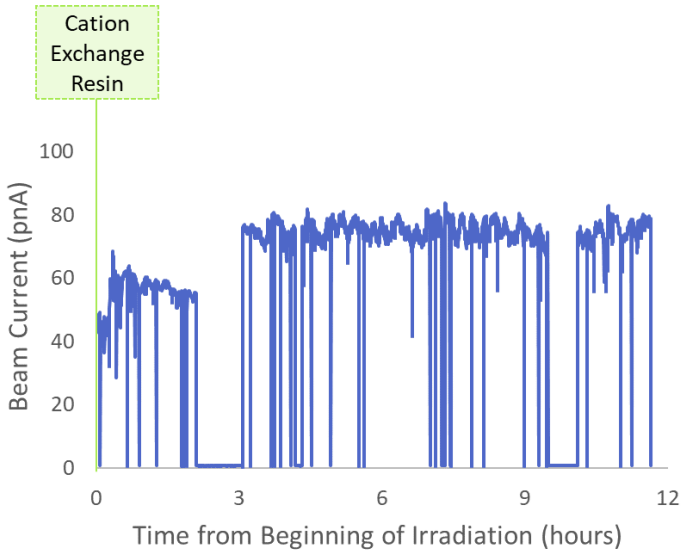

Figure 7.1: Experimental Beam Structure
The green vertical line labeled “cation exchange resin” indicates that a cation exchange resin was in place at the start of the irradiation. This resin bed collected almost all of the activity and was removed for processing 24 hours after the end of the irradiation.

7.2.3 Collection of ^{47}Ca from Isotope Harvesting System

A single cation exchange resin bed was used throughout the nearly 12-hour irradiation and for 24 hours after the irradiation to collect as much ^{47}Ca activity as possible in one batch on the resin bed. The water flow rate over the resin bed for collection was higher than that used in the previous experiment (see Chapter 6 Section 6.2.4) at 570 mL/min. A second resin bed was used to collect the remainder of the activity following the removal of the first resin bed. Based on the collection resin bed elution results from the previous experiment, the first cation exchange resin bed used in this experiment was rinsed with 25 mL of 2 M HCl and the eluent collected in a single fraction.

Both the collection efficiency of ^{47}Ca from the system water and the elution efficiency of ^{47}Ca from the cation exchange resin bed were measured by gamma-ray spectroscopy of the two resin beds and the eluted fraction. Measurements of the activity on the first cation exchange resin bed were made post-elution on the same day and several days after the elution due to the high activity of the scandium isotopes which in large part remained on the resin. The activity in the eluted fraction was estimated by measuring the activity in a 0.1 mL aliquot which had a low enough activity to be quantified at a reasonable distance from the detector face. An elution efficiency was calculated by comparing the activity measured in the eluted fraction to the total activity in the eluted fraction and remaining on the resin bed. To find the collection efficiency of the system a separate measurement of the second cation exchange resin bed was made. Based on the 100% collection efficiencies reported in the previous experiment (Chapter 6 Section 6.3.3) and an identical collection protocol used in the present experiment, a 100% collection efficiency between these two resin beds was assumed. The collection efficiency for only the

first cation exchange resin bed was found based on this assumed total collection efficiency and the gamma-ray spectroscopy measurements of the eluted fraction, the first cation exchange resin bed post-elution, and the second cation exchange resin bed.

7.2.4 Purification of ^{47}Ca

The AG MP-50/HCl separation procedure for the purification of ^{47}Ca from Chapter 6 Section 6.2.5 was slightly adapted for this experiment. Instead of performing replicate purifications with the collection resin bed eluate, the entire acid rinse from this resin bed was purified in a single batch. To accommodate this change and avoid the evaporation step, a dilution of the collection resin bed eluate was performed to reduce the acidity and prepare an appropriate load solution for the purification.

Multiple load solution dilution conditions were tested with stable K^+ and Ca^{2+} ions: 500 mL of 0.1 M HCl, 250 mL of 0.2 M HCl, and 167 mL of 0.3 M HCl. Each of these stable-ion load solutions was followed by a small rinse solution used to rinse the load phase container, the tubing, and the column (20 mL of 0.1 M HCl, 5 mL of 0.2 M HCl, and 5 mL of 0.3 M HCl, respectively). The 250 mL 0.2 M HCl load solution was also used with either a 40 or 100 mL 0.2 M HCl rinse solution following the load step. These larger 0.2 M HCl rinse steps were used when testing the separation to capitalize on the difference between the distribution coefficient for K^+ and Ca^{2+} on AG MP-50. Since 0.2 M HCl was high enough acidity to decrease the distribution coefficient for K^+ (K_d = 165) while that for Ca^{2+} remains high (K_d = 3.7 x 10^3). [80]

The final purification procedure used in this experiment was based on these stable element tests and previous results presented in Chapter 4 Section 4.3.3 and Chapter 6 Section

6.3.3. The 25 mL of 2 M HCl used to elute ^{47}Ca from the collection resin bed was diluted to 250 mL 0.2 M HCl. An additional 40 mL of 0.2 M HCl was used as the first rinse step followed by a 26 mL 2 M HCl rinse. The final elution of ^{47}Ca was performed with 32 mL of 4 M HCl.

7.2.5 Generation of ^{47}Sc

The purification of ^{47}Sc from the ^{47}Ca/^{47}Sc generator was performed in a similar manner to that described in Chapter 6 Section 6.2.6. Figure 7.2 lays out the steps in this purification method. The main difference between the present method and the method used for the final generator solution in the previous irradiation (Generator 6 in Chapter 5) is the timing of the 3 M HNO_3 rinse step in the process. This rinse step was used following the 4 M HCl load phase on the first DGA resin rather than following the 3 M HCl load phase for DGA 2 as done in the previous experiment. Since the first DGA resin is about 3 times larger in mass than DGA 2 and the volume used to elute ^{47}Sc from DGA 1 is less critical than that used for DGA 2, this change allowed for a higher rinse volume with a higher flow rate. The large volume of 30 mL of 3 M HNO_3 was used to ensure the removal of any stable Fe from the column, particularly because the mass of Fe present in the system was not known when this decision was made during the experiment. Following this rinse, a 4 M HCl rinse of 10 mL was used to change the acid matrix in the column back to HCl before the elution of ^{47}Sc. These rinse phases were carried out at 1.2 mL/min as with the other rinse steps for DGA 1. All other rinse steps, flow rates, and fraction collections were carried out as described in Chapter 6 Section 6.2.6.

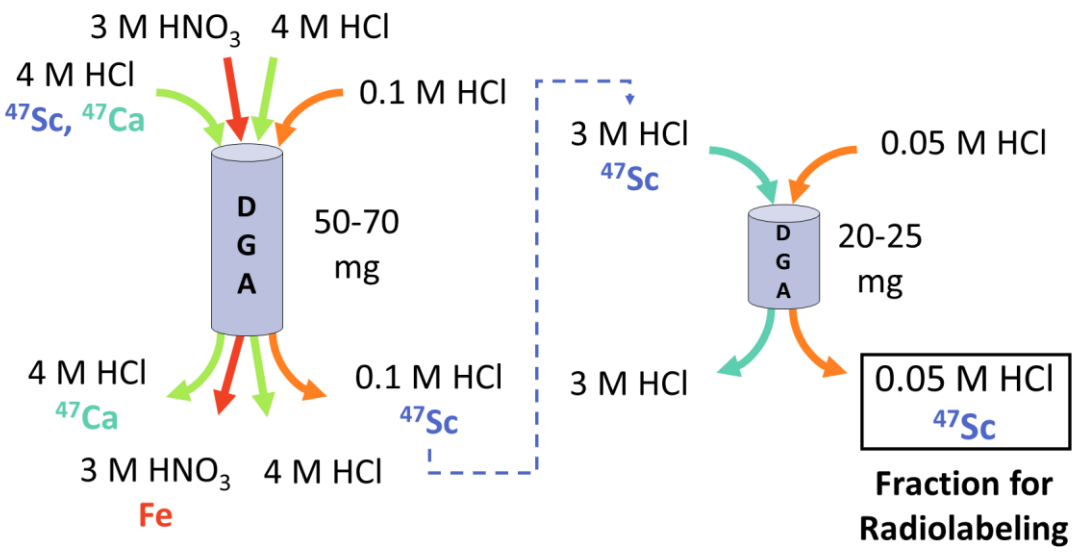

Figure 7.2: Schematic Description of the ^{47}Ca/^{47}Sc Generator Procedure

7.2.6 Radiolabeling DTPA-TOC with ^{47}Sc

The second ^{47}Sc fraction taken from DGA 2 in the generator procedure was the radiolabeling solution. This solution was prepared as described in Chapter 6 Section 6.2.7 by using approximately 50 µL of this fraction for pH adjustment tests, adding the proper ratio of sodium acetate buffer following these tests, adding DTPA-TOC to reach the desired specific activity, and heating the final solution to encourage interaction between ^{47}Sc and DTPA-TOC. Gamma-ray spectroscopy measurements were made of the radiolabeling solution before and after the 50 µL sample was removed. The ^{47}Sc solution to sodium acetate buffer ratios used for pH adjustment of radiolabeling solutions 1-3 were 4:1, 5:1, and 3:1, respectively. The activity of ^{47}Sc, volume of buffer, and nanomoles of DTPA-TOC used in each radiolabeling solution are given in Table 7.1. Each combination resulted in a specific activity just over 6 MBq/nmol.

Table 7.1: Radiolabeling Conditions

Radiolabeling Solution	Activity of ^{47}Sc (mCi)	Activity of ^{47}Sc (MBq)	Buffer Added (µL)	Peptide Added (nmol)	Specific Activity (MBq/nmol)
1	1.871(3)	69.2(1)	178	11.2	6.18(1)
2	1.033(2)	38.21(6)	139	6.0	6.41(1)
3	0.316(2)	11.70(7)	235	1.9	6.16(4)

To check the radiolabeling yield, thin layer chromatography using a sodium citrate mobile phase was carried out as described in Chapter 6 Section 6.2.7 and depicted in Figure 6.6. Due to the higher activity used in these radiolabeling experiments, a two-stage dilution was used to produce a lower activity solution necessary for phosphor imaging. In the first stage, a 9:1 water to ^{47}Sc solution ratio was used. The second step used a 50:1 dilution of water to ^{47}Sc solution. This final solution also contained about 30 nM of DTPA to chelate any free ^{47}Sc. Both the free ^{47}Sc solution (*i.e.*, the 50 uL of the second ^{47}Sc fraction from DGA 2) and the radiolabeling solution were used as the "^{47}Sc solution" in these dilutions. The TLC plates were exposed to the phosphor imaging films for five minutes, and then, the resulting images were analyzed with ImageQuant TL software as described in Chapter 6 Section 6.2.7.

7.2.7 Stable Elemental Analysis

ICP-OES analysis was performed on the 3 M HNO_3 rinse fractions used in the generator procedures, the final Generator 4 solution, and all unused fractions from the two AG MP-50/HCl separations. The unused samples for the separations included the 0.2 M HCl fractions from the first separation and the 0.2 M, 2 M, and last 4 M HCl fractions from the second separation. The same instrument and materials listed in Chapter 6 Section 6.2.1 and the same settings,

standards, calibrations, and uncertainty quantification described in Chapter 6 Section 6.2.8 were used in this analysis. All uncertainties for the observed elements were in the range of 6 to 15%.

7.3 Results and Discussion

7.3.1 Collection of ^{47}Ca from Isotope Harvesting System

Between the irradiation and the cool down period of 24 hours, 95(3)% of the 362(9) MBq of ^{47}Ca produced was removed from the water with a single 1.5 g cation exchange resin bed. After removal from the system, the resin bed was processed with 25 mL of 2 M HCl to elute 84(3)% of the collected ^{47}Ca. This higher acidity rinse was used in the elution from the collection resin bed, as less than half the volume is required to elute a similar percent when compared with 1 M HCl. This was demonstrated with a 1 M HCl elution from resin bed 1 and a 2 M HCl elution from resin bed 2 in the irradiation previously described in Chapter 6 Section 6.3.2.

Table 7.2: Stable K^+/Ca^{2+} Test Separations

Load Phase	Rinse	Separation Yield for Ca^{2+} (%)	Purity of Ca^{2+} (%)
500 mL 0.1 M HCl	20 mL 0.1 M HCl	97.5	99.9
250 mL of 0.2 M HCl	5 mL 0.2 M HCl	98.9	99.7
	40 mL 0.2 M HCl	99.1	99.9
	100 mL 0.2 M HCl	98.8	99.7
167 mL of 0.3 M HCl	5 mL 0.3 M HCl	96.2	99.8

7.3.2 Purification of ^{47}Ca

An AG MP-50/HCl purification procedure was carried out based on the three successful purification replicates from the previous experiment (Chapter 6, Section 6.3.3). The procedure was adjusted so that the entire eluate from the collection resin bed was diluted and purified in one batch to avoid an evaporation step. Separation tests with stable Ca^{2+} and K^{+} ions were performed to optimize the dilution factor used for the load phase. The various load solutions and resulting Ca^{2+} separation yields and purities for these test separations are given in Table 7.2. While all of the conditions tested resulted in high yields and purities for the Ca^{2+} fraction, the 250 mL 0.2 M HCl load solution with an additional 40 mL 0.2 M HCl rinse produced the best results. This load solution and rinse phase relied on the difference in distribution coefficients of Ca and K while controlling zone broadening of the ions on the column due to large volumes and thus minimized the overlap between the two elution peaks. The elution profile for the test separation under these conditions is shown in Figure 7.3.

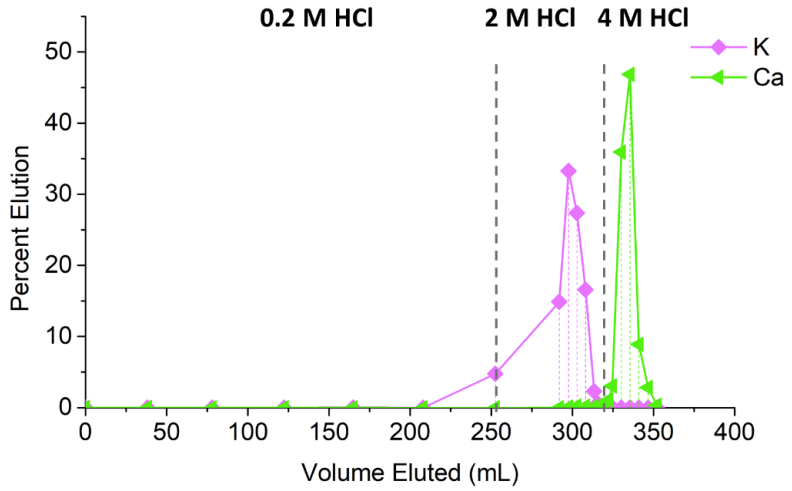

Figure 7.3: Stable Ca^{2+}/K^{+} Separation
This procedure used a 250 mL 0.2 M HCl load phase and a 40 mL 0.2 M HCl rinse phase followed by a 2 M HCl rinse and finally the 4 M HCl elution phase.

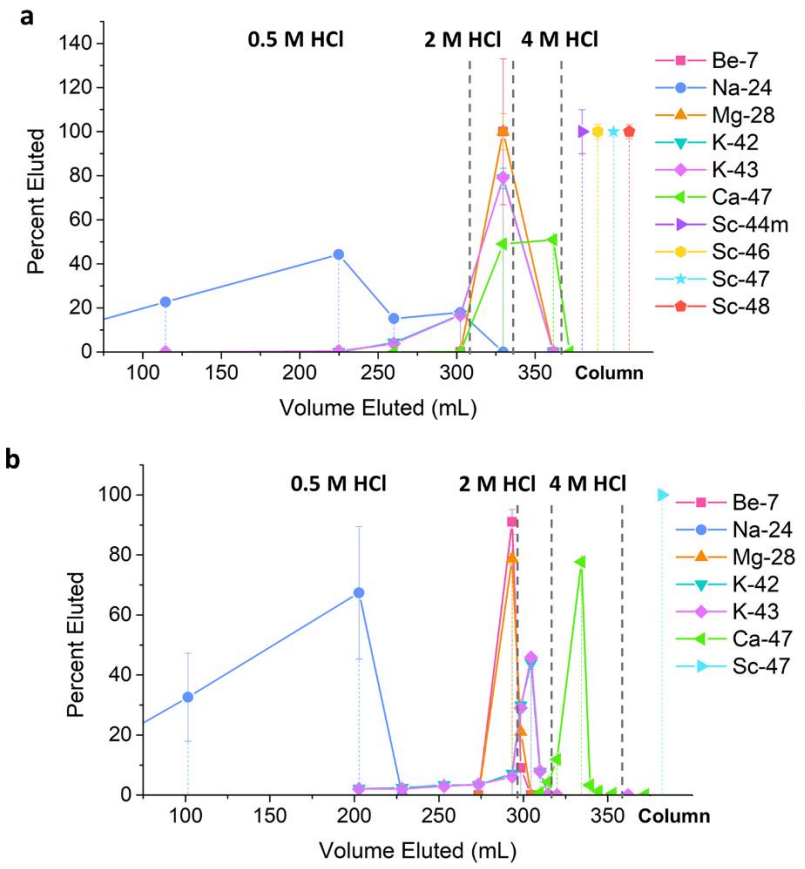

Figure 7.4: Separation Elution Profiles for AG MP-50/HCl Separations
The first (a) and second (b) ^{47}Ca purification from the present experiment. The dashed lines indicate a change in the mobile phase and the text above each section provides the mobile phase composition. The data points to the far right labeled "column" indicate the percent of each radionuclide that remained on the column through the entire separation. The uncertainties given in the data points represent the counting statistics.

The optimized 250 mL 0.2 M HCl load phase was used to purify ^{47}Ca produced in this irradiation. Unfortunately, the active ^{47}Ca produced during this experiment had a different elution profile from that for in the stable element separation tests with Ca and K as can be observed by comparing the elution profiles in Figure 7.3 and Figure 7.4a. The first separation performed with in the present experiment eluted 49.0(6)% of the ^{47}Ca in the 27.2 mL 2 M HCl

rinse step, while only 0.9% of the stable Ca was eluted in the 26 mL 2 M HCl rinse step in the separation procedure with stable ions shown in Figure 7.3. Additionally, the separation performed with stable ions showed that Ca continued to elute slowly in additional volumes of 2 M HCl with only 5.3% of the stable Ca eluted in 33 mL of 2 M HCl. Due to this shift in the elution profile, only 50.9(4)% of the ^{47}Ca in the load solution for this separation was purified with a radionuclidic purity of >99.9%.

A second separation was performed with the 2 M HCl rinse step solution that contained the remaining unpurified 49% of the ^{47}Ca. The elution profile in Figure 7.4b demonstrates a successful purification of ^{47}Ca was obtained with a 26.6 mL 2 M HCL rinse step. This separation resulted in a high separation yield of 99.1(7)% with 99.9(8)% radionuclidic purity. The two purified ^{47}Ca fractions from these separations were combined and resulted in a total separation yield of 97(1)% with a radionuclidic purity of 99.9(6)%. The total recovery yield from production to purification of ^{47}Ca was 78(3)% for this experiment.

7.3.3 Generation of ^{47}Sc

The ^{47}Sc activities as well as the separation yield for ^{47}Sc with DGA 1 and DGA 2 in the generator procedure are given in Table 7.3. The yields for ^{47}Sc from DGA 1 were relatively

Table 7.3: Generator 1-3 Results

Generator #	Activity of ^{47}Sc	Separation Yield from DGA 1 (%)	Separation Yield from DGA 2 (%)	Total Separation Yield (%)
1	2.76(2)	94.9(8)	72.4(1)	68.6(6)
2	1.36(1)	94.6(8)	87.1(5)	82.3(9)
3	0.661(5)	99.7(9)	53.2(5)	53.1(7)

consistent at about 95% or higher. For DGA 2, the yields for ^{47}Sc in fraction 2 were lower, as expected due to the limited volume collected in fraction 2. The elution profile for DGA 2 of generator 1 and 3 are shown in Figure 7.5. The profile is characterized by a sharp peak at low volumes followed by a tailing elution behavior for several milliliters. The separation yield for ^{47}Sc from DGA 2 was substantially lower for generator 3 of this experiment compared to the separation yield from DGA 2 found for either generator 1 or 2 from this irradiation or those presented in Chapter 6 Section 6.3.4. The low yield for the final generator in this experiment is possibly due to the use of a high molarity HCl load solution followed immediately by a low molarity HCl rinse to elute the ^{47}Sc from DGA 2. A high yield in a small volume low molarity HCl phase relies on the low distribution coefficient for Sc on DGA resin under these conditions. However, any residual acidity or droplets from the high molarity load solution can mix with the elution phase and raise the actual acidity of this phase as ^{47}Sc is eluted. It is likely that this contributed to the low yield for generator 3. This explanation is supported by the amount of

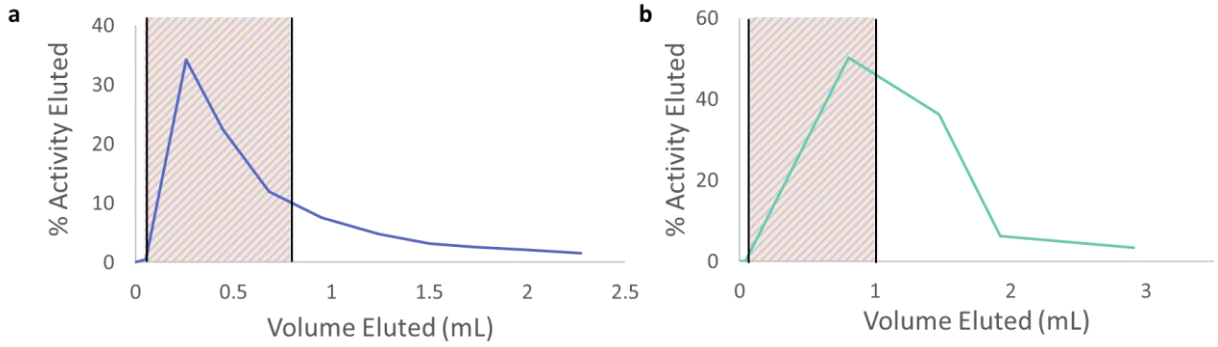

Figure 7.5: Elution Profile for DGA 2 in Generators 1 and 3
The dashed orange/blue area indicates 72.4% (a) and 53.1% (b) of the ^{47}Sc activity was collected in a fraction of about 700 µL in Generator 1 and 3, respectively. The lower yield for Generator 3 resulted from the wider elution peak than that from Generator 1.

Table 7.4: Radiolabeling Results

Radiolabeling Solution	Activity of ^{47}Sc (MBq)	Activity of ^{46}Sc (kBq)	Radionuclidic Purity	Percent ^{47}Sc Radiolabeled	Percent ^{47}Sc Free
1	69.2(1)	2.3(2)	>99.99	96.5	3.5
2	38.21(6)	< 0.5	>99.99	99.1	0.9
3	11.70(7)	< 0.3	>99.99	100	0

sodium acetate required to pH adjust the final radiolabeling solution. A higher ratio of ^{47}Sc solution to buffer (*i.e.*, a lower amount of buffer added) would indicate a lower molarity of HCl in the radiolabeling solution. This ratio was found to be roughly correlated with the ^{47}Sc separation yield for DGA 2 with ratios of 4:1, 5:1, and 3:1 used for generators 1, 2, and 3, respectively. Generator 3 in this experiment required the lowest ratio to reach a pH of 3 to 3.5 indicating that it contained the highest molarity of HCl.

7.3.4 Radiolabeling DTPA-TOC with ^{47}Sc

The radiolabeling solutions were analyzed with TLC to determine the radiochemical yield for [^{47}Sc]-Sc-DTPA-TOC and with gamma-ray spectroscopic measurements to determine the radionuclidic purity of the ^{47}Sc. Each of the radiolabeling experiments had a yield of >95% as shown in Table 7.4 and a specific activity of at least 6 MBq/nmol. The phosphor images of the TLC tests shown in Figure 7.6 demonstrate this high radiochemical yield. At the time of radiolabeling, only ^{47}Sc was observed through gamma-ray measurements. Additional measurements 5 months later allowed for quantification of an ^{46}Sc present in the radiolabeling solution. This radionuclide was found only in radiolabeling solution 1 at a low level as shown in Table 7.4. The limit of detection for this radionuclide by its characteristic gamma-ray energy of

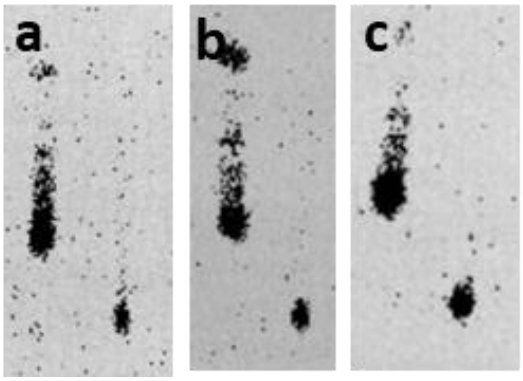

Figure 7.6: Phosphor Images of Thin Layer Chromatography Quality Control Tests
Phosphor images of radiolabeling solution 1-3 in a-c. the single spot in at the origin in the right lane for each TLC test indicates high radiolabeling yields for each solution.

889 keV are also given in Table 7.4 for radiolabeling solutions 2 and 3. The radionuclidic purity for each solution was at least 99.99% with only a low level of ^{46}Sc present in the first solution. The high radiochemical yield and radionuclidic purity as well as the moderate specific activity demonstrate that the final radiolabeled [^{47}Sc]-Sc-DTPA-TOC product was of sufficient quality for preclinical studies.

7.3.5 Stable Elemental Analysis

The results of the stable elemental analysis of several samples from this irradiation are given in Table 7.5. None of the 0.2 M HCl samples from both AG MP-50/HCl separations had significant concentrations of stable ions. The 2 M HCl fractions as well as the last 4 M HCl fraction from the second separation contained the masses shown in the lower half of Table 7.5. The 2 M HCl samples contained mg quantities of Al, Mn, and Ni as well as tens of µg quantities of Co, Cr, Cu, Fe, Mg, and Zn. The last 4 M HCl fraction was not used for the generation of ^{47}Sc due to a low concentration of ^{47}Ca. This sample with low levels of Ca, Mg, and Mn is

representative of the stable ion content of the 4 M HCl fractions that were used in the following chemistry steps. This can also be seen in the stable ion content of the Generator 4 solution with hundreds of μg of Ca and lower levels of Mg and Mn.

The 3 M HNO_3 rinse step used in Generators 1-3 are given in the upper half of Table 7.4. The rinse step for the first generator was measured twice and gave consistent but low-level readings for Fe, Mg, and Zn. These stable ions that were removed in this rinse step are similar to those that were removed through repeating the generator procedure in Chapter 6 Section 6.3.6. In both experiments, after the removal of these ions, a high radiolabeling yield was achieved. Therefore, future experiments should be designed to ensure the removal of Fe, Zn, and Cr from the $^{47}Ca/^{47}Sc$ generator.

Table 7.5: Stable Element Results from Generators 1-4 and AG MP-50 #2 Separation

Group	Fraction	Mass (μg)									
		Al	Ca	Co	Cr	Cu	Fe	Mg	Mn	Ni	Zn
Generator	#1 DGA 1 Fr 2 3 M HNO_3						1.6(2)	0.114(6)			3.7(7)
	#2 DGA 1 Fr 2 3 M HNO_3										
	#3 DGA 1 Fr 2 3 M HNO_3										
	#4 solution 4 M HCl		470(30)					11.2(7)	16(1)		
AG MP-50 #2	Fr 7 2 M HCl	1.5(1) x 10^3	0.35(3)	23(3)	2.2(2)	82(6)	67(6)	40(3)	2.4(2) x 10^3	1.24(9) x 10^3	45(4)
	Fr 8 2 M HCl	3.4(2) x 10^3	0.67(6)	9(1)	8.4(8)	21(1)	64(5)	12(1)	1.8(1) x 10^3	440(30)	6.2(6)
	Fr 9 2 M HCl	680(40)	2.3(2)		3.4(3)	0.57(4)	4.5(4)	0.46(4)	48(4)	12.1(9)	
	Fr 15 4 M HCl		1.8(1)					0.16(1)	0.31(1)		

7.4 Conclusion

The present experiment demonstrated the feasibility of isotope harvesting to produce ^{47}Sc-based radiopharmaceuticals for preclinical studies. An experiment was conducted with the flowing-water aqueous target as the A1900 beam blocker at the full NSCL ^{48}Ca beam power. The ^{47}Ca produced was efficiently collected on a single collection resin bed, eluted from this resin bed, and purified with an AG MP-50/HCl method. Evidence of stable ions was discovered through the unexpected elution behavior during the purification of ^{47}Ca. As a result, a large 3 M HNO_3 rinse step with the first DGA resin of the generator procedure was used to purify ^{47}Sc of metal impurities. ICP-OES measured significant levels of Al and Mn among several other lower level stable ions from the isotope harvesting water system. The 3 M HNO_3 rinse step used in the generator procedure was also shown to remove Fe and Zn which may be impurities that interfere with radiolabeling efficiencies. The generator procedure was used to produce a sample of high purity ^{47}Sc which was then used to radiolabel DTPA-TOC with a high radiochemical yield and at the preclinically relevant specific activity of 6 MBq/nmol. Thus, a series of procedures has been successfully optimized to produce high quality [^{47}Sc]-Sc-DTPA-TOC for further research.

Chapter 8: Measurement of the Three Most Intense Gamma Rays Following the Decay of ^{47}Ca

A sample of ^{47}Ca produced by isotope harvesting at the National Superconducting Cyclotron Laboratory was used to measure branching ratios of 7.17(5)%, 7.11(5)%, and 75.0(5)% for the 489.2, 807.9, and 1297.1 keV characteristic gamma rays, respectively, following the beta-decay of ^{47}Ca. Based on these updated branching ratios, the ground state to ground state ^{47}Ca to ^{47}Sc beta decay branching ratio was inferred to be 17.7(5)% and the ground state to 1297.1 keV excited state as 82.2(5)%. These values represent a greatly increased precision for all five branching ratios compared to the currently accepted values [51]*. The measurements presented here were made relative to the ingrown ^{47}Sc daughter in a ^{47}Ca sample and the well-established 159.4 keV gamma-ray branching ratio and the half-life of ^{47}Sc* [81–83]*. These measurements were supported by verifying that the half-lives measured with the characteristic gamma-ray peaks over multiple spectra for both ^{47}Ca and ^{47}Sc were consistent with previously reported values. Additionally, the half-lives of both ^{47}Ca and ^{47}Sc were independently measured with Liquid Scintillation Counting to re-verify the previously reported values used in this study to support the updated gamma-ray branching ratio values.*

8.1 Introduction

One way to produce high specific activity samples of ^{47}Sc is through the production and subsequent decay of its parent radionuclide, ^{47}Ca [10]. When producing and processing ^{47}Ca, the branching ratios of the most intense characteristic gamma rays are generally used to quantify ^{47}Ca with gamma-ray spectroscopy using High Purity Germanium (HPGe) detectors.

The present evaluated values for these gamma-ray branching ratios as well as the two main ^{47}Ca to ^{47}Sc beta decay branching ratios differ with a larger reported uncertainty from the only published measurements which were made in the 1960s [51,84]. For the quantification of ^{47}Ca, the present 19% uncertainty in the evaluated branching ratio of the 1297.1 keV gamma ray and the present 20% uncertainty for both the 489.2 and 807.9 keV gamma rays lead to similarly large uncertainties in the absolute activity of ^{47}Ca [51]. The change and uncertainty in these evaluated values prompted remeasurement of the three main gamma rays in the decay of ^{47}Ca to ^{47}Sc as part of the present work.

The branching ratios of the characteristic gamma rays in the decay of ^{47}Ca can be measured by using the parent-daughter relationship between ^{47}Ca and ^{47}Sc. In a sample of these radionuclides in which radioactive equilibrium has not yet been reached, the in-growth of ^{47}Sc relative to the decay of ^{47}Ca can be used to quantify the number of ^{47}Ca nuclei present and thereby, measure the branching ratios of characteristic gamma rays of ^{47}Ca decay. These updated gamma-ray branching ratio values allow for a more precise value to be found for the ground state to ground state beta decay branch and for the ground state to 1297 keV excited state beta branch in ^{47}Sc.

In this work, the branching ratios for the three most intense characteristic gamma rays in the decay of ^{47}Ca were remeasured and used to find updated values for the two main ^{47}Ca beta decay branching ratios. All branching ratio values reported here have an increased precision compared to the currently accepted values. Additionally, the half-lives of ^{47}Ca and ^{47}Sc have been remeasured using both HPGe gamma- ray spectroscopy and Liquid Scintillation Counting (LSC) and have been found to agree with those previously reported.

8.2 Methods

8.2.1 Production of ^{47}Ca

The ^{47}Ca used in this measurement was produced with a 140 MeV/nucleon $^{48}Ca^{20+}$ beam at the National Superconducting Cyclotron Laboratory (NSCL) as described in Chapter 7. This ion beam was implanted at an average intensity of 72 pnA for 9.8 hours (see Chapter 7 Section 7.2.1) in a flowing-water target in which ^{47}Ca was produced through nuclear reactions between ^{48}Ca and the ^{16,18}O and ^{1}H nuclei in the water molecules. The flowing-water target and water system used were described in detail in Chapter 2 Sections 2.2.2 and 2.3.3. The product radionuclides formed in the target were transported through the flow of water from the target to a water chemistry system [36] and cationic radionuclides, such as ^{47}Ca, were collected on a cation exchange resin bed (1.5 g resin, AG50W-X8, mesh size 20-50, BioRad). The resin bed was removed from the system after 36 hours to allow for maximum collection of ^{47}Ca from the water and for short lived radionuclides to decay. The process of implanting the ^{48}Ca beam in the target, flowing water through the system, and collecting cations from the water is depicted schematically in Figure 8.1.

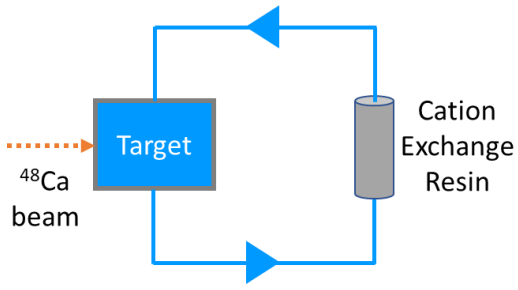

Figure 8.1: Schematic of Main Components of Water System
The ^{48}Ca beam is implanted in the flowing-water target, producing ^{47}Ca that is transported to a cation exchange resin bed where it is adsorbed. The ^{47}Ca is removed from the system on this resin bed and processed for further use.

8.2.2 Purification of ^{47}Ca

The purification of ^{47}Ca that is produced in and collected from the water system was described in Chapter 7 Section 7.2.4. In brief, the ^{47}Ca was removed from the cation exchange resin bed in 2 M HCl. This solution was diluted to 0.2 M HCl to serve as the load solution for purification on a 2 g column of AG MP-50 (AG MP-50, 100-200 mesh size, BioRad). Following the load solution, rinse steps of 0.2 M HCl and 2 M HCl were used to remove other long-lived radionuclides that were produced in the water system and collected on the cation exchange resin bed in addition to ^{47}Ca (i.e., ^{7}Be, ^{24}Na, ^{28}Mg, ^{42,43}K). Finally, 4 M HCl was used to elute purified ^{47}Ca.

The first step in the pseudo generator for this parent-daughter pair described in Chapter 6 Section 6.2.6 was used to produce both a sample of ^{47}Ca out of equilibrium with its daughter ^{47}Sc and a purified ^{47}Sc sample. [10]. About 10 mL of the 4 M HCl solution containing ^{47}Ca was passed over 67 mg of DGA extraction chromatography resin (N,N,N’,N’-tetra-n-octyldiglycolamide, normal resin, particle size 50-100 µm, TrisKem International) in a 1 mL ISOLUTE filtration column. The ^{47}Sc that was generated in this solution was adsorbed on the column and the ^{47}Ca parent remained in solution, resulting in a 10 mL solution of 320 kBq (8.6 uCi) of ^{47}Ca. This solution was used to produce samples for LSC and HPGe measurements. About 2 mL of additional 4 M HCl was used rinse the column and remove any residual ^{47}Ca from the resin. Then, two 1 mL fractions of 0.1 M HCl solution were used to remove the purified ^{47}Sc adsorbed on the column. The second of these 0.1 M HCl fractions, containing 250 kBq (6.7 uCi) of ^{47}Sc, was used to produce a sample for LSC.

8.2.3 LSC Measurements

Liquid scintillation counting was used to verify the half-lives of both ^{47}Ca and ^{47}Sc since these values are crucial to the method used in this work to measure the gamma-ray branching ratios for ^{47}Ca. These measurements were performed with a Perkin Elmer Tri-Carb 4910 TR for three ^{47}Ca samples at different concentrations and a ^{47}Sc sample. Each of the four samples consisted of 10 mL of scintillation cocktail (Optiphase HiSafe 3, Perkin Elmer) and a small spike of activity. The three ^{47}Ca samples (samples 1 to 3) were prepared with 100, 50, and 10 µL spikes of the 4 M HCl solution after it was passed over the DGA resin, producing samples with approximately 3.2, 1.6, and 0.32 kBq of ^{47}Ca, respectively. This range of activities was used to help ensure that spectra were collected with sufficient counting statistics without saturating the detector. Due to the smaller volume and higher activity of the purified ^{47}Sc, a 20 times dilution was first made of the ^{47}Sc solution and then 50 µL of this diluted solution containing approximately 0.5 kBq (10 nCi) of ^{47}Sc was added to 10 mL of scintillation cocktail.

These samples were measured for 30 minutes each several times a day over the course of 21.7 days. A background vial containing 10 mL of scintillation cocktail was measured before and after the four samples were measured at each time point. Additional measurements were made at 62, 93, and 140 days after the first measurement period to observe any long-lived activity in the samples. The spectra were analyzed by summing the counting rate in two different channel windows: 0 to 2000 and 400 to 1000. The larger 0 to 2000 range was used for the purified ^{47}Sc as no major contaminants were observed in this sample. The smaller 400 to 1000 window was selected for the ^{47}Ca samples since ^{47}Sc was generated in these samples over time. This range was chosen because it was verified that only background count rates were

detected for the purified ^{47}Sc sample in the 400-1000 window (*i.e.*, signals from the decay of ^{47}Sc were only observed below channel 400). Therefore, the count rate in this window should have decreased with the half-life of ^{47}Ca over the 21.7 day counting time frame since only the decay of ^{47}Ca contributed to signals in this restricted channel range. Each count rate measured for a sample over a channel range was background corrected using the average measurement over the same range for the two background measurements made each time the set of samples was run. The error for each measurement of a sample was found by propagating the square root of the sum of the counts in the channel window for the sample and the background average used to background correct the sample count rate.

Origin Pro 9 software was used to fit the set of values obtained for both ^{47}Ca and ^{47}Sc decay with user defined functions. For the ^{47}Ca samples, the background corrected count rates measured over channels 400 to 1000 were fitted with a simple exponential function and the uncertainties for each rate used as an instrumental weight:

$$C(t) = C_0 e^{-\lambda t} \tag{8.1}$$

where $C(t)$ is the total background corrected counting rate measured in the 400 to 1000 channel window at time t from the first spectrum collected, C_0 is a fitted variable for the total background corrected counting rate measured in the 400 to 1000 channel window at time $t = 0$, and λ is the fitted decay constant for ^{47}Ca. No background variables were included as the longest time point spectra produced counting rates equivalent to the background in the 400-1000 channel window indicating there was no detectable long-lived contaminant in the ^{47}Ca samples in this window.

For the ^{47}Sc sample, the background corrected counting rates for the 0 to 2000 channel window was fitted with a two-part exponential function with the uncertainty for each rate used as an instrumental weight:

$$D(t) = D_0 e^{-\lambda_1 t} + B_0 e^{-\lambda_2 t} \quad (8.2)$$

where $D(t)$ is the total background corrected counting rate measured in the 0 to 2000 channel window at time t from the first spectrum collected; D_0 and B_0 are fitted variables for the total background corrected count rate measured in the 0 to 2000 channel window at time $t = 0$ for ^{47}Sc and a longer-lived component, respectively; and $\lambda_1$and λ_2 are the fitted decay constants for ^{47}Sc and a longer-lived component, respectively.

8.2.4 HPGe Gamma-Ray Spectroscopic Measurements

The remaining 4 M HCl solution of ^{47}Ca that was purified with the DGA resin (300 kBq or 8.5 uCi of ^{47}Ca) was measured in a 25 mL plastic scintillation vial with an HPGe detector (Canberra BEGe Gamma-ray Detector, BE2020) several times each day over the course of 21.9 days. Spectra were recorded for 30 minutes at each time point with the sample 25 cm from the face of the detector. The sample was not moved over the entire time period that spectra were collected to preserve the exact geometric relationship between the sample and the detector face. A few spectra were taken at 43 and 45 days from the first spectrum collected to ensure there were no long-lived contaminant radionuclides in the sample and that the observed gamma rays followed the decay of ^{47}Ca at long time points. The energy scale of the HPGe detector was previously with a ^{152}Eu point source. Following the ^{47}Ca measurements, a separate 1 µCi ^{152}Eu source suspended in epoxy (Calibrated, NIST Traceable source; 1 g/cm^3 epoxy; 20 mL

fill volume) in an identical scintillation vial as the sample was measured was used to calibrate the efficiency of the detector at 25 cm from the detector face.

The determination of the gamma-ray branching ratios relied on the ingrowth of ^{47}Sc in this ^{47}Ca sample, and required accurate values for the half-life for ^{47}Sc, a characteristic gamma-ray branching ratio for ^{47}Sc (i.e., the branching ratio of 68.3(4)% for the 159.4 keV gamma ray), and the half-life of ^{47}Ca. With this parent-daughter relationship and a gamma-ray spectrum of the sample, one of the Bateman equations can be used to quantify ^{47}Ca in the solution at t = 0, which corresponds to the time of the separation of ^{47}Ca and ^{47}Sc on DGA resin. The activity of ^{47}Ca at t = 0 can then be corrected to the time that the gamma-ray spectrum was taken. Altogether, the use of the Bateman equation and the decay correction can be summarized as

$$A_1(t) = A_1(0)e^{-\lambda_1 t} = \left(\frac{\lambda_2-\lambda_1}{\lambda_2}\right)\frac{A_2(t)-A_2(0)e^{-\lambda_2 t}}{e^{-\lambda_1 t}-e^{-\lambda_2 t}}\ e^{-\lambda_1 t} \tag{8.3}$$

where $A_1(t)$ and $A_2(t)$ are the activity of ^{47}Ca and ^{47}Sc at time t, respectively; λ_1 and λ_2 are the decay constants of ^{47}Ca and ^{47}Sc, respectively; and time is measured from the point at which ^{47}Ca and ^{47}Sc were separated (meaning $A_2(0) = 0$).

The gamma-ray spectra also provide the counting rate for the three highest intensity characteristic gamma rays for ^{47}Ca decay. These counting rates can be adjusted by the efficiency of the detector at each energy to find the emission rate from the sample. The branching ratio for each characteristic gamma ray can then be found by taking the ratio of the emission rate for each gamma ray to the activity of ^{47}Ca for each spectrum.

Additionally, the integrated number of events in each peak from the three most intense ^{47}Ca gamma rays and the 159.4 keV gamma ray from ^{47}Sc were plotted over time to verify the half-life with which these each peak decays. The uncertainty in each data point was from counting statistics (*i.e.*, the square root of the integrated peak sums) and was used as an instrumental weight for each data point to find the decay rate of each gamma ray peak. For the ^{47}Ca peaks, a simple exponential, like that shown in Equation 8.1, was used to find the half-life for each of the three gamma rays. The Bateman equation in Equation 8.3 was used in the following form to fit the integrated events for the 159.4 keV gamma ray peak with the initial ^{47}Sc activity fixed at zero and t = 0 corresponding to the time at which the ^{47}Ca/^{47}Sc separation was performed:

$$A_2(t) = \left(\frac{\lambda_2}{\lambda_2 - \lambda_1}\right) A_1(0)\left(e^{-\lambda_1 t} - e^{-\lambda_2 t}\right) + A_2(0)e^{-\lambda_2 t} \,. \tag{8.4}$$

The half-lives of ^{47}Ca and ^{47}Sc in addition to the initial activity of ^{47}Ca were allowed to vary to find an independent measurement of the half-life of ^{47}Sc. Verifying that each peak sum decayed according to the evaluated half-life confirmed that no gamma rays from other background or contaminant radionuclides contributed significantly to the characteristic gamma rays of interest.

8.2.5 Error Budget

For the total counting rate obtained for each LSC measurement and the integrated peak sum for each HPGe measurement, the uncertainty in these measurements was dominated by counting statistics (i.e., the square root of the number of counts.) For the activity of ^{47}Sc that was found from the 159.4 keV peak and used to find the half-life of ^{47}Ca and ^{47}Sc with the

Bateman equation, only the uncertainty from the counting statistics was used as the uncertainty in each activity point for in the fitting algorithm. Additional uncertainties that were common to all of the ^{47}Sc activity data points were added after the half-lives were fitted. The uncertainty in the 159.4 keV branching ratio and detection efficiency were used one at a time to change the ^{47}Sc activity values used in the fitting routine. For example, the branching ratio for the 159.4 keV gamma ray was increased by one sigma from 68.3% to 68.7%. This new branching ratio value was then used to find the activity of ^{47}Sc, and the fitting algorithm was run again with these new activity values. This process was then repeated by setting the branching ratio back to 68.3% and changing the efficiency by an amount equal to one sigma. Similarly, the times associated with each data point (*i.e.*, the time from the separation of ^{47}Ca and ^{47}Sc) were varied up or down by one sigma and were used in the fit algorithm. The difference between the half-lives found with each of the parameters varied by one sigma were added in quadrature with the uncertainties in the half-life values for ^{47}Ca and ^{47}Sc found with the true values for the parameters.

The uncertainty in each of the three ^{47}Ca gamma-ray branching ratios was found in a similar way as described above for the ^{47}Ca and ^{47}Sc half-lives using the Bateman equation. The branching ratios were calculated with only the counting statistics for each gamma-ray peak as the uncertainty. For example, the counting statistics for the 159.4 keV peak and the 489.2 keV peak were the only uncertainties propagated through the calculation to find the 489.2 keV branching ratios. The weighted average and associated uncertainty for each gamma-ray branching ratio was then found using the errors resulting from these counting statistic uncertainties. Additional uncertainties that were common across all data points were used to

vary their associated constants by one sigma, as explained previously, to observe the effect on the branching ratio weighted average. These uncertainties in the efficiency of the detector at each energy, in the decay constants of ^{47}Ca and ^{47}Sc, the 159.4 keV branching ratio, and in the exact time of separation of ^{47}Ca and ^{47}Sc. The difference between each of these new weighted averages and the original weighted average was assigned as the uncertainty introduced by each parameter used to find the branching ratios. A total uncertainty was calculated by adding the square of all these uncertainties and the uncertainty in the original weighted average in quadrature. Each of the uncertainties and their sources are given in the Results and Discussion section.

8.3 Results and Discussion

Since the measurement of the three ^{47}Ca branching ratios require the use of the half-lives of ^{47}Ca and ^{47}Sc, these half-lives were measured with LSC. The sample used for ^{47}Sc was a purified fraction that contained levels of ^{47}Ca below the limit of detection using HPGe gamma-ray measurements, so the entire channel window for the LSC spectra was considered for the half-life measurement of ^{47}Sc. As ^{47}Ca decays continuously to ^{47}Sc, producing a purified ^{47}Ca fraction containing no other radionuclides over a long period of time was not possible. Therefore, the LSC channel range used for the ^{47}Ca half-life measurement was restricted to a region containing only signals from the decay of ^{47}Ca.

A portion of the earliest LSC data points collected for three ^{47}Ca samples was not included in the determination of the half-life of ^{47}Ca due to random coincidences events in the data with the highest activity level. The number of random coincidence events in an LSC spectrum for a pure ^{47}Ca source has been shown to be proportional to the square of the activity

Table 8.1: Half-Lives of ^{47}Ca and ^{47}Sc
The reduced chi-squared value (*i.e.*, the chi-squared value divided by the degrees of freedom for each fit) is given to provide information on the goodness of fit for each half-life.

Radionuclide	Source	Half-Life (days)	Reduced Chi-Squared (DOF)
^{47}Ca	**Evaluated half-life** [51]	**4.536(3)**	-
	LSC, sample 1	4.53(1)	2.57 (23)
	LSC, sample 2	4.532(9)	1.90 (28)
	LSC, sample 3	4.53(1)	1.56 (36)
	Average of LSC measurements	4.531(5)	-
	HPGe, 489 keV gamma ray	4.54(2)	1.38 (39)
	HPGe, 807 keV gamma ray	4.52(3)	1.35 (39)
	HPGe, 1297 keV gamma ray	4.53(1)	1.19 (39)
	Average HPGe direct measurement	4.534(3)	-
	HPGe, 159 keV gamma ray	4.6(1)	1.07 (38)
^{47}Sc	**Evaluated half-life** [51]	**3.3492(6)**	-
	LSC	3.350(2)	1.03 (39)
	HPGe- 159 keV gamma ray	3.3(1)	1.07 (38)
	HPGe- 159 keV gamma ray; ^{47}Ca decay constant fixed	3.349(8)	3.91 (39)

of ^{47}Ca [85]. In the same study, it was also shown that the number of random coincidences between radiation from both ^{47}Sc and ^{47}Ca is proportional to the product of the activities of the two radionuclides. Since these effects are most prominent at higher activity levels, the earliest data points for each of the samples were systematically removed and the resulting half-life for each sample was seen to approach the accepted ^{47}Ca half-life value as more data points were removed. The maximum number of data points that produced a half-life within one standard deviation of the accepted half-life value were used in the verification (*i.e.*, data points 17 to 41, 11 to 40 and 3 to 40 were used for samples 1 to 3, respectively). These data points and the fitted decay curves for each sample are shown in Figure 8.2a and the resulting half-lives are given in Table 8.1.

Table 8.2: Error Budget for Half-lives Found from 159.4 keV Gamma-Ray Peak
The uncertainty related to the separation time resulted from the approximately 8 minutes required to separate ^{47}Ca and ^{47}Sc on the DGA resin. The separation time was chosen as the midpoint of this separation length and the uncertainty was assigned as half of the separation length. A dash in the table indicates that the source of uncertainty was not relevant for the measurement whereas a value of zero indicates that the source of uncertainty was considered for the measurement but resulted in no additional uncertainty. In particular, the efficiency and branching ratio for 159.4 keV were constants with uncertainties relevant for finding the half-life of ^{47}Sc. However, these uncertainties resulted in no change in the fitted half-life since they uniformly shift all data points and do not affect the decay rate.

Source of Uncertainty	Half-Life Uncertainty		
	^{47}Ca	**^{47}Sc**	**^{47}Sc with Constant ^{47}Ca Half-Life**
Counting Statistics and Baseline Correction	0.084	0.066	0.0067
Efficiency at 159.4 keV	0.040	0.024	0.0000
Branching Ratio- 159.4 keV	0.063	0.044	0.0000
Separation Time	0.085	0.064	0.0032
Decay constant of ^{47}Ca	-	-	0.0026
Total	**0.14**	**0.10**	**0.0078**

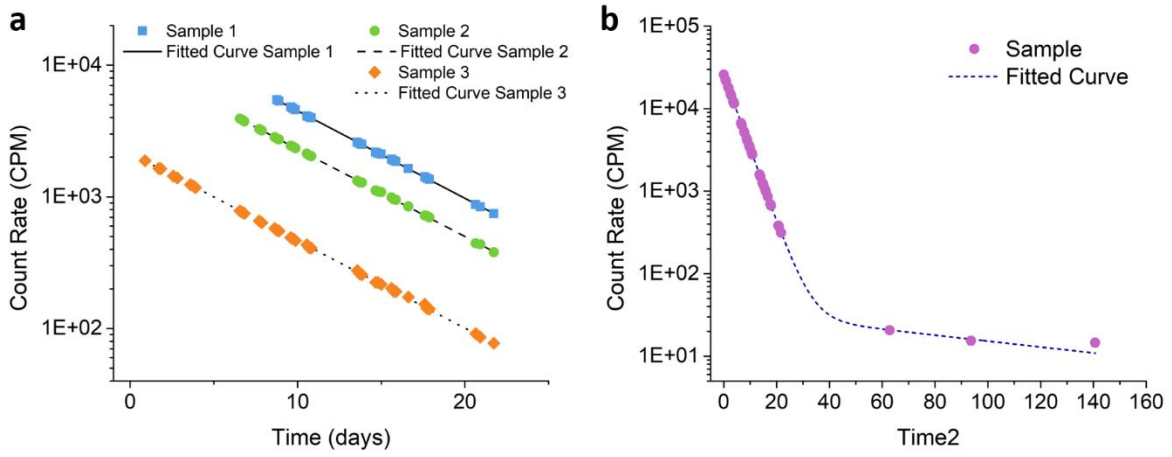

Figure 8.2: Half-Lives for ^{47}Ca: LSC Count Rates
The LSC counting rates are shown for the data points used to fit the half-lives of ^{47}Ca (a) and ^{47}Sc (b). The fitted decay curves found for each sample are overlaid. Error bars from the counting statistics are given for each point but are mostly smaller than the size of the data points.

The ^{47}Sc sample that was measured with LSC was not influenced by random coincidences to the same extent as the ^{47}Ca samples due to a lower activity and the presence of only one radionuclide with a relatively few emissions per decay. Therefore, all the LSC measurements collected for the ^{47}Sc sample were used to verify the half-life of ^{47}Sc as shown in Figure 8.2b. The half-life found by fitting these data points with Equation 8.2 is given in Table 8.1 and is only 0.03% larger than the accepted half-life for ^{47}Sc. The half-lives of ^{47}Ca and ^{47}Sc measured with LSC support the accuracy of the accepted ^{47}Ca and ^{47}Sc half-lives. Therefore, the evaluated values of 4.536(6) and 3.3492(6) days for ^{47}Ca and ^{47}Sc, respectively, were used to find the three ^{47}Ca branching ratios [51].

The half-lives with which the 489.2, 807.9, 1297.1, and 159.4 keV gamma-rays were found to decay in the gamma-ray spectra for the ^{47}Ca/^{47}Sc sample also verified the purity of these gamma-ray peaks since they were in agreement with the evaluated half-lives for these radionuclides. Figure 8.3a shows the integrated number of counts for the three ^{47}Ca gamma rays and a simple exponential fitted function for each peak. Since the background-corrected integrated counts were used, the uncertainties only included contributions from counting statistics and the background correction for each data point. The activity of ^{47}Sc resulting from the integrated counts in the 159.4 keV peak across the gamma spectra are shown in Figure 8.3b. The Bateman equation was used to fit these data points first with the half-life of both radionuclides and the initial activity of ^{47}Ca as variables and then again with only the half-life of ^{47}Sc and the initial activity of ^{47}Ca as variables. Only uncertainties from the background correction and counting statistics were used in both fitting routines. As described previously,

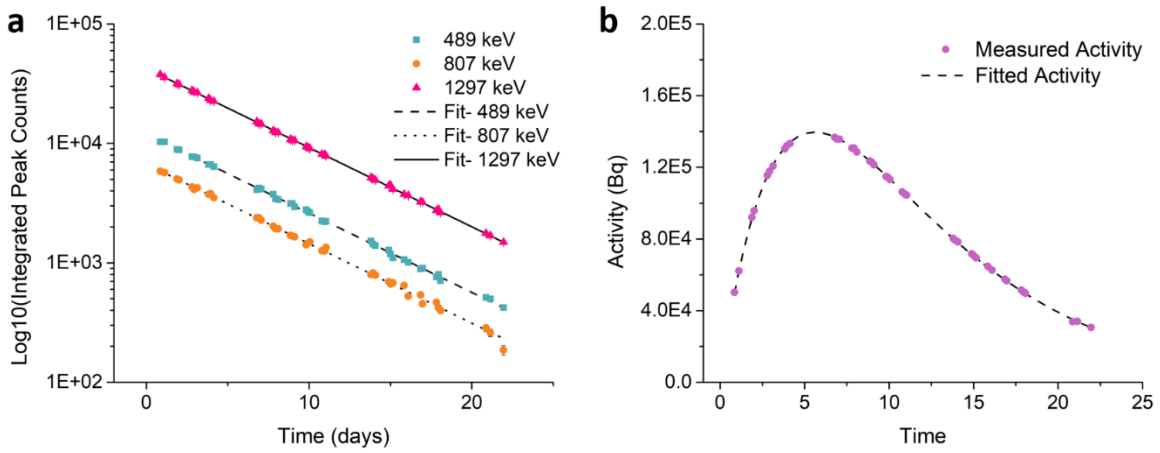

Figure 8.3: Half-Lives for ^{47}Ca and ^{47}Sc: Gamma-Ray Spectroscopic Peaks
The integrated number of counts for the 489.2, 807.9, and 1297.1 keV gamma-ray lines for ^{47}Ca (a) and the ^{47}Sc activity found with the 159.4 keV gamma ray (b) are shown as a function of time for each gamma spectrum. The ^{47}Ca data points were fitted with a simple exponential for the ^{47}Ca gamma rays and the ^{47}Sc data point were fitted with a Bateman equation. Error bars were based on counting statistics and background corrections and are mostly smaller than the data points.

the uncertainties in the parameters used to find the activity of ^{47}Sc for each spectrum were systematically varied to find the uncertainty contribution from each constant (Table 8.2). With the dead time of the detector at 1% or less for each spectrum in this analysis, a dead time correction was not necessary for accurate results.

The four resulting values for the ^{47}Ca half-life and two values for the ^{47}Sc half-life found in this analysis are given in Table 8.1. Each measurement agrees quite well with the corresponding evaluated value with the error bar for the half-lives found using the Bateman equation being larger at 3% for the half-life of ^{47}Sc and 2% for the half-life of ^{47}Ca when these values were both used as variables. When the half-life of ^{47}Ca was fixed at the accepted value, however, the half-life of ^{47}Sc was found with only a 0.2% uncertainty. These results confirm

that, as expected, the 489.2, 807.9, and 1297.1 keV gamma rays come from ^{47}Ca and the 159.4 keV gamma ray comes from ^{47}Sc with little to no interferences from other sources.

With confirmation that both sets of half-lives for ^{47}Ca and ^{47}Sc agree with the evaluated half-lives, the gamma spectra of the ^{47}Ca/^{47}Sc sample were analyzed to extract the branching ratios of the three main ^{47}Ca gamma rays. The branching ratios for each gamma spectrum are shown for the 489.2 and 807.9 keV gamma rays in Figure 8.4a and for the 1297.1 keV gamma ray in Figure 8.4b. The average value across each set of data points is included as a solid or dashed line through the points. The error bars of most points in each of the three sets overlap with their average value demonstrating agreement among the values within each set. At later time points, a larger spread in the values is observed due to lower count rates and therefore, larger statistical uncertainties. The error bars in Figure 8.4 result from the counting statistics from each gamma-ray peak as these are the only uncertainties that vary by data point under the present conditions. The other errors that influence the branching ratio value were

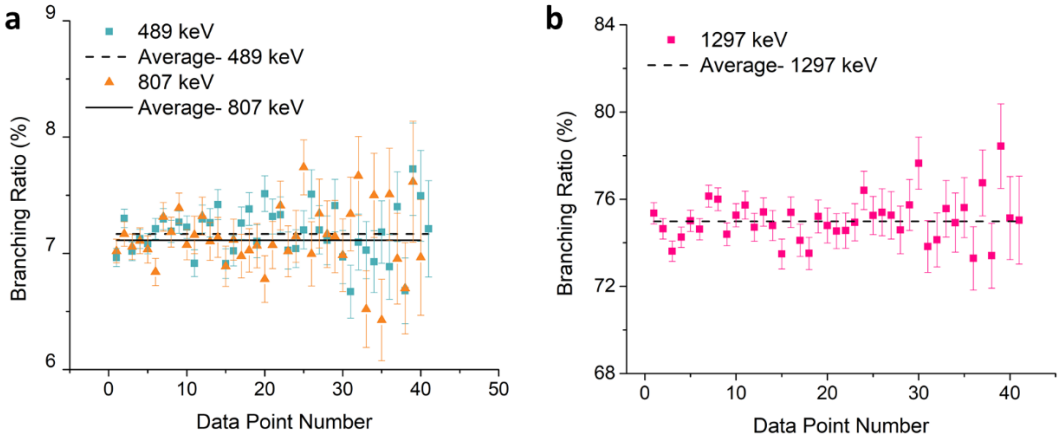

Figure 8.4: Branching Ratios for Three Most Intense ^{47}Ca Gamma Rays
The branching ratios observed in each gamma-ray spectrum are given for the 489.2 and 807.9 keV gamma ray (a) and for the 1297.1 keV gamma ray (b). The solid or dashed line through the data points indicates the average branching ratio for each gamma-ray transition. Note that the error bars for almost all the data points overlap with the respective average.

Table 8.3: Error Budget for Three ^{47}Ca Branching Ratios
The absolute uncertainty for each branching ratio as a percent is given for different sources of uncertainty. The uncertainty related to the separation time resulted from the approximately 8 minutes required to separate ^{47}Ca and ^{47}Sc on the DGA resin. The separation time was chosen as the midpoint of the separation length and the uncertainty was assigned to be half of the separation length. Additionally, the efficiency uncertainty was found by varying the uncertainty at 159.4 keV and one ^{47}Ca gamma-ray energy at the same time since these uncertainties were related.

Source of Uncertainty	Energy of Gamma Ray (keV)		
	489.2	**807.9**	**1297.1**
Counting Statistics	2.06E-2	2.78E-2	1.13E-1
Efficiency	1.84E-2	1.83E-2	5.85E-2
Decay Constant- ^{47}Ca	1.97E-3	1.92E-3	2.18E-2
Decay Constant- ^{47}Sc	5.6E-4	5.7E-4	5.4E-3
Branching Ratio- 159.4 keV	4.2E-2	4.2E-2	4.4E-1
Separation Time	7.0E-3	7.1E-3	2.6.7E-2
Total	**5.1E-2**	**5.4E-2**	**4.6E-1**

incorporated in the final error of the weighted average value. All uncertainties for these measurements are given in Table 8.3 where they are listed by their source.

It is also vital to note for this measurement that the emission of the 489.2 and 807.9 keV gamma rays in the cascade from the 1297.1 keV excited state is isotropic with angular correlation coefficients of A_2 = -0.050(6) and A_4 = 0 [84,86]. With this isotropic distribution, the probability of simultaneously detecting both the 489 and 807 keV emission from the same decay event (*i.e.*, true coincidence summing) is on the order of the detection efficiency for these gamma rays (i.e., 1E-4 for 807.9 keV and 3E-4 for 489.2 keV). Since this probability is small compared to the uncertainties in these measurements, no correction was made to the branching ratios for this coincidence probability.

The final values for the branching ratios of the 489.2, 807.9 and 1297.1 keV gamma rays are 7.17(5)%, 7.11(5)%, and 75.0(5)%, respectively. These values differ significantly from the

current evaluated branching ratios of these gamma rays: 5.9(12)%, 5.9(12)%, and 67(13)%, respectively. Additionally, the precision of the present branching ratios with uncertainties of less than 1% for each is much higher than that of the evaluated values.

With these remeasured branching ratios for ^{47}Ca, other minor gamma-ray branching ratios can be adjusted in the ^{47}Ca decay scheme (see Figure 8.5). In particular, the 41.1, 530.6, 767.1, and 1878 keV gamma rays have been measured previously through a ratio to the more intense gamma rays in the ^{47}Ca decay scheme. Additionally, the 731.6 and 1147 keV gamma rays have been inferred through intensity balancing from the 1878 keV excited state. The branching ratio as an emission percent for ^{47}Ca decays based on the 489.2, 807.9, and 1297.1 keV branching ratios based on this work are given in Table 8.4 and Figure 8.5.

The beta decay from the ground state of ^{47}Ca to both the ground state and the 1297.1 keV excited state of ^{47}Sc are currently reported with high uncertainties. These values can both be found with far lower uncertainty using the 489.2 and 1297.1 keV branching ratios reported here. The relationship between key nuclear data in the decay of ^{47}Ca is shown in the decay

Table 8.4: Minor Gamma-Ray Branching Ratio Values

Gamma-Ray Energy (keV)	Measurement Description	Ratio	Evaluated Branching Ratio (%)	Branching Ratio from This Work (%)
41.1	Relative to intensity 100 for 1297.1 keV gamma ray [87]	0.0085(10)	0.0056(13)	0.0064(8)
530.6	Ratio with 489.2 keV gamma ray [86]	0.0146(10)	0.086(18)	0.105(7)
731.6	Intensity balanced 1878 keV energy level [51]	-	0.011(3)	0.009(2)
767.1	Ratio with 807.9 keV gamma ray [86]	0.0294(10)	0.18(4)	0.209(7)
1147	Intensity balanced 1878 keV energy level [51]	-	0.011(3)	0.009(2)
1878	Relative to intensity 100 for 1297.1 keV gamma ray [87]	0.038(4)	0.025(6)	0.028(3)

scheme in Figure 8.5. Since only the 489.2, 530.6 and 1297.1 keV gamma rays are emitted from the 1297.1 keV excited state for ^{47}Sc, the beta decay branching ratio is equal to the sum of the branching ratios of these three gamma rays. Internal conversion does occur to de-excite this energy level, but the rates are negligible compared to even the small uncertainties in these three gamma-ray branching ratios [51]. With the branching ratios measured in this work and updated 530.6 keV branching ratio given in Table 8.4, the beta decay branching ratio from the ground state of ^{47}Ca to the 1297.1 keV excited state of ^{47}Sc is found to be 82.2(5)% [86]. This updated beta decay branching ratio can be used with the previously reported branching ratios for beta decay from the ground state of ^{47}Ca to the 766.8 and 1878.2 keV excited states of ^{47}Sc (i.e., 0.087(3) and 0.037(8)%, respectively) [51,86–88]. Intensity balancing with these values gives a beta decay branching ratio of 17.7(5)% for the ground state to ground state beta decay

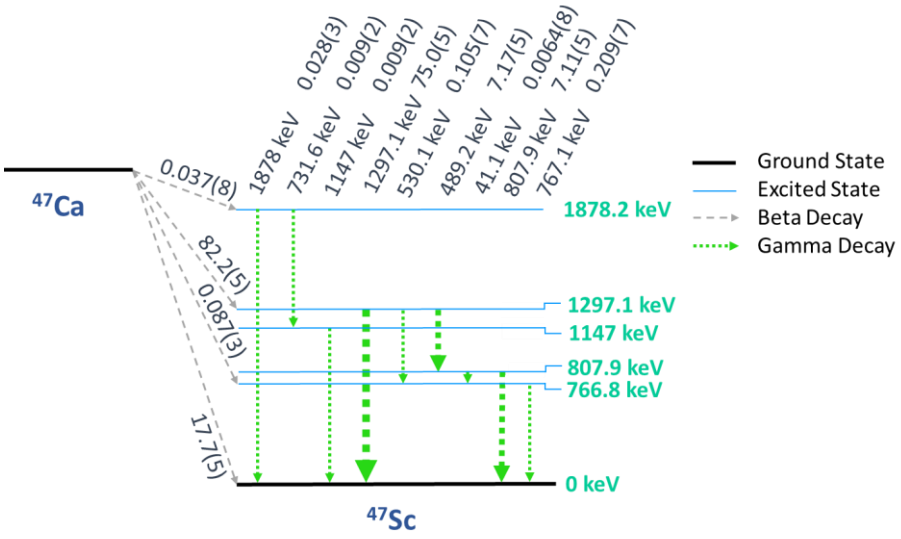

Figure 8.5: Decay Scheme of ^{47}Ca Beta Decay to ^{47}Sc
The four beta decay branches for ^{47}Ca and the subsequent gamma-ray emissions from the excited energy levels in ^{47}Sc are given. The 489.2, 530.6, and 1297.1 keV gamma rays are the dominant emissions from the 1297.1 keV excited state in ^{47}Sc. The branching ratios for each beta and gamma-ray emission branches are indicated in the figure as a percent.

of ^{47}Ca to ^{47}Sc. The branching ratios for the beta decay of ^{47}Ca to the 1297.1 keV excited state and the ground state of ^{47}Sc given here fall within the large uncertainty of the accepted values but are much more precise. The values for all four beta decay branches are given in the decay scheme in Figure 8.5.

8.4 Conclusion

Using a sample of pure ^{47}Ca produced at the NSCL, the half-life of ^{47}Ca and its daughter, ^{47}Sc, were measured with LSC and gamma-ray spectroscopy and were found to agree with the current evaluated half-life values. Using the ingrowth of ^{47}Sc and well-known nuclear data for this radionuclide, the branching ratio for the 489.2, 807.9, and 1297.1 keV ^{47}Ca gamma rays were remeasured as 7.17(5)%, 7.11(5)%, and 75.0(5)%, respectively. These values are more precise than the current accepted branching ratios for these gamma rays. Additionally, the beta decay branching ratio from the ground state of ^{47}Ca to the 1297.1 excited state and the ground state of ^{47}Sc were found to be 82.2(5)% and 17.7(5)%, respectively. Although these values fall within the uncertainty range for the currently reported values, they have a marked increase in precision. These updated values will allow for more accurate and precise quantification of ^{47}Ca when using ^{47}Ca to generate ^{47}Sc for nuclear medicine applications.

Chapter 9: General Discussion

9.1 Introduction

The results and techniques from the three ^{48}Ca irradiations presented here are be critically compared and evaluated in this chapter to provide overall conclusions from the three experiments and identify some of the best techniques for future isotope harvesting experiments. The production rate measurements, separation techniques, and stable elemental analysis results will be examined in this chapter to provide clarity for the recommended next steps for these aspects of the project.

9.2 Production Rate of ^{47}Ca

The production rate of ^{47}Ca in the flowing-water isotope harvesting target was measured during two different experiments as 2.0(4)% in Chapter 4 Section 4.2.3 and 1.67(4)% in Chapter 6 Section 6.3.1, and these two production rates are in agreement. In the first case, the total activity of ^{47}Ca collected on the cation exchange resin bed and water samples or remaining in the water after collection were corrected back to the end of the irradiation and compared to the recorded beam current measurements to find a production rate. For the second measurement, the activity of ^{47}Ca collected in water samples at three different points during the irradiation was extrapolated to find the total activity in the water system and then compared to the recorded beam current measurements. Since the measured production rates agree despite the different methods used to find the values, additional confidence is provided in the accuracy of the production rate measurement.

Additionally, the activity and production rate of ^{47}Ca found in the first irradiation with a ^{48}Ca beam can be recalculated using the remeasured branching ratios for the three main gamma rays following the decay of ^{47}Ca presented in Chapter 8. This results in an updated production rate of 1.71(5)% for this measurement. The average production rate based on these two independent measurements (*i.e.*, 1.71(5)% from Chapter 4 and 1.67(4)% from Chapter 6) is 1.69(2)%. A calculated ^{47}Ca activity for each irradiation in this study can be found with the average production rate, the recorded beam currents throughout each irradiation, and Equation 4.1. These calculated activities are given in Table 9.1 below and are compared to the total measured ^{47}Ca activity for each irradiation. To provide an understanding of the scale of the experiment, the integrated beam current is also given. Since the half-life of ^{47}Ca is long compared to the length of the irradiations, the ratio between the integrated beam current and the produced activity at the end of each irradiation should be relatively consistent between experiments.

The values shown in Table 9.1 demonstrate some variability in the comparison between the measured and calculated activity. These differences may be rooted in sources of

Table 9.1: Comparison of Measured to Calculated ^{47}Ca Activities

Experiment	Integrated Beam Current (pnA h)	Measured Activity (mCi)	Calculated Activity (mCi)	Percent Difference (%)
Chapter 4	4.7	0.086(2)	0.0824(8)	-4.0(2)
Chapter 6	79.4	1.79(6)	1.44(1)	-19.5(8)
Chapter 7	703	9.9(2)	12.08(2)	+22.2(6)

uncertainty in the measurement of the beam current that was impinged on the isotope harvesting target or the activity of ^{47}Ca produced in each irradiation. For example, quantification of the beam current including the calibration of the non-intercepting probes in the beam line and calibration of the target current readings based on the non-intercepting probe readings may have larger uncertainties than estimated. Some of the difference between the measured and calculated activity might be due to the accuracy with which high activity measurements were made with gamma-ray spectroscopy. The non-standard geometries used for many measurements, such as samples of tens to hundreds of milliliters of water or samples collected on columns, may have introduced inaccuracies to the measurements. In particular, measurements of the activities collected on cation exchange resin beds were difficult to measure. These activities were quite high, and aliquots of the activity could not be used for quantification. As a result, the collection resin beds were measured at distances far from the detector face and even so had dead times of 5 to 10%.

Additionally, variations in each experiment may also contribute to the disparity between measured and calculated ^{47}Ca activities in these irradiations. For instance, positioning of the beam spot on the flowing-water target may change the production rate in the target. The energy profile of the beam changes if the beam is lower on the target and passes through the internal wall in the target or if the beam spot is higher and does not pass through the internal wall. While the difference between the measured and predicted ^{47}Ca activities was up to 22% of the measured activity across these three experiments, the measured production rate provided adequate accuracy for predicting the scale of produced activity in future experiments. This should help with both experimental and safety planning in future, higher intensity experiments.

9.3 Separation Procedures for the Purification of ^{47}Ca

In Chapter 4, three separation schemes were explored with all three producing high purity ^{47}Ca in 3 to 5 M HCl. While the separation method involving AG MP-50 and an HCl/methanol gradient was eliminated due to some impracticalities of this method (*i.e.*, high volumes and the use of methanol), the two other methods, 1) AG MP-50/HCl and 2) DGA HNO_3/HCl, were shown to be viable options. The first of these methods was identified as the best choice due to the reported instability of the DGA resin when exposed to high levels of radiation and with repeated use.

After performing several AG MP-50/HCl separations with the harvested ^{47}Ca (see Chapter 6 Section 6.2.5 and 6.3.3 and Chapter 7 Section 7.2.4 and 7.3.2), the suitability of the method became more apparent. The elution of ^{47}Ca from the cation exchange collection resin bed was optimized with 1 and 2 M HCl to carry out the separation without an evaporation step. Following elution of about 85% of the collected ^{47}Ca, the solution was diluted to a lower acid level that would be suitable load solutions for the gradient AG MP-50/HCl separation. A relatively large volume load solution resulted from these optimizations since about 25 mL of 2 M HCl was required to remove about 85% of the collected ^{47}Ca and a 0.2 M HCl load solution provided the highest yield of ^{47}Ca with 99.9% purity. Together, this resulted in a 250 mL 0.2 M HCl load phase, which is a high volume compared to the DGA HNO_3/HCl method. Further optimization including lowering the flow rate and increasing the length of the column could allow for a higher acidity and therefore a lower volume load phase.

The elution of the cation exchange collection resin bed in Chapter 4 (Section 4.2.4 and 4.3.2) demonstrated that a rinse step of about 70 mL of HNO_3 would remove almost all the ^{47}Ca

collected on the resin bed. This volume can be loaded directly onto a DGA resin for purification of ^{47}Ca in the DGA HNO_3/HCl separation and is much smaller than the volume used for the AG MP-50/HCl separations in later experiments. One additional issue that could arise from using the DGA HNO_3/HCl method in future experiments is the low capacity of the resin given the significant amount of stable metal ion impurities observed in the two higher intensity ^{48}Ca experiments. Since a small shift was observed in the elution profile for the two AG MP-50/HCl separations reported in Chapter 7 Section 7.3.2, this may affect the retention of ^{47}Sc on the DGA resin in the 4 M HCl load phase if the stable ion concentration is high enough to compete with ^{47}Sc for interaction with the resin.

Another separation method was tested briefly in the second ^{48}Ca irradiation as discussed in Chapter 6. The fourth fraction from the cation exchange collection resin bed was not purified with the AG MP-50/HCl method. Instead, this portion was purified with the generator procedure and demonstrated that the purification of scandium isotopes despite the presence of other radionuclides such as ^{7}Be, ^{42}Na, and ^{42,43}K in the generator solution (see Figure 6.10). This result showed that the first step in the generator procedure (DGA 1) could be used with 3 to 5 M HCl eluate from the cation exchange collection resin bed to remove all scandium isotopes from the solution. A generator solution would be produced containing ^{7}Be, ^{42}Na, ^{42,43}K, and ^{45,47}Ca produced in the isotope harvesting system and ^{47}Sc generated in this solution. This proposed separation would eliminate the need for a dilution step as required in the AG MP-50 separation and would be simpler than the DGA 3 M HNO_3/HCl separation. The stable ions identified in Chapter 6 Section 6.3.6 and Chapter 7 Section 7.3.5 would either harmlessly follow Ca^{2+} through all the separation steps (*e.g.*, Al, Co, Cu, Mg, Mn, Ni) or could be

removed from the ^{47}Sc product with the 3 M HNO_3 step added to the generator procedure (*e.g.*, Fe and Zn). This separation could be carried out by placing the collection column and a small DGA column (50-70 mg) in parallel and using tens of mL of 3 M HCl rinsed through both columns to rapidly produce a suitable ^{47}Ca/^{47}Sc generator solution.

The drawbacks to the proposed simplified separation procedure are the presence of radionuclides other than ^{47}Ca and ^{47}Sc in the generator solution and the use of DGA resins in both this separation step and the generator procedure. The presence of additional radionuclides in the solution means that higher activity levels would be present. This could lead to more extensive breakdown of the DGA resin than with just ^{47}Ca and ^{47}Sc present in the generator solution. Potential consequences from this breakdown are reduced yield and purity resulting from a separation and the need to use a prefilter resin to remove traces of organic residue removed from the DGA resin. Additionally, such a contaminated generator solution might not pass requirements for the radionuclidic purify of a ^{47}Ca/^{47}Sc generator. While this is not a scientific drawback for the generation of ^{47}Sc, it could limit the use of this method in further applications. As mentioned previously, this method would use DGA resin which is also used in the generator procedure. This repetition may reduce the separation capacity of the overall method compared to using to different resins (*e.g.*, using AG MP-50 in the purification of ^{47}Ca and the DGA resin in the purification of ^{47}Sc).

Any of the three methods discussed here could be used to produce a high quality ^{47}Ca/^{47}Sc generator. As experiments continue moving towards more intense conditions expected for isotope harvesting during the regular operation of FRIB, it may become clear which of these three methods is the most advantageous.

9.4 Stable Elemental Analysis

The stable elements identified and measured in the two higher intensity ^{48}Ca irradiations (Chapter 6 Section 6.3.6 and Chapter 7 Section 7.3.5) showed that a significant amount of stable impurities were collected on the cation exchange resin beds compared to the amount of radionuclidic products of interest. These stable impurities will likely increase as the intensity and duration of irradiations and the amount of exposed metallic surfaces in the isotope harvesting water system increase. The optimization and selection of purification schemes should include measures to remove these stable ions as well as radionuclidic impurities. It is possible that the mass of stable ions in the system could be mitigated by increased effort to recombine radiolysis products in the system. By decreasing the buildup of hydrogen peroxide in the water, lower levels of stable ions may enter the water due to corrosion of metallic components.

One additional interesting finding from the stable elemental analysis of the irradiated water is the presence of Al. From the level of other stable metal ions observed, one likely source of this Al is “common aluminum” or aluminum alloy 3003. This allow would account for the high level of Al and the Mn ions. The other likely source in the water system would be Al from the Ti64 alloy target shell which contains 6% Al and 4% V. Analysis of the stable ions collected on the anion exchange resin was not performed but would add support to either of these metals as the source of aluminum. Any vanadium ions that could have be removed from the target titanium alloy shell would have been collected on the anion exchange column. While the presence of vanadium on the anion exchange column would support target material

degradation, its absence would indicate 3003 aluminum alloy as the source. Future irradiation experiments at high beam intensities could explore the source of Al.

9.5 Conclusion

The series of experiments carried out in this work has explored many techniques for harvesting ^{47}Ca from a heavy-ion beam stop to provide a preclinical supply of ^{47}Sc in the future at FRIB. Such harvesting has been shown to be possible and can provide a significant supply of ^{47}Sc, which is currently difficult to produce for potential theranostic applications such as the targeted treatment of metastatic cancers. The techniques optimized in these experiments have demonstrated the feasibility of this production route using simple procedures with reproducible results. In addition, the branching ratios of the gamma rays following the decay of ^{47}Ca were remeasured, supporting the use of isotope harvested radionuclides for a wide range of applications. As harvesting efforts progress towards harvesting at FRIB, these techniques can be translated to the conditions anticipated with higher intensity irradiations and a somewhat different isotope harvesting water system at FRIB with the ultimate goal of providing large quantities of ^{47}Sc for further preclinical research.

APPENDICES

APPENDIX A: NUCLEAR DATA

Table A1: Nuclear Data Used for Identification, Quantification, and Localization of Radionuclides Produced with a ^{40}Ca Beam in a Flowing-Water Target. [14,15,28,50–56]

Nuclide	**Gamma-Ray Energy (keV)**	**Branching Ratio (%)**
^{7}Be	477.71	10.44(4)
^{18}F	511	193.46(8)
^{24}Na	1368.6	99.9936(15)
^{28}Mg	400.68	36.6(10)
^{34m}Cl	146.36	38.3(5)
^{43}Sc	372.72	22.5(7)
^{44}Sc	1157.020	99.9(4)
^{44m}Sc	271.34	86.7(3)
^{47}Sc	159.47	68.3(4)
^{48}Cr	112.58, 308.4	96.0(20), 100(2)
^{48}V	983.47,1312	99.98(4), 98.2(3)
^{52}Mn	744.22, 935.59, 1434.29	90.0(12), 94.5(13), 100.0(14)

Table A2: **Nuclear Data Used to Quantify Radionuclides Produced By a ^{47}Ca Beam in a Flowing-Water Target**[6,7,11,21,22,30-34]

For the characteristic gamma-rays of ^{28}Mg, no uncertainty for the branching ratio was reported so an uncertainty of 10% was assumed.

Radionuclide	Half-life	Gamma-Ray Energy (keV)	Branching Ratio (%)
^{24}Na	14.997 h	1368.6	99.9936(15)
^{27}Mg	9.458 m	843.8	70.94(9)
^{28}Mg	20.915 h	400.6	36(4)
		941.7	36(4)
		1342.2	54(5)
^{42}K	12.355 h	1524.6	18.08(9)
^{43}K	22.3 h	372.8	86.8(2)
		396.9	11.85(8)
		593.4	11.26(8)
		617.5	79.2(6)
^{44}K	22.13 m	368.2	2.3(4)
		651.4	3.0(5)
		726.5	3.8(6)
		1024.7	7(1)
		1126.1	8(1)
		1157.0	58(9)
		1499.5	8(1)
		1752.6	4.1(6)
^{45}K	17.18 m	174.28	74(5)
		1705.6	53(3)
^{47}Ca	4.536(3) d	489.2	5.9(12)
		807.9	5.9(12)
		1297.1	67(13)
^{44m}Sc	58.61 h	271.2	86.7(3)
^{47}Sc	3.3492 d	159.4	68.3(4)
^{48}Sc	43.67 h	983.4	100.1(5)
		1037.5	97.6(7)
		1312.1	100.1(7)

Table A3: Nuclear Data and Geometry Correction Factor for Production Rate Measurement

Radionuclide	Half-life	Gamma-Ray Energy (keV)	Branching Ratio (%)	Geometry Correction Factor	
				25 cm	50 cm
^{24}Na	14.997 h	1368.6	99.9936(15)	1.09(4)	1.13(5)
^{27}Mg	9.458 m	843.8	70.94(9)	1.14(3)	1.16(4)
		1014.5	28.20(2)	1.13(3)	1.15(4)
^{28}Mg	20.915 h	400.6	36(4)	1.18(3)	1.18(3)
		941.7	36(4)	1.13(3)	1.15(4)
		1342.2	54(5)	1.10(4)	1.13(5)
^{34m}Cl	31.99 m	146.5	38.3(5)	1.20(3)	1.19(3)
^{38}Cl	37.230 m	1643	32.9(5)	1.08(4)	1.12(5)
^{39}Cl	56.2 m	250.3	46.1(1)	1.19(3)	1.19(3)
		1091	2.42(8)	1.12(4)	1.14(4)
		1267	53.6(13)	1.11(4)	1.13(5)
		1517	39.3(10)	1.09(4)	1.12(5)
^{38}S	170.3 m	1943	86.5(22)	1.05(5)	1.10(6)
^{42}K	12.355 h	1524.6	18.08(9)	1.09(5)	1.12(5)
^{43}K	22.3 h	372.8	86.8(2)	1.18(3)	1.18(3)
		396.9	11.85(8)	1.18(3)	1.18(3)
		593.4	11.26(8)	1.16(3)	1.17(3)
		617.5	79.2(6)	1.16(3)	1.17(3)
^{44}K	22.13 m	368.2	2.3(4)	1.18(3)	1.18(3)
		651.4	3.0(5)	1.16(3)	1.17(3)
		726.5	3.8(6)	1.15(3)	1.16(4)
		1024.7	7(1)	1.13(3)	1.15(4)
		1126.1	8(1)	1.12(4)	1.14(4)
		1157.0	58(9)	1.11(4)	1.14(4)
		1499.5	8(1)	1.09(4)	1.12(5)
		1752.6	4.1(6)	1.07(5)	1.11(6)
^{45}K	17.18 m	174.28	74(5)	1.19(3)	1.19(3)
		957.5	7.6(5)	1.13(3)	1.15(4)
		1260.3	8.5(5)	1.11(4)	1.13(5)
		1434.5	4.2(3)	1.09(4)	1.13(5)
		1705.6	53(3)	1.07(5)	1.11(6)
^{47}Ca	4.536(3) d	489.2	5.98(2)	1.17(3)	1.17(3)
		807.9	6.0(3)	1.14(3)	1.16(4)
		1297.1	60.7(2)	1.10(4)	1.13(5)
^{44m}Sc	58.61 h	271.2	86.7(3)	1.19(3)	1.18(3)
^{46}Sc	83.79 d	889.3	99.984(1)	1.14(3)	1.15(4)
		1120.6	99.987(1)	1.12(4)	1.14(4)
^{47}Sc	3.3492 d	159.4	68.3(4)	1.19(3)	1.19(3)
^{48}Sc	43.67 h	983.4	100.1(5)	1.13(3)	1.15(4)
		1037.5	97.6(7)	1.12(3)	1.15(4)

APPENDIX B: PREDICTED NUCLEAR REACTION PROBABILITIES

Chapter 2: ^{40}Ca Irradiation

For the fusion evaporation products found in the system, ^{43}Sc, ^{44,44m}Sc, ^{48}V, ^{48}Cr, and ^{52}Mn, the reaction cross sections were predicted using PACE4 and LiFus in the program LISE++. In the Monte-Carlo simulation used in PACE4, each reaction was sampled 10,000 times (*i.e.,* the number of cascades, "NCASC" = 10,000). The projectile was set as ^{40}Ca and the target was set as ^{16}O. The optical model potentials were left as the default "from systematics" values. Using these settings, the cross section was simulated in PACE4 over a range of lab energies. The spaces between the energy points were 50 MeV for cross-sections between 1 and 10 mb and 25 MeV for cross sections larger than 10 mb. For any jumps in the cross section of greater than 50 mb, the spacing was decreased to 12.5 MeV between energy points. Cross-sections less than 1 mb were not included in the total production calculations. Tables B1-5 give the cross-section values by energy used for the production estimates. It should be noted that these values were generated using a Monte Carlo simulation, meaning identical values may not be produced every time the simulation is run with the same settings.

LisFus was used in LISE++ by selecting the "Fusion->Residual" production mechanism. With this mechanism selected, the projectile was set to ^{40}Ca, the residual was set to one of the radionuclides produced, and the target was set to ^{16}O. The excitation function for each reaction was output with steps of 11.72 MeV in beam lab energy (128 points between 0 and 1500 MeV). As with the PACE4 calculations, only cross-section values of greater than 1 mb were used to

determine production rates. Tables B6-11 provide the cross-section values for a specific energy that were used in the estimate.

FR production rates were simulated with LISE++ using a primary beam of $^{40}Ca^{20+}$ at an energy of 137.59 MeV/nucleon and an intensity of either 0.11 pnA or 0.42 pnA for the low and high intensity beam settings, respectively. The target was set to 0.7 mm of Ti6Al4V followed by an 11 mm water stripper layer, and finally, a thick material block of iron. This set-up allowed for a slight attenuation of the beam intensity and energy in the Ti alloy target shell before the beam entered the water. The water layer thickness was optimized by considering that the water must be thick enough to allow all the possible nuclear reactions to occur in the water while thin enough to allow the particles to pass through the water layer into the iron material, which serves as a particle detector in the simulation. Because the fragmentation reactions occur at high energies, this restriction did not strongly influence the calculation. In practice, the optimum water thickness was found by using a range of water thicknesses and finding the thickness that gave the highest detection of the fragments of interest in the material layer.

Table B1: Cross Section Data from PACE4 for the Production of ^{43}Sc through the ^{16}O + ^{40}Ca Fusion Evaporation Reaction.

Energy of ^{40}Ca Beam (MeV)	Cross Section (mb)
200	2.27
250	10.6
300	4.54
325	8.16
350	17.9
375	33.3
400	41.3
425	49.9
450	43.5
475	33.3
500	27.4
525	27.3
550	36.2
575	38.6
600	46.8
625	43.8
650	41.2
675	34.4
700	27.4
725	25.1
750	18.6
775	18.6
800	14.7
825	14.7
850	12.6
875	9.85
900	9.05
950	5.66
1000	2.38

Table B2: Cross Section Data from PACE4 for the Production of ^{44}Sc through the $^{16}O + ^{40}Ca$ Fusion Evaporation Reaction

Energy of ^{40}Ca Beam (MeV)	Cross Section (mb)
275	7.15
300	27.3
325	52.9
350	65.7
375	68
400	51.1
425	35.2
450	32.9
475	45.4
500	65.5
525	81.7
550	82.5
575	75.8
600	59.1
625	50.7
650	41
675	37.3
700	30.9
725	32.8
750	26
775	27.4
800	24.9
825	18
850	14.4
875	12
900	6.34
950	2.38

Table B3: Cross Section Data from PACE4 for the Production of ^{48}V through the ^{16}O + ^{40}Ca Fusion Evaporation Reaction

Energy of ^{40}Ca Beam (MeV)	Cross Section (mb)
200	13.7
212.5	41.1
225	85.4
237.5	141
250	193
275	229
300	188
312.5	150
325	116
350	69.9
375	56.1
400	73.3
425	86.7
450	94.1
475	91.4
500	74
525	49.7
550	32.2
575	15.9
600	10.4
625	4.76
650	2.72

Table B4: Cross Section Data from PACE4 for the Production of ^{48}Cr through the ^{16}O + ^{40}Ca Fusion Evaporation Reaction

Energy of ^{40}Ca Beam (MeV)	Cross Section (mb)
100	1.21
150	9.97
200	2.04
225	7.72
250	29.6
275	51.7
300	55.1
325	38.3
350	22.7
375	14.4
400	12.1
425	16.3
450	15.7
475	19.6
500	16.1
525	12.5
550	7.82
575	6.46
600	2.04
625	1.59

Table B5: Cross Section Data from PACE4 for the Production of ^{52}Mn through the ^{16}O + ^{40}Ca Fusion Evaporation Reaction

Energy of ^{40}Ca Beam (MeV)	Cross Section (mb)
125	6.11
137.5	43.9
150	135
162.5	243
175	317
200	314
212.5	246
225	194
237.5	123
250	83.2
262.5	52.9
275	29.4
300	8.62

Table B6: Cross Section Data from LisFus for the Production of ^{43}Sc through the ^{16}O + ^{40}Ca Fusion Evaporation Reaction

Energy of ^{40}Ca Beam (MeV)	Cross Section (mb)	Energy of ^{40}Ca Beam (MeV), continued	Cross Section (mb), continued	Energy of ^{40}Ca Beam (MeV), continued	Cross Section (mb), continued
316.43	1.26	644.57	39.11	972.72	73.33
328.15	2.37	656.29	38.82	984.44	68.92
339.87	7.64	668.01	35.53	996.16	64.52
351.59	13.28	679.73	31.39	1007.88	60.13
363.31	18.59	691.45	29.68	1019.60	55.39
375.03	23.81	703.17	29.53	1031.32	50.03
386.74	24.77	714.89	30.34	1043.04	43.99
398.46	22.93	726.61	32.37	1054.76	34.95
410.18	20.24	738.33	34.26	1066.48	25.97
421.90	16.48	750.05	35.74	1078.20	24.34
433.62	13.11	761.77	37.48	1089.92	22.72
445.34	10.72	773.49	41.69	1101.64	19.49
457.06	8.73	785.21	45.90	1113.36	15.93
468.78	9.69	796.93	47.93	1125.08	13.18
480.50	10.66	808.65	49.77	1136.79	10.84
492.22	13.57	820.37	53.77	1148.51	8.90
503.94	16.58	832.09	58.48	1160.23	7.40
515.66	21.17	843.81	65.84	1171.95	6.05
527.38	26.19	855.53	75.13	1183.67	5.05
539.10	31.11	867.25	81.67	1195.39	4.09
550.82	35.96	878.96	84.12	1207.11	3.42
562.54	38.30	890.68	85.91	1218.83	2.75
574.26	37.63	902.40	85.43	1230.55	2.29
585.98	37.77	914.12	84.92	1242.27	1.84
597.70	39.89	925.84	83.68	1253.99	1.51

Table B6 (cont'd)

609.42	41.63	937.56	82.43	1265.71	1.23
621.14	40.53	949.28	79.92	1277.43	1.01
632.85	39.44	961.00	77.23		

Table B7: Cross Section Data from LisFus for the Production of ^{44}Sc through the ^{16}O + ^{40}Ca Fusion Evaporation Reaction

Energy of ^{40}Ca Beam (MeV)	Cross Section (mb)	Energy of ^{40}Ca Beam (MeV), continued	Cross Section (mb), continued	Energy of ^{40}Ca Beam (MeV), continued	Cross Section (mb), continued
292.99	1.68	574.26	17.02	855.53	38.85
304.71	3.59	585.98	16.13	867.25	35.96
316.43	5.30	597.70	15.24	878.96	32.74
328.15	6.11	609.42	12.74	890.68	29.36
339.87	6.66	621.14	10.23	902.40	25.91
351.59	5.97	632.85	11.01	914.12	23.39
363.31	5.20	644.57	11.87	925.84	21.27
375.03	4.00	656.29	13.02	937.56	19.15
386.74	2.88	668.01	14.18	949.28	17.05
398.46	2.15	679.73	16.47	961.00	15.08
410.18	1.60	691.45	18.85	972.72	13.19
421.90	2.15	703.17	21.32	984.44	11.53
433.62	2.95	714.89	23.80	996.16	10.03
445.34	5.53	726.61	24.32	1007.88	8.66
457.06	8.25	738.33	24.58	1019.60	7.39
468.78	12.18	750.05	27.47	1031.32	6.25
480.50	15.92	761.77	30.78	1043.04	5.23
492.22	17.63	773.49	33.86	1054.76	4.36
503.94	19.29	785.21	36.90	1066.48	3.64
515.66	20.21	796.93	36.84	1078.20	2.90
527.38	21.07	808.65	36.07	1089.92	2.13
539.10	20.87	820.37	38.41	1101.64	1.60
550.82	20.61	832.09	41.57	1113.36	1.31
562.54	18.81	843.81	40.81	1125.08	1.03

Table B8: Cross Section Data from LisFus for the Production of ^{48}V through the ^{16}O + ^{40}Ca Fusion Evaporation Reaction

Energy of ^{40}Ca Beam (MeV)	Cross Section (mb)	Energy of ^{40}Ca Beam (MeV), continued	Cross Section (mb), continued	Energy of ^{40}Ca Beam (MeV), continued	Cross Section (mb), continued
210.95	4.96	363.31	9.20	515.66	25.39
222.67	10.94	375.03	16.74	527.38	21.11
234.39	24.75	386.74	24.44	539.10	17.41
246.11	36.77	398.46	33.09	550.82	13.75
257.83	41.37	410.18	41.51	562.54	11.14
269.55	43.27	421.90	48.52	574.26	8.55
281.27	33.88	433.62	54.42	585.98	6.83
292.99	24.76	445.34	52.43	597.70	5.11
304.71	16.82	457.06	50.30	609.42	3.93
316.43	9.79	468.78	47.10	621.14	2.75
328.15	6.88	480.50	43.56	632.85	2.05
339.87	4.77	492.22	36.54	644.57	1.38
351.59	6.52	503.94	29.71	656.29	1.01

Table B9: Cross Section Data from LisFus for the Production of ^{48}Cr through the ^{16}O + ^{40}Ca Fusion Evaporation Reaction

Energy of ^{40}Ca Beam (MeV)	Cross Section (mb)	Energy of ^{40}Ca Beam (MeV), continued	Cross Section (mb), continued	Energy of ^{40}Ca Beam (MeV), continued	Cross Section (mb), continued
105.48	1.66	304.71	46.58	503.94	81.33
117.20	2.03	316.43	27.61	515.66	67.60
128.91	2.24	328.15	22.79	527.38	54.00
140.63	1.35	339.87	20.64	539.10	42.54
152.35	0.57	351.59	31.26	550.82	31.31
164.07	0.32	363.31	44.55	562.54	26.14
175.79	0.45	375.03	71.56	574.26	20.99
187.51	2.41	386.74	97.72	585.98	16.82
199.23	9.68	398.46	119.12	597.70	12.65
210.95	40.11	410.18	138.62	609.42	9.68
222.67	71.99	421.90	146.12	621.14	6.71
234.39	109.94	433.62	152.34	632.85	4.84
246.11	139.76	445.34	149.30	644.57	2.99
257.83	135.91	457.06	144.95	656.29	2.25
269.55	127.02	468.78	129.61	668.01	1.57
281.27	97.12	480.50	114.17	679.73	1.17
292.99	68.69	492.22	97.65		

Table B10: Cross Section Data from LisFus for the Production of ^{52}Mn through the ^{16}O + ^{40}Ca Fusion Evaporation Reaction

Energy of ^{40}Ca Beam (MeV)	Cross Section (mb)
128.91	1.99
140.63	13.01
152.35	32.64
164.07	98.41
175.79	152.92
187.51	154.53
199.23	146.06
210.95	93.70
222.67	47.54
234.39	27.30
246.11	10.15
257.83	5.76
269.55	2.05
281.27	1.16

Chapter 3: ^{48}Ca Irradiation

The program LISE++ was used to verify the relative production rate of ^{47}Ca through fragmentation reactions with a 140 and a 189 MeV/nucleon ^{48}Ca. To find these values, the following settings where used in the program with both beam energies. The components in the beam line were (in order) a 0.57 mm thick target of Ti64 alloy (86% Ti, 10% Al, and 4% V by stoichiometry, 4.43 g/cm^3), a stripper layer of water (67% H, 33% O by stoichiometry, 1 g/cm^3), and a material layer of iron. This set up represents the isotope harvesting target as a thin shell of Ti64 alloy and a thick internal layer of water. As the beam travels through the water layer, ^{47}Ca is formed through fragmentation reactions on ^{1}H and ^{16}O/^{18}O nuclei. The product continues with a forward momentum and must reach the material layer to be “detected” by

the program. Therefore, the thickness of the water layer was optimized for each beam energy, as it needs to be thick enough to allow for the beam to complete all possible fragmentation reactions and thin enough to allow for the products to have enough energy to escape and implant in the material layer. The water layer was optimized to 14.5 mm and 25.6 mm for the 140 and 189 MeV/nucleon beam, respectively. These settings and a beam intensity of 4.992 X 10^{11} pps for both beam energies for were used to find the percent primary beam conversion to ^{47}Ca.

APPENDIX C: STABLE ELEMENTAL ANALYSIS

Table C1: Wavelengths Used for Identification and Quantification of Stable Elements in System Water

Element	Wavelength Analyzed (nm)
Al	396.152
Fe	238.204
Ni	231.604
Si	212.412, 251.611
P	213.618
Ca	317.933, 396.847, 422.673
K	766.491, 769.897
Mg	279.553
Na	568.821, 589.592
B	249.772
Zn	213.857
S	181.972

Table C2: ICP-OES Instrument Settings Used in Chapter 5 and 6
The boost and the snout purge were both turned on during all calibrations and sample runs. Also, the "fast pump" was turned off during rinse times.

Instrument Setting	Value Set
Pump speed	11 rpm
Pump uptake rate (mL/min)	25 mL/min
Pump inject rate (mL/min)	7.0 mL/min
Valve uptake delay	6.1 seconds
RF power	1.3 kW
Bubble injection time	0 seconds
Preemptive rinse time	0 seconds
Uptake delay	0 seconds
Rinse time	0 seconds
Read time	8 seconds
Viewing mode	SVDV
Nebulizer flow	0.70 L/min
Plasma flow	12.0 L/min
Aux flow	1.00 L/min

APPENDIX D: PRODUCTION RATE MEAUSREMENTS IN CHAPTER 5

Water Volume Measurements

The volume in the system was carefully measured to accurately find the total activity in the system when each water sample was taken. Throughout the irradiation, every water sample taken was carefully weighed and the mass and time of removal were recorded. Following the experiment, the total remaining water volume in the system was measured twice in the same manner. Together, this information gave the total water volume in the system at the time in which each water sample was withdrawn for the production rate measurement. This is important because the activities for each radionuclide measured in the 250 mL water samples were multiplied by a factor to account for the total activity in the isotope harvesting system water.

The water volume remaining in the system after the irradiation was measured by quantifying the dilution factor of a $CaCl_2$ sample added to the system. 100 mL of a 7500 ppm Ca^{2+} solution was spiked into the water reservoir of the isotope harvesting system. The water was circulated through all components of the system to thoroughly mix the spiked Ca^{2+}. Mixing was verified by steady readings on the conductivity probes used throughout the system to indicate the level of dissolved ions in the water. A water sample of about 40 mL was then removed and weighted. This dilution method was repeated after using the large mixed bed resins to reduce the conductivity of the system water to a background of about 200 nS/cm. Another sample was taken to measure the baseline concentration of Ca^{2+} before the second measurement.

These diluted samples from the system as well as a sample of the original $CaCl_2$ solution were diluted with 1.4% HNO_3 and the Ca^{2+} concentration was quantified with ICP-OES. Standards of 0-10 ppm Ca^{2+} were produced in 1.4% HNO_3 and wavelengths of 318, 396, and 422 nm were used to measure the Ca^{2+} concentration. The relative standard deviation between replicate measurements of each sample at each wavelength was taken as the error in the concentration measurements. Then, an average concentration was found across the three wavelengths for each sample.

Using the known volume of spike solution added to the system and the measured concentrations for the spike solution and the diluted sample from the water system, a volume of 50.33(1) L was found for the first measurement and 49.05(1) L for the second measurement. With the known water volumes that were removed from the system through these measurements and during the irradiation, an initial average volume of 52.8(6) L was found. Additionally, multiplication factors for water samples 1-4 were found to be 211.1(4), 206.1(4), 201.7(4), and 190(2) respectively. The factors for water samples 1-3 were used in the production rate calculations, while the factor for water sample 4 was used to find a collection efficiency of ^{47}Ca from the water system.

Geometry Correction Measurements

A point source of the radionuclides eluted from the collection resin bed in Chapter 6 was made by putting 0.1 mL of this eluate into a microcentrifuge tube. This sample was measured at 25 and 50 cm from the detector face. The contents of the tube were then transferred completely (transfer verified with gamma spectroscopy measurements of the tube) to a 250 mL volume of water in the same plastic container used for measurements of the water samples for

the production rate measurement. This sample contained the same activity as the point source so any differences in the measured activity other than a decay correction was attributed to the difference in geometry and the larger volume of water that could attenuate the gamma rays before they escape the sample.

Measurements of both the point source and the 250 mL water volume were compared at 25 and 50 cm to find the geometry correction factors. These factors demonstrated a general trend of decreasing with increasing gamma-ray energies. A linear fit was determined for the geometric correction factors with errors from counting statistics at each distance from the detector. The fit was used to determine correction factors for each gamma ray, including those from shorter-lived radionuclides, such as ^{44,45}K, ^{34m,38,39}Cl, and ^{38}S, and the longer-lived ^{46}Sc which were not detected in the sample used but did require a correction factor for other measured samples. The errors associated with each factor were found by propagating the uncertainty in the slope and y-intercept determined with the linear fit. The measured correction factors and the linear trend found for each distance are shown in Figure 5.2. In practice, the geometry correction factors were used to multiply the measured activities by each gamma line in the water samples used to calculate the production rates. This correction was necessary as the raw activity measurements from the water samples are 5-20% lower than the true activity present and would have produced an underestimated production rate for all radionuclides.

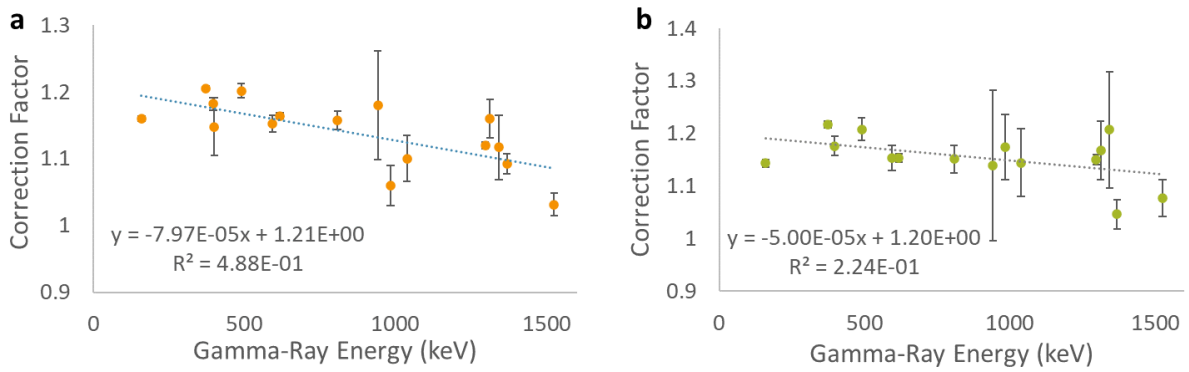

Figure D1: Linear Trends Used to Interpolate Geometry Correction Factors
The correction factors for 25 cm (a) and 50 cm (b) from the detector face are given with a linear fit to these data points.

REFERENCES

REFERENCES

[1] M. Heron, Natl. Vital Stat. Reports **66**, (2017).

[2] M. B. Sporn, Lancet **347**, 1377 (1996).

[3] C. Müller, Molecules **18**, 5005 (2013).

[4] K. Siwowska, R. Schmid, S. Cohrs, R. Schibli, and C. Müller, Pharmaceuticals **10**, 72 (2017).

[5] C. Müller, M. Bunka, S. Haller, U. Köster, V. Groehn, P. Bernhardt, N. Van Der Meulen, A. Türler, and R. Schibli, J. Nucl. Med. **55**, 1658 (2014).

[6] M. Fani, L. Del Pozzo, K. Abiraj, R. Mansi, M. L. Tamma, R. Cescato, B. Waser, W. A. Weber, J. C. Reubi, and H. R. Maecke, J. Nucl. Med. **52**, 1110 (2011).

[7] S. C. Srivastava, Semin Nucl Med **42**, 151 (2012).

[8] T. W. Burrows, Nucl. Data Sheets **108**, 923 (2007).

[9] J. A. O'Donoghue, M. Bardies, and T. E. Wheldon, J. Nucl. Med. **36**, 1902 (1995).

[10] K. A. Domnanich, C. Müller, M. Benešová, R. Dressler, S. Haller, U. Köster, B. Ponsard, R. Schibli, A. Türler, and N. P. van der Meulen, EJNMMI Radiopharm. Chem. **2**, 5 (2017).

[11] C. Müller, K. A. Domnanich, C. A. Umbricht, and N. P. Van Der Meulen, Br. J. Radiol. **91**, (2018).

[12] E. Eppard, A. De La Fuente, M. Benešová, A. Khawar, R. A. Bundschuh, F. C. Gärtner, B. Kreppel, K. Kopka, M. Essler, and F. Rösch, Theranostics **7**, 4359 (2017).

[13] C. Muller, M. Bunka, J. Reber, C. Fischer, K. Zhernosekov, A. Turler, and R. Schibli, J. Nucl. Med. **54**, 2168 (2013).

[14] B. Singh and J. Chen, Nucl. Data Sheets **126**, 1 (2015).

[15] J. Chen, B. Singh, and J. A. Cameron, Nucl. Data Sheets **112**, 2357 (2011).

[16] E. A. McCutchan, Nucl. Data Sheets **113**, 1735 (2012).

[17] F. G. Kondev, Nucl. Data Sheets **159**, 1 (2019).

[18] R. P. Baum, A. Singh, M. Benešová, C. Vermeulen, S. Gnesin, U. Köster, K. Johnston, D.

Müller, S. Senftleben, H. R. Kulkarni, A. Türler, R. Schibli, J. O. Prior, N. P. van der Meulen, C. Müller, J. Stanja, F. Wienholtz, and K. Zuber, Dalt. Trans. **54**, 2121 (2017).

[19] R. Misiak, R. Walczak, B. Wąs, M. Bartyzel, J. W. Mietelski, and A. Bilewicz, J. Radioanal. Nucl. Chem. **313**, 429 (2017).

[20] M. U. Khandaker, K. Kim, M. W. Lee, K. S. Kim, G. N. Kim, Y. S. Cho, and Y. O. Lee, Appl. Radiat. Isot. **67**, 1348 (2009).

[21] L. F. Mausner, K. L. Kolsky, V. Joshi, and S. C. Srivastava, Appl. Radiat. Isot. **49**, 285 (1998).

[22] S. Rane, J. T. Harris, and V. N. Starovoitova, Appl. Radiat. Isot. **97**, 188 (2015).

[23] M. Yagi and K. Kondo, Int. J. Appl. Radiat. Isot. **28**, 463 (1977).

[24] M. Mamtimin, F. Harmon, and V. N. Starovoitova, Appl. Radiat. Isot. **102**, 1 (2015).

[25] C. S. Loveless, L. L. Radford, S. J. Ferran, S. L. Queern, M. R. Shepherd, and S. E. Lapi, EJNMMI Res. **9**, (2019).

[26] D. A. Rotsch, M. A. Brown, J. A. Nolen, T. Brossard, W. F. Henning, S. D. Chemerisov, R. G. Gromov, and J. Greene, Appl. Radiat. Isot. **131**, 77 (2018).

[27] L. K. Peker, Nucl. Data Sheets **68**, 271 (1993).

[28] T. W. Burrows, Nucl. Data Sheets **107**, 1747 (2006).

[29] O. B. Tarasov and D. Bazin, (2008).

[30] E. P. Abel, M. Avilov, V. Ayres, E. Birnbaum, G. Bollen, G. Bonito, T. Bredeweg, H. Clause, A. Couture, J. DeVore, M. Dietrich, P. Ellison, J. Engle, R. Ferrieri, J. Fitzsimmons, M. Friedman, D. Georgobiani, S. Graves, J. Greene, S. Lapi, C. S. Loveless, T. Mastren, C. Martinez-Gomez, S. McGuinness, W. Mittig, D. Morrissey, G. Peaslee, F. Pellemoine, J. D. Robertson, N. Scielzo, M. Scott, G. Severin, D. Shaughnessy, J. Shusterman, J. Singh, M. Stoyer, L. Sutherlin, A. Visser, and J. Wilkinson, J. Phys. G Nucl. Part. Phys. **46**, 100501 (2019).

[31] D. J. Morrissey, B. M. Sherrill, M. Steiner, A. Stolz, and I. Wiedenhoever, Nucl. Instruments Methods Phys. Res. Sect. B Beam Interact. with Mater. Atoms **204**, 90 (2003).

[32] A. Pen, T. Mastren, G. F. Peaslee, K. Petrasky, P. A. Deyoung, D. J. Morrissey, and S. E. Lapi, Nucl. Instruments Methods Phys. Res. Sect. A Accel. Spectrometers, Detect. Assoc. Equip. **747**, 62 (2014).

[33] T. Mastren, A. Pen, G. F. Peaslee, N. Wozniak, S. Loveless, S. Essenmacher, L. G. Sobotka, D. J. Morrissey, and S. E. Lapi, Sci. Rep. **4**, 6706 (2014).

[34] T. Mastren, A. Pen, S. Loveless, B. V. Marquez, E. Bollinger, B. Marois, N. Hubley, K. Brown, D. J. Morrissey, G. F. Peaslee, and S. E. Lapi, Anal. Chem. **87**, 10323 (2015).

[35] C. S. Loveless, B. E. Marois, S. J. Ferran, J. T. Wilkinson, L. Sutherlin, G. Severin, J. A. Shusterman, N. D. Scielzo, M. A. Stoyer, D. J. Morrissey, J. D. Robertson, G. F. Peaslee, and S. E. Lapi, Appl. Radiat. Isot. **157**, 109023 (2020).

[36] K. A. Domnanich, E. P. Abel, H. K. Clause, C. Kalman, W. Walker, and G. W. Severin, Nucl. Instruments Methods Phys. Res. Sect. A Accel. Spectrometers, Detect. Assoc. Equip. **959**, 163526 (2020).

[37] E. P. Abel, H. K. Clause, and G. W. Severin, Appl. Radiat. Isot. **158**, 109049 (2020).

[38] T. Mastren, A. Pen, G. F. Peaslee, N. Wozniak, S. Loveless, S. Essenmacher, L. G. Sobotka, D. J. Morrissey, and S. E. Lapi, Sci. Rep. **4**, 1 (2014).

[39] M. Avilov, A. Aaron, A. Amroussia, W. Bergez, C. Boehlert, T. Burgess, A. Carroll, C. Colin, F. Durantel, P. Ferrante, T. Fourmeau, V. Graves, C. Grygiel, J. Kramer, W. Mittig, I. Monnet, H. Patel, F. Pellemoine, R. Ronningen, and M. Schein, Nucl. Instruments Methods Phys. Res. Sect. B Beam Interact. with Mater. Atoms **376**, 24 (2016).

[40] E. P. Abel, K. Domnanich, C. Kalman, W. Walker, J. W. Engle, T. E. Barnhart, and G. Severin, Nucl. Instruments Methods Phys. Res. Sect. B Beam Interact. with Mater. Atoms **478**, (2020).

[41] E. P. Abel, K. Domnanich, H. K. Clause, C. Kalman, W. Walker, J. A. Shusterman, J. Greene, M. Gott, and G. W. Severin, ACS Omega (2020).

[42] D. W. McKee, J. Catal. **14**, 355 (1969).

[43] A. Gavron, Phys. Rev. C **21**, 230 (1980).

[44] D. B. O.B. Tarasov, Nucl. Instruments Methods Phys. Res. B **204**, 174 (2003).

[45] V. Kanike, J. meesungnoen, and J. P. Jay-Gerin, Austin J. Nucl. Med. Radiother. **2**, 1011 (2015).

[46] V. Kanike, J. Meesungnoen, and J.-P. Jay-Gerin, RSC Adv. **5**, 43361 (2015).

[47] J. Meesungnoen and J. P. Jay-Gerin, J. Phys. Chem. A **109**, 6406 (2005).

[48] B. Pastina and J. A. LaVerne, J. Phys. Chem. A **103**, 1592 (1999).

[49] J. F. Ziegler, M. D. Ziegler, and J. P. Biersack, Nucl. Instruments Methods Phys. Res. Sect. B Beam Interact. with Mater. Atoms **268**, 1818 (2010).

[50] M. S. Basunia, Nucl. Data Sheets **114**, 1189 (2013).

[51] T. W. Burrows, Nucl. Data Sheets **108**, 923 (2007).

[52] Y. Dong and H. Junde, Nucl. Data Sheets **128**, 185 (2015).

[53] R. B. Firestone, Nucl. Data Sheets **108**, 2319 (2007).

[54] N. Nica and B. Singh, Nucl. Data Sheets **113**, 1563 (2012).

[55] D. R. Tilley, C. M. Cheves, J. L. Godwin, G. M. Hale, H. M. Hofmann, J. H. Kelley, C. G. Sheu, and H. R. Weller, Nucl. Phys. A **708**, 3 (2002).

[56] D. R. Tilley, H. R. Weller, C. M. Cheves, and R. M. Chasteler, Nucl. Phys. A **595**, 1 (1995).

[57] N. E. Bibler, J. Phys. Chem. **79**, 1991 (1975).

[58] J. A. LaVerne, J. Phys. Chem. **92**, 2808 (1988).

[59] J. A. LaVerne, in *Charg. Part. Phot. Interact. with Matter Chem. Physicochem. Biol. Consequences with Appl.* (n.d.).

[60] F. Nelson, T. Murase, and K. A. Kraus, J. Chromatogr. A **13178**, 505 (1964).

[61] K. A. Kraus and F. Nelson, in *Proc. Int. Conf. Peac. Uses At. Energy Nucl. Chem. Eff. Irradiat.* (1956), pp. 113–125.

[62] N. Takeno, *Atlas of Eh-PH Diagrams: Intercomparison of Thermodynamic Databases* (2005).

[63] C. S. Loveless, B. E. Marois, S. J. Ferran, J. T. Wilkinson, L. Sutherlin, G. Severin, J. A. Shusterman, N. D. Scielzo, M. A. Stoyer, D. J. Morrissey, J. D. Robertson, G. F. Peaslee, and S. E. Lapi, Appl. Radiat. Isot. **157**, 109023 (2020).

[64] T. Sato, Y. Iwamoto, S. Hashimoto, T. Ogawa, T. Furuta, S. Abe, T. Kai, P. Tsai, N. Matsuda, H. Iwase, N. Shigyo, L. Sihver, and K. Niita, J. Nucl. Sci. Technol. **55**, 684 (2018).

[65] M. Shamsuzzoha Basunia, Nucl. Data Sheets **112**, 1875 (2011).

[66] B. Singh and J. A. Cameron, Nucl. Data Sheets **92**, 1 (2001).

[67] T. W. Burrows, Nucl. Data Sheets **109**, 171 (2008).

[68] K. Neubauer and L. Thompson, Spectroscopy **26**, 24 (2011).

[69] R. (Eds. . Qaim, S.M., Tárkayáni, F., Capote, Iaea-Tecdoc-1211 292 (2001).

[70] E. P. Abel, H. K. Clause, and G. W. Severin, Appl. Radiat. Isot. **158**, (2020).

[71] T. E. Gangwer, M. Goldstein, and K. K. S. Pillay, (1977).

[72] Y. Sugo, Y. Izumi, Y. Yoshida, S. Nishijima, Y. Sasaki, T. Kimura, T. Sekine, and H. Kudo, Radiat. Phys. Chem. **76**, 794 (2007).

[73] E. P. Horwitz, D. R. McAlister, A. H. Bond, and J. E. Barrans, Solvent Extr. Ion Exch. **23**, 319 (2005).

[74] S. S. Raiman, A. Flick, O. Toader, P. Wang, N. A. Samad, Z. Jiao, and G. S. Was, J. Nucl. Mater. **451**, 40 (2014).

[75] P. Wang and G. S. Was, J. Mater. Res. **30**, 1335 (2015).

[76] W. Jimin and H. Xiaolong, Nucl. Data Sheets **144**, 1 (2017).

[77] F. T. Tárkányi, A. V. Ignatyuk, A. Hermanne, R. Capote, B. V. Carlson, J. W. Engle, M. A. Kellett, T. Kibedi, G. N. Kim, F. G. Kondev, M. Hussain, O. Lebeda, A. Luca, Y. Nagai, H. Naik, A. L. Nichols, F. M. Nortier, S. V. Suryanarayana, S. Takács, and M. Verpelli, *Recommended Nuclear Data for Medical Radioisotope Production: Diagnostic Gamma Emitters* (2019).

[78] J. M. Alexander and D. H. Sisson, Physical **128**, 2288 (1962).

[79] M. de Jong, R. Valkema, F. Jamar, L. K. Kvols, W. A. P. Breeman, C. Smith, S. Pauwels, and E. P. Krenning, Semin. Nucl. Med. **XXXII**, 133 (2002).

[80] F. W. E. Strelow, **56**, 1053 (1984).

[81] D. Reher, H. H. Hansen, R. Vaninbroukx, M. J. Woods, C. E. Grant, S. E. M. Lucas, J. Bouchard, J. Morel, and R. Vatin, Appl. Radiat. Isot. **37**, 973 (1986).

[82] J. W. T. Meadows and V. A. Mode, J. Inorg. Nucl. Chem. **30**, 361 (1968).

[83] H. Mommsen, I. Perlman, and J. Yellin, Nucl. Instruments Methods **177**, 545 (1980).

[84] M. B. Lewis, Nucl. Data Sheets 313 (1970).

[85] L. Burkinshaw, D. H. Marshall, and C. B. Oxby, Int. J. Appl. Radiat. Isot. **20**, 393 (1969).

[86] M. S. Freedman, F. T. Porter, and F. Wagner, Phys. Rev. **152**, 1005 (1966).

[87] R. E. Wood, J. M. Palms, and P. V. Rao, Nucl. Physics, Sect. A **126**, 300 (1969).

[88] H. J. Fischbeck, Phys. Rev. **173**, 1078 (1968).